Deterministic Dynamics of Stimulated Brillouin Scattering in Optical Fibres

Paul M Ripley

Submitted for the Degree of Doctor of Philosophy

Heriot-Watt University

Department of Physics

September 1995

This copy of the thesis has been supplied on condition that anyone who consults it is understood to recognise that the copyright rests with its author and that no quotation from the thesis and no information derived from it may be published without written consent of the author or the University (as may be appropriate).

I dedicate the work contained within this thesis to my Parents Eileen and Peter Ripley, for their love, support and encouragement over the years. The actual thesis I dedicate to my friends, they know who they are....

"To be, or not to be? That is the question. Whether it is nobler in the mind to bear the slings and arrows of outrageous fortune or by bearing arms oppose them".

William Shakespeare, Hamlet.

ACKNOWLEDGEMENTS

A thesis represents the final summation of several years research work. The thesis is similar to a Swan gliding upon the surface of a lake, the graceful appearance of the creature masks the turbulent struggle engaged below the waters surface. It is therefore my pleasure to acknowledge the people whose assistance has made this thesis possible, and who without this opportunity would remain anonymous and hidden from view.

I would first like to express my gratitude to Professor R.G.Harrison for his guidance and supervision over the last four years. Many thanks go to the members of the research group in particular Dr.Yu for his collaboration and providing the theoretical results, Dr.Lu and R.McIntyre for valuable discussions regarding the nature of nonlinear dynamics, Dr.Uppal who gave insight into the darker side of Nd:YAG lasers, and N.Swanston for his assistance in the laboratory and with the analytical algorithms. I would also like to thank Dr.Dambly for his thorough proof reading of the original manuscript and vital discussions concerning suggestions and constructive criticism of the work. Special thanks got to the technical staff in both the Mech.Eng and Electronic workshops whose diligence and willingness have made many an eleventh hour project possible.

Finally I would to thank my family for their support over the last four years, and a special thankyou goes to my good friends Andy, Fiona, Steve, Jørn, Wenche, Bjørn, Anne and Helena for keeping tabs on my sanity. Last but not least I thank SERC/EPSRC for the research grant and allowing me the pleasure of interailing around Europe while on conference.

ABSTRACT

This thesis presents an experimental investigation of the dynamical behaviour of stimulated Brillouin scattering (SBS), generated under cw pump conditions in a single-mode optical fibre. The dynamical features of the Stokes emission were found to be dependent upon both the incident pump power and reflectivity.

For SBS generated in an optical fibre without external feedback, both the Stokes emission and transmitted pump displayed aperiodic behaviour over a range of pumping conditions. Dimensional analysis of temporal recordings revealed the SBS process to be stochastic, and was attributed to the initiation of the stimulated process from spontaneous Brillouin scattering (noise).. The inclusion of external feedback (R_1R_2 = 0.12%) produced a dramatic transformation in the dynamical behaviour of the Stokes emission when examined with a variable pump. Below SBS threshold the dynamics were found to be stochastic and were attributed to spontaneous scattering. Operation above SBS threshold revealed a transition from stochastic to deterministic behaviour, with both periodic and quasiperiodic motion being observed. However, further variation in the pump intensity revealed the existence of a chaotic state via the quasiperiodic route, and the fractal dimension of the strange attractor was found to be ~2.1. Experiments performed with a fixed pump intensity and variable reflectivity showed a range of similar dynamical features.

Finally, the dynamical behaviour of a periodically driven, spatially extended SBS oscillator was studied for a range of both drive frequency and modulation depth. The addition of an acousto-optic modulator to provide additional degrees of freedom revealed several new forms of dynamics including a new strange attractor with a higher fractal dimension of 3.15.

TABLE OF CONTENTS

CHAPTER 1

CHAPTER 2

CHAPTER 3

CHAPTER 4

CHAPTER 5

LIST OF FIGURES

CHAPTER 1

CHAPTER 2

CHAPTER 3

CHAPTER 4

CHAPTER 5

1. Introduction

1.1 Introduction

One of the greatest unresolved problems of classical physics was the understanding of turbulence or complex evolution in a system [1]. Turbulent or chaotic behaviour was thought to exist in only complex systems described by a large/infinite number of variables. In 1963 E.N.Lorenz demonstrated chaotic behaviour for a set of three deterministic equations [2]. The significance of this breakthrough was to emphasise how chaotic and complex behaviour could be generated by a system with a low number of degrees of freedom. Prior to Lorenz's discovery, scientific thought had concentrated upon breaking down and reducing the complexity of system until an insight could be found on a simple and basic level. However, unlike conventional treatments of complex scenarios through reduction and simplification, the study of chaos and nonlinear dynamics involved the observation of a system's behaviour in its entirety. A casual glance at a nonlinear dynamical system exhibiting chaos, e.g. a driven Van der Pol oscillator [3], reveals aperiodic behaviour which appears both random and unpredictable. Erratic and unpredictable behaviour can be attributed to the presence of noise in a linear system. However, aperiodic behaviour can also be produced by a deterministic system i.e. a system described by a finite set of deterministic differential equations, and the complex temporal evolution is a direct consequence of the nonlinearity.

At the turn of the twentieth century a French mathematician, Henri Poincaré (1892), began to raise questions addressing the nature of nonlinear systems, and more

importantly developed techniques to help visualise and gain an insight into the nature of complex evolution. Concepts developed by Poincaré for studying complex behaviour involved analysing the topological structure of dynamical trajectories in an abstract phase space. In deterministic behaviour, successive states evolve continually from each other. Therefore, to construct the dynamical trajectories required for the analysis of the phase space trajectory, the set of deterministic equations that describe the nonlinear system must be treated in their full complexity. This involves considerable numerical simulation and computation. Progress in nonlinear dynamics was delayed for 50 years until the advent of the high-speed digital computer which dramatically simplified the task of numerical simulation, and the availability of graphical displays enhanced the interpretation of trajectories in the abstract phase space.

As mentioned previously the first report of chaotic behaviour in a simple low dimensional system was presented by Lorenz in 1963 [2]. While investigating turbulence in an atmospheric model in an attempt to understand weather prediction, Lorenz found that a system described by three first order nonlinear differential equations could exhibit chaotic behaviour for certain parameter values. In the same model, two characteristic features emerged which had profound implications for the interpretation and understanding of chaotic behaviour. By numerically solving the equations describing the system for a known initial condition, a unique dynamical trajectory could be found. Lorenz observed that for the same system a slight finite change in the initial conditions had a dramatic effect upon the resulting dynamical trajectory. Initially the new trajectory would closely follow the path mapped out by the original set of initial conditions. However, over a period of time the new trajectory started to move or diverge away exponentially from the original path and follow its own unique direction. This sensitivity

to initial conditions or "Butterfly effect" placed severe restrictions upon the long term predictability of a system's behaviour. The term "Butterfly effect" was used to emphasise the sensitivity of a nonlinear system by describing how the flap in a Butterfly's wings in South America could effect the weather prediction in North America, thus demonstrating how an initial small change can dramatically change the evolution of the system. Interpretation of the complex evolving trajectories obtained for different initial conditions was aided by topological analysis of the trajectories in phase space. Regardless of the initial conditions and after transients had died out, all the dynamical trajectories were attracted to a specific region in the phase space called a "strange attractor".

Since this breakthrough by Lorenz in 1963 and the rapid advances made in digital computer technology, the field of nonlinear dynamics and chaos has experienced a prolific and significant period of growth. The study of chaos has provided new conceptual and theoretical tools for understanding complex behaviour. Through analysing different nonlinear systems from various disciplines such as physics, chemistry, biology, electronics, engineering, neural networks, meteorology, geophysics and economics, characteristic universal features have been identified which are independent of the parameters describing the system. A key universal signature of the onset of chaos is the route the dynamical system undergoes before exhibiting chaotic behaviour. For a dissipative system with a low number of degrees of freedom there exists three routes to chaos which depend upon the equations and mainly the parameters of the system. Chaotic behaviour is accessed by adjusting a "control" parameter of the system. By monitoring the temporal behaviour of the system one of the three universal routes such as period-doubling [4], quasiperiodicity [5] and intermittency[6] can be identified.

The period-doubling route typically consists of a fixed period which through a change in the control parameter undergoes successive doubling in its base period until chaotic motion is observed. The quasiperiodic route occurs when a new fundamental frequency appears in the original system as the control parameter is adjusted. This new frequency mixes with the frequencies already present in the system creating complex quasiperiodic motion, and as the control parameter is changed further the quasiperiodic motion becomes unstable and the system becomes chaotic. The intermittency route to chaos begins when a regular periodic signal is interrupted by intermittent bursts of aperiodic behaviour. As the control parameter is adjusted the irregular bursting becomes more frequent in occurrence until the system fully undergoes a transition to chaos. Apart from the routes to chaos which are both universal and distinctive, there also exists several features related to chaotic behaviour which can be quantified. These quantifiable features such as Lyapunov exponents, entropy [7] and correlation dimension[8] are useful when applied to any nonlinear dynamical system. Analysis will produce powerful and interesting results for different forms of distinguishable dynamical behaviour. For example, consider the Lyapunov exponent which gives a measure of the divergence/convergence of a trajectory from an initial condition, related to a point in phase space. Two independent nonlinear systems such as a driven diode resonator [9] and a pump-modulated NdP_5O_{14} laser [10] may undergo the same route to chaos e.g. period-doubling, but both systems could have different Lyapunov exponents.

The main objective for the universal study of nonlinear systems was to provide an interchange of concepts and ideas which would improve the understanding of complex behaviour. Interest was generated in nonlinear optical systems when Haken [11] demonstrated that the Lorenz model developed to aid weather prediction was similar to

the Maxwell-Bloch model used to describe a simple laser. The normalised Maxwell-Bloch equations dictate the temporal evolution of the laser field (E), the medium polarisation (P), and the population inversion (D) of a resonantly tuned, single-mode, travelling wave, homogeneously broadened two level laser [12].

$$\frac{\partial \vec{E}}{\partial t} = \kappa \vec{P} - \kappa\left(1 + i\Delta_C\right)\vec{E}$$

$$\frac{\partial \vec{P}}{\partial t} = \gamma_{\perp}\left[\vec{E}D - \left(1 + i\Delta_A\right)\vec{P}\right]$$

$$\frac{\partial D}{\partial t} = -\gamma_{\parallel}\left[\mathrm{Re}\left(\vec{E}^{*} \cdot \vec{P}\right) + D + 1\right]$$

The parameters κ, $\gamma_{\perp}$, and $\gamma_{\parallel}$ represent the decay rates of the laser field, polarisation and population inversion respectively. The cavity and atomic detuning are given by Δ_C and Δ_A. Recognition that the Maxwell-Bloch equations were isomorphic to the Lorenz equations raised the question if lasers could exhibit chaotic behaviour. The motivation for studying instabilities and deterministic chaos in lasers had a dual purpose. Firstly, the unique simplicity and flexibility of the laser offered an invaluable nonlinear system for fundamental investigation into chaos and universality. Secondly, the recognition that most real laser systems can exhibit chaos intrinsically or by the incorporation of additional parameters, provided an important source of information for innovations in optical science and applications in technology. Another major advantage of the laser was the operating time scales inherent to the optical system [13], typically in the region of nanoseconds to microseconds. The short time scales provided an accessible system whose dynamical evolution could be studied extensively with reproducibility i.e. stochastic environmental contributions minimised, and flexibility i.e. simple selection of control parameters. The first experimental observation of chaotic laser dynamics was

made by Arecchi et al in 1982 [14] using a CO_2 laser with modulated loss. Most lasers have a reduced set of Maxwell-Bloch equations because one or two of the physical variables can be adiabatically eliminated. To permit the possibility of chaotic emission the laser system must possess at least three independent variables. Therefore, the inclusion of an additional parameter e.g. a modulator, is required to provide the necessary degrees of freedom. The first evidence of Lorenz type chaos through a period doubling route was reported by Weiss et al [15] in 1986 with an optically pumped molecular laser (NH_3) experiment.

Recently, attention has focused upon several new areas of interest, most notably spatial-temporal complexity where consideration is given to both the temporal and transverse structure of an optical beam, and also the investigation into the dynamical behaviour of fundamental nonlinear optical processes e.g. harmonic generation, optical mixing and stimulated scattering phenomena. In the next section a brief introduction will be presented outlining some of the most commonly occurring nonlinear optical processes.

1.2 Nonlinear Optics and Stimulated Scattering Phenomena

The unique ability of the laser (invented by Maiman in 1960 [16]) for providing a directional, coherent source of light gave rise to the birth of nonlinear optics. The second nonlinear optical process to be observed was second-harmonic generation by Franken et al in 1961 [17]. The beam from a Q-switched ruby laser operating at a wavelength of 694.3μm was focused upon the surface of a quartz crystal. The emerging

radiation was examined with a spectrometer and found to contain a new wavelength at 347.1μm corresponding to the second harmonic. In linear optics the response of an optical material is proportional to the incident optical field. However, in nonlinear optical phenomena the response of the material depends in a nonlinear manner upon the intensity of the incident optical field. For example, in the second-harmonic generation process the atomic response of the optical material has a quadratic dependence upon the amplitude of the optical field. A description of the optical nonlinearity requires a precise relationship between how the macroscopic dipole moment per unit volume, or polarisation P of the material depends upon the strength E of the applied optical field. The nonlinear optical response is described by the following power series

$$\vec{P} = \vec{\chi}^{(1)} \cdot \overline{E} + \vec{\chi}^{(2)} \cdot \overline{E} \cdot \overline{E} + \vec{\chi}^{(3)} \cdot \overline{E} \cdot \overline{E} \cdot \overline{E} + \cdots \quad (1)$$

The polarisation P is expressed in terms of the electric field E and the optical susceptibility χ. The first term in the power series represents the conventional i.e. linear response of the optical material. The nonlinear terms are given by $\chi^{(2)}$ and $\chi^{(3)}$ which are referred to as the second- and third-order nonlinear optical susceptibilities, respectively. Second-order nonlinear optical processes include second-harmonic generation, optical rectification, sum and difference frequency generation and optical parametric oscillation. For second order effects to occur the optical material or crystal must have a non-centrosymmetric geometry i.e. display non-inversion symmetry. Dynamical instabilities and chaos have been reported for both intracavity second-harmonic generation [18] and optical parametric oscillation [19]. The main application of nonlinear optical processes is to extend the range of wavelengths available from a fixed wavelength laser. The observation of chaotic behaviour in optical processes with important technological

applications has motivated research into both fundamental light-matter interactions and also algorithms for controlling chaos via selective system parameters [20]. Third order nonlinear optical processes can occur in both centrosymmetric and non-centrosymmetric media. These processes include third-harmonic generation, four-wave mixing and stimulated scattering phenomena. All the optical processes outlined so far involve the interaction of light waves with a medium. There are three stimulated scattering processes, Rayleigh, Raman and Brillouin and these are characterised by the physical mechanism involved in the light-medium interaction. Rayleigh scattering is the scattering of light from non-propagating density fluctuations in the optical medium. It is called a quasi-elastic scattering process because the frequency shift induced in the scattered light is almost negligible compared with the Raman and Brillouin processes. Raman scattering is the direct result of the interaction of light with the vibrational modes of the molecules which constitute the medium. The frequency shifts induced by Raman scattering are quite large, e.g. for a silica cored fibre pumped at a wavelength of 1μm the resulting frequency spectra is broadened to 40THz [21]. In Brillouin scattering the light waves are scattered by acoustic waves present in the medium, and is described as the scattering of light by acoustic waves. The frequency shifts involved in Brillouin scattering are relatively small compared to Raman scattering, typically in the region of GHz. The first studies made addressing the nonlinear dynamical behaviour of third-order effects were performed by Silberberg et al [22], and indicated that two counter-propagating light beams in a third order nonlinear medium could undergo a transition to a chaos. The first report of experimental evidence in support of chaotic stimulated Brillouin scattering generated in an optical fibre was made by Harrison et al [23]. The main objective of the

work presented in this thesis is to determine experimentally if stimulated Brillouin scattering generated in an optical fibre can exhibit deterministic dynamical features and in particular undergo a transition to chaos. The optical material selected for the Brillouin medium is a silica cored optical fibre. In the next section both a brief description of optical fibres, and the advantages offered by guiding media for the study of nonlinear optical effects are presented.

1.3 Nonlinear Fibre Optics

The first demonstration of light-guiding by total internal reflection in a dielectric medium was made by Tyndall at a Royal Institution Lecture in 1870 using a water jet. From these humble origins, the fields of optical fibre technology and guided communications evolved. Today, optical fibre technology has made possible the expansion of global telecommunications and provides an essential communication link for future developments in Information technology. Optical fibres have also facilitated the study of nonlinear optical effects due to a combination of their geometry and transmission characteristics. Recent advances in nonlinear fibre optics has made possible new techniques and optical hardware such as pulse compression, Raman- and Brillouin-fibre lasers/amplifiers and solitons.

1.3.1 Optical Fibres

Initial attempts at fabricating lightguides resulted in the production of glass rods which lacked a cladding layer. The transmission of light through the glass rod was poor

due to a combination of absorption and poor guiding. The addition of a cladding layer led to considerable improvements in the guiding of the light. Further developments in fibre fabrication technology has led to the production of fibres with very low optical attenuation. For a silica cored optical fibre the attenuation minimum of 0.2dB/km occurs at a wavelength of 1.55μm and is limited by the fundamental Rayleigh scattering process. A typical fibre geometry is shown in Figure 1.1. The central core of the fibre is doped with an impurity to increase the refractive index. The surrounding cladding layer is also doped in order to reduce the refractive index and produce a characteristic step in the index profile. The outer jacket layer is usually an acrylate material which improves the mechanical rigidity and protects the fibre from environmental damage i.e. chemical attack. A typical telecommunication fibre is fabricated by first forming the preform using the modified chemical vapour deposition (MCVD) process. Both the core and cladding are made from silica. The core is doped with germanium oxide (GeO_2) and the cladding is doped with fluorine. The preform is then drawn mechanically into a fibre of the desired dimensions. Two parameters which are used extensively to characterise optical fibres are the relative core-cladding index difference Δ defined by the following expression

$$\Delta = \frac{n_1 - n_2}{n_2},$$

and the normalised frequency parameter V by

$$V = k_0 a \sqrt{\left(n_1^2 - n_2^2\right)}$$

where $k_0 = 2\pi / \lambda$, a is the radius of the core and λ is the wavelength of light the fibre is designed to guide. Step index fibres are either single-mode or multi-mode depending upon the relative value of the normalised frequency parameter. If $V < 2.405$ then the fibre will only support a single mode, and at a wavelength of 1.55μm the corresponding

core size will be in the region of 4-6μm. Increasing the core size will allow the fibre to support more optical modes and diameters of 100μm are easily achieved.

An important and fundamental characteristic of an optical fibre is the transmission loss experienced by light travelling inside the fibre. For fixed power P_0 launched into a fibre of length L, the transmitted power P_T is given by the relationship

$$P_T = P_0 \exp(-\alpha L)$$

where α is the attenuation constant or loss of the fibre. The fibre loss depends upon the wavelength of the light with a minimum of 0.2dB/km occurring at 1.55μm, Figure 1.2.

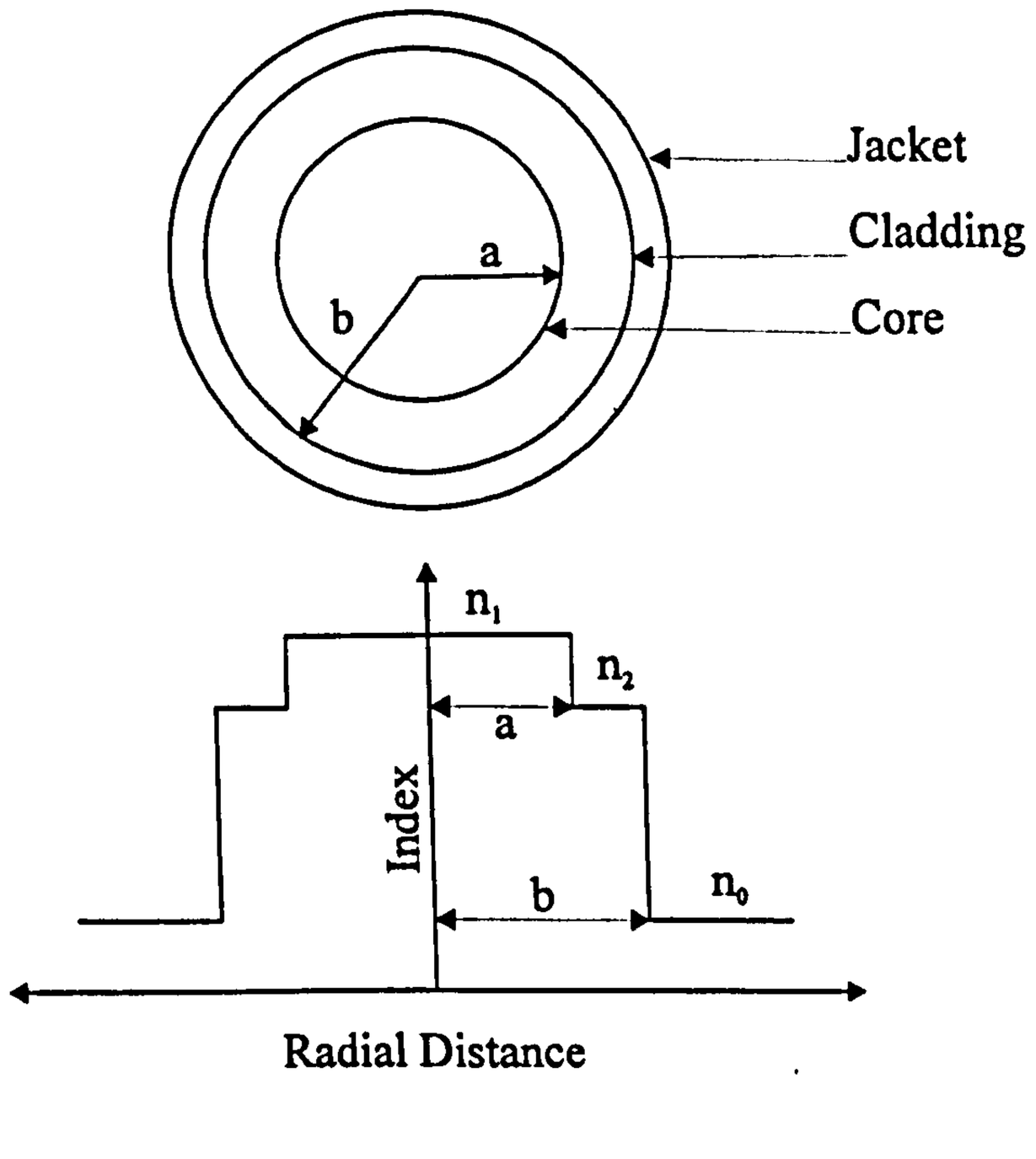

Figure 1.1 Schematic illustration of the cross-section and the refractive index profile of a step-index fibre.

There are several loss mechanisms in an optical fibre which contribute to the overall attenuation coefficient. Absorption by impurities present in the fibre creates the

predominant peak located at a wavelength of 1.37μm, Figure 1.2. The main peak is an overtone of the OH^- ion impurity which has a fundamental vibrational absorption peak located at 2.73μm. The minimum loss at 1.55μm is limited by intrinsic Rayleigh scattering which occurs because of density fluctuations frozen into the fused silica during fabrication. The Rayleigh scattering loss varies as λ^{-4} and is dominant at the shorter wavelengths, particularly in the visible region 0.4-0.75μm.

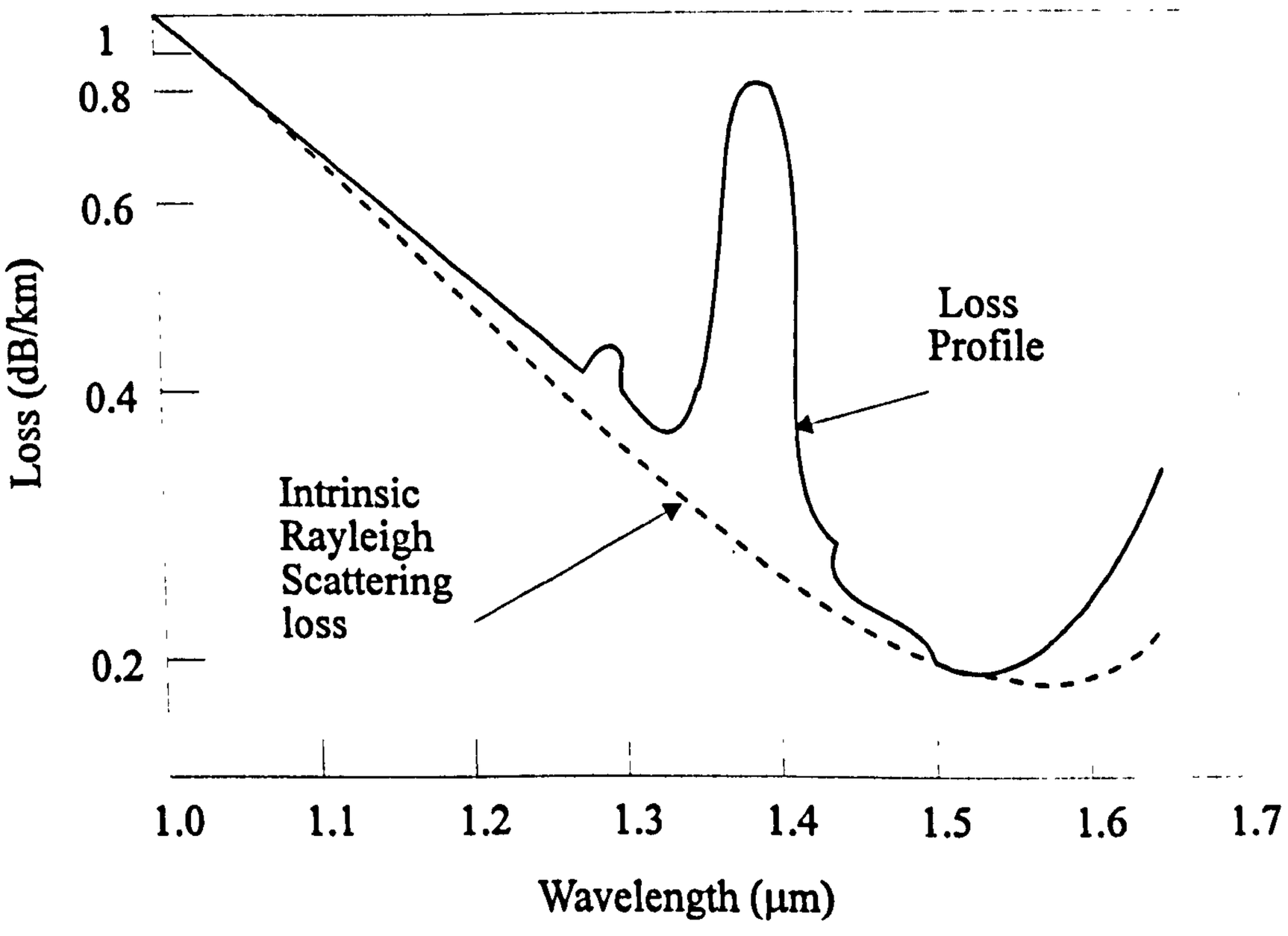

Figure 1.2 Measured loss profile of a single-mode fibre.

Another important characteristic of optical fibres is chromatic dispersion. The origin of chromatic dispersion is related to the characteristic resonant frequencies of the atoms. The refractive index of the fibre core has a frequency dependence $n(\omega)$, and therefore different spectral components will propagate at different speeds, given by

c/n(ω), through the fibre. Chromatic dispersion plays an important role in the propagation of optical pulses, and is represented by the dispersion parameter β_2 which is more commonly referred to as the group velocity dispersion parameter. For a pulse with a group velocity v_g, the group velocity dispersion parameter is given by the expression

$$\beta_2 = -\frac{1}{v_g^2}\left(\frac{dv_g}{d\omega}\right).$$

The type of dispersion experienced by a pulse depends upon the wavelength of the light. For a silica cored fibre doped with germanium oxide (GeO_2) zero dispersion occurs at a wavelength of 1.32μm. Below this wavelength the fibre exhibits normal dispersion which causes the higher frequency (blue shifted) spectral components of a pulse to propagate slower than the lower frequency (red shifted) spectral components. Above the zero dispersion wavelength the fibre displays anomalous dispersion and the higher frequency components travel faster than the lower frequency components. Acting alone dispersion can cause detrimental effects in optical communication systems due to the deformation of the optical pulses. However, group velocity dispersion when combined with self-phase modulation can produce useful effects such as pulse compression or broadening.

1.3.2 Advantages of Optical Fibres

There are several significant advantages for implementing optical fibre technology in the study and generation of nonlinear-optical effects. The improvements offered by optical fibres arise from a combination of both the fibre geometry and the material. Stimulated Brillouin scattering is a third-order nonlinear optical process,

equation (1). Most optical fibres are fabricated from silica (SiO_2) which is a centrosymmetric molecule. Therefore, the second-order nonlinear susceptibility $\chi^{(2)}$ is zero, and the lowest order nonlinearities are due to the third-order nonlinear susceptibility $\chi^{(3)}$. Even though the $\chi^{(3)}$ for silica fibres is several times smaller than other nonlinear media, nonlinear effects in fibres can be observed at relatively low power levels. The two important characteristic features of optical fibres which contribute to the possibility of nonlinear effects at modest power levels are the extremely low optical loss ($\leq$ 1 dB/km) and the small spot size (4-6μm). In an optical fibre the spot size of the optical beam is determined by the size of the core. The dielectric waveguiding property of the fibre maintains this spot size over the entire length of the fibre. Therefore the efficiency of a nonlinear optical process is significantly enhanced due to the high photon density being maintained throughout the length of the fibre. The efficiency of a nonlinear optical process generated in an optical fibre, compared to a process in a bulk medium is found by comparing the product IL_{eff} [24]. This product is used as a figure of merit for the efficiency of a nonlinear process where I is the intensity of the beam and L_{eff} is the interaction length over which the required intensity for the process can be maintained. The increase in efficiency for a nonlinear process in an optical fibre is improved by a factor [25],

$$\frac{(IL_{eff})_{fibre}}{(IL_{eff})_{bulk}} = \frac{\lambda}{\pi\omega_0^2\alpha}$$

where λ is the wavelength of the light source, α is the fibre loss and ω_0 is the radius of the fibre core. For a silica fibre with a pump laser emitting at the minimum loss wavelength 1.55μm with a fibre loss of $\alpha = 5\times10^{-7}cm^{-1}$ (0.2dB/km) and a spot radius ω = 2.5μm, the enhancement can be improved by a factor ~10^9. This dramatic enhancement

in the efficiency of the nonlinear optical process demonstrates the significant advantage of implementing optical fibres instead of bulk media for the generation of nonlinear effects at low power levels. The relatively small $\chi^{(3)}$ of silica is compensated by the characteristics of the fibre geometry which achieve a high intensity inside a low loss medium. Nonlinear effects generated inside fibres can be detrimental to optical communications. However, the contribution of these effects are minimised due to the high-speed modulation of the optical signal which reduces the average power inside the fibre.

1.3.3 Intensity Dependent Refractive Index Effects

In a silica optical fibre the lowest order nonlinear effects originate from the third-order susceptibility $\chi^{(3)}$ because of the centrosymmetricity of silica ($\chi^{(2)}=0$). The third order processes which create new frequencies such as third-harmonic generation and four-wave mixing are not particularly efficient in optical fibres due to the difficulty in achieving the appropriate phase matching conditions. Therefore, the majority of the nonlinear effects observed in a fibre are a result of the intensity dependent nonlinear refractive index, expressed below

$$\bar{n} = n_0 + n_2|E|^2 \quad \text{where} \quad n_2 = \frac{3}{8n_0}\chi^{(3)}.$$

The linear refractive index is represented by n_0 and the intensity dependent nonlinear refractive index by n_2. The two most dominant effects which occur as a result of the fibre's nonlinearity are self-phase modulation (SPM) and cross-phase modulation. Self-phase modulation describes how an optical field self-induces a phase shift as it

propagates through the fibre. SPM is most dramatic for ultrashort pulses where SPM causes spectral broadening of the pulse. Cross-phase modulation occurs when two or more optical waves co-propagate inside the fibre and interact via the nonlinear refractive index. An insight into XPM and SPM can be gained by considering the total electric field of two co-propagating waves with different frequencies,

$$\vec{E} = \hat{e}\left[E_1 \exp(-i\omega_1 t) + E_2 \exp(-i\omega_2 t) + c.c.\right].$$

The change in phase of the optical wave E_1 due to E_2 is given by the following expression

$$\phi_{NL} = n_2 k_0 L\left(|E_1|^2 + 2|E_2|^2\right).$$

This simplified expression reveals that SPM always accompanies XPM and the contribution of XPM is twice that of SPM for equally intense optical fields.

1.4 Methods for Determining Dynamical Behaviour

As discussed in the previous introductory section there exists several methods for quantifying and identifying the various forms of dynamical behaviour encountered in a nonlinear dynamical system. The techniques employed in characterising nonlinear behaviour fall into two discrete categories; qualitative and quantitative analysis. Qualitative analysis of chaos refers to techniques which can be utilised in both experiments and theoretical models to provide information concerning the route to chaos, and the actual existence of chaotic behaviour. These techniques include inspection of the time series, Phase Portrait analysis and the use of the Fast Fourier Transform algorithm. Having established the existence of chaos through the observation of a particular route,

the next important stage of analysis is to provide a quantitative statement addressing the properties of the chaos. To provide a quantitative statement several techniques can be implemented. The most commonly used techniques involve the calculation of the correlation dimension or Lyapunov exponents from a time series. Unlike the route to chaos which belongs to one of three universal signatures, the calculation of the correlation dimension, for example, will provide information relating to the nonlinear dynamical system of interest. In an experiment only the evolution of one variable is observed e.g. the output voltage of a chaotic electrical circuit or the intensity of a laser beam exhibiting instabilities. Visual inspection of the time series , e.g. an oscilloscope trace, may reveal a particular route to chaos, however, the incorporation of phase portrait and Fourier analysis can help to identify distinguishable forms of dynamical behaviour. Phase Portraits can be reconstructed from a time series using delay co-ordinates [26]. These can easily be obtained from either sampled data or real time systems utilising an oscilloscope in x-y mode with one of the channels delayed with respect to the other. Fourier analysis incorporating the Fast Fourier Transform algorithm is particularly useful for monitoring the dynamics of a system as a control parameter is adjusted. Both period-doubling and quasi-periodic routes to chaos reveal distinctive and recognisable changes in their spectrum when observed in the Fourier domain. The reaching of chaos is signified by a continuous Fourier power spectrum. A comparison of the three different methods for visualising dynamical behaviour are illustrated in Figure 1.3 for both a periodic and chaotic behaviour. The periodic state forms a closed loop or limit cycle in phase space with a discrete frequency peak occurring in the Fourier spectrum. By contrast, the chaotic signal appears aperiodic with a distinctive geometry or "attractor" in phase space. The aperiodicity of the waveform can be seen directly in the Fourier

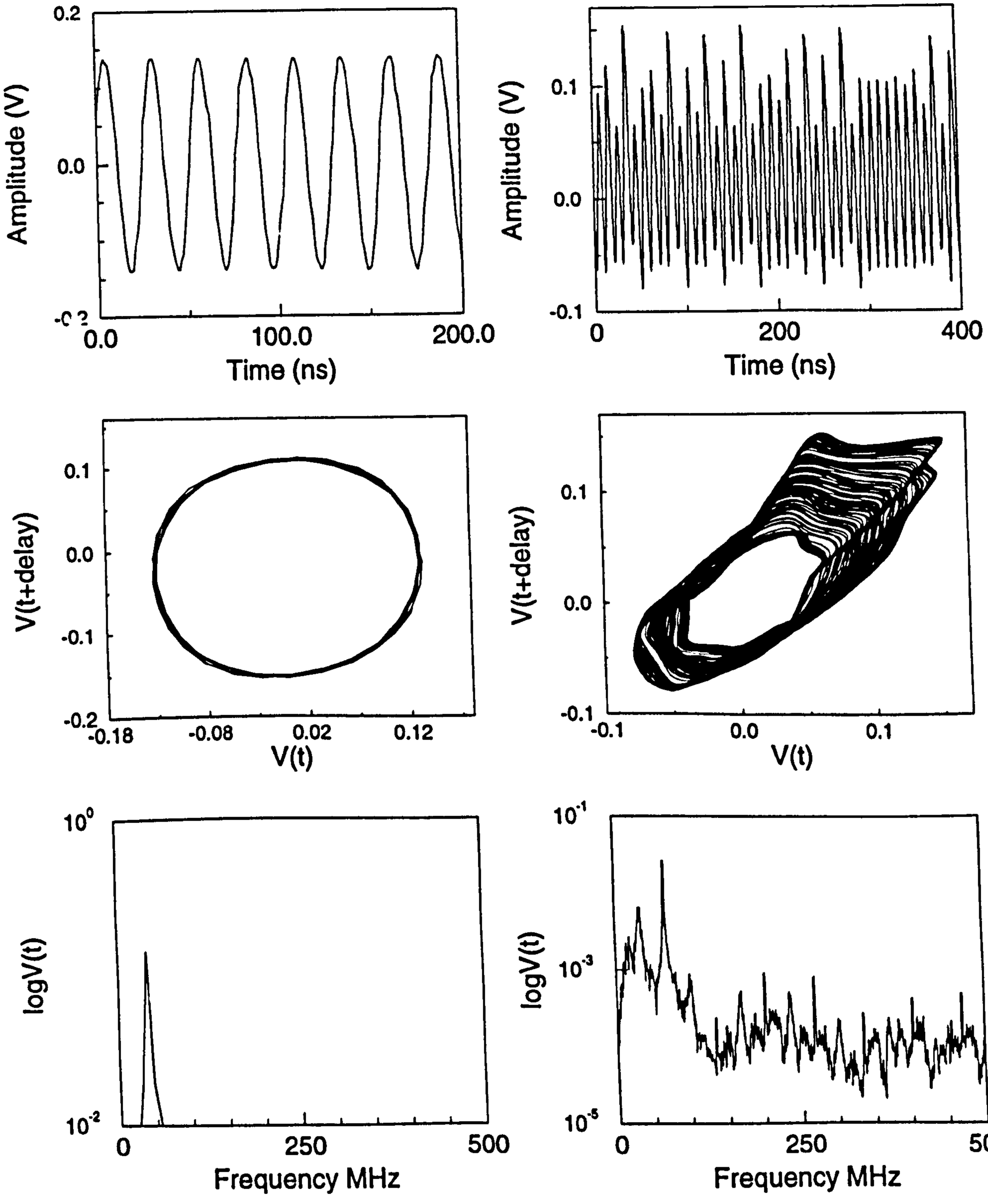

Figure 1.3 A comparison of the time series (top row), phase portrait (middle row) and Fast Fourier Transform (bottom row) for a periodic (left column), and chaotic (right column) signal. Attention is drawn to the continuous spectrum of the FFT for the chaotic signal when compared to the spectrum of the periodic signal.

spectrum. However a continuous power spectrum can also be created by noise. Thus, the presence of an aperiodic signal and a continuous spectrum is not necessarily conclusive evidence for the existence of low dimensional 'chaos. Therefore, to resolve the type of dynamical behaviour present in a system further analytical techniques are employed. The most commonly used and accepted technique for revealing the presence of chaotic behaviour is to measure the dimension or strangeness of the attractor [8] in phase space.

To calculate the dimension of the attractor in phase space a box-counting technique is used. Initially, the geometric object is covered with boxes of size R in phase space. For a two dimensional phase space squares would be used, and in a three dimensional space the squares will become cubes.The number of boxes N(R) that cover the attractor are counted. The capacity dimension is a measure of the number boxes in phase space needed to cover the attractor when the size of the boxes R goes to zero,

$$D = -\lim_{R \to 0} \frac{\log N(R)}{\log R}.$$

The previous method can become cumbersome for small values of R because of the processing required to calculate the increase in the number of boxes. A recent development for calculating the dimension of an attractor was proposed by Grassberger et al [8]. The method consists of finding the correlations between random points on the attractor. "For a set of points $\{X_i, i=1...N\}$ on the attractor obtained by embedding the time series with a delay, the exponential divergence of trajectories implies that most pairs of points (X_i, X_j) with $i \neq j$ will be dynamically uncorrelated pairs of random points" [8]. However, the points lie on the attractor and will therefore be "spatially" correlated. The spatial correlation can be measured with the correlation function defined as

$$C(R) = \lim_{N\to\infty} \frac{1}{N^2} \times \{\text{number of pairs}(i,j) \text{ whose distance } |X_i - X_j| \text{ is less than R } \}$$

Therefore by calculating the correlation function for a decreasing R, the correlation dimension can be estimated from the following expression

$$D_c = \lim_{R\to 0} \frac{\log C(R)}{\log R}.$$

Figure 1.4 shows a plot of the correlation dimension versus the embedding dimension for noise and a chaotic set of data. The embedding dimension is the dimension of the phase space in which the attractor is projected. At an embedding dimension of 4 the chaotic data has a correlation dimension of ~2.4. The non-integer dimension confirms that the attractor is a fractal and is called a "strange attractor". However, the correlation dimension for the noise keeps on increasing with the embedding dimension. This occurs because the noise is composed of random points which have no spatial correlation. Therefore, the correlation dimension does not saturate at any particular embedding dimension, and the noise expands to fill the phase space.

1.5 Thesis Outline

This thesis contains five chapters. In chapter 1 a brief introduction of nonlinear deterministic behaviour was presented with emphasis placed upon the historical background of chaos in the field of optics. Chapter 2 is concerned with the selection of a pump laser for the stimulated scattering experiments. The particular operating characteristics of the pump laser required by the nonlinear optical process are discussed.

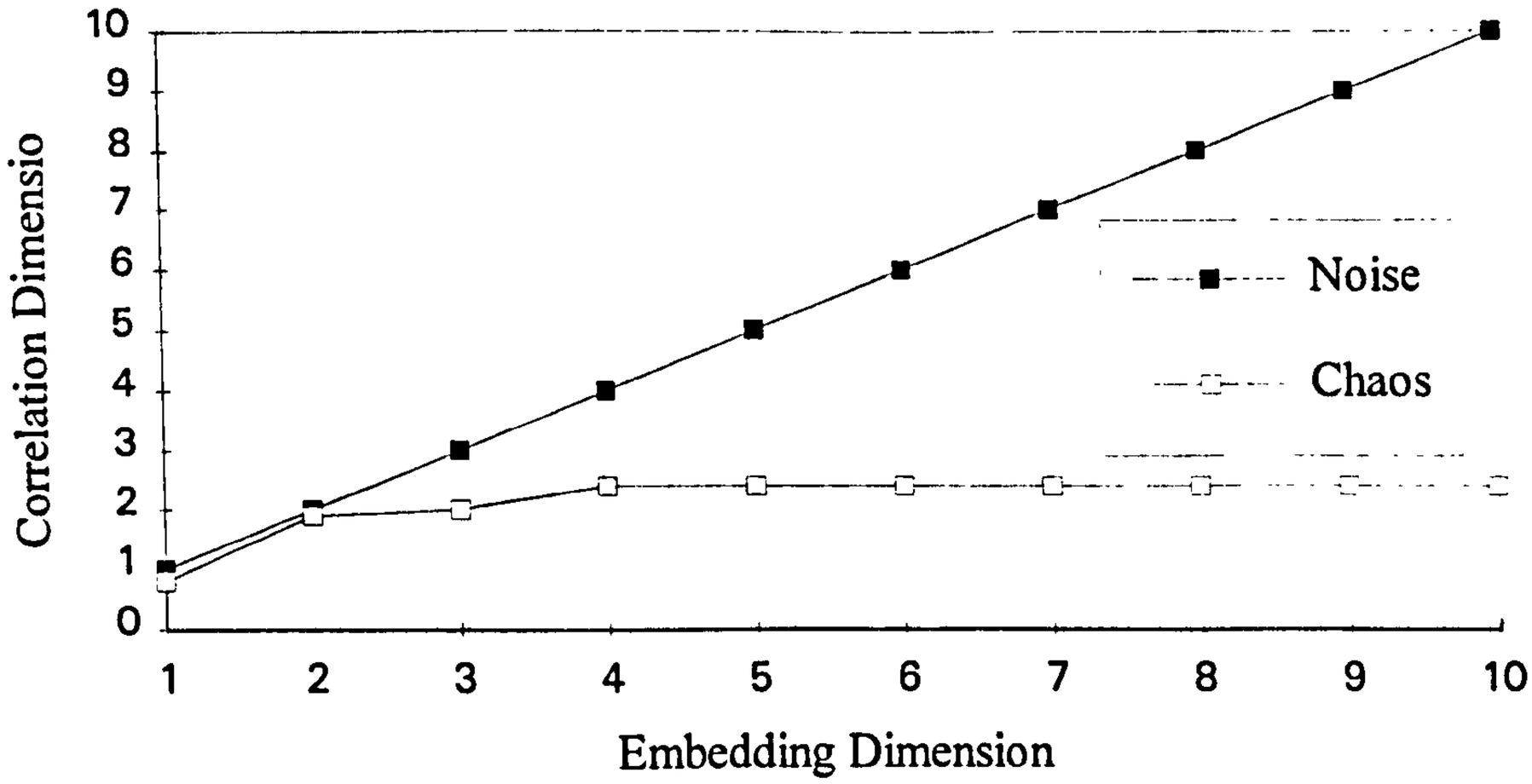

Figure 1.4 A plot of the correlation dimension for an increasing embedding dimension using a chaotic set of data and noise. The correlation dimension saturates at ~ 2.4, and the noise keeps on increasing

Special emphasis is placed upon the role of the pump laser in enhancing the dynamical behaviour of the nonlinear optical process Having established the pump laser that can fulfil the selection criteria, the remaining sections in the chapter address the design and construction of a Nd:YAG ring laser for use in the scattering experiments.

Chapter 3 contains a theoretical description of stimulated Brillouin scattering (SBS) and a review of this nonlinear optical process. Attention is directed to the dynamical behaviour of (SBS) generated in optical fibres with a new theoretical model to describe the temporal evolution. The dynamics of SBS generated in an optical fibre without additional external feedback are presented with theoretical results obtained by other members of the research group.

In Chapter 4 the temporal behaviour of SBS generated in an optical fibre with the addition of external feedback is investigated in detail. A revised theoretical model is presented which includes the addition of external feedback, and also an explanation of

how feedback can suppress stochastic spontaneous scattering. The dynamical behaviour of SBS is examined for a choice of several different parameters. For fixed external reflectivity the intensity of the pump laser is used as the control parameter for exploring the temporal evolution of SBS. Also, the effect of variable external reflectivity is investigated for a fixed pump intensity. The experimental findings and analysis are compared directly with theoretical observations.

Chapter 5 is associated with the study of a driven SBS oscillator. The inclusion of an acousto-optic modulator provides an additional two of degrees of freedom for the SBS oscillator. First, the acousto-optic modulator is characterised and then used to modulate the pump signal in an open flow optical fibre system. External feedback is then added to the system and the dynamical behaviour of the SBS oscillator is then investigated for different depths of modulation and frequency.

1.6 References

[1] P.Bergé, Y.Pomeau and C.Vidal, *Order Within Chaos*, (Wiley & Sons, 1984).

[2] E.N.Lorenz, "Deterministic Non-Periodic Flow", J.Atmos.Sci., Vol.**20**, pp.130, (1963).

[3] B.Van der Pol, "Forced Oscillations in a Circuit with Nonlinear Resistance", Phil.Mag.Vol.7(3), pp.65-80, (1927).

[4] F.J.Feigenbaum, "The Universal Metric Properties of Nonlinear Transformations", J.Statist.Phys., Vol.**21**, pp.669-706, (1979).

[5] S.Newhouse, D.Ruelle and F.Takens, "Occurrence of Strange Axiom A Attractors near Quasi-Periodic Flows on T_m (m=3 or more)" , Commun.Math.Phys., Vol.**64**, pp.35, (1978).

[6] Y.Pomeau and P.Manneville, "Intermittent Transition to Turbulence in Dissipative Dynamical Systems", Commun.Math.Phys., Vol.**74**, pp.189, (1980).

[7] P.Grassberger and I.Procaccia, "Estimation of the Kolmorov Entropy from a Chaotic Signal", Phys.Rev.A., Vol.**28**(4), pp.2591-93, (1983).

[8] P.Grassberger and I.Procaccia, "Characterisation of Strange Atractors", Phys.Rev.Lett., Vol.**50**(5), pp.346-49, (1983), and "Measuring the Strangeness of Strange Attractors", Physica D, Vol.**9**, pp.189-208, (1983).

[9] C.M.Kim, C.H.Cho, C.S.Lee, J.H.Yim, J.T.Kim and Y.D.Kim, "Period-doubling bifurcation in an electronic circuit with a fast recovery diode and square wave input", Phys.Rev.A., Vol.**38**(3), pp.1645-48, (1989).

[10] W.Klische, H.R.Telle and C.O.Weiss, Opt.Lett., Vol.**9**, pp.561, (1984).

[11] H.Haken, "Analogy Between Higher Instabilities in Fluids and Lasers", Physics Lett., Vol.**53**A(1), pp.77-78, (1975).

[12] C.O.Weiss, "Chaotic Laser Dynamics", Opt. & Quant. Elec., Vol.**20**, pp.1-22, (1988).

[13] R.G.Harrison and D.J.Biswas, "Chaos in Light", Nature, Vol.**321**(6068), pp.394-401, (1986), and R.G.Harrison, "Dynamical Instabilities and Chaos in Lasers", Contemp.Phys., Vol.**29**(4), pp.341-371, (1988).

[14] F.T.Arecchi, R.Meucci, G.P.Pucioni and J.R.Tredicci, Phys.Rev.Lett., Vol.**49**, pp.1217, (1982).

[15] C.O.Weiss and J.Brook, "Evidence for Lorenz-Type Chaos in a Laser", Phys.Rev.Lett., Vol.**57**(22), pp.2804-06, (1986).

[16] T.H.Maiman, "Stimulated Optical Radiation in Ruby Masers", Nature Vol.**187**, pp.493-94, (1960).

[17] A.P.Franken, A.E.Hill, C.W.Peters and G.Weinreich, "Generation of Optical Harmonics", Phys.Rev.Lett., Vol.7, pp.118-20, (1961).

[18] G.E.James, E.M.Harrell, C.Bacikowski, K.Wiesenfeld and R.Roy, "Elimination of chaos in an intra-cavity doubled Nd:YAG laser", Opt.Lett., Vol.**15**(20), pp.1141-43, (1990).

[19] R.G.Harrison and J.S.Uppal, *Nonlinear Dynamics and Spatial Complexity in Optical Systems*, (Institute of Physics 1992).

[20] E.Ott, C.Grebogi and J.A.Yorke, "Controlling Chaos", Phys.Rev.Lett., Vol.**64**(11), pp.1196-99, (1990) and R.Roy, T.W.Murphy, T.D.Maier, Z.Gills and E.R.Hunt, "Dynamical control of a chaotic laser: Experimental stabilisation of a globally coupled system", Phys.Rev.Lett., Vol.68(9), pp.1259-62, (1992).

[21] R.H.Stolen, Proc. IEEE, Vol.**68**, pp.1232-38 (1980).

[22] Y.Silberberg and I.Bar-Joseph, Phys.Rev.Lett., Vol.**48**, pp.1541, (1982).

[23] R.G.Harrison, J.S.Uppal, A.Johnstone and J.V.Moloney, "Evidence of Chaotic Stimulated Brillouin Scattering in optical Fibres", Phys.Rev.Lett., Vol.**65**(2), pp.167-70, (1990).

[24] E.P.Ippen, *Laser Applications to Optics & Spectroscopy*, Vol.2, (Addison-Wesley,1975).

[25] G.P.Agrawal, *Nonlinear Fibre Optics*, (Academic Press, 1989).

[26] N.H.Packard, J.P.Crutchfield, J.D.Farmer and R.S.Shaw, "Geometry from a Time Series", Phys.Rev.Lett., Vol.**45**(9), pp.712-16, (1980).

2. Design and Construction of a Single Mode cw Nd:YAG Ring Laser

2.1 Introduction

The investigation of a nonlinear dynamical optical process imposes stringent demands upon the operational characteristics of the pump laser to be implemented into the experiment. In the following section the required operational characteristics of the pump laser will be discussed in detail. The main emphasis will be placed upon the role of the pump laser in the generation of the nonlinear optical phenomena of interest. After careful selection of the ideal pump laser, the remaining chapter addresses the design and construction of a ring laser from a modified commercial system.

2.2 Selection Criteria for Nd:YAG

The main operational characteristics of a laser are; the mode content i.e. multi-mode or single-mode; the operating conditions i.e. pulsed or continuous; the wavelength of operation; and the output power. The investigation of deterministic dynamics in Stimulated Brillouin scattering (SBS) using optical fibres as the Brillouin medium imposes specific considerations affecting the choice of pump laser. The main factors to be considered in order to determine the optimum choice of pump laser were the following:

Single-Mode - This had a significant dual role in the optical scattering process. Primarily, a single-mode (single frequency) pump will only excite under certain operating conditions [1] a single first order Stokes signal. Multi-mode excitation has been shown to generate several Stokes signals [2], each one corresponding to the particular mode that initiated the scattering process. These Stokes signals interact and compete with both the pump frequencies and each other via the nonlinear medium [3] producing complicated dynamical behaviour. Also the threshold for SBS depends upon the bandwidth of the pump source, with a narrow bandwidth producing SBS at low threshold powers in comparison to a broad pump source. Secondly, single frequency operation reduces instabilities in the laser output caused by mode beating of the longitudinal and transverse modes. To summarise, a single-mode laser will dramatically simplify the scattering process and reduce the threshold for stimulated scattering to occur.

Continuous Operation - This eliminated any transient effects that would exist with pulsed operation ensuring that any observed dynamics were produced by the optical mixing process itself. It also prevented the excitation of Raman phenomena thus ensuring that only Brillouin scattering was initiated.

Output Power - The power required to reach the Brillouin threshold in an optical fibre is inversely proportional to the length of the fibre. For a 150 meter length of fibre, with a germania doped silica core, the SBS threshold is typically in the region of several hundred milliwatts. A relatively high operating power will therefore allow the use of relatively short lengths of optical fibre i.e. several hundred metres instead of kilometres. This will reduce the amount of linear loss in the fibre due to Rayleigh scattering and the power budget will facilitate the exploration of dynamics in regions above SBS threshold.

Also the use of a relatively short medium, i.e. length of optical fibre, will significantly reduce the amount of computational time required to numerically solve the equations describing the system [4]. This is especially important for providing a realistic comparison of experimental results with theoretical findings.

Wavelength of operation - Careful selection of the pump wavelength can minimise optical loss in the medium through scattering and absorption. The loss mechanisms in optical fibres are Rayleigh scattering, and absorption of the radiation by hydroxyl (OH^-) impurities present in the fibre. The amount of scattering and absorption is wavelength dependent. Ideally, the wavelength of the pump laser should operate in a region of low loss. For fibres fabricated in the visible, and near infra-red region of the electromagnetic spectrum, the regions of minimum loss are located at 1.1μm, 1.32μm and 1.55μm.

The most suitable pump laser that could fulfil all of the selection criteria was the Neodymium YAG laser system. Neodymium YAG lasers can be made to lase on a single-mode with instantaneous linewidths less than 100kHz by employing a travelling wave resonator configuration. Relatively high output power, continuous operation is readily achieved using Krypton arc flashlamps as the excitation source for the laser medium. The Nd:YAG lasing wavelength of 1.064μm is close to a region of low loss for an optical fibre, with a typical attenuation of 1.45 dB/km occurring at this wavelength.

Clearly the Nd:YAG laser system satisfies all of the previous requirements for a suitable pump laser, without compromising any of the key prerequisites demanded by the experiment.

2.3 Properties of Nd:YAG

The first demonstration of laser action was in a solid state ruby laser by Maiman [5] in 1960. Less than one year later the first continuously operating crystal laser was reported by Johnson and Nassau [6] using calcium tungstate doped with Neodymium ions (Nd^{3+}:$CaWO_4$). Calcium tungstate was prone to fracturing during fabrication and a replacement host material was essential. Three years later Geusic et al [7] used Yttrium Aluminium Garnet ($Y_3Al_5O_{12}$) as the host material for Nd^{3+} and its superior robust mechanical properties compared to other host materials was quickly demonstrated.

Pure Yttrium Aluminium Garnet (YAG) is a colourless crystal with a cubic structure. YAG crystals with high quality optical and mechanical properties can be grown and doped with Nd^{3+} ions by the Czochralski process [8]. The addition of the optically active Nd^{3+} ions into the YAG host lattice produces a sharp fluorescent linewidth. The sharp fluorescent linewidth is a result of the electronic bonding between the active ions and the host atoms. The outer valence electrons of the active ions are involved in ionic bonding with the valence electrons of the host atoms. The remaining electron orbitals in the active ions which are not involved with electronic bonding are free to undergo optical transitions. Therefore, the host material effectively reduces the number of available optical transitions which improves the sharpness of the fluorescent linewidth. In Nd:YAG approximately 1% of the trivalent Yttrium Y^{3+} ions are substituted by Neodymium Nd^{3+} which are charge compensated because both ions have the same valency. Higher doping concentrations are difficult to achieve due to the slight difference in the radii of the ions. A higher concentration of dopants in the host medium

induces distortions and mechanical weakness in the rod. The deterioration in the quality of the host medium is a direct result of the mismatched ions impairing the strength and uniformity of the crystal lattice.

Today, Nd:YAG lasers outnumber any other solid state laser system to date. The main reasons behind the prolonged success of this system are as follows :

- Improvements in both the doping and growth of Nd:YAG has led to high optical quality crystals which can have their doping concentration optimised depending upon the mode of operation i.e. 1.2% for Q-switched and 0.6 - 0.8% for cw.
- Advancements in the optical excitation technology, has made possible a range of Nd:YAG systems. These range from small compact diode pumped lasers delivering milliwatts to large flashlamp driven pulsed amplifier chains capable of producing peak powers of TeraWatts.
- Advances in nonlinear optical technology have extended the wavelength region of operation of the Nd:YAG laser system. Processes such as second, third, fourth harmonic generation and optical parametric oscillation provide tuneable wavelengths from the vacuum ultra-violet (266nm) to the near infra-red (2.5μm).

2.3.1 Laser Mechanism

The Nd:YAG laser is a four level system as shown by a simplified energy level diagram in Figure 2.1. The most efficient pump bands for exciting the Neodymium atoms from the ground state are located between 22-18000cm^{-1} corresponding to 0.75μm and 0.8μm respectively. Once the Neodymium ions are excited to the higher energy levels, they relax to a metastable state producing a population inversion between the $^4F_{3/2}$

and $^4I_{11/2}$ states. The $^4F_{3/2}$ state is composed of two sub-levels R_1 and R_2 occurring at 11414cm^{-1} and 11502cm^{-1} respectively. The inverted population is divided unequally between the two sub-levels. At room temperature (300K) the population of sublevel R_2 is 40% with the remaining 60% being allocated to sublevel R_1. The wavelength of the lasing transition is 1.0641μm and occurs only between the R_2 sublevel of the $^4F_{3/2}$ state and the lower level $^4I_{11/2}$ state with the sublevel R_1 replenishing the upper lasing sublevel via thermalisation. The terminal $^4I_{11/2}$ level decays by a fast nonradiative process to the ground state with a lifetime of ~30ns.

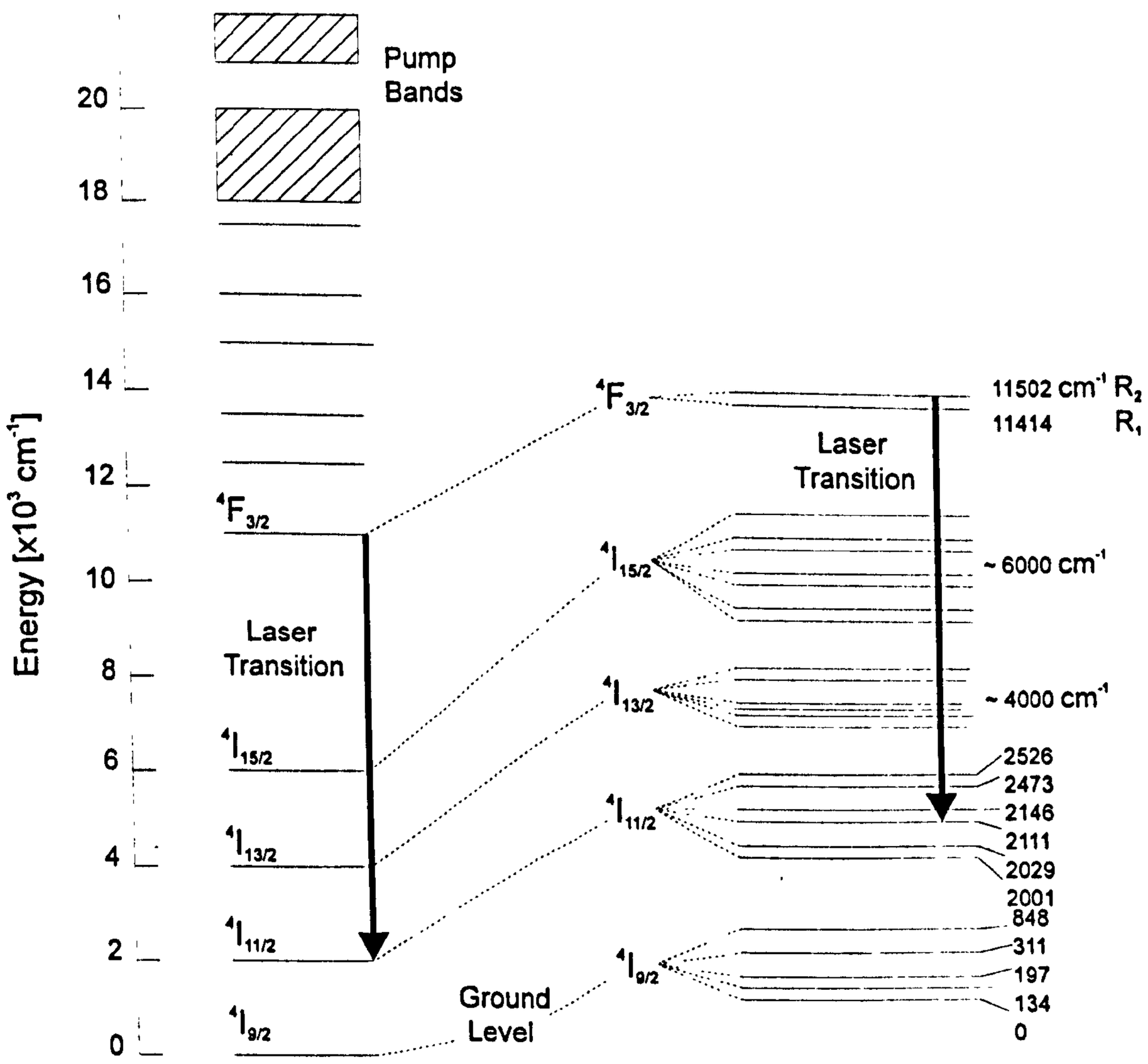

Figure 2.1 Energy Level Diagram of Nd:YAG at 300K.

The terminal $^4I_{11/2}$ lasing level is a true discreet fourth level and has important implications for lasing threshold. The population density of the terminal laser level can be calculated relative to the ground state. The population density will depend upon the thermal distribution within the levels. The terminal level is 2111cm^{-1} above the ground state and therefore the population is a factor $\exp(\Delta E / kt) \approx \exp(-10) \approx 10^{-5}$ of the ground state density. This implies because the terminal level is very weakly populated most of the pump energy is used in exciting the ground level. Hence The threshold for lasing is low and easy to obtain with most of the excitation energy being used for direct pumping.

The fluorescence efficiency of the upper laser level $^4F_{3/2}$ is greater than 99.5% and has a radiative lifetime of 230μs. The branching ratio of emission from the $^4F_{3/2}$ is shown below.

$$^4F_{3/2} \rightarrow {}^4I_{9/2} = 0.25$$

$$^4F_{3/2} \rightarrow {}^4I_{11/2} = 0.60$$

$$^4F_{3/2} \rightarrow {}^4I_{13/2} = 0.14$$

$$^4F_{3/2} \rightarrow {}^4I_{15/2} = 0.05$$

From the branching ratios it can be seen that almost all the ions are transferred from the ground state to the upper laser level. At the largest branch ratio 60% of the ions present in the upper laser level cause fluorescent output at the $^4I_{11/2}$ lasing transition manifold. The high fluorescence efficiency and large branching ratio at the main lasing transition combine to produce a laser with high gain. At room temperature the main lasing wavelength of 1.064μm in Nd:YAG is homogeneously broadened by thermally activated lattice vibrations of the host crystal.

Neodymium YAG lasers are optically pumped by continuous or pulsed noble gas flashlamps or more recently by AlGaAs semiconductor diode lasers. The fact that the energy states of the ions are narrow and well defined limits the choice of optical excitation source. The absorption characteristics of Nd:YAG are shown in Figure 2.2. The main absorption bands are located at 0.59μm, 0.75μm and 0.81μm. In high power systems Krypton arc flashlamps are used as the pump source because of the close matching of the emission spectra with the absorption bands of the Nd:YAG crystal, Figure 2.3.. The emission peaks with the strongest spectral irradiance are located at 0.75μm, 0.81μm and 0.89μm. Although the strongest absorption line of Nd:YAG is 0.59μm the emission characteristics of the Krypton arc flashlamp match with the three remaining absorption bands. The use of diode laser arrays to optically pump Nd:YAG lasers is becoming increasingly popular. However, Krypton arc flashlamps have provided an electrically efficient, robust and relatively economical alternative to diode laser arrays since the advent of the solid state laser.

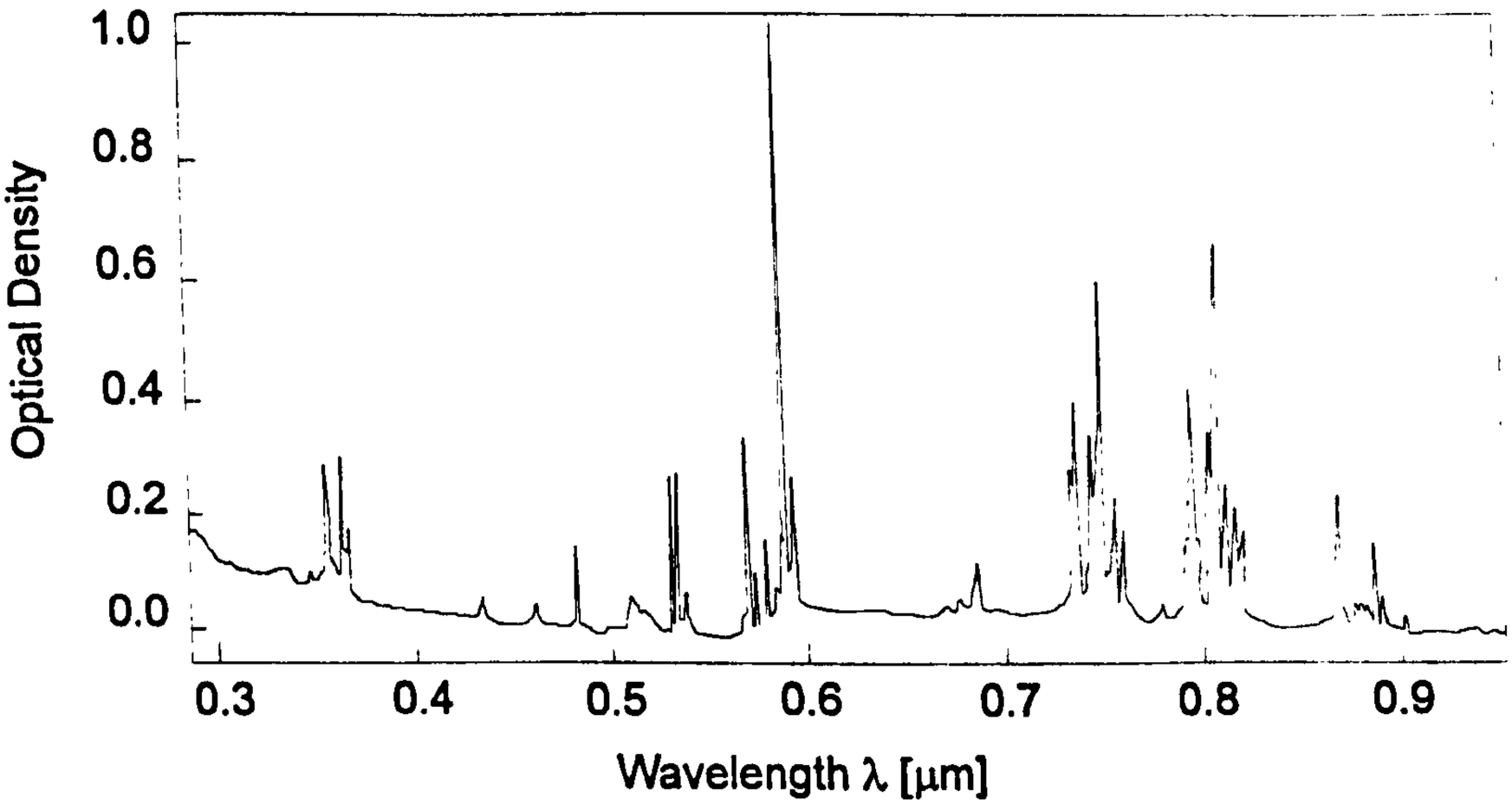

Figure 2.2 Absorption Spectrum of Nd:YAG at 300K

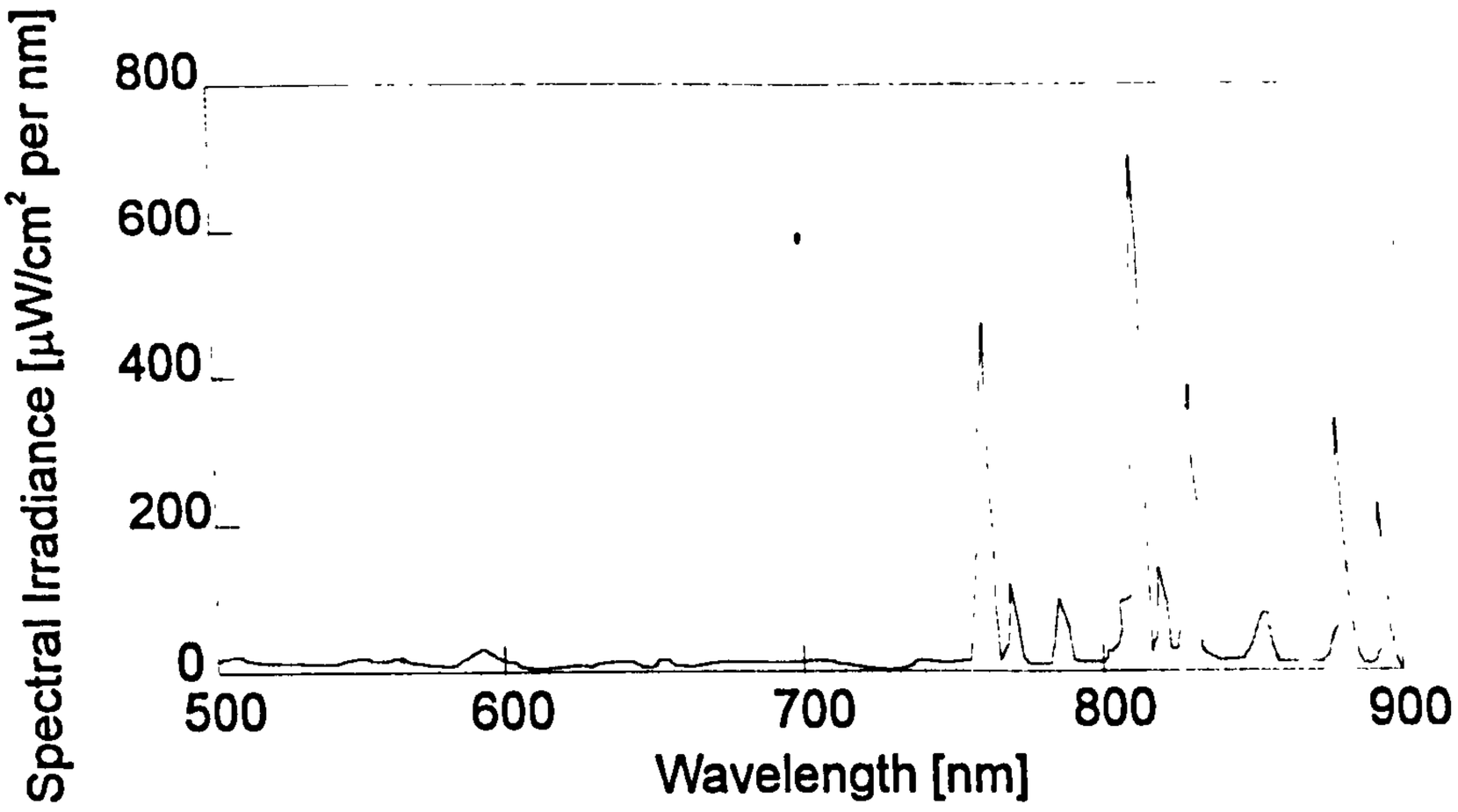

Figure 2.3 Emission Spectrum of a Typical cw-pumped Krypton-arc Flashlamp

2.3.2 Laser Head

A commercial Nd:YAG laser system, Spectron Laser Systems SL900, was used to supply the laser head. The laser system used a standing wave resonator, lased on several longitudinal modes and was capable of delivering a maximum of 30Watts under continuous conditions. The laser head contained the Nd:YAG rod and flashlamp both sealed into a water cooled flashchamber. The YAG rod had the following dimensions 103mm x 4mm (length x diameter), and was doped to a concentration of 1% Neodymium atoms. The end faces of the rod were polished to a flatness of $\lambda/10$ with a plane parallel geometry and had an anti-reflection coating of Magnesium Fluoride.

The laser rod was housed in the bottom section of the pumping chamber. Close coupled ceramic reflectors were used to optimise the coupling of the flashlamp radiation into the rod. The total reflector assembly was in two halves, one beneath the laser rod and the other above the flashlamp in the lamp housing Figure 2.4. An ultra-violet filter was placed in-between the flashlamp and rod to prevent solarisation of the Neodymium atoms

in the YAG host material. The flashlamp was a cw Krypton arc lamp with a maximum output of 4.5kWatts.

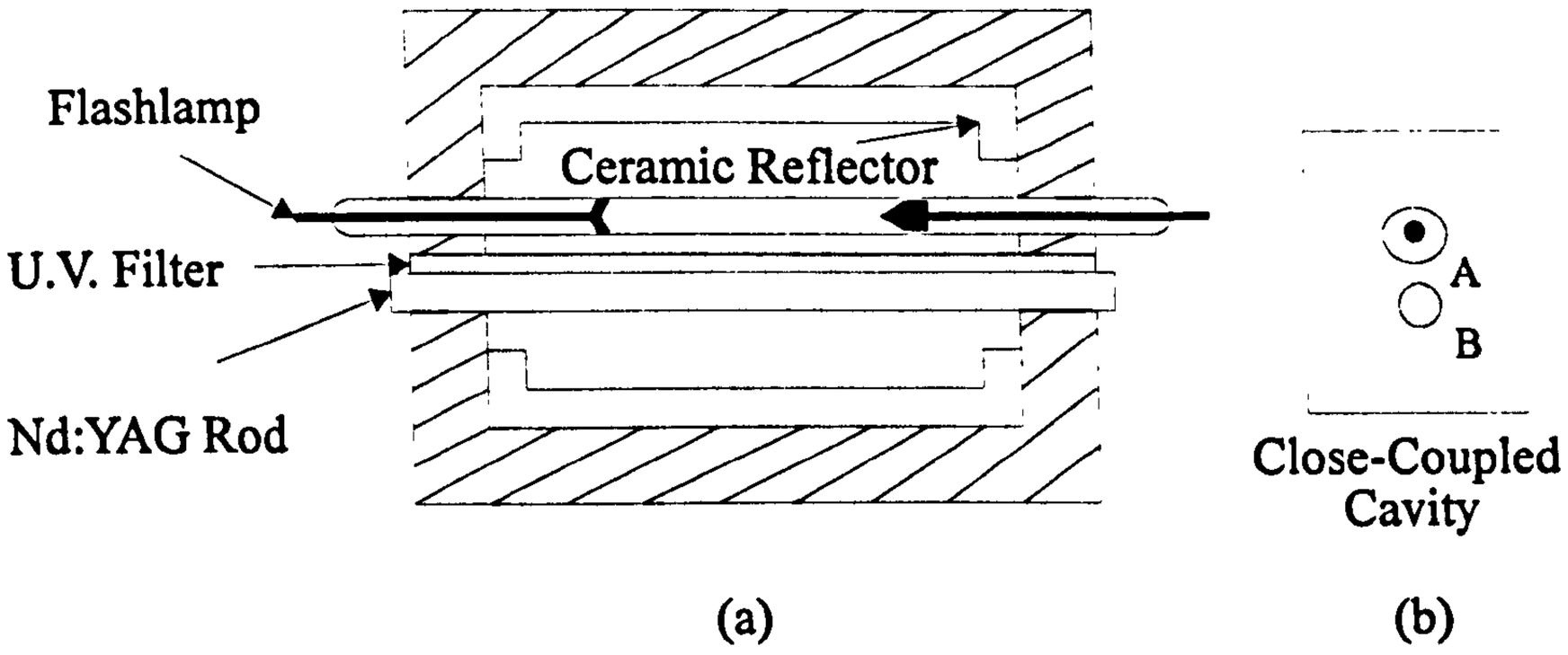

Figure 2.4 Laser head (a), and pumping configuration.

A regulated circulating water system was used to remove heat from the flashchamber. The cooling system comprised of a primary and secondary circuit. The primary circuit used pure de-ionised water as the coolant and this was circulated via a sealed pump around the flashchamber. The secondary circuit used a heat exchanger cooled by mains water to extract the heat from the primary system. The de-ionised water was filtered in the circuit to prevent particle contaminants circulating around the flashlamp and YAG rod. Contaminants create hot spots by absorbing the broadband emissions from the flashlamp and this can damage the rod and lead to catastrophic failure of the flashlamp. The sealed system is used to prevent the admittance of air in the cooling circuit. It has been recognised [9] that air bubbles in the flashchamber are a main factor in producing low frequency fluctuations in the output of the laser.

The laser head was vibration isolated from the optical bench by using an isolation plinth. The isolation plinth consisted of two aluminium plates sandwiched with rubber pads. The water cooling pipes were lifted clear of the optical bench to minimise vibrations and acoustically decouple the pipes from the laser head. Both of these precautionary measures were required to ensure stable lasing and isolate the system from the environment [10].

2.3.3 Thermal Effects in a Nd:YAG Rod

Thermal effects in solid-state laser rods are caused by a combination of heat generation by absorption of pump radiation and heat flow due to the cooling process. Heat generated by the absorption process is produced by several physical mechanisms :

1. the energy difference between the pump bands and the fluorescence energy levels is lost to the host lattice through radiationless transitions;
2. the quantum efficiency of the fluorescence process involved is less than unity (<99.5%), therefore some of the photon energy is lost to the host lattice;
3. the de-excitation of electrons from the lower energy level state to the ground state involves a non-radiative thermal transition which contributes heat to the lattice;
4. the spectral distribution of the pump light contains emissions in the ultra-violet and infrared bands, which are not involved in the laser mechanism, but are absorbed directly by the host material and converted to heat.

Heating and cooling of the laser material leads to a nonuniform temperature of the rod, which results in a distortion of the laser beam due to a temperature- and stress-dependent variation of the refractive index. The type of optical distortions which occur in a laser rod as a result of nonuniform temperature distribution are thermal lensing and

thermally induced birefringence. Thermal lensing is caused by stress dependent variations of the refractive index and birefringence is induced in the rod as a result of thermal strains. A precise knowledge of the extent of thermal lensing and induced birefringence , and their dependence upon excitation power is essential for the optimised design of the laser resonator.

2.3.4 Determination of Thermal Lensing for CW Operation

For a cylindrical laser rod with cw pumping, the uniform internal heat generation and constant surface temperature create an approximate quadratic radial temperature dependence. The temperature profile is almost parabolic, with the highest temperature at the centre of the rod and the lowest temperature at the surface which is in contact with the coolant. The temperature gradients produce mechanical stresses in the laser rod, because the hotter inside area is constrained from expansion by the cooler outer zone. There are two types of stress which exist within the rod. The centre of the rod is under compression because it is prevented from expansion due to the ends of the rod being fixed within the flashchamber. The second form of stress is tension which occurs at the rod ends due to greater bulk expansion in the rod's centre compared with the circumference. An optical beam propagating along the rod axis undergoes a quadratic spatial phase variation. This perturbation is equivalent to the effect of a spherical lens, with the focal length being dependent upon the temperature profile within the rod.

Several authors have proposed techniques for determining the thermal focal length of a rod by direct experimental measurement [10,11,12]. The estimation of induced focal length based upon the physical constants of the rod material does not lead to correct results. The lack of knowledge and experimental difficulty in determining the

exact fraction of pump energy that is dissipated as heat inside the laser rod, impedes accurate calculations.

A sensitive technique for the measurement of thermal focal lengths (<10m) was suggested by Marchetti et al [11]. The light from a He-Ne probe beam was collimated and allowed to propagate along the axis of the laser rod under investigation. The emerging beam of light was incident upon an aperture of fixed diameter placed at a known distance away from the laser rod. By measuring the intensity variation of the probe beam through the aperture for a range of flashlamp settings, the thermal focal length could then be estimated. The experimental set-up for the measurement of induced focal length is shown in Figure 2.5.

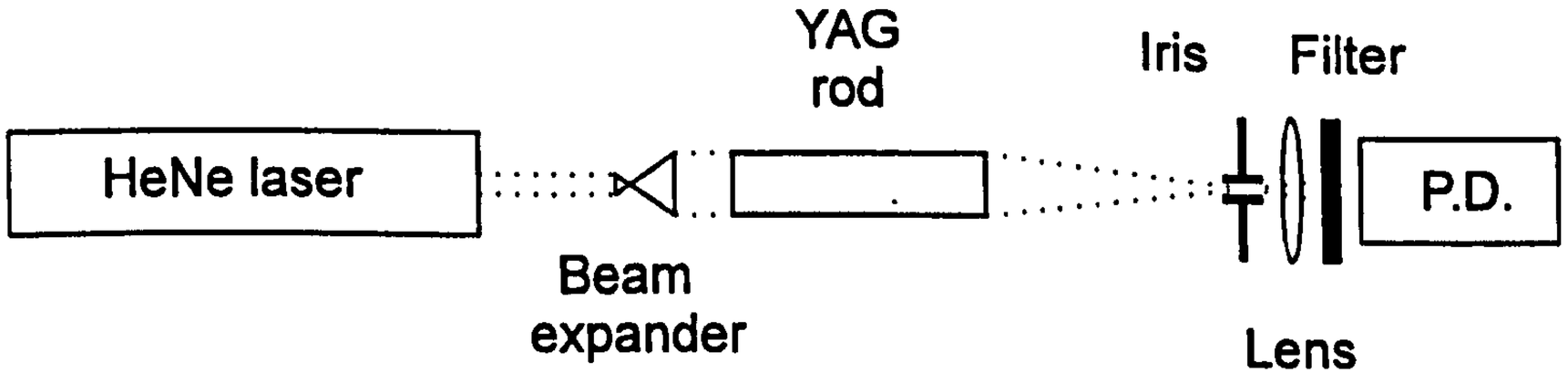

Figure 2.5 Experimental Set-up for Measuring the Thermal Lensing

The Gaussian beam from a He-Ne laser was expanded and collimated by a beam expander to provide a beam with a parallel waist and a diameter of 4mm. The expanded beam had the same diameter as the rod and was made to pass along the optical axis as shown in Figure 2.5. The optical power of the He-Ne beam that emerged from the YAG rod had reduced by ~20%. This was due to a combination of reflections from the end faces of the rod and direct absorption and scattering by the bulk of the rod. The emerging beam propagated a fixed distance L and was incident upon an iris of diameter 700μm.

The distance of the iris from the laser rod exit was determined by observing the approximate beam focus for a mid-range setting of the flashlamp power. A lens was used to collect the entire light transmitted through the iris (700μm) and the intensity variations in the beam due to induced thermal lensing were measured using a photodiode. A narrow band He-Ne notch filter was used to prevent any flashlamp and 1.064μm radiation from reaching the photodiode. By measuring the changes in optical power of the probe beam over the dc level on an oscilloscope, the induced focal length of the laser rod for different flashlamp pump powers was determined by the following procedure.

For a fixed pump power, the laser rod will behave as a thick positive lens of focal length f_{th}. By measuring the amount of radiation transmitted through the iris the beam spot size can be found and hence the thermal lens that produced this spot size can be determined.

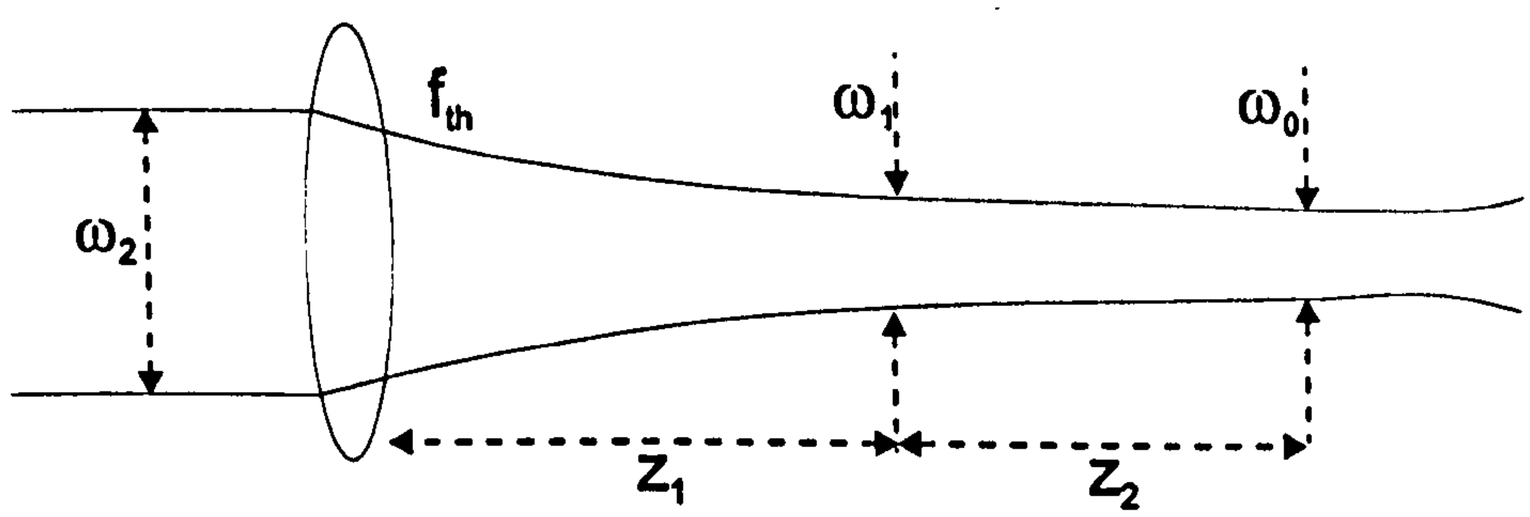

Figure 2.6 Gaussian beam analysis for Determining the thermal focal length

The equation for determining the focal length was derived as follows:- in Figure 2.6 the rod is represented by a thick lens of focal length f_{th} and the iris by an aperture of diameter ω_1 located at a distance z_1 from the lens. The expanded and collimated probe beam with a known beam waist ω_2 is incident upon the lens and brought to a focus upon

the aperture. The true minimum spot size ω_o will be at the focus of the thermal lens a position z_2 from the aperture (iris). The spot size ω of a Gaussian beam, at a position z is given by

$$\omega^2(z) = \omega_0^2\left(1+\frac{z^2}{z_0^2}\right)$$

where $z_o = \omega_o{}^2\pi / \lambda$. From Figure 2.6 expressions can be found for ω_1 and ω_2 ,

$$\omega_1^2(z_1) = \omega_0^2\left(1+\frac{z_1^2}{z_0^2}\right) \quad \text{(a)} \qquad \omega_2^2(z_2) = \omega_0^2\left(1+\frac{(z_1+z_2)^2}{z_0^2}\right) \quad \text{(b)} \qquad (1)$$

and the focal length

$$f_{th} = z_1 + z_2. \qquad (2)$$

Re-arranging and substituting the equation for the focal length (2) into equations 1(a) and 1(b) yields the following expressions;

$$\omega_1^2(z_1) = \omega_0^2\left(1+\frac{(f_{th}-z_2)^2}{z_0^2}\right) \quad \text{(c)} \qquad \omega_2^2(z_2) = \omega_0^2\left(1+\frac{f_{th}^2}{z_0^2}\right) \quad \text{(d)} \qquad (3)$$

since ω_1 , ω_2 and z_2 can be determined experimentally, expressions are required for ω_0 and z_0 which cannot be measured.

Equation 3(d) can be simplified by considering the properties of the focused He-Ne beam. A lens can typically focus a beam down to a diameter of approximately 100μm ($2\omega_0$). An estimated value for z_0 can be calculated using the following relationship $z_0 = \pi\omega_0{}^2 / \lambda$. Inserting the values $\omega_0 = 50\mu m$ and $\lambda = 633nm$ yields a value of ~1.24cm. For a

thermal focal length typically in the region of 50-100cm, the approximation $(f_{th}/z_0)^2 >> 1$ can be made and the parameters ω_0 and z_0 can now be expressed as follows;

$$\omega_0 = \frac{f_{th}\,\lambda}{\pi\omega_2} \qquad \text{and} \qquad z_0 = \frac{f_{th}^2\,\lambda}{\pi\omega_2^2}.$$

Further substitution of these expressions into equation 3(c) produces the following quadratic equation for f_{th} in terms of the experimental parameters ω_1 , ω_2 and z_2.

$$\alpha f_{th}^4 + \beta f_{th}^2 + \gamma f_{th} + \delta = 0$$

where $\alpha = (\lambda / \pi\omega_2)^2$, $\beta = (\omega_2^2 - \omega_1^2)$, $\gamma = -2 z_2 \omega_2^2$, and $\delta = z_2^2 \omega_2^2$. The experimental parameters had the following values; $\omega_2 = 4$mm, $z_2 = 70$cm and $\lambda = 633$nm.

The transmission of the probe beam through the iris for a range of flashlamp pump power is shown in Figure 2.7. The maximum transmission of 90% occurred at a flashlamp power of 2.9kW. From the transmission of the probe beam for any given flashlamp power setting through an iris of radius a , a value for ω_1 was calculated from the relationship,

$$T = 1 - \exp\left(-\frac{a^2}{\omega_1^2}\right).$$

By substituting values for ω_1 into the equation for f_{th}, the corresponding thermal focal length was evaluated by solving the quadratic equation using the Newton-Raphson method. The graph in Figure 2.8 shows the variation of thermal focal length with flashlamp pump power determined by the Marchetti technique and as a function of the flashlamp power. For the results obtained using the Marchetti technique, at low pump powers typically 2kW, the thermal focal length is approximately 1m. As the flashlamp

pump power is increased the thermal focal length reduces to a value of 55cm for a pump power of 3.7kW.

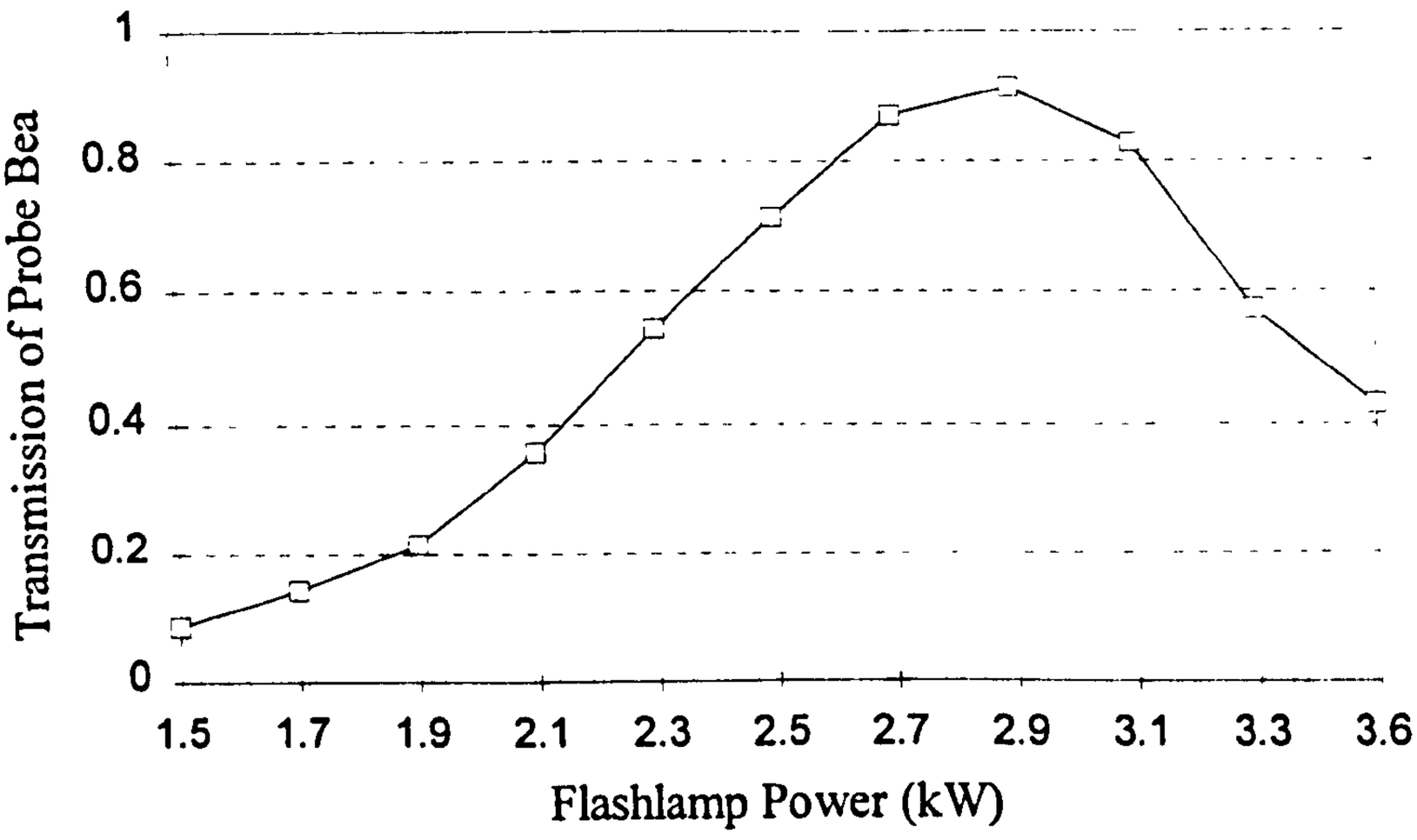

Figure 2.7 Transmission of He-Ne Probe beam through iris.

A closer inspection of the experimental data obtained from the He-Ne probe set-up shows that the variation in the focal length is inversely proportional to the lamp input power. The second experimental curve displayed in figure 2.8 is based upon an approximate method which uses the output power of the flashlamp to estimate the focal length., Figure 2.9. For a cylindrical rod where heat is generated uniformly within the bulk material the focal length is related to the pump power by [8],

$$f_{th} = MP_{in}^{-1.5}$$

where M is a constant of proportionality and depends upon the material of the laser rod e.g. for Nd:YAG $M = 20 \times 10^4$ W cm. The exponent of the input power $P_{in}^{-1.5}$ is also fixed by the laser material and has a value of -1.2 for non-garnet materials.

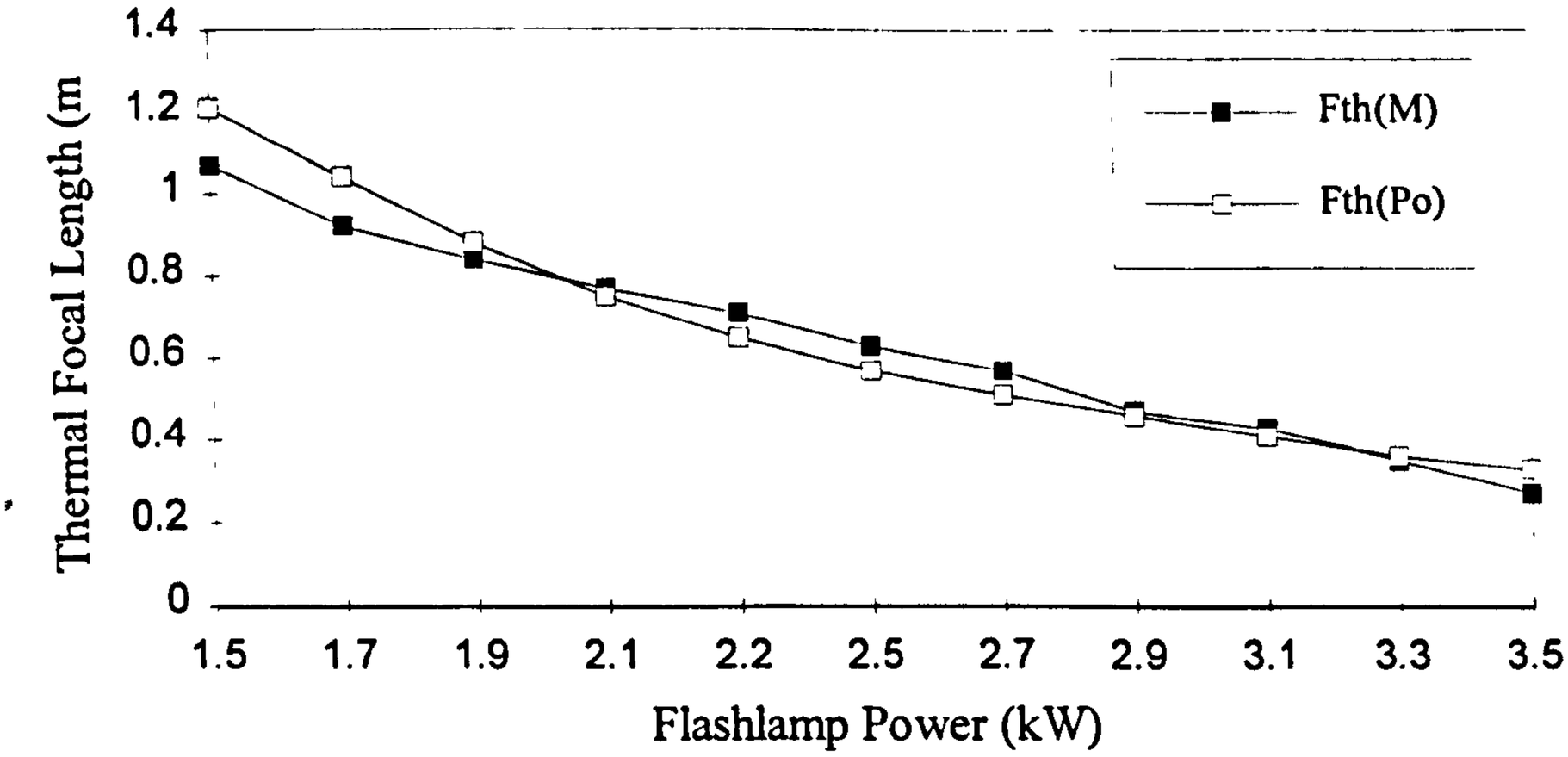

Figure 2.8 Thermal lensing determined by the Marchettti Iris technique Fth(m) and estimations based upon the flashlamp power Fth(Po).

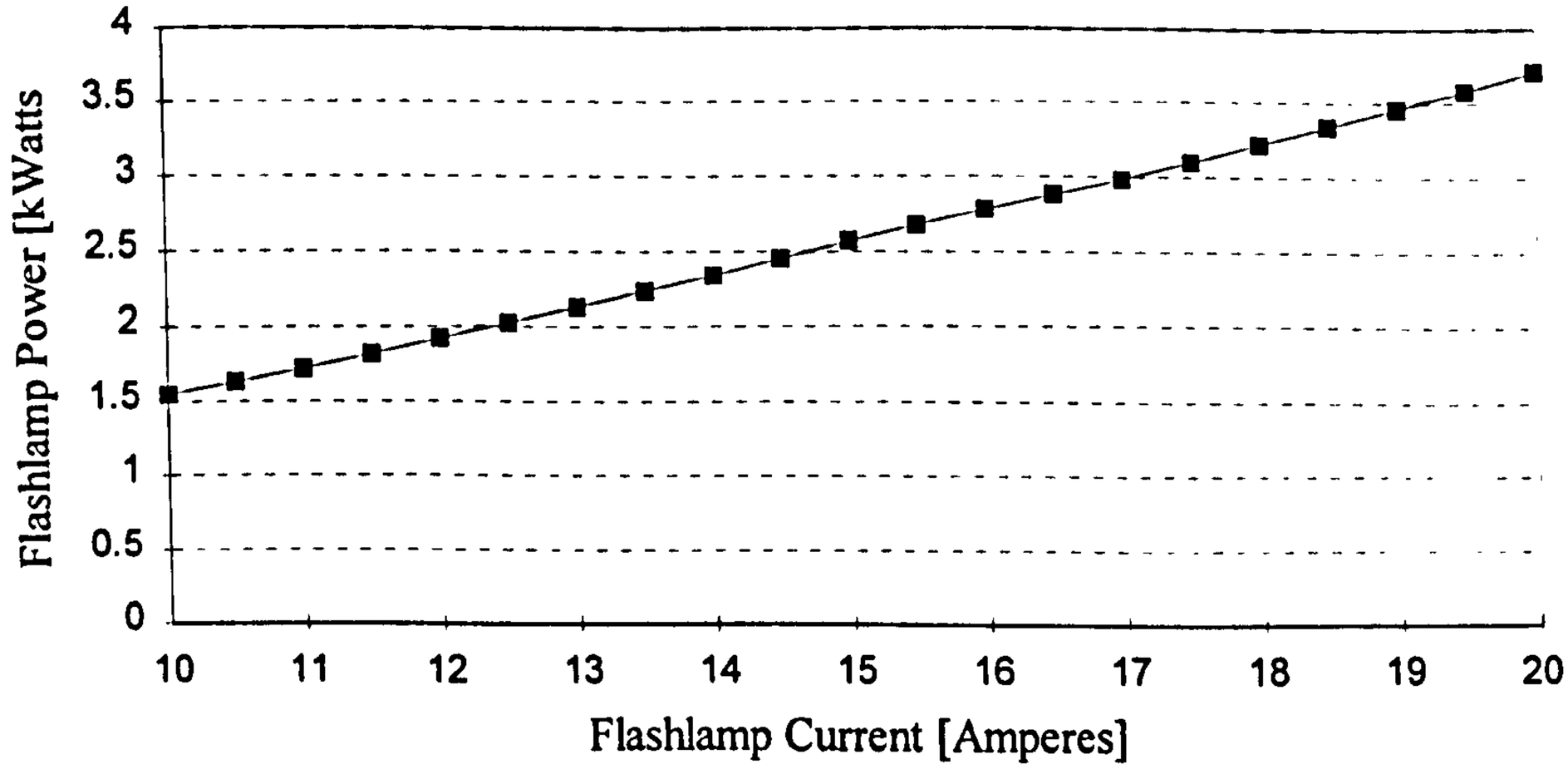

Figure 2.9 Flashlamp power versus Current for a Krypton arc flashlamp.

The results obtained by estimating the focal length based upon the flashlamp power have a characteristic curvature. Comparison of both sets of results shows a similar variation in the focal length. This is more pronounced at the lower flashlamp settings where the difference between the two values is ~15cm.

In addition to the thermal lensing effect, a prismatic effect was also observed in the YAG rod. To measure the prismatic effect, the iris was mounted on an x-y opto-mechanical mount, therefore allowing the transmission through the iris to be optimised for any lateral displacement in the beam. For an input power of 3.7kW the displacement was measured to be as high as 1mrad.

The prismatic effect depends upon the pumping geometry of the laser rod and the flashlamp [11,12]. The close-coupled pumping geometry, figure 4(b), creates an asymmetric intensity distribution across the YAG rod. The side of the rod which is facing the flashlamp (side A) has more light impinging upon the surface than the opposite side (B). Consequently, an asymmetrical temperature distribution exists between the two surfaces. The net result is a prism-like effect created within the rod which deflects the He-Ne probe beam.

2.3.5 Determination of Thermally Induced Birefringence in a Nd:YAG rod

In order to cross-check the measured values of induced focal length, another independent experiment was performed to determine the amount of thermal lensing by observing another thermally dependent physical mechanism. The degree of thermal lensing can be estimated from the measurement of depolarisation induced by thermal birefringence in the laser rod [13 ,14].

As discussed in the previous section the nonuniform temperature distribution in the laser rod generates a temperature gradient with the centre of the rod being hotter than the cooled surface. The centre of the rod is constrained from expansion by the cooler outer zone, and therefore the centre of the rod is under compression and the ends of the rod are in tension. These mechanical thermal stresses such as compression give rise to

thermal strains which act along the radial direction of the rod, and generate variations in the refractive index through the photo-elastic effect, making the laser rod birefringent.

Since Nd:YAG is a cubic crystal, the optical indicatrix is a sphere. Under stress the indicatrix becomes an ellipsoid, Figure 2.10(a). Nd:YAG rods are grown with the cylindrical axes along the [111] direction. The light propagates in this direction, and thus the change of refractive index along the [111] direction can be studied.

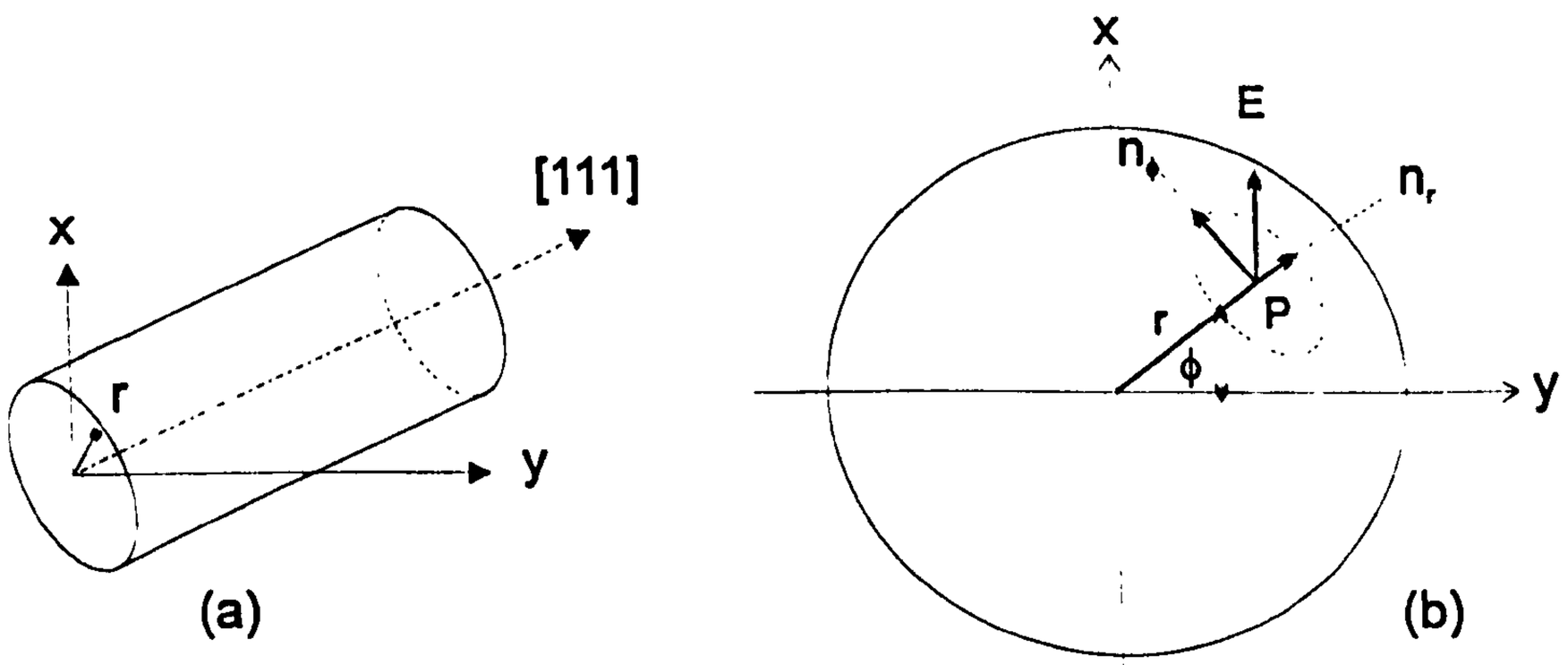

Figure 2.10 (a) Crystal orientation for a Nd:YAG rod , and (b) orientation of the indicatrix for a stressed Nd:YAG rod in a plane perpendicular to the rod axis.

A linearly polarised beam passing through the laser rod will experience depolarisation. For a Nd:YAG rod, the two principal axes of induced birefringence are along the radial and tangential directions. An incident electromagnetic wave with a polarisation vector **E** incident at a point $P(r,\phi)$ in a plane perpendicular to the rod axes Figure 2.10(b), will be resolved into two different polarisation components. There will be a radial refractive index component n_r , which is inclined at an angle ϕ with respect to the y-axis and a tangential component n_ϕ perpendicular to n_r . The two different polarisation

components will propagate along the crystal experiencing different refractive indices. Since $n_r \neq n_\phi$, there will be a phase difference between the two components and the light will emerge elliptically polarised.

The differences of the changes in refractive indices along these directions can be written as [15]

$$\left(\Delta n_r - \Delta n_\phi\right) = \frac{-2n_0^3 \alpha \Delta T\left(C_r - C_\phi\right) r^2}{a^2}$$

where α is the linear coefficient of thermal expansion, and C_r and C_ϕ are functions of the elasto-optical coefficients for the radial and tangential components of polarised light respectively. The radius of the rod is a, and r corresponds to an arbitrary position along the rod radius. The temperature difference between the centre and the edge of the rod is represented by ΔT.

Foster et al [16] and Koechner [17] have derived the expressions for the elasto-optical coefficients C_r and C_ϕ for Nd:YAG,

$$C_r = \frac{(17\nu - 7)P_{11} + (31\nu - 17)P_{12} + 8(\nu + 1)P_{44}}{48(\nu - 1)}$$

$$C_\phi = \frac{(10\nu - 6)P_{11} + 2(11\nu - 5)P_{12}}{32(\nu - 1)}$$

where ν is the Poisson's ratio, and P_{11}, P_{12} and P_{44} are the elasto-optical strain coefficients. The output intensity $I_{out}(r)$, i.e. the amount of depolarisation, of a probe beam after passing through the laser rod placed between two crossed polarizers is [14]

$$I_{out}(r) = I_{in}(r)\sin^2(\delta)\sin^2(2\phi)$$

$$\text{where } \delta = \frac{\pi l}{\lambda}\left(\Delta n_r - \Delta n_\phi\right).$$

$I_{in}(r)$ is the input intensity of the probe beam, ϕ is the angle between the incident polarisation and one of the principal birefringent axes Figure 2.10(b), l is the length of the rod, and λ is the wavelength of the probe beam radiation.

For a probe beam with a Gaussian radial profile, the input intensity distribution is given by

$$I_{in}(r) = I_{out}\exp\left(-r^2/\omega^2\right)$$

where ω is the spot size of the beam and I_{out} is the peak intensity at the centre of the beam. The total output power P_{out} of the laser beam is therefore

$$P_{out} = I_{out}\int_0^{2\pi}\int_0^a \exp(-2r^2/\omega^2)\sin^2(\delta/2)\sin^2(2\phi)\,r\,\partial r\,\partial\phi$$

and the fractional power transmitted through the crossed polarisers is

$$T = \frac{P_{out}}{P_{in}} = \frac{\dfrac{2L^2}{1+4L^2} - \dfrac{\exp(-x_0)}{2}\left[1 + \dfrac{2L\sin(2Lx_0) - \cos(2Lx_0)}{1+4L^2}\right]}{2[1-\exp(-x_0)]} \qquad (4)$$

where

$$L = \frac{\pi l n_0^3 \alpha \Delta T (P_{11} - P_{12})(1+\nu)}{4\lambda x_0 (1-\nu)} \qquad (5)$$

and

$$x_0 = 2a^2/\omega^2. \qquad (6)$$

The experimental set-up used to measure the amount of depolarisation for a probe beam is illustrated in Figure 2.11. The Nd:YAG rod was placed between two crossed polarizers. A He-Ne laser was used as the probe beam and passed through the optical axis of the laser rod. A photodiode was used to detect the signal and a narrow pass filter was inserted before the photodiode to minimise background radiation from the flashlamp and rod. The transmission of the probe beam through the crossed polarisers for different pump powers is shown in Figure 2.12.

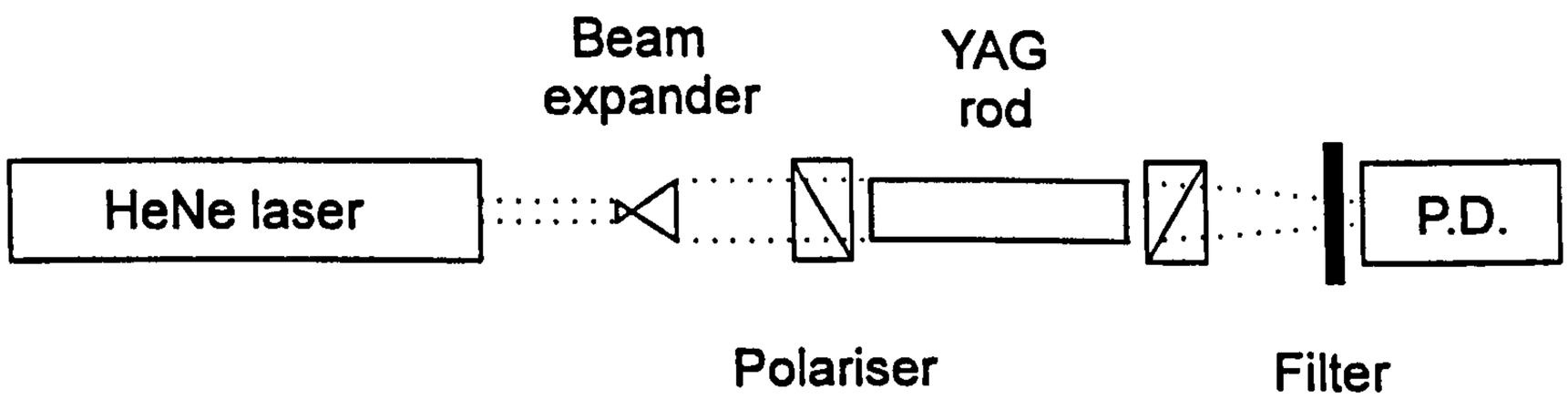

Figure 2.11 Experimental Set-up for measuring the depolarisation of a He-Ne probe beam.

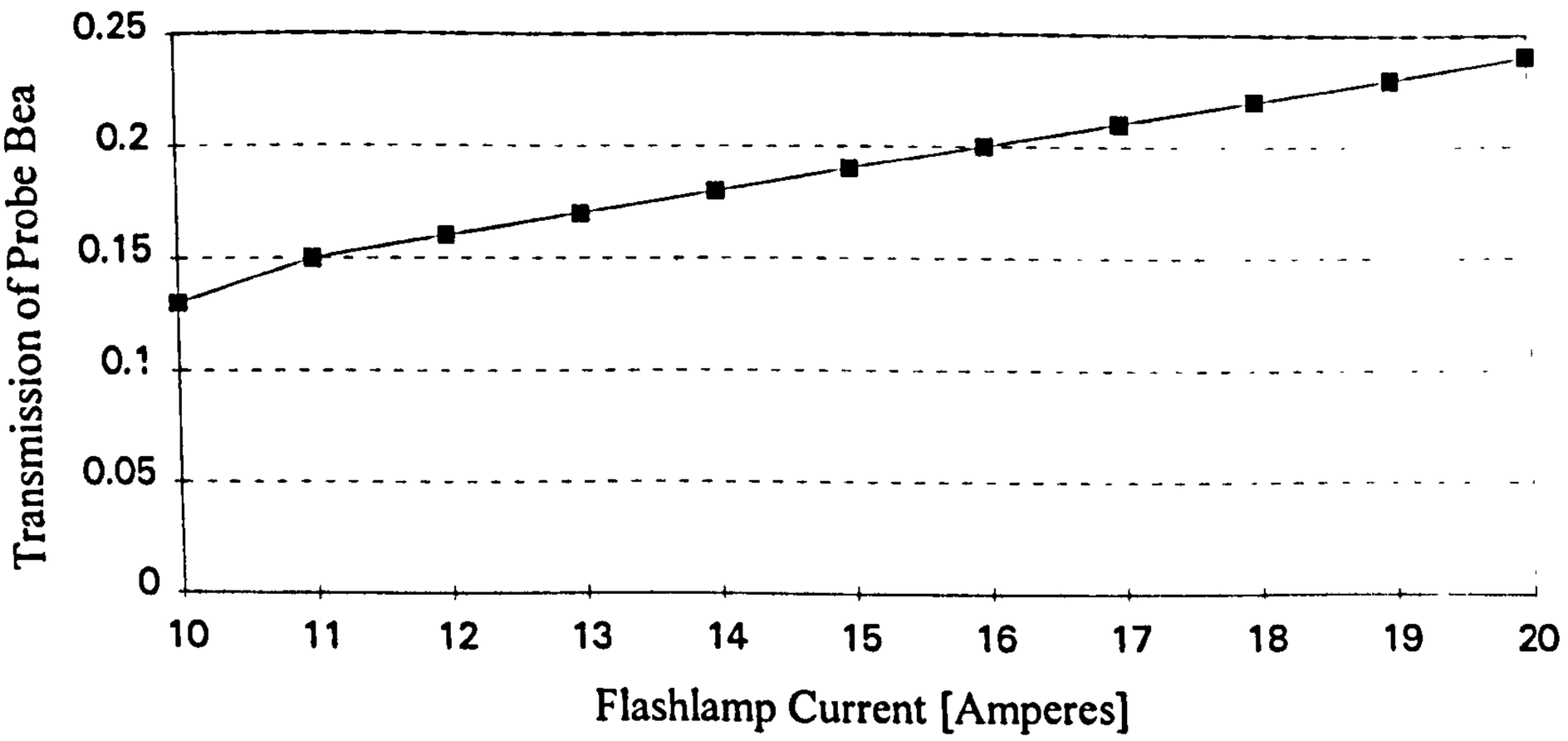

Figure 2.12 Depolarisation Vs Flashlamp Power.

Physical and Optical Constants	Symbol	Numerical Value
Refractive Index @ 633nm	n_0	1.82
Thermal Coefficient of Refractive Index /°C	$\frac{1}{n_0}\left(\frac{\partial n}{\partial T}\right)$	4.01×10^{-6}
Linear Expansion Coefficient /°C	α	7.9×10^{-6}
Poisson's Ratio	ν	0.3
Elasto-optic Coefficients	P_{11}	-0.029
	P_{12}	0.0091
	P_{44}	-0.0025
Functions of Elasto-optic Coefficients	C_r	0.0195
	C_ϕ	-0.0025

Table 2-1 Physical and Optical constants For Nd:YAG [18].

The amount of light transmitted i.e. the amount of depolarisation, has a linear dependence upon the flashlamp power. From the measurement of the transmission T of the probe beam, the temperature difference ΔT between the centre and the edge of the rod was calculated using equations (4) to (6) and physical values from Table 2-1. The induced focal length of the laser rod corresponding to the temperature difference ΔT was obtained from the following equation

$$[f_{th}]_{r,\phi} = \frac{a^2}{4l\Delta T}\left[\frac{1}{2}\frac{\partial n}{\partial T} + \alpha C_r C_\phi n_0^3 + \frac{\alpha a(n_0 - 1)}{l}\right]^{-1} \quad (7)$$

The first two terms in the parenthesis of the equation refer to the contributions of the temperature and stress dependent variations of the refractive index respectively. The third term is due to the end face curvature caused by elongation of the rod. A comparison of the thermal focal length determined by measuring the induced birefringence, and the focal length measured by the aperture technique is shown in

Figure 2.13 for a range of flashlamp pump powers (1.5 - 3.5kW).

The threshold for lasing occurs at 12 amperes, which corresponds to a pump power of approximately 2kW. Both sets of independent measurements show a strong agreement with each other. For low pump powers i.e. below threshold, the thermal focal length is 110cm. However, for higher pump powers above threshold both experimental curves have a tendency to decrease linearly for increasing pump power reaching a value a minimum focal length of 25cm for a pump power of 3.5kW.

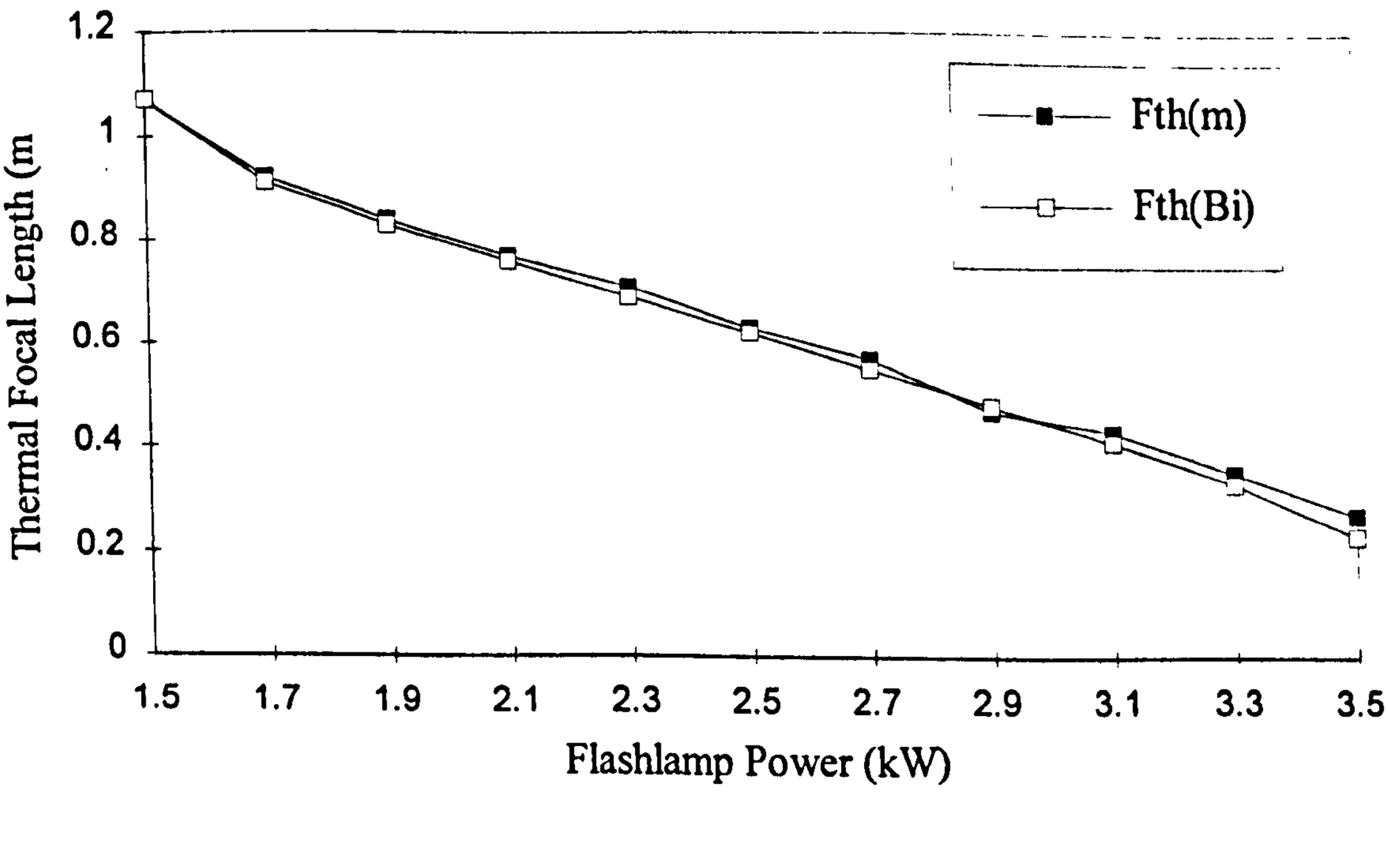

Figure 2.13 Comparison of thermal lensing determined by iris technique Fth(m) and induced birefringence Fth(Bi) for variations in Flashlamp Power.

For a fixed rod geometry, the thermal lensing is inversely proportional to the temperature difference across the rod radius. The terms in the parenthesis are physical constants and depend upon the material of the laser rod. Clearly, the thermal lensing action in the laser rod is directly dependent upon the pump power. In the next section the stability of the laser resonator will be analysed and the optimum pump power and hence thermal focal length will be deduced.

2.4 Laser Performance

The characterisation of the Nd:YAG rod's operational parameters provided a firm foundation for the design and construction of the laser resonator. The following section examines both the stability of the resonator, and the performance of the laser resonator for both standing and travelling wave configurations.

2.4.1 Resonator Stability

The main limitation in achieving large output power with a single longitudinal mode, homogeneously broadened laser, in a Fabry-Perot cavity is the spatial hole burning process. The effect of spatial hole burning is eliminated for travelling waves in a ring resonator. Compared to a Fabry-Perot cavity the ring resonator has a decreased sensitivity to misalignment in the plane of the cavity. The ring geometry also provides a degree of flexibility in the design of the resonator especially the inclusion of intra-cavity optical elements.

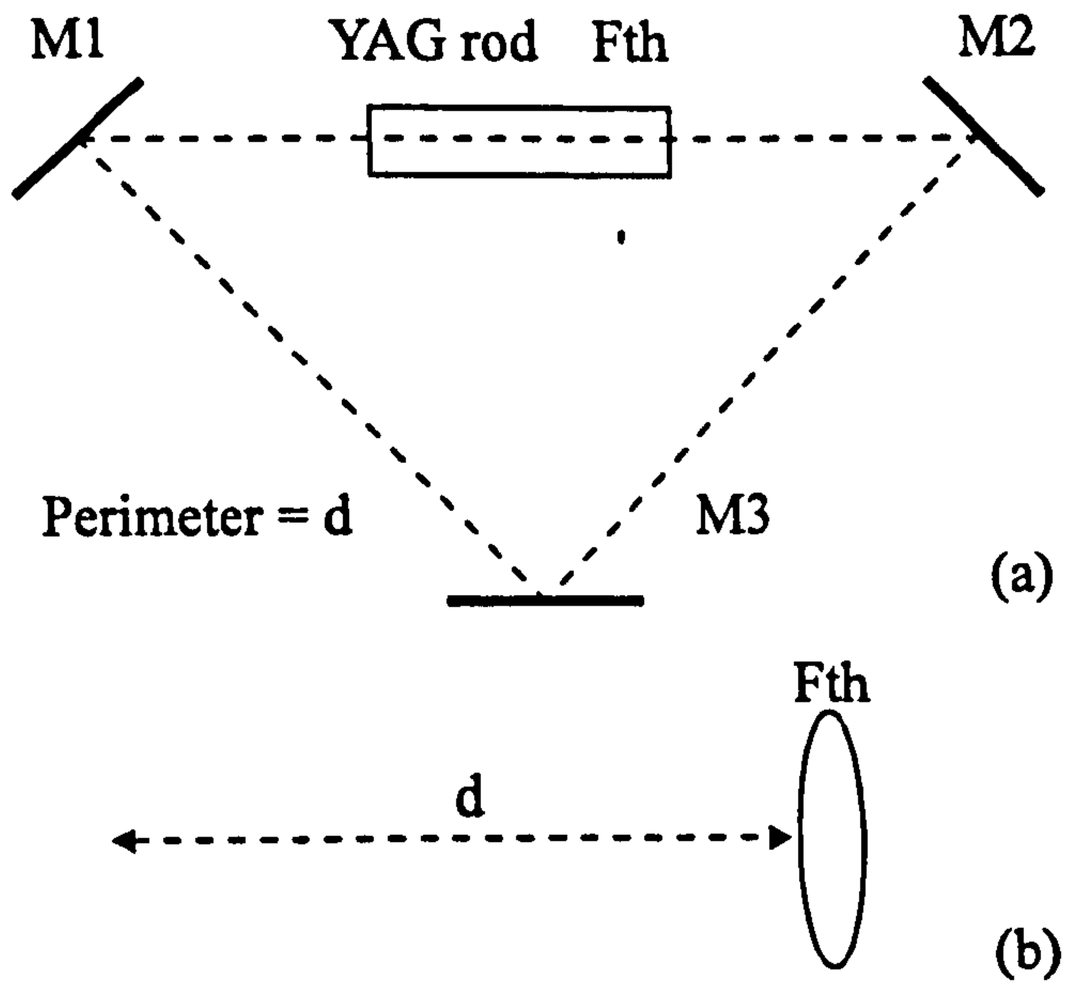

Figure 2.14 Ring Laser Geometry (a), and Lens Equivalent Waveguide (b).

The ring resonator comprised of three planar mirrors (R = ∞) Figure 2.14(a). Two of the mirrors were high reflectors (R=99.9%) and the third mirror was the output coupler with a transmission of 10%. The laser rod represented by a lens of focal length f_{th} in figure 2.14(a), was located at an equidistant position between two mirrors. The perimeter of the ring cavity i.e. length of the cavity, was fixed at a distance of 1.5m and gave a free spectral range of 220MHz. The perimeter of the cavity was kept short in length in order to increase axial mode spacing and competition between the modes.

The lens equivalent waveguide for the resonator is illustrated in figure 14(b) and simply consists of a lens representing the thermal lensing of the rod and the propagation over a distance d. The transmission matrix M corresponding to one round trip through the cavity is the following:

$$M=\begin{bmatrix} 1 & 0 \\ \frac{-1}{f_{th}} & 1 \end{bmatrix}\bullet\begin{bmatrix} 1 & d \\ 0 & 1 \end{bmatrix}=\begin{bmatrix} 1 & d \\ \frac{-1}{f_{th}} & \left(1-\frac{d}{f_{th}}\right) \end{bmatrix}. \tag{8}$$

The stability condition for the ring resonator is given by:

$$-1\leq\left[1-\frac{d}{2f_{th}}\right]\leq \tag{9}$$

which provides the maximum value of the perimeter $d \leq 4f_{th}$. For a ring resonator with a perimeter of 1.5m, marginal stability corresponds to a minimum thermal focal length of 37.5cm (e.g. maximum flashlamp power of 3.5 kW).

2.4.2 Bi-directional Operation

The threshold for lasing occurred at a flashlamp power of 1.92 kW and to achieve stable lasing the flashlamp was operated at a level of 2.7 kW, with only a Brewster plate present in the cavity. The laser had two output beams, one in the clockwise direction (cw), and one in the counter-clockwise direction (ccw). Each beam had an output power of 10 Watts. A CCD camera was used to display the transverse mode content of the beam in the far field. A radio frequency spectrum analyser and fast analogue oscilloscope were used to monitor the cavity beat frequencies and the temporal output respectively.

Figure 2.15 illustrates examples of both transverse and longitudinal mode structure with the corresponding temporal output for the bi-directional laser. The output of the R.F. Spectrum analyser is shown in Figure 2.15(a). The R.F. spectra is composed of many different frequency peaks indicative of multimode operation. The discrete frequency peaks in the R.F. spectrum are attributed to both longitudinal mode beating

(~220MHz) and transverse mode beating (60-80MHz). Confirmation of the existence of higher order transverse modes was provided by the output of the CCD camera, Figure 2.15(b). The competition of these modes leads to large fluctuations and instabilities in the output power of the laser, Figure 2.15(c). A ceramic aperture with an optimum diameter of 1.2mm was inserted into the cavity to select single transverse mode TEM_{00}. The output power was reduced to 6Watts for each beam. The laser operated on a single transverse mode with reduced instabilities in the temporal output. However, the R.F. spectrum indicated the simultaneous oscillation of several longitudinal modes.

2.4.3 Unidirectional Operation

The instabilities observed in the bi-directional laser with TEM_{00} mode selection were produced by a combination of longitudinal mode beating and competition between the two counter-propagating waves in the gain medium [19]. Nd:YAG and other solid-state lasers are homogeneously broadened [20] at room temperature and undergo spatial hole burning [21].

The process of spatial hole burning arises due to the rate of energy diffusion between lattice sites being too small to average out the energy of the excited ions. The interaction of a standing wave with the excited Nd^{3+} ions partially depletes the population inversion near the maxima of the standing wave, but there is no interaction at the nodes of the wave. The modulation of the population inversion, or spatial hole burning, favours the oscillation of other longitudinal modes that have some of their wave maxima close to the nodes of the original standing wave i.e. the maxima in the density of the excited ions. The ring resonator allowed propagation in the two counter-propagating directions. It was

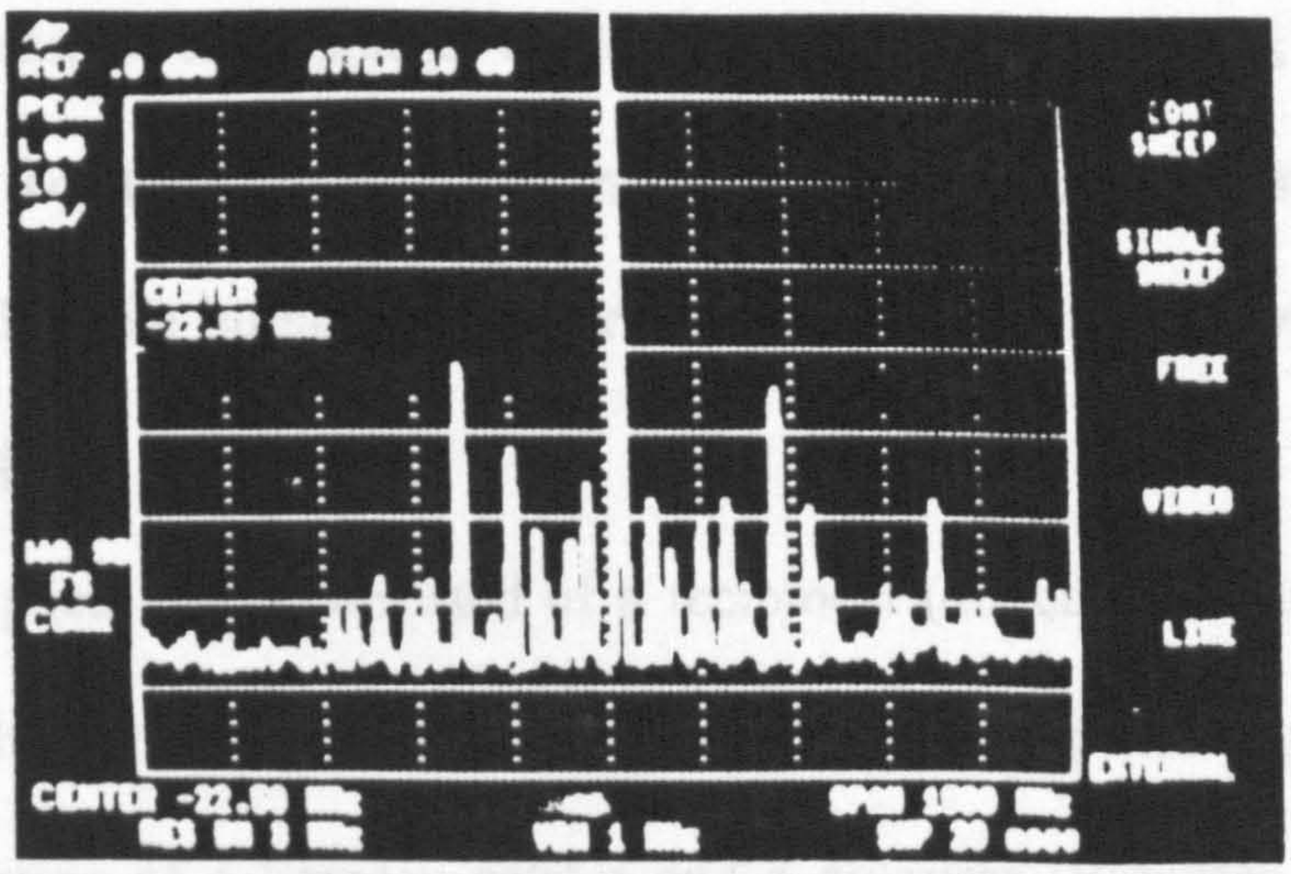

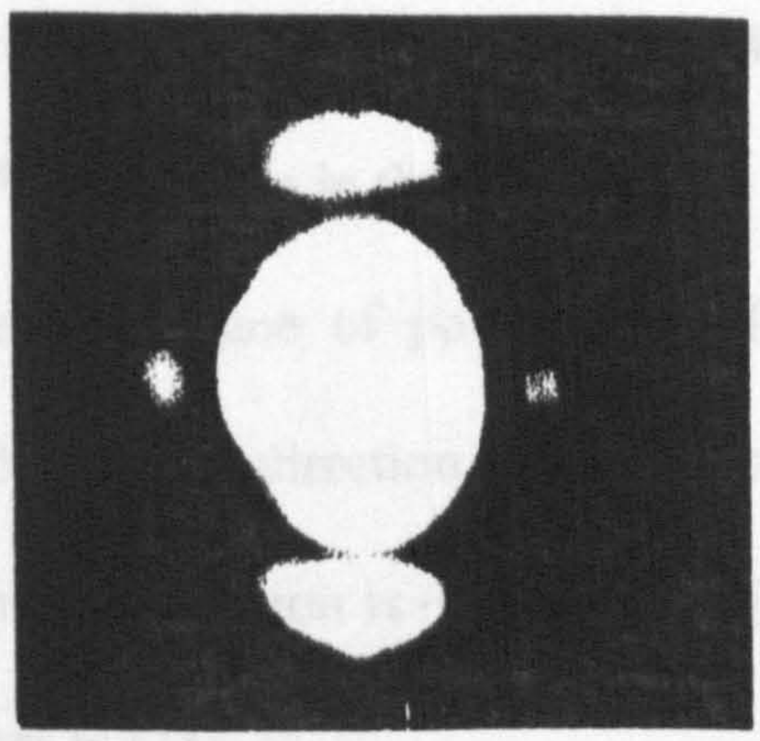

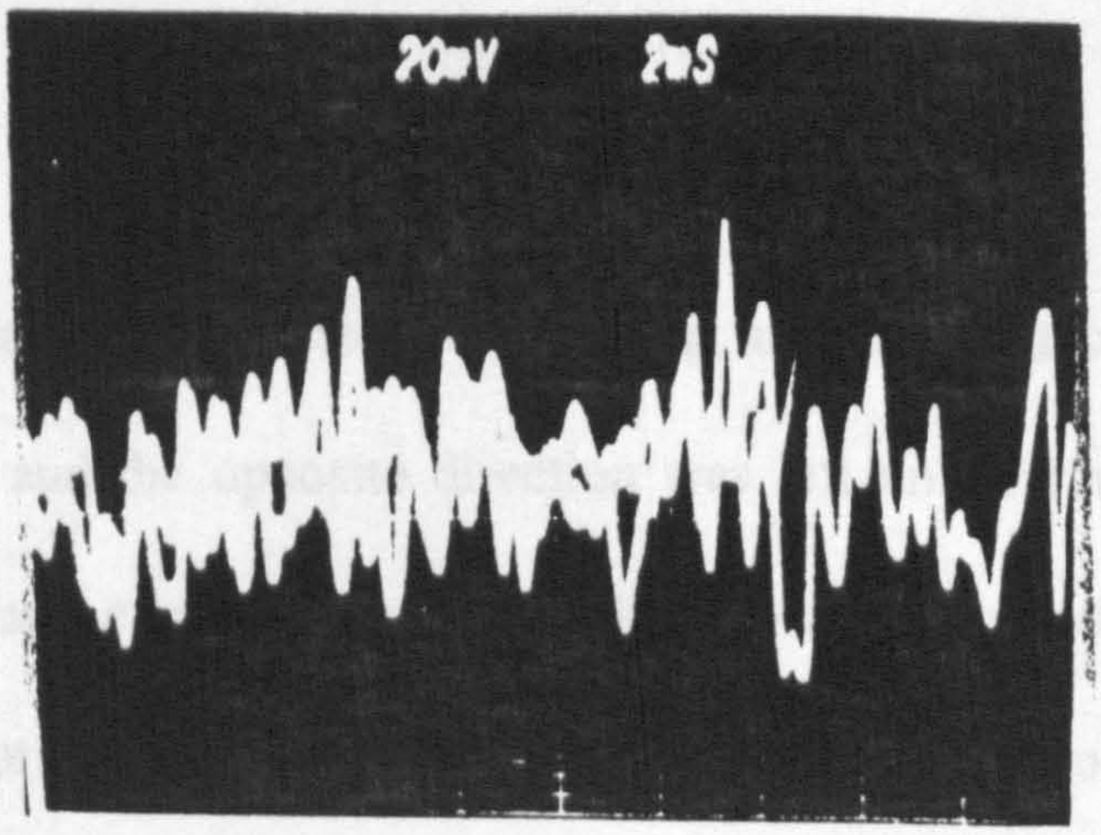

Figure 2.15 R.F. Spectrum illustrating multi-mode oscillation (top), CCD camera indicating higher order transverse mode (middle) and the temporal response (bottom) of a bi-directional Nd:YAG ring laser.

therefore necessary to suppress one of the counter-propagating beams to prevent backscattered radiation from coupling the two waves and forming a standing wave, thus inducing spatial hole burning. Unidirectional operation was achieved by the use of an optical diode [22 ,23].

The optical diode consisted of a reciprocal (direction independent) polarisation rotator i.e. a half-wave plate (φ), and a non-reciprocal (direction dependent) polarisation rotator consisting of a Faraday rotator and a polariser (Brewster plate). The Faraday rotator was constructed from an undoped YAG rod placed in a fixed magnetic field of 0.4 Tesla, and produced a 25° (ϕ) rotation in the polarisation. The Faraday rotator was placed in the cavity and rotated the plane of polarisation of the waves travelling in each direction by an angle of $\pm\,\phi$. In one direction the total rotation of the plane of polarisation is ($\phi + \varphi$), and in the other the rotation is ($\phi - \varphi$). The differential loss , $\Delta\alpha$ between the counter-propagating waves is [23]

$$\Delta\alpha = \sin^2(\phi+\varphi) - \sin^2(\phi-\varphi).$$

The half-wave plate was adjusted so that $\phi = \varphi$, and this produced maximum attenuation in one direction and the opposite direction was left unattenuated. The extinction ratio between the cw and cww direction was 1000:1. An etalon with a free spectral range of 30GHz and a coating of 20% (@ 514nm) was also inserted into the cavity to increase the loss of the higher order longitudinal modes and ensure single frequency operation.

Figure 2.17 illustrates the various output characteristics of the unidirectional ring laser illustrated in Figure 2.16. Figures 2.17(a) and (b) illustrate both single longitudinal mode and single transverse mode operation. The temporal output of the laser shown in

figure 2.17[c] confirms there are no high frequencies due to mode beating, and that the output of the laser is stable.

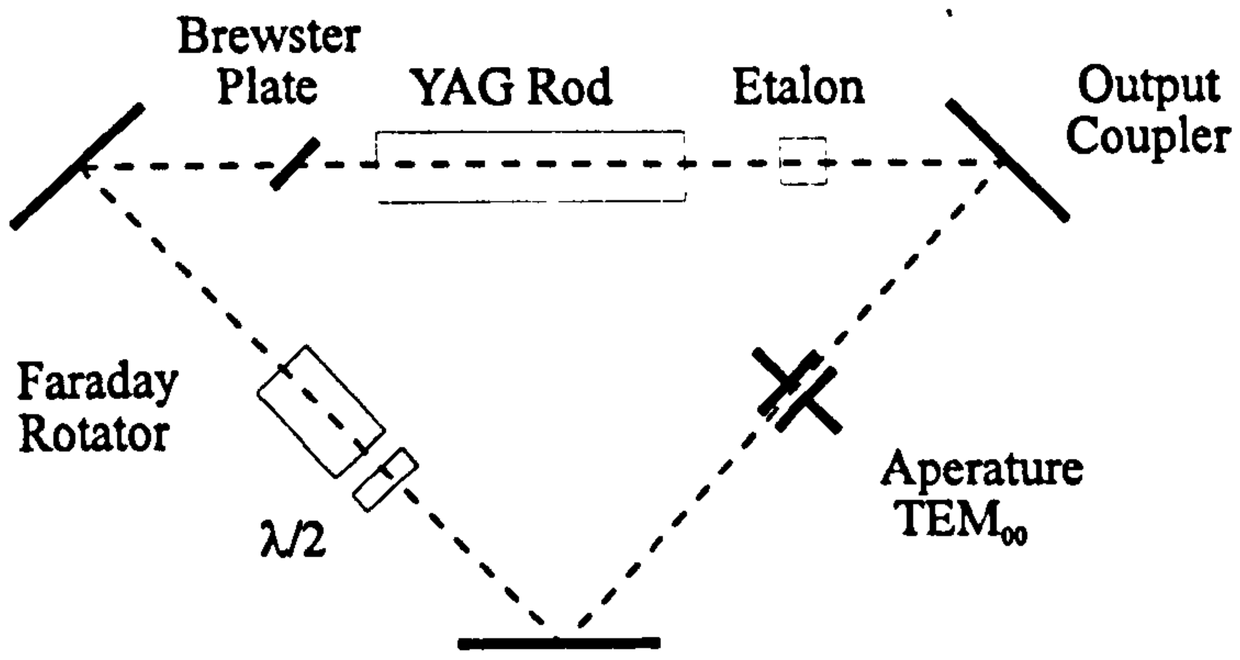

Figure 2.16 Schematic diagram of the travelling wave ring laser.

2.5 Conclusions

In this chapter the key operational characteristics of a pump laser to be employed in the studies of stimulated Brillouin scattering were addressed. The main demands placed upon the pump laser were for a single-mode, high power, cw system which lased on a wavelength which experienced low attenuation in an optical fibre (i.e. the Brillouin medium). The Nd:YAG laser was selected as the pump source because this system could potentially meet all of the demands imposed by the experimental requirements.

Prior to the construction of the laser resonator, the thermal properties of the laser rod were investigated to ensure the optimisation of the cavity stability. The most significant thermal effect, thermal lensing, was determined by two independent experiments. The Marchetti technique which involved determining the thermal lensing of the rod by measuring the transmission of a probe through a fixed aperture, displayed an

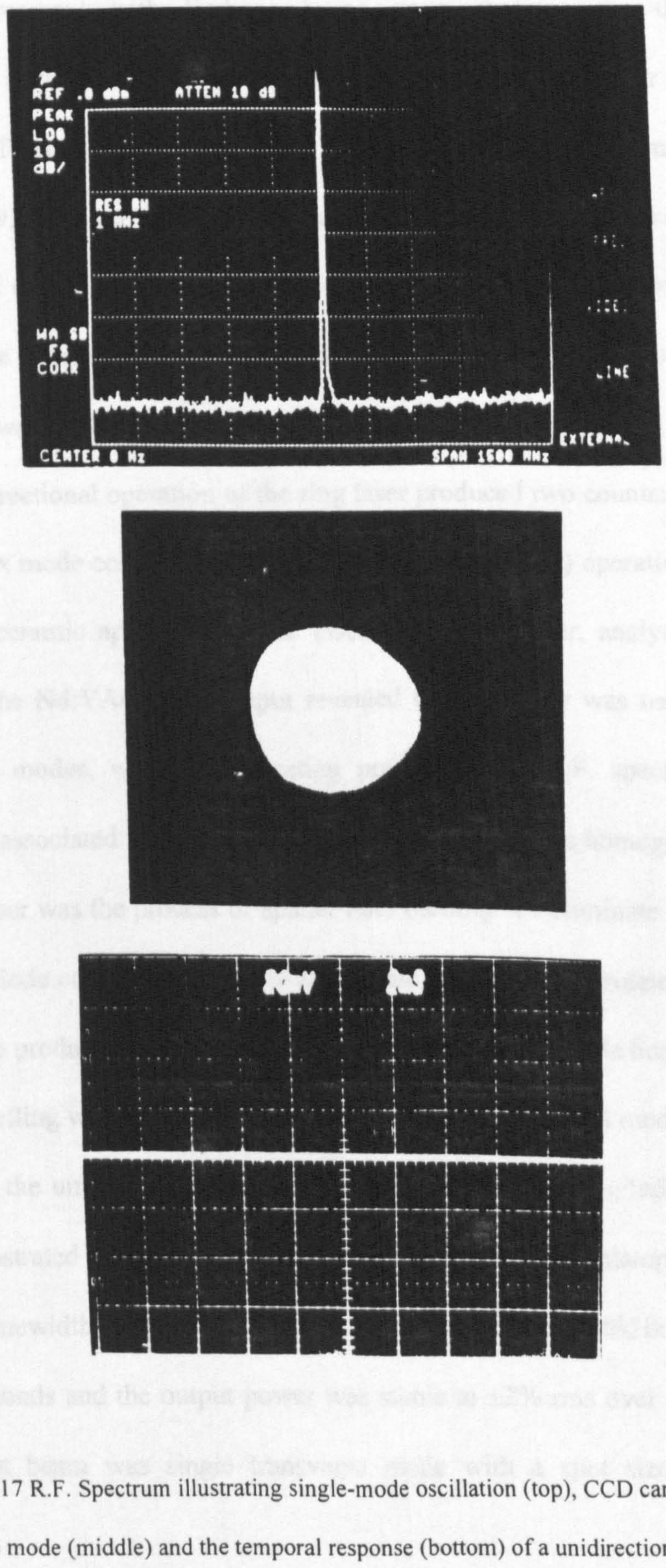

Figure 2.17 R.F. Spectrum illustrating single-mode oscillation (top), CCD camera indicating single transverse mode (middle) and the temporal response (bottom) of a unidirectional Nd:YAG ring laser.

excellent agreement with findings based upon studying the thermally induced birefringence in the laser rod. The maximum value for the perimeter d of the ring laser was $d \leq 4f_{th}$. The operating region of the laser was found to range from a flashlamp pump power of 1.92 kW up to a maximum power of 3.5 kW. The lower pump power corresponded to the lasing threshold of the ring laser. The maximum pump power was limited by the marginal stability condition of the resonator, and at this power the thermal focal length was 37.5cm.

Bi-directional operation of the ring laser produced two counterpropagating beams with complex mode content. Single transverse mode (TEM_{00}) operation was achieved by inserting a ceramic aperture into the laser cavity. However, analysis of the temporal content of the Nd:YAG laser output revealed that the laser was oscillating on several longitudinal modes, with mode beating present in the R.F. spectrum. The physical mechanism associated with the multi-mode oscillation of the homogeneously broadened Nd:YAG laser was the process of spatial hole burning. To eliminate spatial hole burning an optical diode consisting of a half-wave plate and a Faraday rotator were inserted into the cavity to produce unidirectional propagation. The spatial hole burning was eliminated for the travelling wave cavity and lasing on a single longitudinal mode was achieved.

For the unidirectional geometry, continuous single-longitudinal mode operation was demonstrated with an output power of 5 Watts for a flashlamp pump power of 2.7 kW. The linewidth of the ring laser was determined to be < 40kHz over a time scale of several seconds and the output power was stable to ±2% rms over a similar time range. The output beam was single transverse mode with a spot size of 2-3 mm and a

divergence of 2.4 mrads. In the next chapter the ring laser will be used as the pump for the investigation of the dynamical behaviour of stimulated Brillouin scattering.

2.6 References

[1] K.O.Hill, D.C.Johnson and B.S.Kawasaki, "CW Generation of Multiple Stokes and anti-Stokes Brillouin-shifted Frequencies,", Appl.Phys.Lett.Vol.29(3), 185-87, (1976).

[2] Y.Aoki and K.Tajima, "Stimulated Brillouin Scattering in a long single mode Fibre Excited with a Multimode Pump Laser,", J.Opt.Soc.Am.B/Vol.5(2), 358-63, (1988).

[3] K.O.Hill, D.C.Johnson, B.S.Kawasaki and R.I.MacDonald, "CW Three-Wave Mixing in Single-mode Optical Fibres,", J.Appl.Phys.49(10), 5098-106, (1978).

[4] W.Lu, "Nonlinear Dynamics of Optical Systems", Ph.D Thesis (unpublished), Heriot-Watt University, Edinburgh, 1991.

[5] T.H.Maiman, "Stimulated Optical Radiation in Ruby,", Nature 187,493-94, (1960).

[6] L.F.Johnson and L.Nassau, Proc.IRE 49, 1704, (1961).

[7] J.E.Geusic, H.M.Marcos and L.G. Van Uitert, "Laser Oscillations in Nd-doped Yttrium Aluminium, Yttrium Gallium and Gandolinium Garnets,", Appl.Phys.Lett. Vol.4, 182-87, (1964).

[8]W.Koechner, *Solid-State Laser Engineering*. New York: Springer, 1976, pp354-55.

[9] W.Koechner, "Output Fluctuations of CW-Pumped Nd:YAG Lasers,", IEEE J.Quant.Elec., Vol.QE-8(7), 656-61,(1972).

[10] H.Nagai,"Laser Frequency Fluctuations Due to Mechanical Vibrations,", IEEE J.Quant.Elec.,Vol.QE-8(12), 857-65,(1972).

[11] R.Marchetti, E.Penco, A.Perito, M.Tomassini and A.Tranquilli, "Thermal Transient Effects in Silicate and Phosphate Rods Pumped in Pseudoelliptic Close-Coupled Cavities,", Opt.Commun., Vol.29, 347-52, (1979).

[12] N.Subhash and K.Sathianandan, "Thermal Effects in a Nd:Glass Laser Rod Pumped in a Double Circular Close-Coupled Cavity", IEEE J.Quant.Elec. Vol.**QE-20**(2), 111-16, (1984).

[13] J.S.Uppal, J.C.Monga and D.D.Bhawalkar, "Study of Thermal Effects in an Nd Doped Phosphate Glass laser Rod", IEEE J.Quant.Elec. **QE-22**(12), 2259-65, (1986).

[14] J.S.Uppal, P.D.Gupta and D.D.Bhawalkar, "Study of Thermally Induced Active Birefringence in Nd:Glass Laser Rods", J.Appl.Phys.Vol.**54**(11), 6615-19, (1983).

[15]W.Koechner, *Solid-State Laser Engineering*. New York: Springer, 1976, pp344-90.

[16] J.D.Foster and L.M.Osterink, "Thermal Effects in a Nd:YAG Laser", J.Appl.phys., Vol.**41**, 235-58, (1970).

[17] W.Koechner, "Thermal Lensing in a Nd:YAG Laser Rod", Appl.Opt., Vol.**9**, 2548-53, (1970).

[18] J.F.Nye, *Physical Properties of Crystals, New York: Clarendon*, 250-51, (1957).

[19] P.A. Khandokhin and Ya.I.Khanin, "Instabilities in a Solid-State Ring Laser", J.Opt.Soc.Am. B/Vol.**2**(1), 226-31, (1985).

[20] C.L.Tang, H.Statz and G.DeMars, "Regular Spiking and Single mode Operation of Ruby Laser", Appl.Phys.Lett., Vol.**2**, 223-24, (1963).

[21]C.L.Tang, H.Statz and G.DeMars, "Spectral Output and Spiking behaviour of Solid-State Lasers", J.Appl.Phys., Vol.**34**(8), 2289-95, (1963).

[22] D.A.Draegert, "Efficient Single-Longitudinal-Mode Nd:YAG Laser", IEEE J.Quant.Elec., Vol.**QE-8**(2), 235-39, (1972). A.R.Clobes and M.J.Brienza, "Single-Frequency Travelling-wave Nd:YAG laser", Appl.Phys.Lett., Vol.**21**(6), 265-67, (1972).

[23] S.M.Jarret and J.F.Young, "High-efficiency single-frequency cw ring dye laser", Optics Lett., Vol.4(6), 176-78, (1979). T.F.Johnston and W.Proffitt, "Design and Performance of a Broad-Band Optical Diode to Enforce One-Direction Travelling-Wave Operation of a Ring Laser", IEEE J.Quant.Elec., **QE-16**(4), 483-88, (1980).

3. Dynamical Behaviour of SBS in Optical Fibres without Feedback

3.1 Introduction

The first experimental observation of stimulated Brillouin scattering (SBS) was made by Chiao and co-workers in 1964 [1]. In the experiment a Q-switched Ruby laser was used as the light source and the Brillouin medium was a Quartz crystal. The light incident upon the Quartz crystal was scattered by a grating formed through the coupling of the light wave with the acoustic waves present in the medium. The scattered light was found to be comparable in intensity with the original light source. Spontaneous Brillouin scattering involves the scattering of light waves by acoustic waves or density variations, and the medium is macroscopically unaffected by the process. In contrast, the mechanism for stimulated Brillouin scattering requires the presence of the light field to induce fluctuations in the medium, and create a macroscopic effect which will enhance the scattering of the incident light waves.

A schematic illustration of stimulated Brillouin scattering is shown below in Figure 3.1.

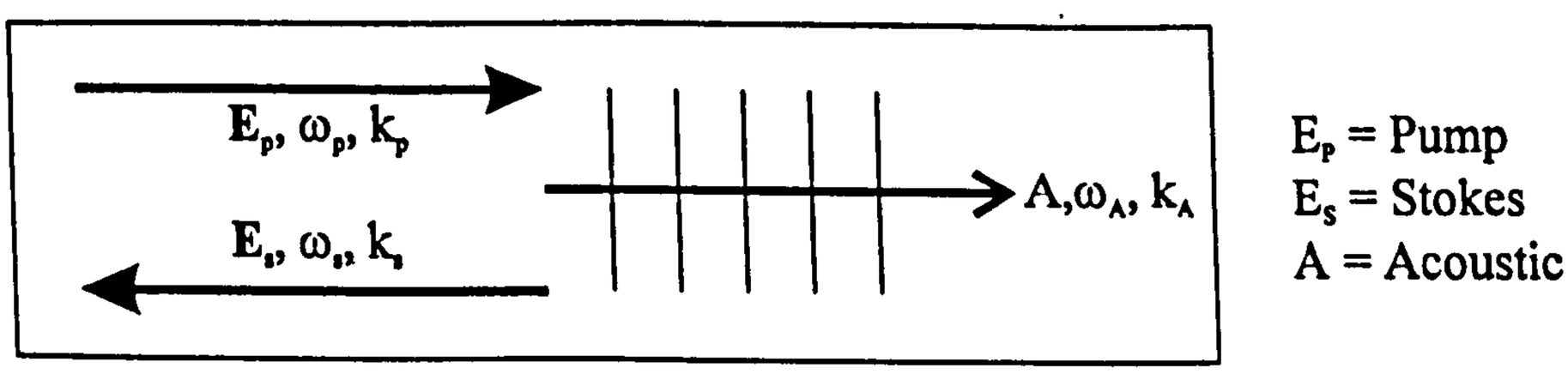

Figure 3.1 Schematic Diagram of Stimulated Brillouin Scattering in a Medium.

For an incident laser beam of frequency ω_P, the light is initially scattered by an acoustic wave ω_A (spontaneous Brillouin scattering). The scattered counter-propagating light is downshifted in frequency by the Doppler effect to a Stokes frequency $\omega_S = \omega_P - \omega_A$, because the acoustic wavefronts are propagating away from the incident laser light. The Stokes wave ω_S will then interfere with the incident pump wave ω_P, creating an interference term $\omega_A = \omega_P - \omega_S$. This interference term reinforces the acoustic wave ω_A via electrostriction, which is the compression of the material due to the presence of the electric field. The electrostrictive process generates a refractive index grating in the medium. The incident pump wave is then scattered by the index grating through Bragg diffraction. As the intensity of the Stokes wave increases, the beating term $\omega_P - \omega_S$ adds constructively to the acoustic wave and thus the index grating scatters more of the incident pump light. The positive feedback caused by the interaction of the two optical waves with the acoustic wave via electrostriction produces an exponential growth of the amplitude of the Stokes wave, i.e. stimulated scattering.

3.2 Theory of Stimulated Brillouin Scattering

A theoretical description of stimulated Brillouin scattering (SBS) must account for the optical fields and material properties, and the coupling between them through the electrostrictive effect which is the key process of SBS. In the following conventional analysis a simple three-wave interaction is considered, Figure 3.1, with the Stokes wave propagating in the opposite direction to the pump.

3.2.1 Optical Equations

In order to describe the propagation of optical waves inside a non linear medium, the most general Maxwell wave equation is used:

$$\nabla^2\vec{E} - \frac{n^2}{c^2}\frac{\partial^2\vec{E}}{\partial t^2} = \mu_0\frac{\partial^2\vec{P}^{(NL)}}{\partial t^2} \qquad (1)$$

where $\vec{E}$ and $\vec{P}^{(NL)}$ represent the total electric and nonlinear polarisation fields; c, n, μ_0 are the speed of light, the linear refractive index and the magnetic permeability of the medium respectively. The electric fields of the pump and Stokes wave are given by

$$\vec{E} = E_p\hat{e}_p\exp\left[i(\omega_p t - k_p z)\right] + E_S\hat{e}_S\exp\left[i(\omega_S t + k_S z)\right] + c.c. \qquad (2)$$

where E, $\hat{e}$, ω, and k are the amplitude, the polarisation unit vector, the frequency and the longitudinal component of the wave vector of the electric waves. The subscripts P and S refer to the pump and Stokes wave respectively. The energy and momentum of the optical fields are conserved by the following relationships:

$$\omega_A = \omega_p - \omega_S$$
$$k_A = k_p + k_S .$$

Before the optical equation is inserted into the general Maxwell equation, the slowly varying amplitude approximation will be assumed. This approximation is justified because the amplitude of the electric field varies slowly on the wavelength scale and during an optical period;

$$\left|\frac{\partial^2 E}{\partial t^2}\right| \langle\langle \left|\omega\frac{\partial}{\partial t}E\right| \langle\langle |\omega^2 E|$$

$$\left|\frac{\partial^2 E}{\partial z^2}\right| \langle\langle \left|k\frac{\partial}{\partial z}E\right| \langle\langle |k^2 E| .$$

For all the performed stimulated scattering experiments a single-mode fibre is used as the Brillouin medium. Therefore the transverse terms in the x and y plane are neglected and only spatial variations in the z direction are considered. Application of the slowly varying amplitude approximation and replacing the electric field in equation (1) with the expression for the optical fields (2) yields the following set of equations:

$$\left[\frac{\partial}{\partial z}+\frac{n_P}{c}\frac{\partial}{\partial t}\right]E_P=-\frac{\mu_0}{2ik_P}\exp\left[-i\left(\omega_P t-k_P z\right)\right]\frac{\partial^2}{\partial t^2}\left(\hat{e}_P^{+}\cdot\vec{P}_P^{(NL)}\right)$$
$$\left[\frac{\partial}{\partial z}-\frac{n_S}{c}\frac{\partial}{\partial t}\right]E_S=\frac{\mu_0}{2ik_S}\exp\left[-i\left(\omega_S t+k_S z\right)\right]\frac{\partial^2}{\partial t^2}\left(\hat{e}_S^{+}\cdot\vec{P}_S^{(NL)}\right) \qquad (3)$$

These equations describe the spatial, temporal evolution of the amplitude of the optical waves inside the fibre. In the next section a model of the reaction of the medium is derived.

3.2.2 Material Equation

The presence of electric fields in a medium causes field-induced density redistribution of the medium through the electrostriction process. The density of the medium increases in the vicinity of a strong electric field region, in order to minimise the free energy of the system. The density fluctuation $\Delta\rho$ is described by a damped acoustic wave equation [2]:

$$\left[\frac{\partial^2}{\partial t^2}-\Gamma_B\nabla^2\frac{\partial}{\partial t}-v_A^2\nabla^2\right]\Delta\rho=-\left(\vec{\nabla}\cdot\vec{F}\right).$$

The density variation is related to the medium by $\Delta\rho = \rho - \rho_0$, where ρ_0 is the equilibrium density of the medium. The acoustic damping coefficient Γ_B is related to the spontaneous Brillouin linewidth by the relationship $\Gamma_B = 2\pi\Delta\nu_B$. The driving force $\vec{F}$ represents the coupling between the matter and the optical waves. The velocity v_A of the acoustic wave is related to the medium by

$$v_A = \sqrt{\frac{Y_0}{\rho_0}}$$

where Y_0 is the Young's modulus of the medium. As the SBS process is a coupling between optical and acoustic waves, the following expression is used for the density variation:

$$\Delta\rho = A\exp\left[i\left(\omega_A t - k_A z\right)\right] + c.c..$$

Introducing this expression into the material equation and making the slowly varying amplitude approximation,

$$\left|\frac{\partial^2 \Delta\rho}{\partial t^2}\right| \langle\langle \left|\omega_A \frac{\partial}{\partial t}\Delta\rho\right| \langle\langle \left|{\omega_A}^2 \Delta\rho\right|$$

yields the following equation

$$\left[\frac{\partial}{\partial t} + \frac{\Gamma_B}{2v_A} + v_A \frac{\partial}{\partial z}\right] i2A\omega_A \exp\left[-i\left(\omega_A t - k_A z\right)\right] = -\left(\vec{\nabla}\cdot\vec{F}\right).$$

3.2.3 Coupling Between the Optical and Material Waves

The material equation is coupled to the light wave equations by the driving force $\vec{F}$, which is generated by the two light waves through electrostriction:

$$\vec{F} = \vec{\nabla}\left(\frac{1}{2\pi}\varepsilon_0 \gamma_e E_P \cdot E_S^*\right). \tag{4}$$

Equation (4) represents the field induced intensity change which contributes to the change in the optical susceptibility of the material. The electrostrictive coefficient is related to the change in permittivity ε with density ρ by the expression

$$\gamma_e = \rho_0 \frac{\partial \varepsilon}{\partial \rho}.$$

The nonlinear polarisation $\vec{P}^{(NL)}$ is given by

$$\vec{P}^{(NL)} = \frac{\varepsilon_0 \gamma_e}{\rho_0} \Delta\rho \vec{E}$$

and the resonant nonlinear polarisation's governing the pump and Stokes waves are

$$\vec{P}_P{}^{(NL)}(\omega_S) = \frac{\varepsilon_0 \gamma_0}{\rho_0} E_S A \hat{e}_S \exp i\left[(\omega_S + \omega_A)t + (k_S - k_A)z\right]$$

$$\vec{P}_S{}^{(NL)}(\omega_P) = \frac{\varepsilon_0 \gamma_0}{\rho_0} E_P A^* \hat{e}_P \exp i\left[(\omega_P - \omega_A)t - (k_P - k_A)z\right]$$

By the conservation of energy law, $\omega_A = \omega_P - \omega_S$, and maximum power transfer occurs when the phase matching condition $k_A = k_P + k_S$ is met by the wave vectors of the fields. The Doppler frequency shift between the pump and Stokes wave is

$$\omega_A = |k_A| v_A = 2 v_A |k_P| \sin(\theta/2)$$

where θ is the angle between the pump and the scattered Stokes wave. The approximation $|k_P| \approx |k_S|$ is made because the acoustic frequency (GHz) is several orders of magnitude lower than the optical frequencies (THz). In solving the equations only the backward SBS process will be considered, because the frequency shift is zero

when the two optical waves are propagating in the same direction close to threshold. Substitution of the resonant nonlinear polarisation terms into the optical equations, and inclusion of the electrostrictive driving force into the material equation produces three first order coupled equations for the pump, Stokes and acoustic wave respectively:

$$\left[\frac{\partial}{\partial z}+\frac{n_P}{c}\frac{\partial}{\partial t}+\frac{\alpha}{2}\right]E_P = -igE_S A\exp(i\Delta kz)$$

$$\left[\frac{\partial}{\partial z}-\frac{n_S}{c}\frac{\partial}{\partial t}+\frac{\alpha}{2}\right]E_S = igE_P A^*\exp(-i\Delta kz) \qquad (5)$$

$$\left[\frac{\partial}{\partial t}+\frac{\Gamma_B}{2}+iv_A\Delta k\right]A = h\,E_P E_S^*\exp(-i\Delta kz)$$

$$g=\frac{\omega_P^2}{2k_P c^2}\frac{\partial\varepsilon}{\partial\rho}\left(\hat{e}_P^+\cdot\hat{e}_S\right)$$

$$h=\frac{ik_A\varepsilon_0}{4\pi v_A^2}\rho_0\frac{\partial\varepsilon}{\partial\rho}\left(\hat{e}_P\cdot\hat{e}_S^+\right)$$

In the material equation the amplitude of the acoustic wave is assumed to satisfy the following equation $\partial A/\partial z = i\Delta kA$ [2 ,3] where the phase mismatch term is represented by $\Delta k = k_P + k_S - k_A$. For the steady state solutions the waves are assumed to be phase matched and the phase mismatching term $\Delta k = 0$. A linear attenuation factor α is included in the optical equations to account for the optical loss of the medium. The steady state equations for the pump and Stokes waves are:

$$\left[\frac{\partial}{\partial z}+\frac{\alpha}{2}\right]E_P = -G_B\left|E_S\right|^2 E_P$$

$$\left[\frac{\partial}{\partial z}+\frac{\alpha}{2}\right]E_S = G_B\left|E_P\right|^2 E_S$$

where the Brillouin gain G_B, and the polarisation factor κ are given by

$$G_B = \frac{2gh}{\Gamma_B} = \left[\frac{\kappa}{2v_A}\left(\frac{\partial\varepsilon}{\partial\rho}\right)\right]^2 \frac{ik_A\varepsilon_0\rho_0}{\pi nc\Gamma_B}.$$

$$\kappa = \left(\hat{e}_P \cdot \hat{e}_S\right)^2$$

The polarisation factor κ depends upon the polarisation preserving properties of the medium. For the silica cored fibres used in the experiments the polarisation directions are not preserved as the pump and Stokes wave propagate along the fibre. The polarisation directions are rapidly changing along the fibre, and as a result $\left(\hat{e}_P \cdot \hat{e}_S\right)^2$ is no longer constant. To account for the polarisation scrambling an average $K = \overline{\left(\hat{e}_P \cdot \hat{e}_S\right)^2}$ is taken over the whole length of the fibre from which the depolarisation factor K is defined. If the fibre is polarisation preserving the depolarisation factor K is equal to unity for the whole length of the fibre. If depletion of the pump is neglected, the evolution of the Stokes intensity is the following:

$$\left|E_S(z)\right|^2 = \left|E_S(L)\right|^2 \exp\left[\left(G_B - \alpha\right)(L - z)\right]. \qquad (6)$$

The threshold condition for stimulated scattering to occur is similar to a laser resonator. The requirement is for the gain in the system to be greater than the losses and hence the backwards travelling Stokes will grow in amplitude . The threshold condition is simply

$$G_B = \alpha.$$

Clearly equation (6) illustrates that through the process of electrostriction, the scattered Stokes wave can experience an exponential gain as it propagates counter- directionally to the incident pump. In the next section a brief review will be presented outlining the dynamical behaviour of SBS in optical fibres.

3.2.4 SBS in Optical Fibres

The main motivation for studying stimulated scattering phenomena in optical fibres, was to determine the implications these nonlinear processes may have for low loss optical communication links [4]. The first report of SBS and dynamical behaviour in optical fibres by Ippen and Stolen in 1972 [5], indicated the presence of oscillations in both the transmitted pump and scattered Stokes signal. In the experiment a pulsed Xenon Chloride laser (XeCl) was used as the pump and SBS was generated for an input power of 1W with a pulse duration of 600ns. The period of the oscillations observed depended upon the round trip of the medium $\tau_R = 2T_R = 2nL/c$ and agreed with earlier theoretical predictions by Johnson et al [6]. The presence of oscillations in both the transmitted pump and the Stokes intensity were attributed to the weak Fabry-Perot effect of the fibre cavity. This was formed by the Fresnel reflectivity at the cleaved ends of the fibre.

An experiment performed by Cotter [7] in 1982 demonstrated an SBS threshold as low as 5mW for 13km of silica cored fibre pumped by a continuous, single frequency Nd:YAG laser at a wavelength of 1.3μm. The low threshold had dramatic implications for the power budget handling of low loss optical fibres, particularly for long haul systems. The SBS process introduced additional signal attenuation, noise and increased backward coupling into the pump laser. However, the SBS problem was resolved by the introduction of digital optical communication systems. For digital optical communications, information is transferred by the direct modulation and direct detection of light. The duration of the pulses produced by the modulation of the pump laser were comparable to the lifetime of the acoustic phonons in the fibre. This created a significant increase in the SBS threshold through a combination of dramatically reducing the

efficiency of the opto-acoustic wave coupling process [8], and decreasing the average pump power.

Attention focused upon SBS with the investigation of coherent optical communications, where the coherent properties of the light source would be utilised to increase the bandwidth of the system. This created the necessity for all optical amplification [9] in order to increase both the speed and length of the communication link. The low threshold, high gain, and narrow bandwidth of the SBS process led to the development of Brillouin amplifiers [10] and Brillouin fibre lasers [11]. However, the low threshold of SBS also provided additional problems for optical amplifiers based upon the stimulated Raman scattering process. Fibre Raman amplifiers, have a wider bandwidth compared to Brillouin amplifiers. The threshold for stimulated Raman scattering is greater than the threshold for SBS (2~3 SBS_{th}). Studies have revealed Brillouin scattering accompanying Raman scattering in optical fibre based amplifiers. The presence of Brillouin scattering in the form of noise [12] imposes limitations upon the operating capabilities of Raman amplifiers.

The source of noise in the Stimulated Brillouin scattering process had been attributed to the presence of spontaneous Brillouin scattering. A report by Bar-Joseph et al [13] revealed the importance of reflectivity for producing oscillatory SBS behaviour. The report concluded that the oscillations were a source of noise in optical communication systems and were also responsible for multimode operation of Brillouin fibre lasers. The physical mechanism responsible for the formation of the oscillations also agreed with original observations made by Ippen and Stolen [5].

Alternative experiments addressing the dynamical aspects of the Stokes wave used pulsed lasers [14 ,15], additional pump beams [16 ,17] and higher order Stokes-

anti-Stokes generation [18]. Although these experiments employed non-guiding media as the Brillouin medium, chaotic and other forms of dynamical behaviour were observed.

To overcome the analytical restrictions inherent to pulsed experiments, Harrison et al [19] used continuous pumping conditions and reported first evidence of chaotic SBS generated in optical fibres. In the experiment a cw single mode laser was used to generate first order Stokes in a single-mode optical fibre [7]. For a fibre with no reflectivity the SBS emission indicated strong aperiodic behaviour. In the case of weak feedback, i.e. natural Fresnel reflections at the cleaved ends of the fibres, the SBS displayed a range of dynamics including sustained relaxation oscillations and quasiperiodic motion.

The broad band features of a chaotic signal could offer a simple explanation to the noise associated with stimulated scattering phenomena in Brillouin fibre amplifiers / lasers and also Raman fibre amplifiers. Boyd et al [20] had established the initiation of SBS from spontaneous Brillouin scattering and reported stochastic dynamics for SBS in an optical fibre without feedback [21]. The effect of nonlinear refraction upon promoting deterministic dynamical behaviour was reported theoretically by Lu et al [22], and experimentally by Johnstone et al [23]. However, no experimental statement exists confirming the observation of deterministic chaotic SBS generated in an optical fibre.

In the next section the nonlinear dynamics of SBS generated in an optical fibre without feedback are investigated experimentally. Theoretical solutions obtained by co-workers will also be presented to provide a comparison with the experimental findings. The conventional theoretical equations presented in section 3.2, are modified to include terms to account for both the nonlinear refractive index [22,23] and the noise associated

with spontaneous Brillouin scattering [20,21]. To provide a comparison with experimental findings the new set of modified equations were numerically solved,

$$\frac{\partial E_P}{\partial \eta} + \frac{\partial E_P}{\partial \xi} + \frac{1}{2}\beta E_P = -gE_S A_N + iu\left[|E_P|^2 + 2|E_S|^2\right]E_P \tag{7}$$

$$\frac{\partial E_S}{\partial \eta} - \frac{\partial E_S}{\partial \xi} + \frac{1}{2}\beta E_S = gE_P A_N^* + iu\left[|E_S|^2 + 2|E_P|^2\right]E_S \tag{8}$$

$$\frac{1}{\beta_A}\frac{\partial A_N}{\partial \eta} + A_N = E_P E_S^* + f(\eta, \xi) \tag{9}$$

where $A_N = \dfrac{2\omega_A \Gamma_B A}{i\varepsilon_0 \gamma_e q |A_P|^2}$.

E_P, E_S and A_N are the slowly varying amplitudes of the forward pump, the Stokes and the acoustic wave. The normalisation parameters are

$$\beta = \alpha L,\ \eta = \frac{t}{T_R},\ T_R = \frac{nL}{c},\ \xi = \frac{z}{L},\ \text{and}\ \beta_A = \pi \Delta \nu_B T_R$$

where T_R is the transit time of a length of fibre L, α is the optical attenuation coefficient of the fibre and $\Delta\nu_B$ is the spontaneous Brillouin linewidth. The amplitude of the material wave A, is normalised by the amplitude A_P which is the pump amplitude at $\xi = 0$. A Langevin noise term was introduced into the material equation (9) to describe the random thermal fluctuations of the density and had a Gaussian distribution [20,21]. The additional coupling terms (in the square brackets) in both optical equations (7) and (8) represent the self phase modulation and cross-phase modulation introduced by the nonlinear refractive index [22,23]. For a fixed pump power P_0 and a length of fibre L, the pump dependent gain g in the SBS equations is given by

$$g = \frac{P_0 g_B K L}{2 a_{eff} \delta_e}.$$

The fibre used in the experiment had a germanium (GeO_2) doped silica (SiO_2) core with a pure silica cladding. The fibre was non-polarisation preserving and had a core of diameter 5μm. The depolarisation factor K of the fibre had the value 1/2 for a non-polarisation preserving fibre and the effective core of interaction a_{eff} was 27.01μm^2. The geometry of the fibre core enhances the guiding of the acoustic waves and creates an enlargement of the Brillouin gain [24]. The enlargement of the Brillouin gain δ_e was 2.36 for a pump wavelength λ_p of 1.064μm [25]. At this wavelength the peak Brillouin gain g_B coefficient which is material dependent was determined from the expression

$$g_B = \frac{2\pi n^7 p_{12}^2}{c\lambda_P^2 \rho_0 v_A \Delta\nu_B}$$

and had a value 4.83 x 10^{-11} m/W. The physical constants in the gain equation are the refractive index n (1.4616), the longitudinal elasto-optic coefficient p_{12} (0.286), the equilibrium density of the medium (2.21 x 10^3 kg/m^3) and the acoustic velocity of sound in fused silica v_A (5960 ms^{-1}).

Finally, the phase modulation term u was power dependent and given by the equation below where the Brillouin gain g_B and the pump dependent gain g are used to normalise the expression

$$u = g\frac{n_2}{g_B}.$$

The nonlinear refractive index coefficient $n_2 = 3\chi^{(3)}/8n$, had a value of 3.85 x 10^{-22} m^2/V^2 for a fibre with a fused silica core.

3.3 Experimental Set-up

The experimental set-up used for performing the investigations into the dynamical behaviour of SBS is illustrated in figure 3.2. The ring laser designed and constructed in chapter 2 was used as the pump laser. The Brillouin gain in a medium depends upon the bandwidth of the pump source [26], and is related to the Brillouin bandwidth by the following expression

$$g_B' = \left(\frac{\Delta \nu_B}{\Delta \nu_P + \Delta \nu_B} \right) g_B \qquad (10)$$

The instantaneous linewidth of the pump laser ,$\Delta\nu_P \leq 40\text{kHz}$, is several orders of magnitude smaller than the Brillouin bandwidth, $\Delta\nu_B \leq 33.5\text{MHz}$, and therefore the Brillouin gain is unaffected by the pump ($g_B' \approx g_B$).

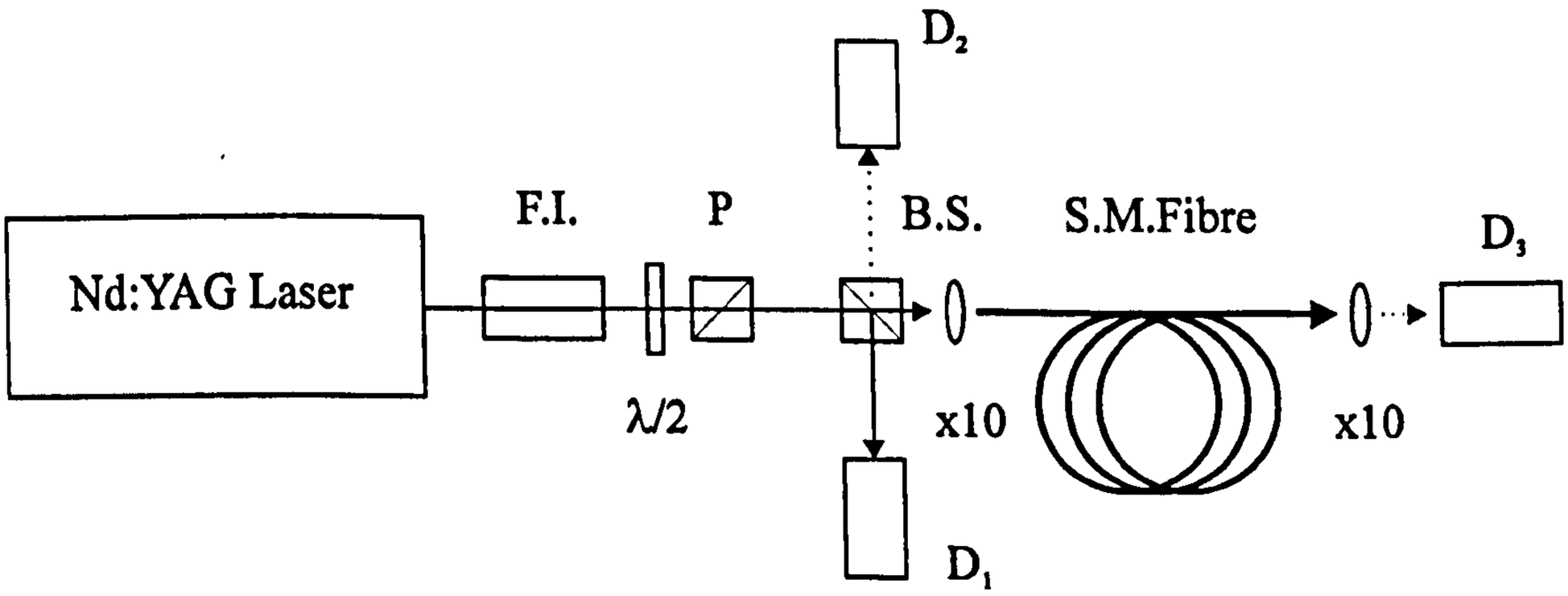

Figure 3.2 Experimental set-up for steady state and temporal analysis of SBS.

The laser was optically isolated from the experiment by inserting a Faraday isolator (F.I. model OFR No. IO-5-YAG) in the path of the incident pump beam. The isolator provided an isolation greater than 35dB and reduced the transmitted power by 10%. The light from the laser contains a small percentage (~5%) of depolarised light

induced by the thermal birefringence of the YAG rod and this is blocked by the front polariser of the isolator. The second mechanism which contributed to a 5% reduction in the transmitted power was absorption by the optical Verdet material used in the isolator to rotate the polarisation.

The three main reasons for justifying optical isolation were as follows :

1. External feedback injected into a stable laser can lead to temporal instabilities and large fluctuations in the output power.
2. The scattered Stokes wave propagates in a counter-directional manner relative to the pump, and is downshifted in frequency by several GHz. The gain bandwidth of Nd:YAG is 180GHz and the injection of the shifted Stokes signal could initiate the lasing of another longitudinal mode.
3. Isolation eliminates the formation of any external cavities created by the fibre entrance and the laser output coupler. The introduction of the shifted Stokes signal travelling co-directional to the pump can lead to the generation of multiple orders of Stokes and Anti-Stokes frequencies [27 ,28] through parametric four wave mixing.

The combination of a quarter-wave plate and polariser cannot provide sufficient isolation due to the polarisation scrambling of the fibre and hence a non-reciprocal device such as a Faraday isolator must be implemented.

Adjustment of the incident pump intensity was provided by a half-wave plate ($\lambda/2$) used in conjunction with a Glan-Taylor polariser (P). The light was coupled into and out of the fibre by two x10 microscope objective lenses. The beam spot size was 2-3mm and slightly under-filled the microscope objective. The under-filling of the lens

improved the matching of the numerical apertures of both the lens and the fibre, providing a launch efficiency greater than 65%.

The launch efficiency and the attenuation of the fibre were measured using the traditional 'cutback' technique. For a fixed length of fibre, the pump power is launched into the fibre and optimised. The transmitted power is measured and then the fibre is cutback a few tens of centimetres, and again the transmitted power is measured for the new fibre length. The launch efficiency was found by dividing the power transmitted through the fibre by the input power. The difference in the two transmitted powers taken before and after a fixed length was cutback allows the fibre loss to be determined. The fibre was manufactured to be single-mode at a wavelength of 1.064μm and this was confirmed by observing the fibre output with a CCD camera to ensure the emerging beam was an LP_{00} mode.

A 50/50 (B.S.) beamsplitter cube was positioned before the entrance of the launch microscope objective to facilitate the monitoring of the pump and counter-propagating Stokes signal. A scanning Fabry-Perot interferometer with a free spectral range of 100GHz, a resolution of 1.6GHz at FWHM and a finesse of 60 was used to examine the spectral content of both the transmitted pump and scattered light. A pyro-electric power meter (Coherent model No. 210) was used to measure the relative power levels of all the signals.

Temporal measurement of the optical signals required the use of fast photodiodes (type BPX-65: bandwidth 700MHZ) positioned at locations D_1, D_2 and D_3 to monitor the pump, the SBS and the transmitted pump respectively. The signal generated in the photodiode was amplified by two linear amplifiers (Comlinear CLC100) cascaded

together to provide a gain of 40dB. A more detailed analysis of the photodiode and amplifiers is presented in section 3.3.2.

Real time analysis of the signals required a fast analogue oscilloscope (Tektronic-7104) with a bandwidth of 1GHz, and a radio frequency spectrum analyser (HP8590D) with a bandwidth ranging from 30kHz-2GHz limited to a resolution of 10kHz. The time series was observed directly and the corresponding phase portrait of the signal was reconstructed using the oscilloscope in the x-y mode. By selecting an appropriate length of co-axial cable a time delay was introduced to one of the scope channels and thus the phase portrait was constructed by plotting the original signal against the delayed signal.

The spectrum analyser provided detailed analysis of the temporal signals in the frequency domain, and for long sweep periods the Fast Fourier Transform (FFT) could be calculated by the analyser. Data acquisition and handling was performed by a transient digitiser/digitising scope (Lecroy 9354L) which had a maximum sampling rate of 2GHz, and was connected to an IBM-PC for data storage. The data was transferred from the PC to a SUN workstation for further signal processing and analysis.

3.3.1 Reduction of Natural Reflectivity

To eliminate the effects of feedback and create an open flow system the natural Fresnel reflectivity present at the cleaved ends of the fibre had to be removed. Two different techniques were employed. The first technique consisted of placing a small reservoir of index matching fluid at each end of the fibre. This method had several undesirable features. The relatively high pump powers involved would cause burning of the index fluid and localised heating at the ends of the fibre. The launch efficiency was

also reduced because the fibre launch had to be re-optimised to allow the inclusion of the index matching reservoirs.

A more suitable solution was found by polishing the end of the fibre to a small angle from the normal. Light reflected from the angled fibre/air interface is lost into the fibre cladding , and is prevented from being guided back down the fibre core. If the fibre axis is at an angle of θ radians to a front surface of reflectivity R, then the fraction ρ of the incident power that is successfully coupled back into the fibre can be approximated by [29],

$$\rho = R\exp\left(-k_{cl}^2\omega_0^2\theta^2\right)$$

where k_{cl} is the propagation constant in the cladding. For an angle θ of 4°, $\rho = 1\text{x}10^{-4}$ R for the fibre used, therefore an angle of only a few degrees can dramatically reduce the amount of reflected light.

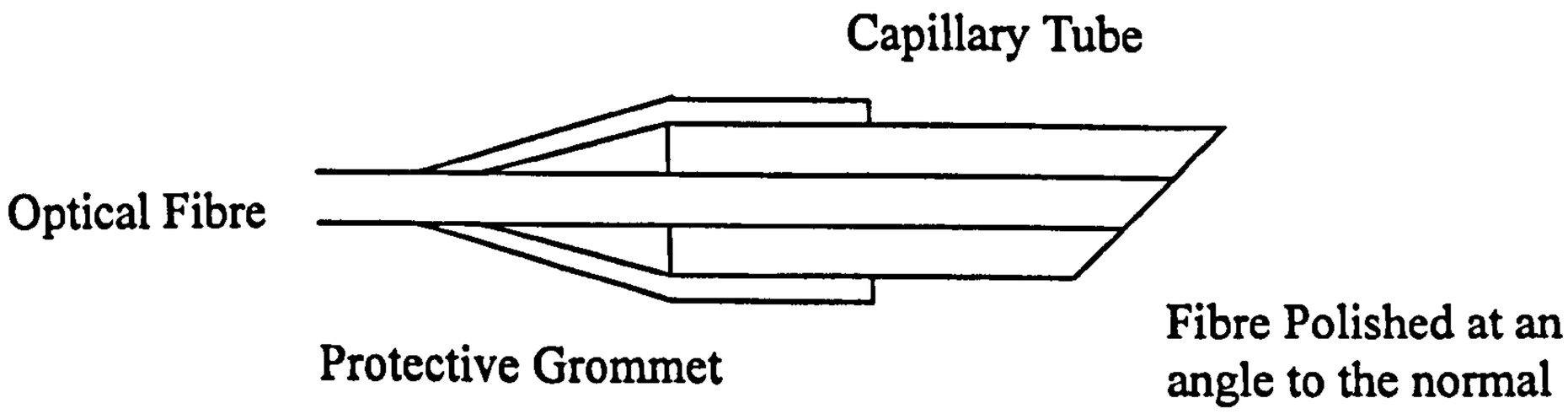

Figure 3.3 Schematic diagram of the protected fibre tip polished at an angle θ to the normal.

To improve and aid the polishing process, the fibre was inserted into a support to improve the mechanical rigidity. The support was formed by guiding the end of the fibre along the bore of a capillary tube filled with a u.v. curing epoxy adhesive. The fibre was prepared for the tube by removing the protective outer buffer coating and cleaning the bare fibre with acetone to enhance adhesion. After the adhesive had been cured a semi-

rigid shrink wrap grommet was attached at the fibre/capillary tube interface to form a robust mechanical joint and protect the assembly from damage during polishing, Figure 3.3 The fibre/capillary tube assembly was polished at an angle θ to the normal using several grades of abrasives, and a flatness of λ/4 was easily achieved.

3.3.2 Noise Considerations

Prior to any experimental investigation into a system's dynamics, the issue of noise has to be addressed and considered carefully. To improve the differentiation between a stochastic or deterministic process, the contribution of noise should be kept to an absolute minimum. For the previous experimental arrangement, the main forms of noise were optical and electronic.

Although optical isolation reduced stray reflections which could induce undesirable features in the SBS process, the main source of optical noise was caused by multi-longitudinal operation of the pump laser. The beating of two longitudinal modes in the laser gave rise to two prominent effects. The beat frequency of 220MHz depended upon the free spectral range of the laser resonator, and was clearly visible in the form of a sinusoid which was superimposed upon the SBS signal. The spacing of the longitudinal modes (220MHz) was larger than the Brillouin gain bandwidth ($\Delta\nu_B$ = 33.5MHz) and each pump mode generated its own Stokes signal. This process also imposed complex features upon the SBS signal. However, by monitoring both the pump and the SBS signals with the spectrum analyser and Fabry-Perot interferometer respectively, data could easily be obtained for single mode pumping and single first order Stokes generation.

The main contribution to electronic noise was the photodiode and post detection amplifier. The signal to noise ratio (SNR) of the detection system employed in the experiment [30] was

$$SNR = i_s\left[2e\Delta f\left(i_s + i_d\right) + \frac{4k_B T\Delta f}{R_L}\left(F_1 + \frac{\left(F_2 - 1\right)}{A_i}\right)\right]^{-\frac{1}{2}} \qquad (11)$$

where Δf is the bandwidth of the post detection system, e is the electronic charge, i_s is the signal current, i_d is the dark current of the photodiode, k_B is the Boltzman constant, T is the temperature, F is the noise figure of the amplifiers, A_i is the insertion loss between the amplifiers and R_L is the load resistor.

The first term in the parenthesis represents the quantum noise, the second term describes the noise generated in the detector and the third term includes the thermal noise and shot noise of the load resistor and cascaded amplifiers. The following parameter values were used in the detection system: $\Delta f = 500MHz$, $i_s = 100\mu A$, $i_d = 5nA$, T=300K, $R_L = 10k\Omega$, $F_1 = F_2 = 6dB$ and $A_i = 0.25dB$. Inserting these parameters into equation (11) reveals that the second and third terms are negligible. therefore, the photodiode was quantum noise limited and equation (11) was simplified to

$$SNR = \left(i_s / 2e\Delta f\right)^{\frac{1}{2}}.$$

The shot noise of the signal generates a voltage of $v_s = R(2e\ \Delta f\ i_s)^{1/2}$ at the output of the photodiode. With the same values as before the voltage $v_s = 1.2$ mV. The signal voltage was kept in a region between 300 - 400 mV throughout the experiments to minimise the influence of noise.

Optimisation of the transient digitiser was necessary to prevent under-sampling of the signal. Under-sampling of a waveform introduces distortion through loss of

information, and can seriously impede the analysis of the synthesised data. Before digitisation the SBS signal was measured over a period of several seconds to ensure enough data for the calculation of the Fast Fourier Transform by the spectrum analyser. The maximum frequency or Nyquist frequency determined by the FFT was 100MHz . The minimum sampling rate (2f) at which a frequency f can theoretically be recovered is known as the Nyquist rate. For a Nyquist frequency of 100MHz (f_1) a Nyquist rate of 200MHz ($2f_1$) would be required to reconstruct the waveform. A LeCroy transient digitiser 9354L of maximum sampling rate 2GHz is used to record the data. For a sampling rate of 1GHz the corresponding Nyquist frequency was 500MHz which corresponded to the maximum bandwidth of the cascaded amplifiers.

3.4 Time Averaged (Steady State) Behaviour

The time averaged (steady state) solutions for an SBS generator without feedback were obtained by solving the modified equations (7) - (9) in section 3.2.4. To find the steady state the time derivatives are set equal to zero and the noise term is omitted in the material equation (9). The noise term was considered to be a constant noise signal present at the rear of the SBS medium i.e. the location from which the SBS is initiated [31]. The self-phase modulation and cross-phase modulation terms were also removed from the steady state SBS equations because their contribution does not modify the steady state intensities. The two steady state equations which govern both the Stokes and transmitted pump intensities are given by

$$\frac{\partial I_1}{\partial \xi} = -\beta I_1 - G I_1 I_2$$

$$-\frac{\partial I_2}{\partial \xi} = -\beta I_2 + G I_1 I_2 \qquad (12)$$

where the normalised intensities are $I_1 = |E_P|^2$ and $I_2 = |E_S|^2$, the attenuation in the fibre is represented by $\beta = \alpha L$, and the single pass Brillouin gain G is related to the absolute intensity I_P by

$$G = \frac{I_P}{2a_{eff}}.$$

The numerical solutions to equations (12) and the experimental results obtained for a 124m length of fibre are illustrated in

Figure 3.4. Inspection of both sets of results reveals a good agreement between experimental and theoretical solutions. Both curves display the general behaviour of an SBS generator without feedback [3,31].

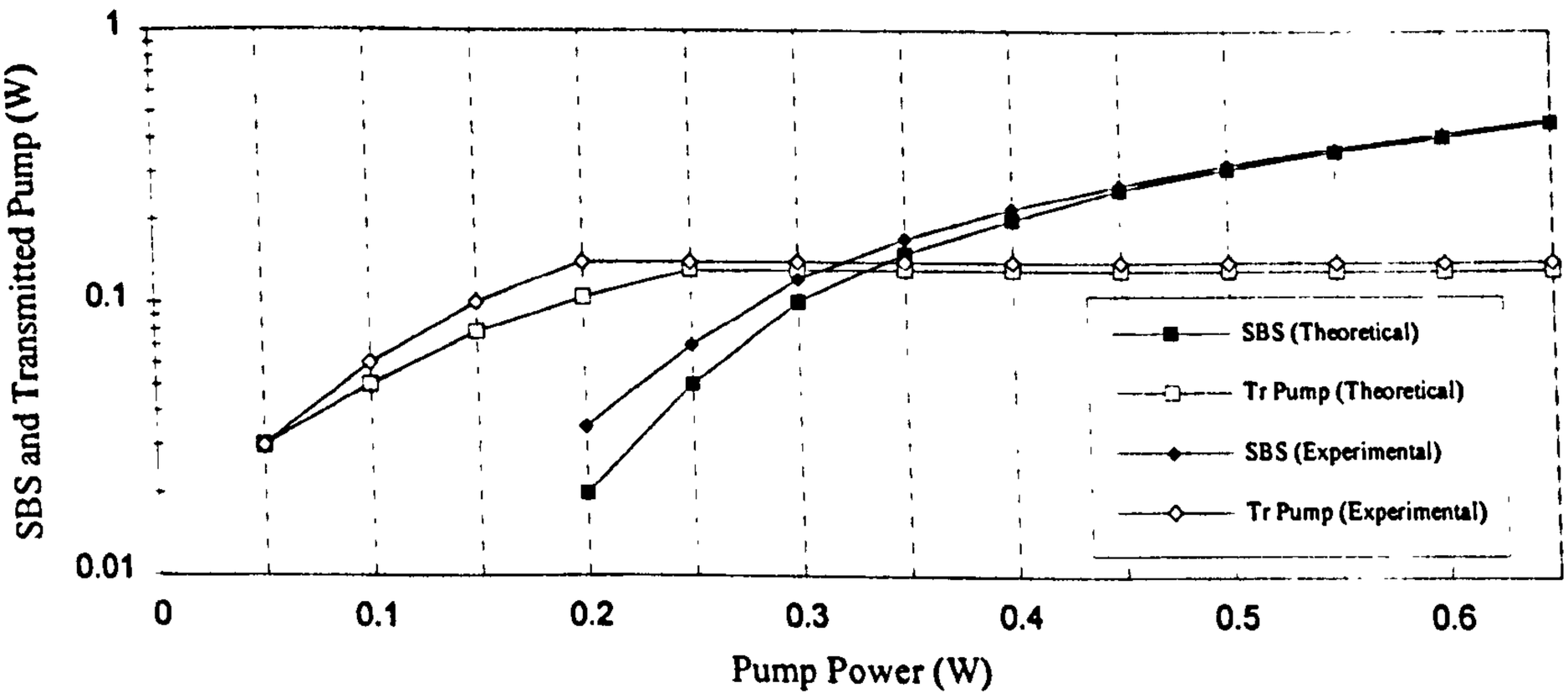

Figure 3.4 Steady State Solutions of an SBS Generator without Feedback.

For low pump powers the transmitted pump displays a linear dependence which is related to the launch efficiency and the attenuation of the fibre. At the onset of SBS, the transmitted pump becomes clamped due to pump depletion through the SBS process. As the pump power is increased, the amount of pump transmitted through the fibre remains clamped as more of the pump energy is converted to SBS. The threshold for stimulated scattering is defined as the pump required to generate a Stokes signal that is 1% of the incident pump intensity [16,32]. The SBS threshold for a length of fibre L, is determined from the widely accepted expression [3],

$$P_{th} = \frac{21a_{eff}}{g_B L_{eff}} \quad \text{where} \quad L_{eff} = \frac{(1-\exp(-\alpha L))}{\alpha}.$$

The term L_{eff} is the effective length of interaction region and is introduced to account for the attenuation of the pump by the fibre. For a long length of fibre the effective length is limited by the attenuation. From the values for the fibre a threshold of 220mW is predicted and this compares well with the experimentally measured value of 200mW. The SBS signal shows an exponential growth which becomes linear at high pump power due to saturation of the gain. The experimental results are slightly higher than their theoretical counterparts due to spurious reflections from the optical components.

The frequency shift between the Stokes wave and the pump wave can be calculated from the expression of ω_A obtained in section 3.2 by

$$\omega_A = |k_A| v_A = 2v_A |k_p| \sin(\theta/2).$$

For an optical fibre the Stokes wave is counter-propagating to the pump wave and therefore the angle θ has a value of 180° and modifies the above equation accordingly,

$$\Delta\nu_B = \frac{\omega_A}{2\pi} = \frac{2v_A n}{\lambda}$$

where v_A is the acoustic velocity of sound in the silica fibre (5960 ms^{-1}), n is the refractive index of the core (1.4616), and λ is the pump wavelength (1.064μm). From these parameters the frequency shift $\Delta\nu_B$ was found to be 16.4GHz. The shift was measured using a scanning Fabry-Perot interferometer which had a free spectral range of 100GHz, a finesse of 60 and a resolution of 1.6GHz (FWHM).

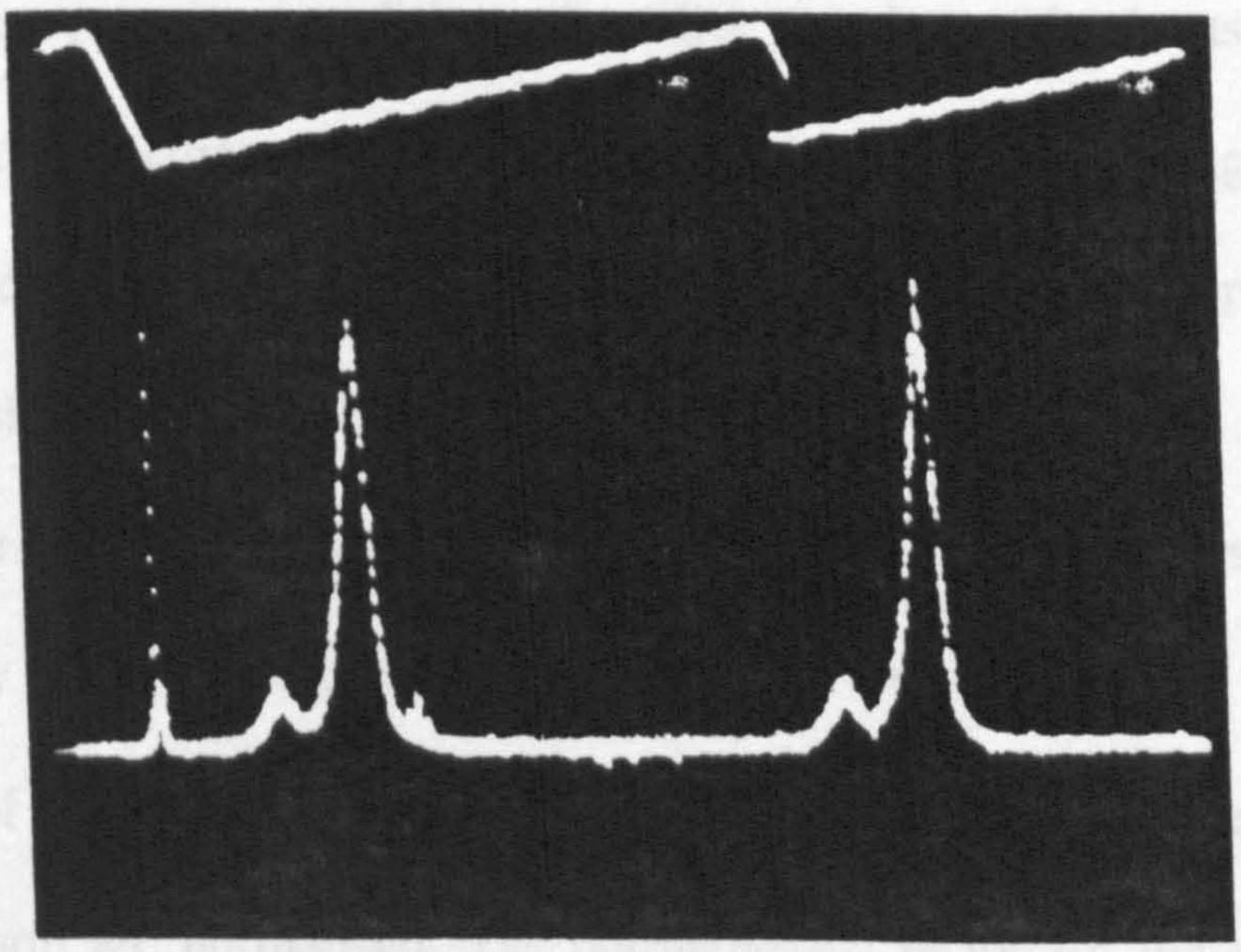

Figure 3.5 Photograph displaying the frequency shift of the Stokes signal from the pump. The sharp peak close to the spectra on the left of the picture was caused by the PZT driver.

From the photograph in Figure 3.5 ,the Stokes wave was found to be downshifted in frequency to a value of 15.2GHz and compares favourably with the calculated value allowing for the resolution of the interferometer. By observing the spectral content of the scattered signal using the scanning Fabry-Perot interferometer, the SBS was found to be first order Stokes for the range of pump powers used. In the next section the temporal behaviour of the SBS will be presented and compared with theoretical results obtained by co-workers.

3.5 Dynamical Behaviour of SBS without Feedback

For low pump powers, below threshold, the transmitted pump displayed stable d.c. behaviour. However, once the SBS threshold was reached the transmitted pump displayed sustained aperiodic oscillations which persisted through to high pump powers. Under continuous pumping conditions the SBS signal contained sustained aperiodic oscillations with modulation depths of almost 100% under all operating conditions. The digitised data presented in this section were obtained for a fixed pump power of 300mW above SBS threshold.

The time series recordings shown in Figure 3.6 of the SBS (a) and the transmitted pump (b) show the aperiodic behaviour. The data set shown was recorded with a sampling rate of 1GHz and contained 25,000 points. Both the time series and the Fast Fourier Transform are normalised. The normalisation factor for the time series is the fibre transit time T_R. For a fibre of length 124m with a refractive index of 1.4616 for the core material, the calculated transit time is $T_R = nL/c = 605ns$. The frequency was normalised by the inverse of the transit time and had the corresponding value of $(1/T_R) =$ 1.65MHz The SBS emission and the transmitted pump were digitised simultaneously using both sampling heads of the transient digitiser.

The temporal effect of pump depletion by the SBS can be observed in the transmitted pump displayed in figure 3.6 (b). By conservation of energy, a peak in the SBS signal creates a corresponding depletion in the transmitted pump. Conversely, a peak in the transmitted pump gives rise to a depletion in the SBS emission. The phase portraits illustrated in Figure 3.6 (c) and (d) were generated by reconstructing the

digitised data with an embedded delay. Both phase portraits exhibit outward spiralling and folding motion. The Fast Fourier Transforms of the digitised data are displayed in Figure 3.6 (e) and (f). The maximum frequency span was determined by the fixed sampling rate Δt by the relationship, span = $1/2\Delta t$. The resolution of the FFT was dependent upon the sampling time and the number of data points recorded (n), and obeyed the relationship, resolution = $1/n\Delta t$. For a sampling rate of 1ns and 25,000 data points, the span was 500MHz and the resolution was 40kHz. The power spectra of both signals indicates broad band emission. Broad band spectra is suggestive of either a stochastic or a deterministic chaotic process. In the next section the temporal evolution of the SBS emission is examined over a range of values including threshold.

3.5.1 Spontaneous and Stimulated Scattering

For SBS generated in an optical fibre without external feedback, the pump power was used as the control parameter to investigate both the existence of chaos and the precursive route. The SBS emission was monitored using real time analysis for pump powers ranging from threshold (200mW) to 600mW. Over the control parameter range, the SBS emission displayed sustained aperiodic temporal behaviour. However, there was no marked or significant change in the temporal evolution of the SBS emission for variations of the control parameter. Digitised data, Figure 3.7, displays the temporal behaviour of the Stokes emission. At threshold, (a), the signal is aperiodic with a broad band power spectrum, (b). Increasing the pump power reveals no significant change in the temporal structure of the Stokes emission. The only difference between the spontaneous emission at threshold and the stimulated emission sampled at a higher pump

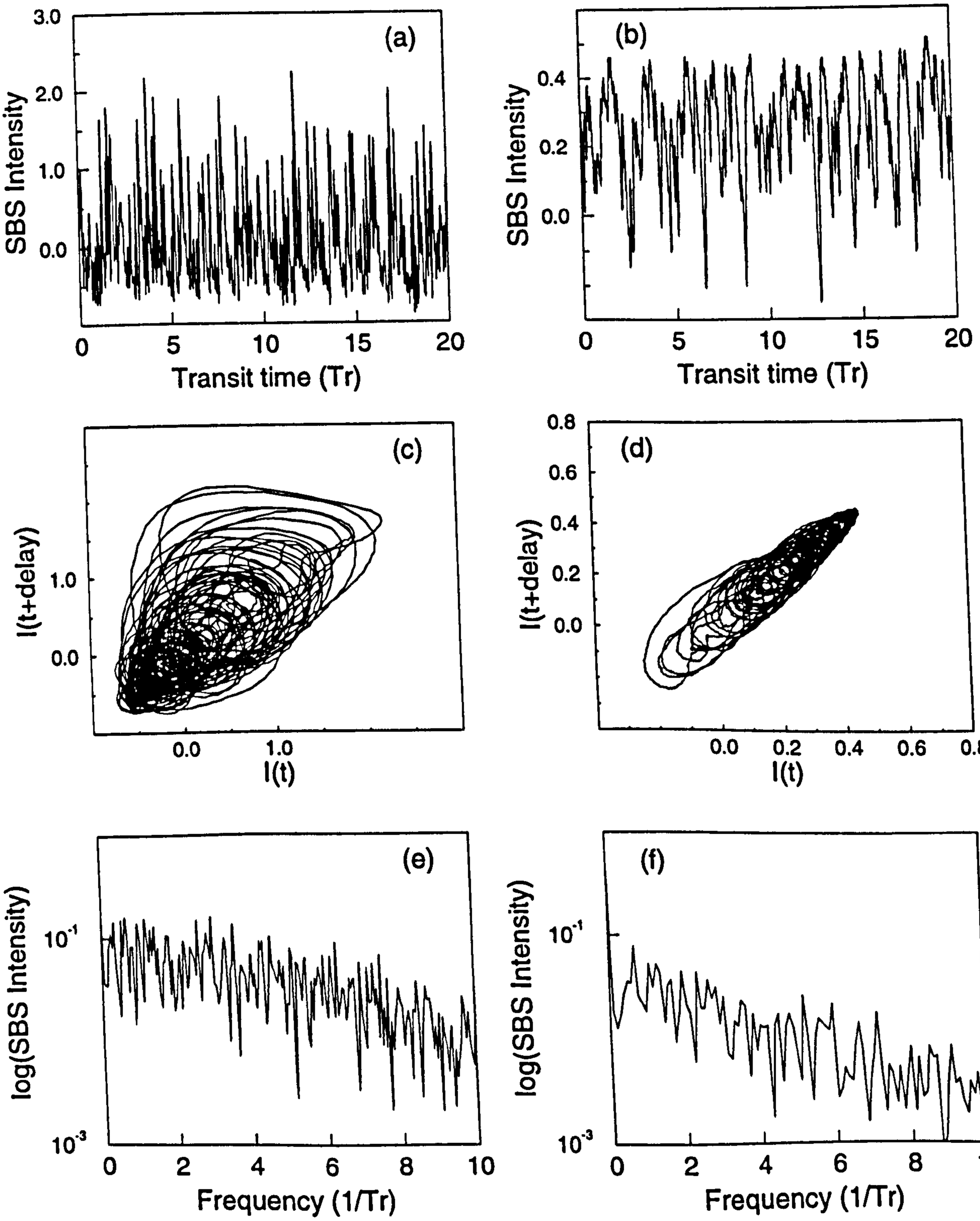

Figure 3.6 Time series (a) and (b), phase portraits (c) and (d) and Fast Fourier Transforms (e) and (f) of the backscattered Stokes and transmitted pump intensities for a pump power of 300mW.

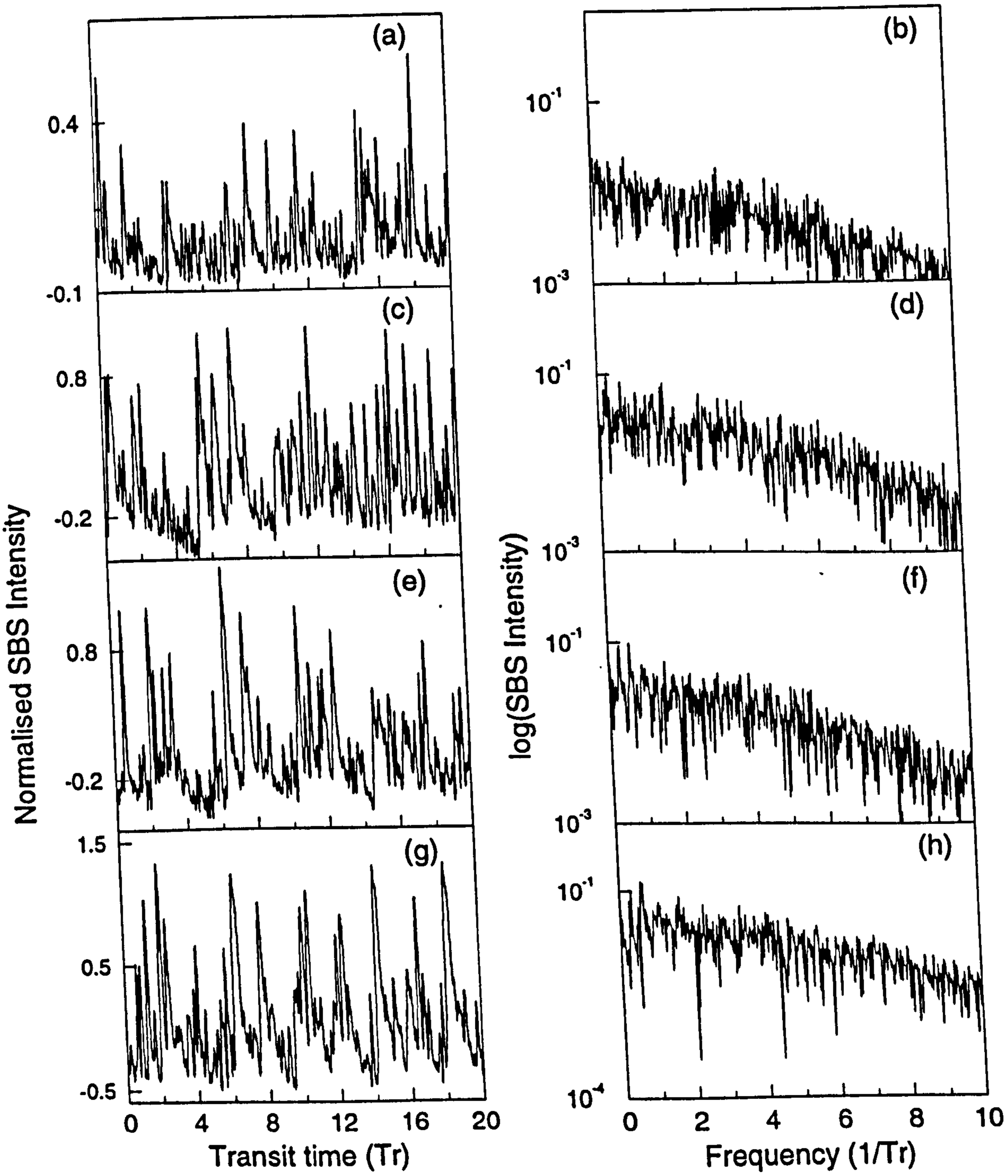

Figure 3.7 Experimental Time series and Power Spectra (FFT) of the Backscattered Stokes signal for Increasing Pump power. (a-b) 200mW (threshold), (c-d) 300mW, (e-f) 400mW, and (g-h) 500mW.

power is the occurrence of bursting and the emergence of stimulated emissions with higher peak powers. Over the complete parameter range, the power spectra remains broad band without the emergence of any parameter dependent characteristic features, and the bandwidth of the signal remains constant.

3.5.2 Analysis of Dynamics

Initial inspection of the SBS dynamics for a range of pump powers did not reveal sensitivity to variations in the control parameter or a distinguishable route to chaos. To differentiate between a deterministic or stochastic process a more rigorous technique is required to provide strong empirical information about a system's dynamics. An attempt was made to measure the attractor dimension for a data set by using the Grassberger-Procacccia algorithm [33] to determine the correlation dimension. In Figure 3.8 the correlation dimension was calculated for an increasing embedding dimension. The data (P = 400mW) shows an increase in correlation dimension for increasing embedding dimension. The failure of the data to converge to a particular dimension implies the system has many degrees of freedom and is therefore stochastic.

3.5.3 Comparison with Theoretical Predictions

The theoretical findings presented in this section were obtained by co-workers in the group. The solutions were obtained by solving the fibre SBS equations, (7) - (9) in section 3.2.4, which contained both phase modulation terms and Gaussian noise [34], representing the spontaneous Brillouin scattering [20].

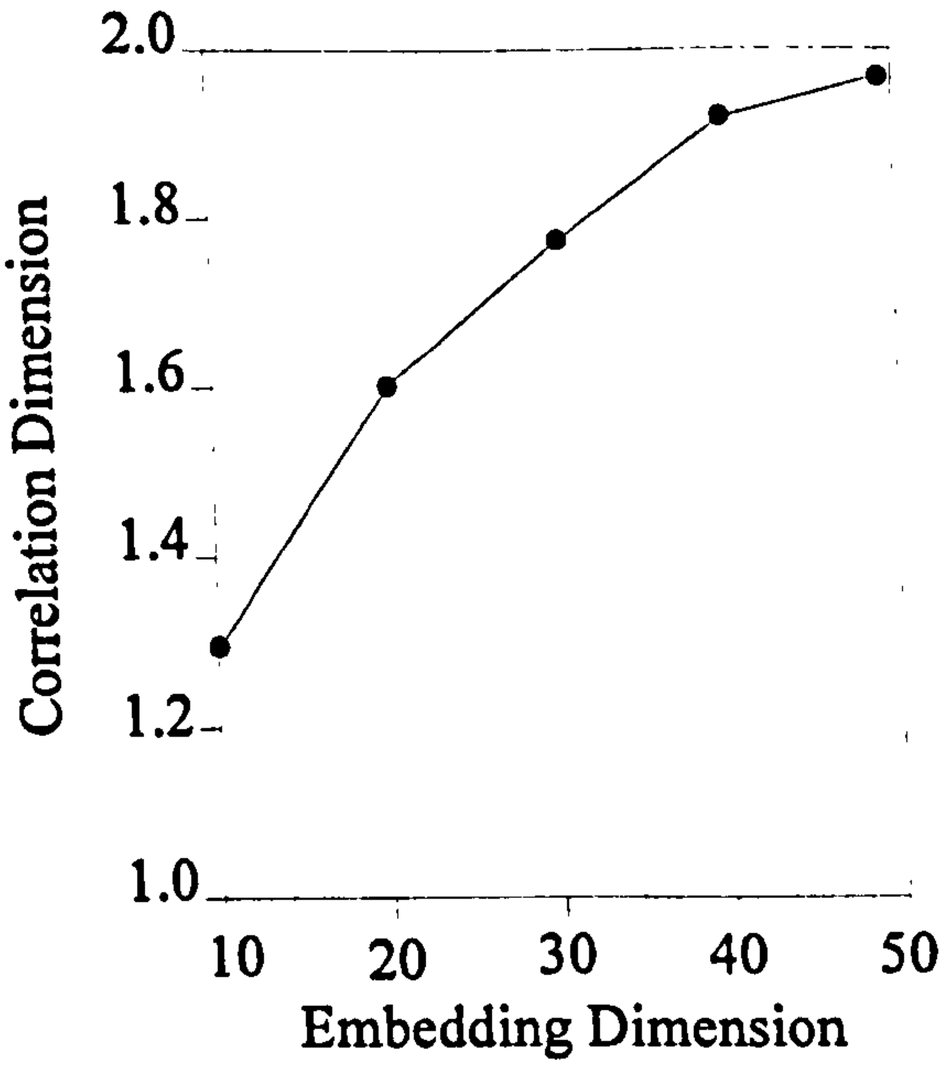

Figure 3.8 Correlation Dimension of an SBS data set for different embedding dimension.

The sets of data shown in Figure 3.9 exhibit similar characteristics when compared with the experimental data (Figure 3.7) for the equivalent settings of the control parameter. Once again the backscattered Stokes signal (SBS) and the transmitted pump demonstrate the effects of pump depletion. Both signals display depths of modulation approaching 100% for high pump powers. At low pump levels the SBS emission is composed of sustained aperiodic oscillations, which become increasingly more complex with the appearance of higher harmonics corresponding to higher pump levels (compare Figure 3.9(b) with (h). However, there are no precursive routes to chaos and the aperiodic behaviour persists from the onset of stimulated emission for all values of the control parameter. Both experimental and theoretical findings provide a qualitative agreement with recent findings reported by Dammig et al [35] and Yu [31]. The inclusion of the nonlinear refractive index is essential for the promotion and sustaining of dynamics [3,22,23].

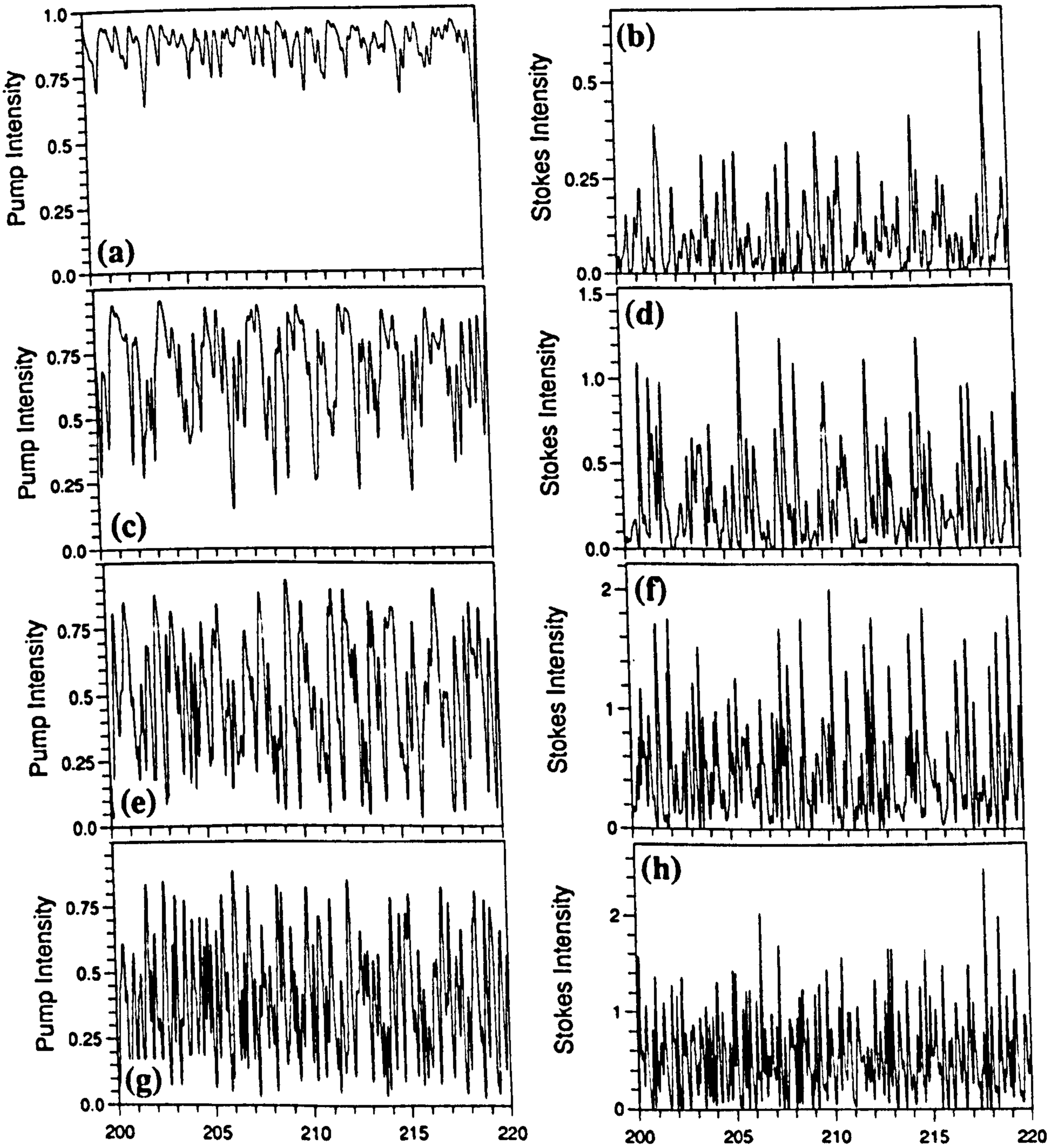

Figure 3.9 Theoretical Data sets of the transmitted Pump (left column) and Backscattered Stokes (right column) Intensities for increasing Pump; (a-b) 150mW, (c-d) 200mW, (e-f) 300mW, and (g-h) 400mW.

However, for an SBS generator without feedback, the stimulated scattering process is initiated from spontaneous Brillouin scattering (noise) and the temporal evolution of the system is Stochastic.

3.6 Conclusions

The dynamical behaviour of SBS generated in an optical fibre without external feedback has been investigated experimentally. The steady state solutions obtained by measuring the time averaged SBS and transmitted pump signal, matched the findings from the theoretical model. The threshold for SBS was found to be 200 mW which showed a close comparison with the predicted value of 220 mW. The transmitted pump in both the experiment and the model became depleted by the onset of strong SBS emission. The transmitted pump became clamped at a pump power of ~200 mW, and further increments in the pump power resulted in more energy being converted into SBS. For the range of pump powers used in the experiment, the SBS was found to be first order Stokes with a frequency down-shift of 15.2GHz.

The temporal behaviour of SBS was analysed for variations in the control parameter i.e. pump power. At low pump powers, below SBS threshold, spontaneous Brillouin scattering dominated the temporal signal. Above threshold the Stokes emission did not exhibit any control dependent characteristics. The SBS signal was composed of aperiodic oscillations with almost 100% depth of modulation which persisted over the whole pump region. The lack of any distinguishable features in the Stokes intensity was also confirmed by the Fast Fourier Transform which remained broad band with a

constant bandwidth throughout. The correlation dimension failed to converge for an embedding dimension of 50 indicating that the Stokes emission was stochastic. The experimental results agree with the theoretical model which includes a noise term to account for the initiation of stimulated scattering from spontaneous Brillouin scattering.

3.7 References

[1] R.Y.Chiao, C.H.Townes and B.P.Stiocheff, "Stimulated Brillouin Scattering and Coherent Generation of Intense Hypersonic Waves", Phys.Rev.Lett.Vol.12(21), 592-95, (1964).

[2] R.W.Boyd, *Nonlinear Optics*, (Academic Press, INC., Boston,1992).

[3] A.Johnstone, Phd Thesis, Heriot-Watt University, 1992 (unpublished).

[4] R.G.Smith, "Optical Power Handling Capacity of Low Loss Optical Fibres as Determined by Stimulated Raman and Brillouin Scattering", Appl.Optics Vol.12(11), 2489-94, (1972).

[5] E.P.Ippen and R.H.Stolen, "Stimulated Brillouin Scattering in Optical Fibres", Appl.Phys.Lett. Vol.21(11), 539-40, (1972).

[6] R.V.Johnson and J.H.Marburger, "Relaxation Oscillations in Stimulated Raman and Brillouin Scattering", Phys.Rev.A. Vol.4(3), 1175-82, (1971).

[7] D.Cotter, "Observation of Stimulated Brillouin Scattering on Low Loss Silica Fibre at 1.3μm", Electron.Lett. Vol.18(12), 495-96, (1982).

[8] D.Cotter, "Transient SBS in Long Single Mode Fibres", Electron.Lett. Vol.18(12), 504-505, (1982).

[9] Y.Yamamoto, IEEE.J.Quant.Elect. Vol.QE-16, 1073-,(1980).

[10] C.G.Atkins, D.Cotter, D.W.Smith and R.Wyatt, "Application of Brillouin Amplification in Coherent Optical transmission", Electon.Lett., Vol.22(10), 504-505, (1986).

[11] "Stabilised Single-Frequency Stimulated Brillouin fibre Ring Laser", Opt.Lett. Vol.6, 398-400, (1981).

[12] J.Stone and A.R.Chraplyvy, "Spontaneous Brillouin Noise in long distance High Bandwidth Optical Fibre Transmission", Electron.Lett. Vol.**19**(8), 275-, (1983).

[13] I.Bar-Joseph, A.A.Frieseman, E.Lichtman and R.G.Waarts, "Steady and Relaxation oscillations of stimulated Brillouin scattering in single-mode optical fibres", J.Opt.Soc.Am.B/Vol.**2**(10), 1606-11, (1985).

[14] N.F.Andreev, V.I.Bespalov, A.M.Kiselev, A.M.Kubarev and G.A.Pasmanik, "Formation of pulses in stimulated scattering of light in extended media. Modulation of the intensities of transmitted and backscattered radiations", Sov.J.Quant.Electron. Vol.6(10), 1223-25, (1976).

[15] C.J.Randall and J.R.Albritton, "Chaotic Nonlinear Stimulated Brillouin Scattering", Phys.Rev.Lett. Vol.52(21), 1887-90, (1984).

[16] P.Narum, A.L.Gaeta, M.D.Skeldon and R.W.Boyd, "Instabilities of laser beams counterpropagating through a Brillouin-active medium", J.Opt.Soc.Am.B Vol.**5**(3), 623-28, (1988).

[17] A.L.Gaeta, M.D.Skeldon, R.W.Boyd and P.Narum, "Observation of Instabilities of laser beams counterpropagating through a Brillouin medium", J.Opt.Soc.Am.B Vol.**6**(9), 1709-13, (1989).

[18] C.Montes and J.Coste, "Optical turbulence in multiple stimulated brillouin backscattering", Laser and Particle Beams, Vol.**5**(2), 405-411, (1987).

[19] R.G.Harrison, J.S.Uppal, A.Johnstone and J.V.Moloney, "Evidence of Chaotic Stimulated Brillouin Scattering in Optical Fibres", Phys.Rev.Lett. Vol.**65**(2), 167-170, (1990).

[20] R.W.Boyd, K.Rzazewski and P.Narum, "Noise initiation of stimulated Brillouin scattering", Phys.Rev.A Vol.**42**(9), 5514-21, (1990).

[21] A.L.Gaeta and R.W.Boyd, "Stochastic dynamics of Stimulated Brillouin scattering in an optical fibre", Phys.Rev.A Vol.**44**(5), 3205-09, (1991).

[22] W.Lu and R.G.Harrison, "Nonlinear Dynamical and Chaotic features in Stimulated Scattering Phenomena", Europhys. Lett. Vol.**16**(7), 655-90, (1991).

[23] A.Johnstone, W.Lu, J.S.Uppal and R.G.Harrison, "Sustained and Bursting oscillations in stimulated Brillouin scattering with external feedback in optical fibre", Opt.Comm. Vol.**81**(3,4), 222-24, (1991).

[24] N.Shibata, R.G.Waarts and R.P.Braun, Opt. Lett. Vol.12, pp.269, (1987).

[25] Y.Azuma, N.Shibata, T.Horriguchi and M.Tateda, Electron. Lett. Vol.24, pp.250, (1988).

[26] G.C.Valley, "A Review of Stimulated Brillouin Scattering Excited with a Broad-Band pump laser", IEEE J.Quant.Elec. Vol.QE-**22**(5), 704-12, 1986.

[27] K.O.Hill, D.C.Johnson and B.S.Kawasaki, "CW generation of multiple Stokes and anti-Stokes Brillouin shifted frequencies", Appl.Phys.Lett. Vol.**29**(3), 185-87, 1976.

[28] P.Labudde, P.Anlinker and H.P.Weber, "Transmission of Narrow Band High Power Laser Radiation through Optical Fibres", Opt. Commun., Vol.(32), 385-390, (1980).

[29] D.Marcuse and J.Stone, "Coupling Efficiency of Front Surface and Multi-layer Mirrors as Fibre-End Reflectors", Jou.of Lightwave.Techn. Vol.L-T-4(4), 377-81, 1986.

[30] F.R.Connor, and W Koechner, "Output Fluctuations of CW-Pumped Nd:YAG Lasers", IEEE J.Quant.Elec. QE-8(7), 656-51, 1972.

[31] Dejin Yu, "Deterministic Dynamics and Noise of Stimulated Light Scattering in Optical Fibres", Phd Thesis, Heriot-Watt University, Edinburgh, 1994 (unpublished).

[32] A.L.Gaeta, "Stochastic and Deterministic fluctuations in stimulated Brillouin scattering", Phd. Thesis, University of Rochester, New York, (1990).

[33] P.Grassberger and I.Procaccia, Phys.Rev.Lett. Vol.50(), 346-, 1983.

[34] R.F.Fox, I.R.Gatland, R.Roy and G.Vemuri, "Fast, accurate algorithm for numerical simulation of exponentially correlated coloured noise", Phys.Rev.A Vol.38(11), 5938-40, 1988.

[35] M.Dammig, G.Zinner, F.Mitschke and H.Welling, "Stimulated Brillouin Scattering in fibres with and without feedback", Phys.Rev.A Vol.48(4), 3301-09, 1993.

4. Dynamical Behaviour of SBS in Optical Fibres with Feedback

4.1 Introduction

In the previous chapter experiments addressing the dynamical behaviour of SBS generated in optical fibres were performed without external feedback. This allowed the case of intrinsic feedback provided by the coupling of the pump and Stokes wave through the nonlinear refractive index to be examined. In the following chapter, attention will focus upon experimental investigations into the dynamical behaviour of SBS generated in an optical fibre with the inclusion of external feedback. Previous findings have indicated how the addition of external feedback can have a profound effect upon the temporal behaviour of the Stokes emission. To account for the effects of external feedback, the model described in chapter 3 (section 3.2.4) is modified. Several different configurations are presented including; weak and natural feedback with the incident pump being utilised as the control parameter, and variable feedback where the incident pump is fixed and the reflectivity is varied.

4.1.1 SBS in Optical Fibres

The first experimental observation of SBS generated in a silica cored optical fibre by Ippen and Stolen[1], revealed the presence of oscillations in both the transmitted pump and Stokes emission. The period of the oscillations was found to be equivalent to the round trip time of the fibre. The oscillations were attributed to the presence of a weak

Fabry-Perot cavity formed by external feedback associated with the natural Fresnel reflectivity of the cleaved fibre ends.

Bar-Joseph and co-workers [2] performed a joint theoretical and experimental investigation into the role of reflectivity upon the temporal behaviour of SBS. The SBS equations discussed in chapter 3 (section 3.2.3) were solved with the boundary conditions imposed by the finite length and reflectivity of the medium. For a fibre with minimum reflectivity the intensity of the Stokes signal consisted of relaxation oscillations which had a period dependent upon the round trip time of the fibre. The addition of a small amount of feedback ($R=5x10^{-3}$ %) led to the relaxation oscillations becoming sustained. A further increase in the reflectivity (R=2%) changed the sustained oscillations back to relaxation oscillations. Experiments performed for a fixed pump intensity using a single-mode fibre with variable reflectivity demonstrated a close agreement with findings from the theoretical model. However, the theoretical model used did not include any interaction between the pump and the counter propagating Stokes wave via the nonlinear refractive index, and the dependence of the SBS dynamics upon the pump intensity were not addressed.

The response time of the field induced electrostriction responsible for the stimulated Brillouin scattering process is in the range of 5~10 ns [3]. The field induced change in the refractive index was considered to be near instantaneous, (time scale of 2~4 fsec for silica based fibres [4]), and was excluded from the SBS process. The contribution of external feedback and nonlinear refraction were investigated theoretically by Lu et al [5 ,6], and experimentally by Johnstone et al [7]. To account for the effects of optical four-wave mixing occurring through the intensity-dependent nonlinear refractive index, self-phase modulation (SPM) and cross-phase modulation (XPM) terms

were included in the SBS equations. At low pump intensities, both reports confirmed earlier observations made by Bar-Joseph et al. The addition of external feedback gave rise to sustained oscillations, and the periodicity of the oscillations was directly related to the round trip of the fibre. However, an increase in the pump intensity produced complicated dynamical features, most notably quasi-periodicity and quasi-d.c. "bursting" behaviour in the presence of external feedback. The emergence of these new complicated, intensity-dependent features was attributed to the interplay of the Stokes and pump wave through SPM and XPM. However, chaotic behaviour and a parameter controlled route to chaos were not observed.

The theoretical model presented in chapter 3, which gave a description of the SBS equations for a fibre geometry, require further modification. The inclusion of external feedback introduces two new features. Firstly, the equations now have boundary conditions which are determined by the reflectivity and the finite length of the medium. Secondly, a new equation is included to represent the reflected Stokes signal which co-propagates with the pump wave. A schematic diagram illustrating these new features is shown in Figure 4.1.

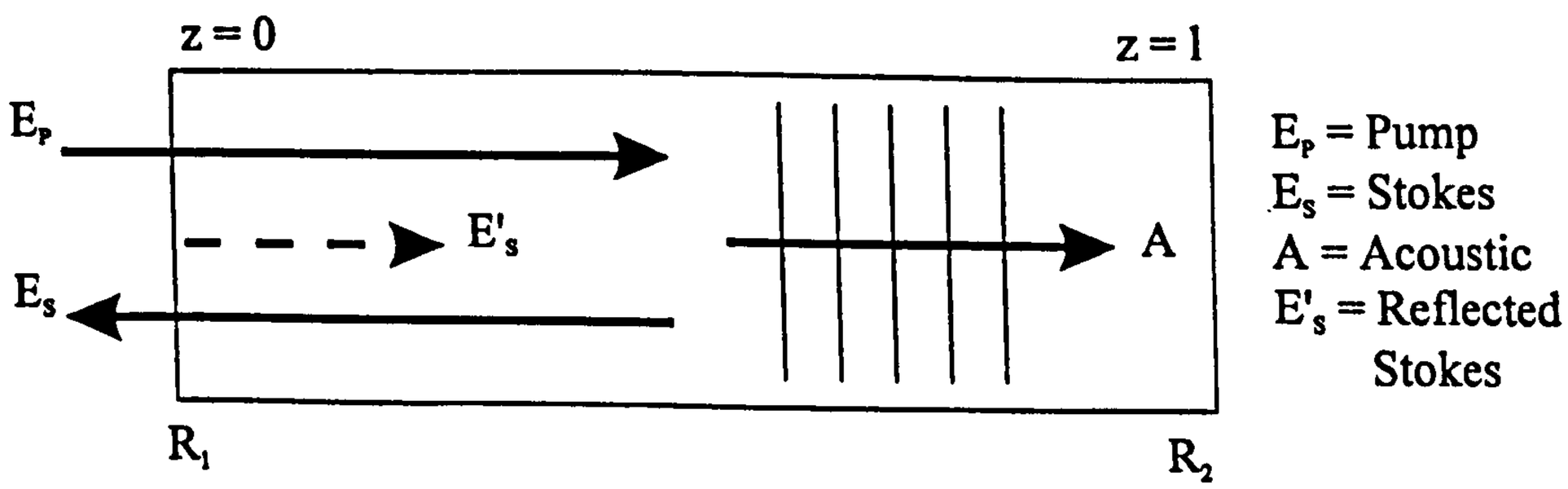

Figure 4.1 Schematic diagram of SBS generated in the presence of external feedback.

A theoretical description of the modified SBS equations is presented below in normalised form,

$$\frac{\partial E_P}{\partial \eta}+\frac{\partial E_P}{\partial \xi}+\frac{1}{2}\beta E_P = -gE_S A + iu\left[\left|E_P\right|^2+2\left|E_S\right|^2\right]E_P$$

$$\frac{\partial E_S}{\partial \eta}-\frac{\partial E_S}{\partial \xi}+\frac{1}{2}\beta E_S = gE_P A^* + iu\left[\left|E_S\right|^2+2\left|E_P\right|^2\right]E_S$$

$$\frac{1}{\beta_A}\frac{\partial A}{\partial \eta}+A = E_P E_S^* + f(\eta,\xi)$$

$$\frac{\partial E'_S}{\partial \eta}+\frac{\partial E'_S}{\partial \xi}+\frac{1}{2}\beta E'_S = 2iu\left[\left|E_P\right|^2+2\left|E_S\right|^2\right]E'_S .$$

E_P, E_S, A, and E'_S represent the slowly varying amplitudes of the pump, Stokes, acoustic and reflected Stokes wave respectively. The equations describing the pump, Stokes and reflected Stokes wave contain terms (in the square brackets) to account for optical four-wave mixing i.e. SPM and XPM due to the nonlinear refractive index. The material equation includes a Langevin noise term $f(\eta,\xi)$ to describe the spontaneous Brillouin scattering which initiates the stimulated scattering process. The corresponding boundary conditions for the optical fibre with weak feedback ($R_1R_2 \approx 1$) are

$$E'_S(\eta,\xi=0) = \sqrt{R_1}E_S(\eta,\xi=0)$$

$$E_S(\eta,\xi=1) = \sqrt{R_2}E'_S(\eta,\xi=1).$$

The free experimental parameters of the system are; the reflectivity's R_1 and R_2 of the fibre cavity, and the pump intensity. In the next section the effects of cavity filtering will be discussed with emphasis being placed upon the deterministic evolution of SBS from spontaneous noise.

4.1.2 Suppression of Noise by Fibre Cavity Effects

As discussed in the previous section, SBS generated in the presence of external feedback gives rise to deterministic periodic behaviour. The transition in the dynamical evolution of SBS from stochasticity to determinism is similar to that of a laser system at threshold. Both systems posses feedback and gain, and are initiated by spontaneous emission. However, there is a fundamental difference. In a laser system, the energy providing the gain is stored in the active medium by population inversion. Selective filtering of the spontaneous emission by the laser cavity provides feedback which induces stimulated emission leading to coherent amplification.

In stimulated Brillouin scattering the pump wave carries the energy for the gain of the system. Feedback only causes multiple amplifications of the injected Stokes wave, and for a single round trip of the cavity there is no phase synchronisation. A simple physical model has been developed [8] to explain how the effect of spontaneous scattering noise can be suppressed in the presence of feedback, Figure 4.2.

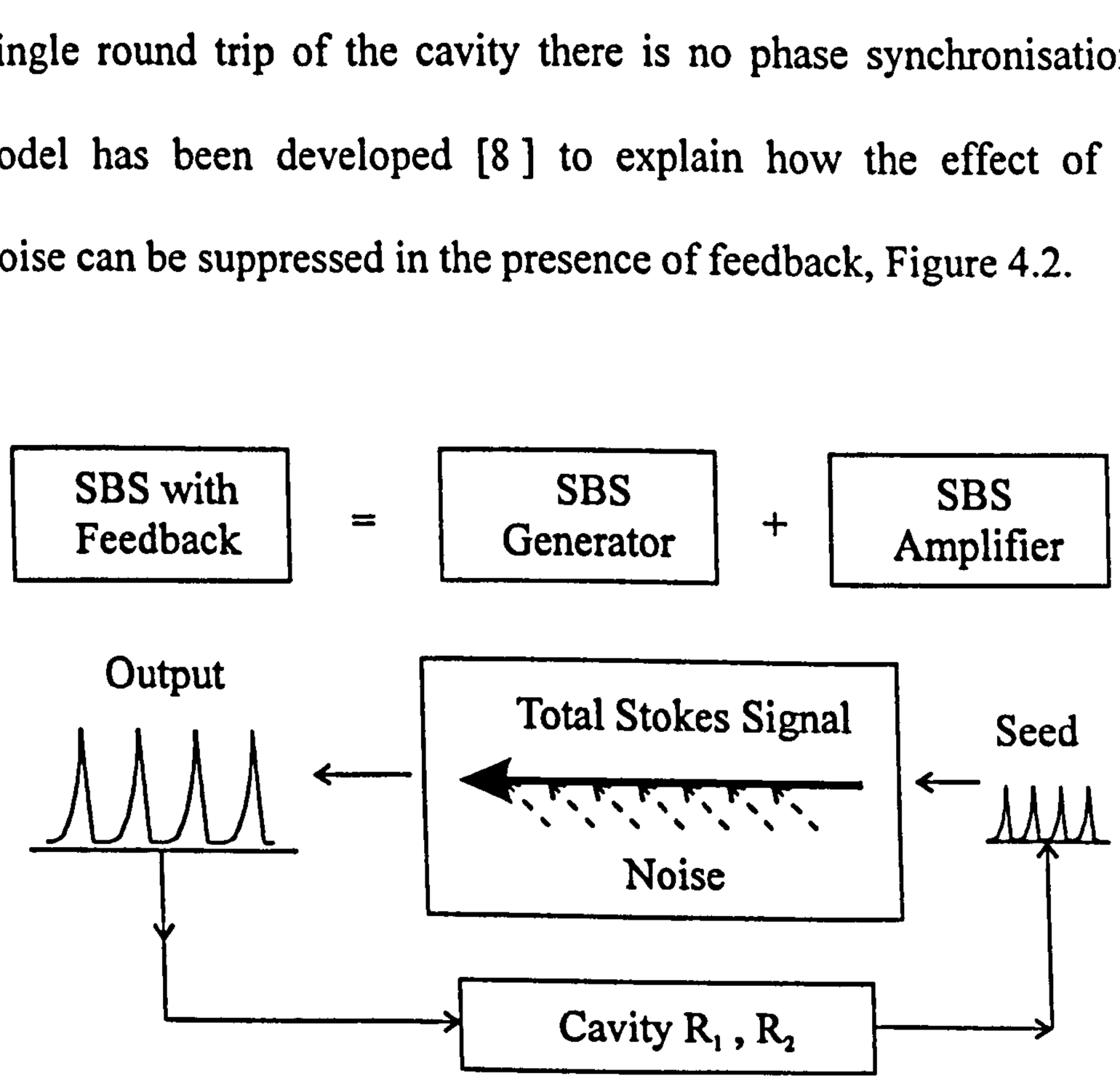

Figure 4.2 Schematic diagram illustrating the physical mechanism which suppresses noise.

The model consists of an SBS generator without feedback and an SBS amplifier. The SBS generator is associated with the stochastic nature of the amplified spontaneous scattering. The SBS amplifier is responsible for the successive amplification of the Stokes signal reflected by the external cavity.

Below SBS threshold spontaneous scattering dominates the temporal output of the system. However, at SBS threshold the external cavity has a dramatic effect upon the SBS emission. The output from the SBS generator is filtered by the external cavity. The resulting "seed" is then injected into the SBS amplifier. It has been demonstrated [9] that for a high seed strength, relative to the spontaneous noise, the dynamical behaviour of an SBS amplifier becomes highly deterministic. Even for the case of weak feedback where the natural Fresnel reflectivity is small (R_1=R_2=3.5%), the effective seed intensity is still strong enough to dominate the noise and produce a deterministic temporal output. Consequently, when an optical fibre system is operated above SBS threshold with feedback, the stimulated scattering process is highly deterministic and the contribution of noise (spontaneous scattering) is suppressed.

4.2 Weak Feedback

In this section, the role of weak external feedback upon the dynamical behaviour of SBS generated in an optical fibre is examined in order to provide experimental confirmation of noise suppression. The experimental set-up described in chapter 3 (section 3.3), was utilised for the investigation of SBS with the inclusion of weak external feedback. A non-polarisation preserving optical fibre was used as the Brillouin

medium. Weak external feedback was imposed upon the fibre by polishing one end of the fibre (R_2=3.3×10^{-4} %), as described in section 3.3.1, and cleaving the remaining end. The pump was launched into the cleaved end of the fibre to ensure that a significant Stokes signal was reflected from the cleaved fibre/air interface (R_1). For a fixed pump power below threshold, the Fresnel reflectivity was measured directly. A fraction R_1 of the optical power incident perpendicularly upon the surface of the fibre cleave is reflected. This Fresnel reflection is given by the following expression R_1 [10]

$$R_1 = 1 - \frac{4n_{co}}{(1+n_{co})^2}.$$

For the fibre used in the experiment, the refractive index of the core n_{co} , was 1.4616 [11]. The theoretical Fresnel reflection at normal incidence was found to be 3.5%. By careful cleaving of the fibre the maximum experimental value of 3.3 ± 0.5% was achieved giving a reflectivity close to the predicted value. The maximum experimental value of the Fresnel reflectivity was limited by the accuracy of the cleaving tool and the amount of specular reflection at the fibre/air interface. The intensity of the Stokes signal reflected at the cleaved fibre/air interface (R_1) depends upon the intensity of the incident pump power. Therefore, variation in the pump power will effectively vary the size of the reflected "seed" in the weak fibre cavity. The temporal response of SBS generated in a fibre with weak feedback ($R = R_1R_2 = 1.1x\ 10^{-5}$), was then investigated for a range of pump powers. The digitised temporal recordings of the Stokes signal are displayed in Figure 4.3. The signal to be digitised contained an a.c. and d.c. component. Only the predominant a.c. signal was of interest and the d.c. component was removed by d.c. blocking capacitors to ensure that only the a.c. signal was amplified and digitised. The

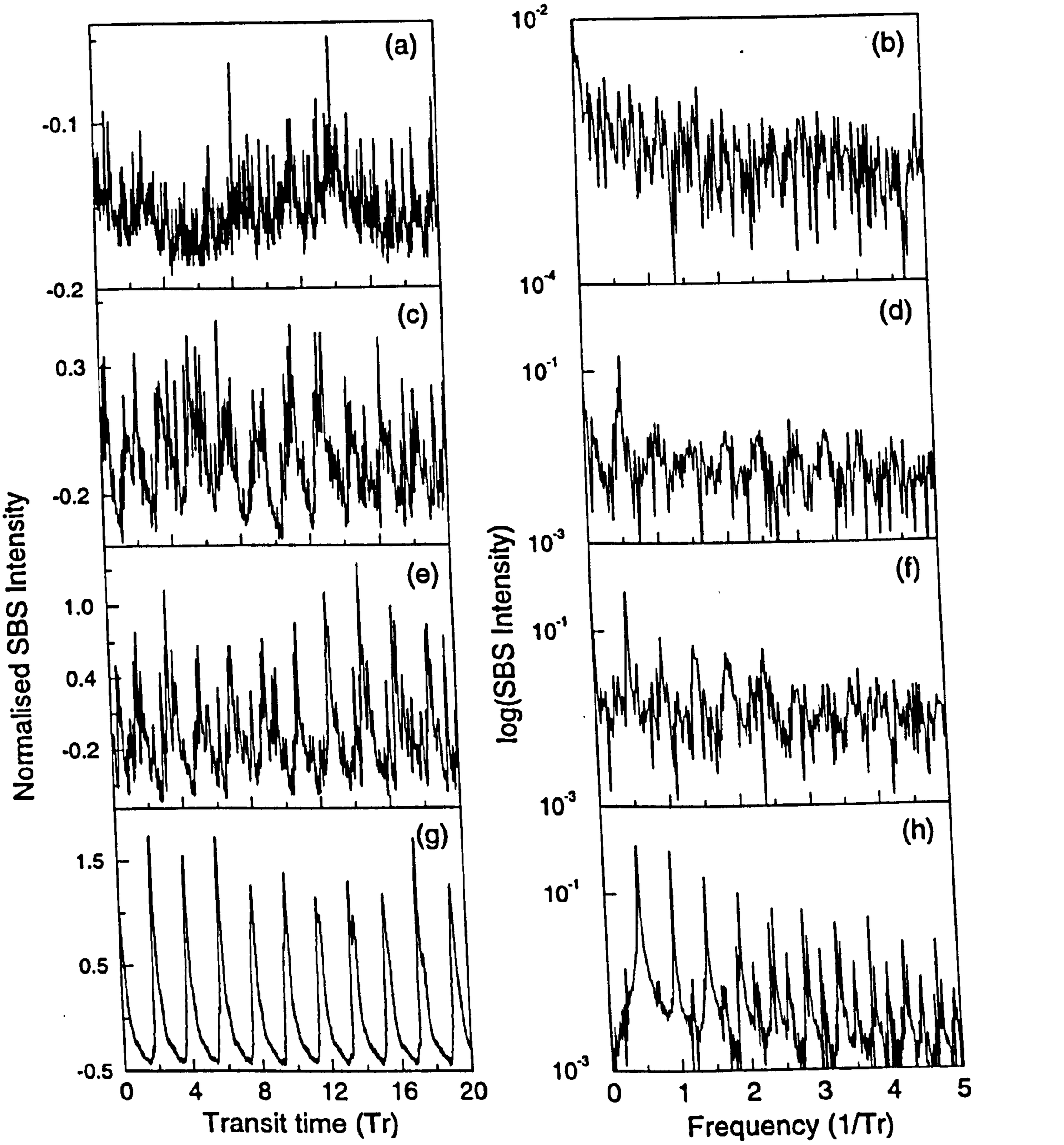

Figure 4.3 Time series (left hand column) and fast Fourier transform (right hand column) of SBS in the presence of weak feedback ($R = 3.3\times10^{-6}$) for different pump power. (a-b) 200mW, (c-d) 250mW, (e-f) 300mw, and (g-h) 350mW

d.c. component was a combination of spurious reflections from the optical components and an offset introduced by the cascaded amplifiers.

Below SBS threshold the Stokes signal is aperiodic with a broad power spectrum, Figure 4.3(a) and (b). This stochastic behaviour is reminiscent of the spontaneous Brillouin scattering observed in a fibre without external feedback, (section 3.5.1). An increase in the pump intensity reveals the emergence of very weak periodic structure in the time series and the appearance of discrete peaks in the power spectrum, Figure 4.3(c) and (d). A further increment in the pump intensity shows the periodic structure becoming more pronounced in both the time series and the occurrence of harmonics in the spectrum, Figure 4.3(e) and (f). However, the relatively slow, weak periodicity of the Stokes emission is still heavily modulated by a faster aperiodic signal. The effect of weak feedback upon the dynamics is starting to become apparent. Finally, with a pump power 150mW above SBS threshold periodic oscillations with a period equal to the round trip time of the fibre ($2T_R = 2nL/c = 1.2\mu s$) dominate the Stokes signal, Figure 4.3(g). The power spectrum, Figure 4.3(h), confirms the periodic nature of the signal with a strong peak occurring at $1/2T_R$ and higher harmonics appearing clearly above the noise floor of the spectrum.

For the case of a fibre with weak feedback ($R = 1.1x10^{-5}$), the pump has to operate 150mW above SBS threshold before periodic oscillations can be observed in the Stokes emission. At this pump setting, the reflected Stokes intensity is strong enough compared to the spontaneous noise, to generate deterministic behaviour. Therefore, with the inclusion of weak external feedback, to create a reflected Stokes signal with the appropriate intensity, noise can be suppressed giving rise to deterministic dynamics.

4.3 Natural Feedback

The first experimental evidence in support of chaos in SBS generated in an optical fibre, examined the effect of natural feedback upon the temporal response of the Stokes emission. The inclusion of natural reflectivity demonstrated the significant role feedback has upon the dynamical evolution of SBS, with both periodic and quasiperiodic behaviour being observed in the Stokes emission. In the previous section (4.2) the addition of weak feedback ($R = 1.1x10^{-5}$) gave rise to periodic emission when the Stokes intensity was greater than the noise attributed to spontaneous Brillouin scattering. Therefore, increasing the external feedback by using the Fresnel reflectivity inherent to the cleaved ends of the fibre ($R_1R_2 = 3.5\%$) will increase the Stokes field and then enhance the SBS process. In the next section, an experimental investigation is undertaken to study the dynamical behaviour of SBS generated in an optical fibre with natural external feedback.

4.3.1 Steady State (Time averaged) Behaviour

To determine the time averaged features of SBS generated in a fibre with natural reflectivity, the procedure outlined in section 3.4 was followed. Both ends of a single-mode, non-polarisation preserving fibre were cleaved to provide a Fresnel reflection of 3.3 ± 0.5 % at each end. The time averaged intensities of both the transmitted pump and the backscattered stokes signal are displayed in Figure 4.4. Below SBS threshold the transmitted pump increases linearly with the incident pump power. The SBS threshold

was determined by measuring the pump power for which the Stokes emission is detectable. The threshold was found to be 110mW.

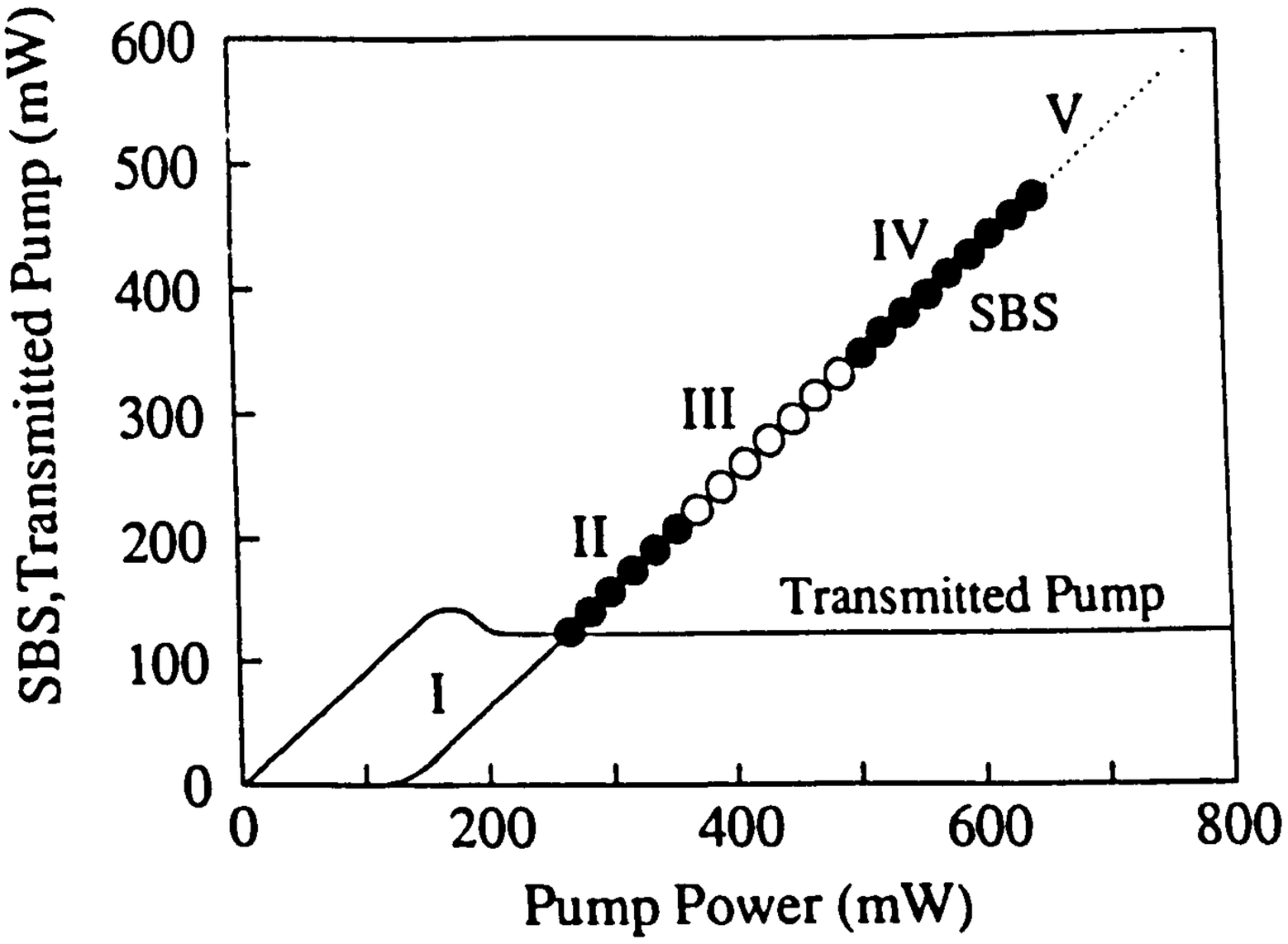

Figure 4.4 Experimental steady state characteristics of the SBS and the transmitted pump. Regions marked I-V indicate windows of dynamical behaviour.

This value is almost half the experimental value for SBS generated in an optical fibre without feedback. The effect of an external cavity is to increase the effective Brillouin gain, thus the threshold for stimulated scattering is reduced. Slightly above SBS threshold the transmitted pump displays a "shoulder" prior to becoming saturated. The shoulder is attributed to the onset of strong pump depletion. The SBS signal intensity increases linearly with the pump intensity, and the conversion efficiency increases from 5% at threshold to 85% at a pump power of 800mW. The regions marked I-V on the SBS

curve represent various forms of stochastic and dynamical behaviour which will be addressed in detail in the next section.

4.3.2 Dynamical Behaviour

As discussed in the previous chapter, the intensity of the pump is used as the control parameter for exploring the temporal response of the SBS signal. Well below SBS threshold at the start of region I (Figure 4.4), interference fringes were clearly visible in the back reflected pump signal, Figure 4.5. The optical fibre formed a weak Fabry-Perot cavity with a small finesse ($f = 0.1$). The random phase changes observed in the interference pattern are caused by random fluctuations in the environment. Increasing the pump power closer to threshold produces large bursts of SBS which are heavily modulated by the interference fringes of the fibre, Figure 4.6.

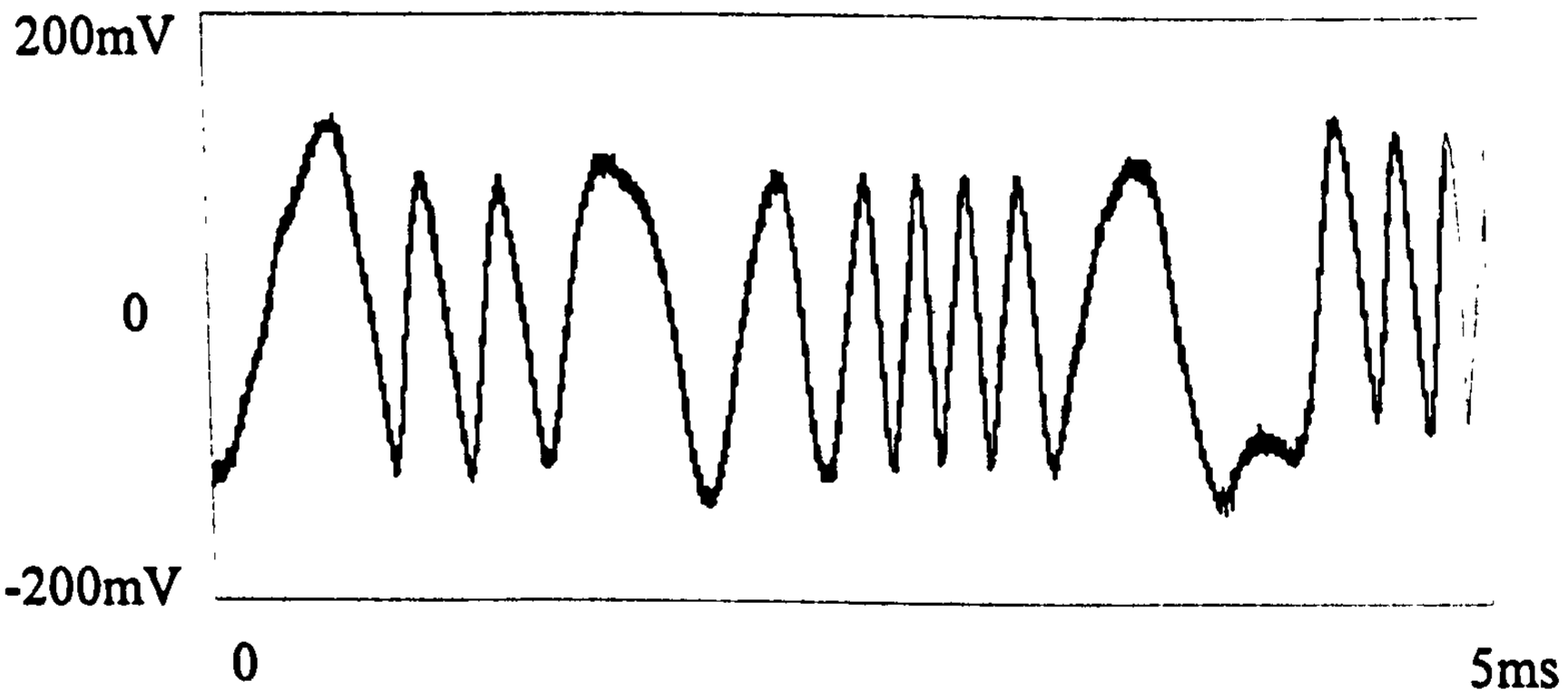

Figure 4.5 Interference fringes observed in the a.c. component of the back reflected pump signal below SBS threshold.

The relative time scale of the fringes (millisecond) is slow in comparison to the round trip time of the fibre ($2T_R$ = 1.21μs). Increasing the pump intensity just above SBS threshold revealed the temporal structure of the SBS signal to consist of fast relaxation oscillations of period $2T_R$ contained within relatively slow erratic bursts, Figure 4.6. The dominant frequency component of the fast relaxation oscillations, $1/2T_R$ corresponds to the round trip time of the fibre cavity. The duration of the slower, erratic bursts increased typically over a range of tens to hundreds of $2T_R$ as the pump power was varied from 120 to 270 mW. The irregularity of the bursts revealed the dynamics to be stochastic in this region.

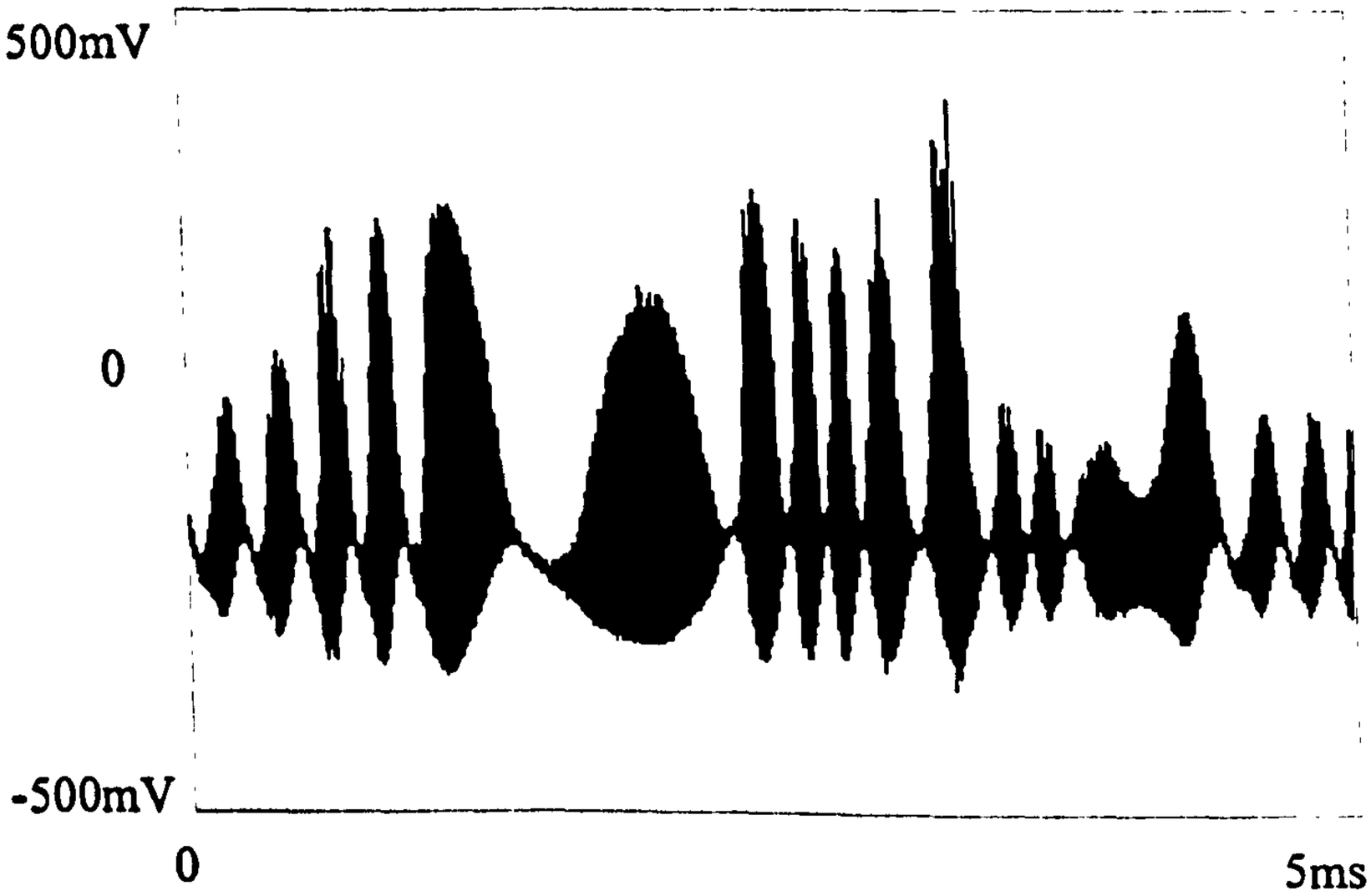

Figure 4.6 Bursting SBS superimposed upon interference fringes, close to threshold.

Bad cleaving of the fibre produced reflectivity's significantly less than the Fresnel limit. The SBS emission generated by decreasing the finesse of the fibre cavity displayed fast aperiodic oscillations, similar to observations made in the absence of external feedback.

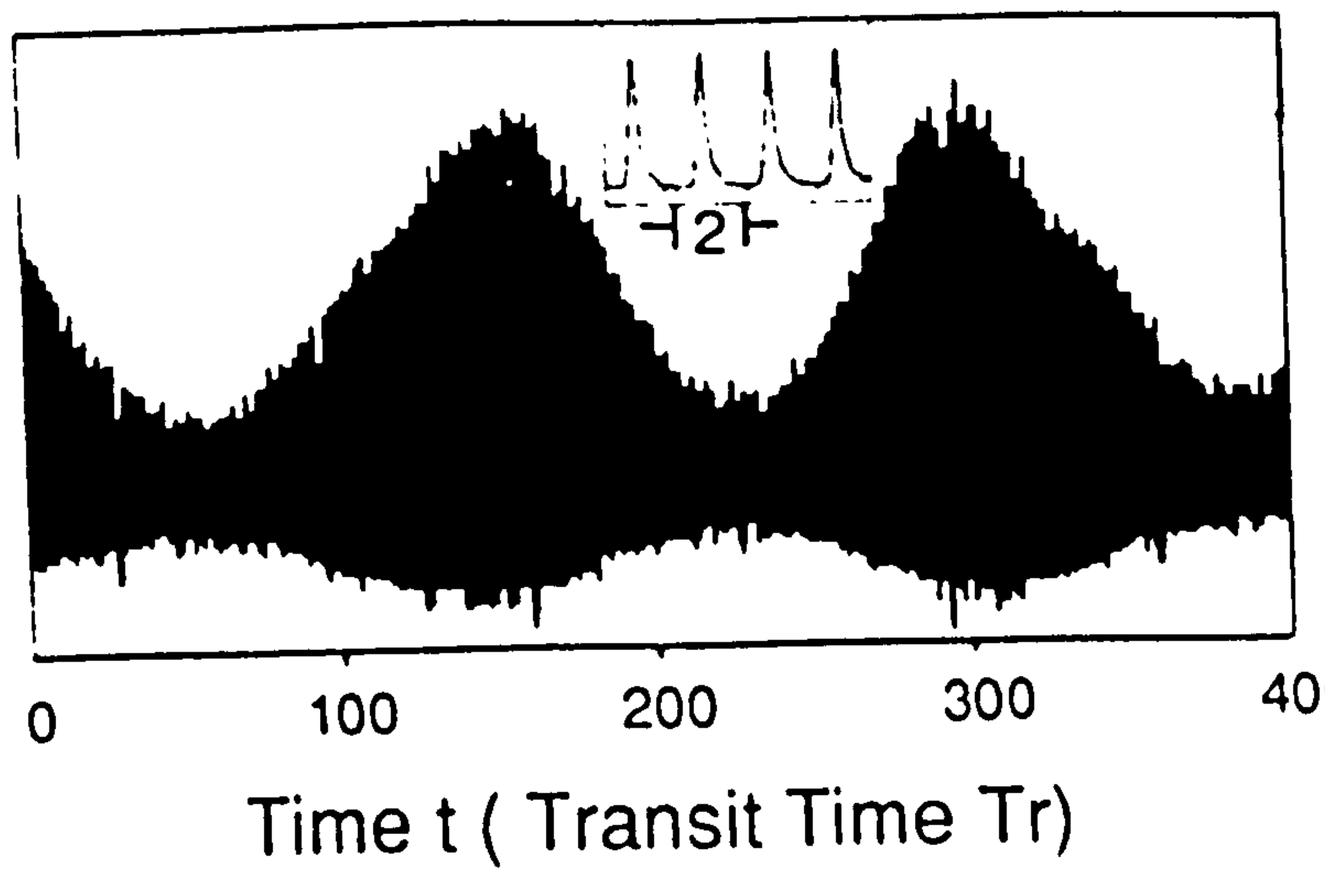

Figure 4.7 Dynamics of the Stokes emission in region I. The insert displays an expanded window showing the fast $2T_R$ oscillation contained in the slowly varying envelope.

The dynamic behaviour of the Stokes emission above region I was very distinct and reproducible, exhibiting different classifiable forms of behaviour in the regions marked in Figure 4.4. In region II the relaxation oscillations became sustained, Figure 4.8, corresponding to an incident pump power of 280 mW. The onset of the sustained relaxation oscillations coincided with the intensities of the SBS and clamped transmitted pump being equal. The period of the sustained relaxation oscillations was equal to $2T_R$, Figure 4.8(a). These periodic features are identical to those first reported by Bar-Joseph et al [2] which were physically interpreted as arising from the interplay of the SBS with the feedback from the external cavity. The amplitudes of the oscillations were quite stable over a time scale of hundreds of the cavity round trip time, ~ 50 periods. This provided a substantial window for data capture and characterisation of the dynamics. The robust periodic behaviour of the sustained relaxation oscillations is demonstrated by the limit cycle behaviour of the phase portrait, Figure 4.8(b). The Fast Fourier Transform

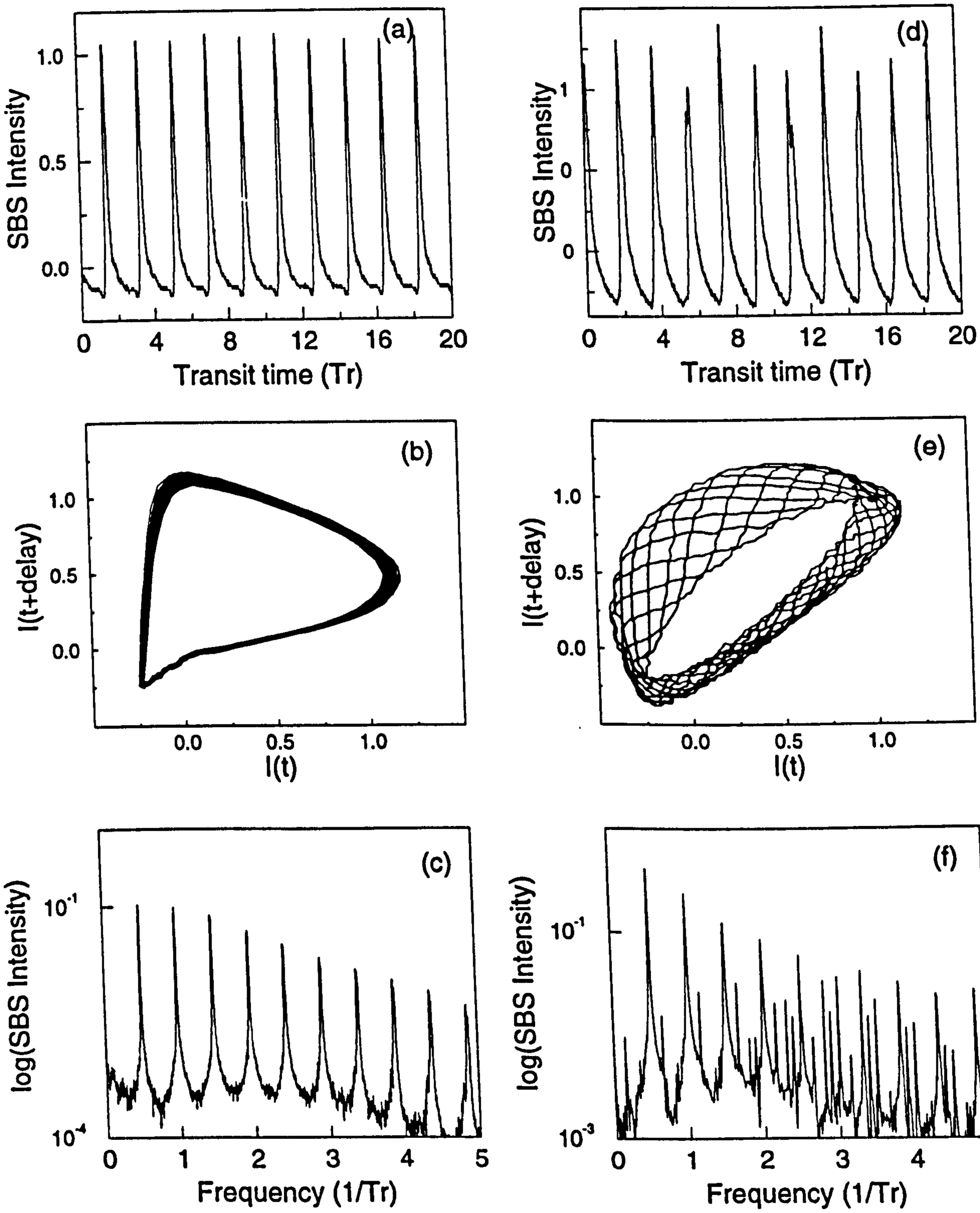

Figure 4.8 Time series (top row), phase portrait (middle row) and fast Fourier transform (bottom row) of the Stokes emission. Region II sustained relaxation oscillations (a-c), and region III quasiperiodic motion (d-f).

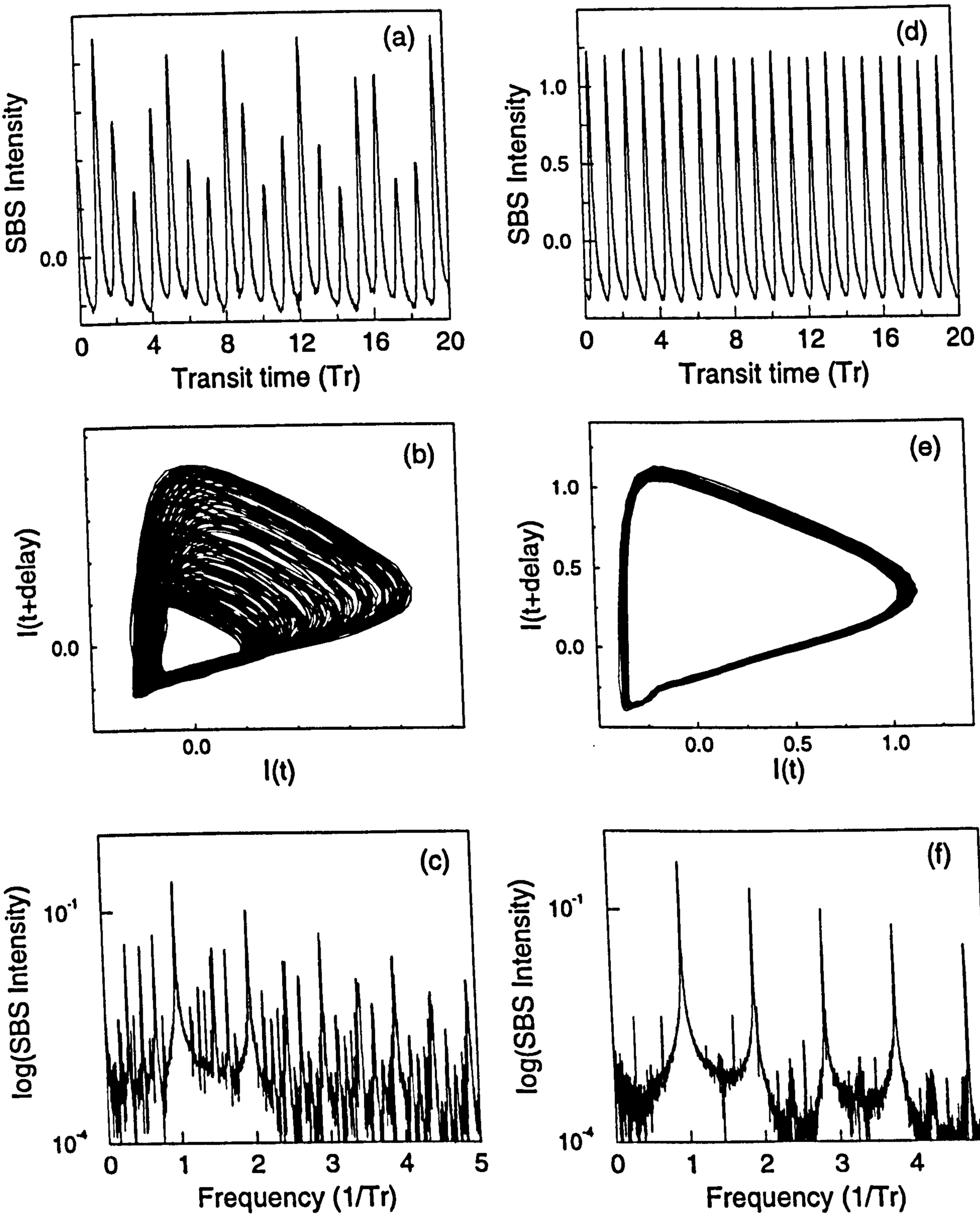

Figure 4.9 Time series (top row), phase portrait (middle row) and fast Fourier transform (bottom row) of the Stokes emission. Region III chaotic motion (a-c), and region IV sustained oscillations T_R (d-f).

confirms the main frequency component of the oscillations to be $1/2T_R$, with higher harmonics clearly visible above the noise floor, Figure 4.8(c).

A further increase in the incident pump power to 380 mW, reveals a third window of interest, (region III Figure 4.4), where two distinct forms of new dynamical behaviour exist. On increasing the pump power from region II to III, a new temporal frequency f_2 emerged in the Stokes emission. This new frequency f_2 was smaller than the characteristic round trip frequency of the fibre $f_1 = 1/2T_R$, Figure 4.8(f). The irrationality of these two frequencies resulted in a quasiperiodic signal in the time series and distinctive toroidal motion in the phase portrait, Figure 4.8(d) and 4.8(e) respectively. The dynamics of this region were always evolving in time and would undergo dramatic transformations depending upon the change in the frequency components.Limit cycles were occasionally observed when the two frequencies locked. However, within this region loss of stability of the quasiperiodicity through environmental contributions led to low dimensional chaotic states. The irregular aperiodic nature of the time series illustrates the transition from quasiperiodicity to chaos, Figure 4.9(a). The phase portrait in Figure 4.9(b) created from the time series with an embedded time delay shows a strange attractor which has densely packed trajectories and a distinctive non-geometric structure. The fast Fourier transform displays characteristic broad band features, with the two main frequency components just visible above the peaks of the chaotic spectrum, Figure 4.9(c). Chaos only prevailed in this region when the system was optimised to provide good launch of the laser beam in the fibre, and accurate cleaving of the fibre. Lack of optimisation in region III gave only quasiperiodic motion.

Upon leaving the chaotic window, (pump power > 500 mW) the irregular form of the dynamics gave way to periodic oscillations (region IV). The structure of these new

oscillations showed strong similarities with the sustained relaxation oscillations observed previously in region II. However, the period of oscillation decreased from $2T_R$ to T_R Figure 4.9(d), with a predominant frequency peak occurring at $1/T_R$, Figure 4.9(f).

Approaching region V, the SBS emission was characterised by slow modulations on the periodic structure, Figure 4.10. The modulation depth increased with pump power, eventually breaking the sustained dynamics of region IV into increasingly long regions of temporally stable cw emission. The quasi-d.c. bursting features of the Brillouin "mirror" [12] are comparable to those reported earlier by previous authors investigating SBS in optical fibres generated using a cw pump laser [5-8]

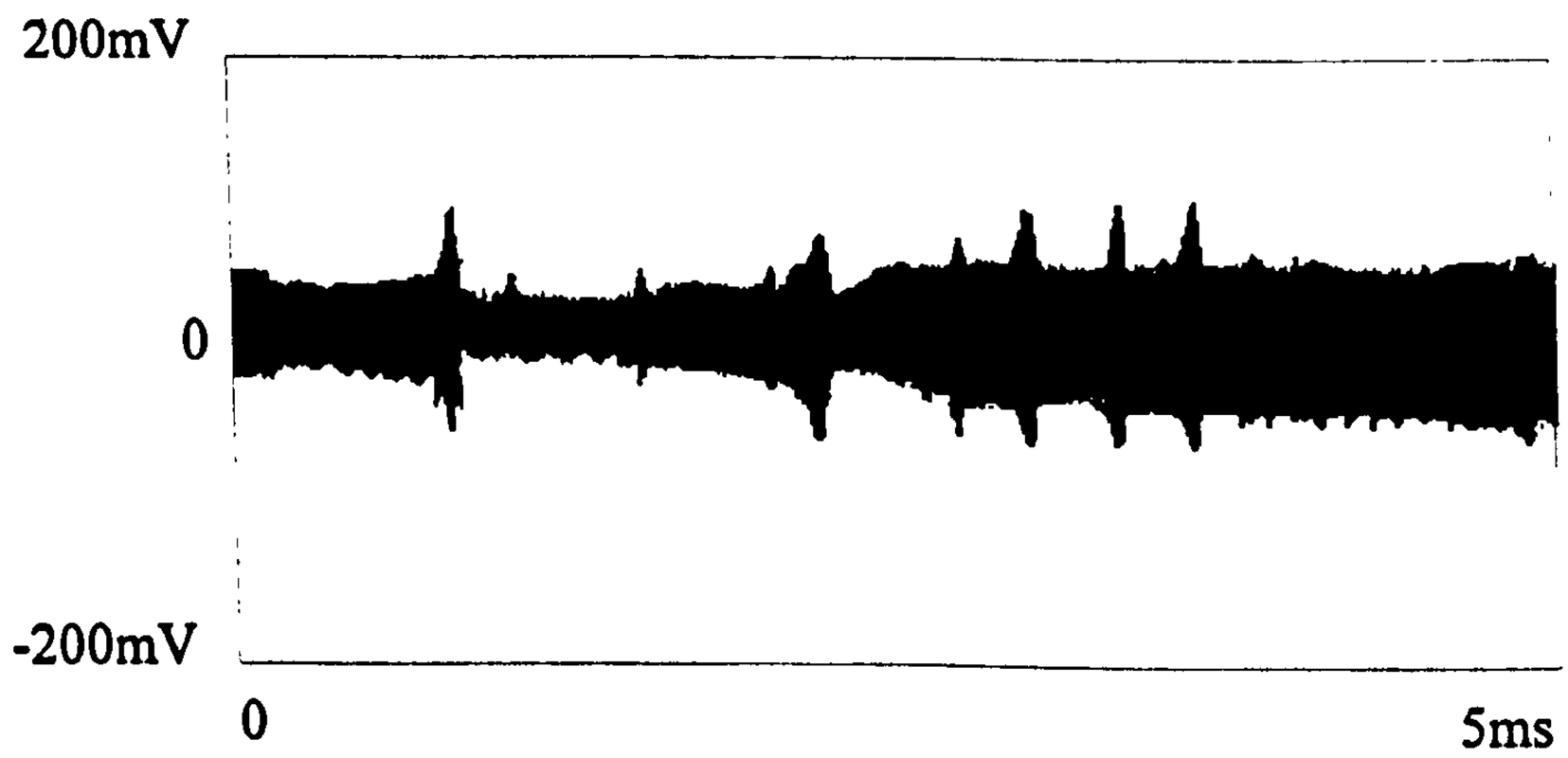

Figure 4.10 Quasi-d.c. bursting behaviour observed in region V.

4.3.3 Four Wave Mixing and Cascaded SBS

The inclusion of external feedback can result in the generation of new optical frequencies through cascaded stimulated Brillouin scattering (CSBS). Previous reports investigating the spectral content of SBS generated in optical fibres with external feedback, indicated the presence of higher order Stokes and anti-Stokes components. The

formation of the higher order Stokes, anti-Stokes components was due to the cascaded stimulated Brillouin scattering process[13]. If the first-order Stokes signal reaches a significantly high intensity, it to can act like a pump wave and generate a new Stokes signal through the SBS process. This new Stokes wave is downshifted in frequency by twice the Stokes shift, travels in a counter-propagating direction to the pump and is referred to as second-order Stokes ω_{2S}. For a sufficiently high intensity the second-order Stokes can generate higher order signals again through the SBS process, thus leading to a cascade of Stokes signals. These findings were produced using relatively high reflectivity's ranging from R = 0.012 to R = 0.78, and used an argon ion laser (λ = 514.5nm) as the pump source [13 ,14].

New optical frequencies can also be produced through parametric four wave mixing (FWM) [14]. The wave mixing process does not require a definitive threshold condition and can occur once first-order Stokes has been produced by SBS. Four wave mixing in optical fibres has been shown to accompany SBS and produce both second-order Stokes ω_{2S}, and anti-Stokes waves ω_{aS} via the following energy conserving relationships, [15]

$$\omega_{aS} = 2\omega_P - \omega_S$$

$$\omega_{2S} = 2\omega_S - \omega_P.$$

Conservation of momentum (phase matching) is imposed by the following relationships,

$$k_{aS} = 2k_P - k_S$$

$$k_{2S} = 2k_S - k_P.$$

Exact phase matching conditions are difficult to achieve in single-mode fibres due to the relatively small core of the fibre restricting the bandwidth of the wave-vectors. Four-wave mixing is therefore limited to small frequency shifts. The FWM process has been observed in experiments using single-mode, silica cored fibres. Either long lengths of fibre (~km's) were implemented to introduce small frequency shifts through anomalous group velocity dispersion (GVD), or high reflectors were used to produce counter-propagating pump and Stokes waves.

Careful monitoring of both the backward Stokes emission and the forward transmitted pump did not reveal the emergence of any new frequencies through CSBS or FWM. The transmitted pump contained a very small first-order Stokes signal which had been reflected from the fibre/air interface at the entrance of the fibre. The length of single-mode fibre used in the experiment had only natural Fresnel reflectivity and a relatively short length (124m). For a fibre with natural reflectivity ($R = 1.1\times10^{-3}$), the effective Brillouin gain is substantially reduced in comparison to cavities where cascaded SBS was observed. A reduction in the Brillouin gain will produce a significant increase in the threshold for second-order Stokes hence, higher order Stokes components generated through the CSBS process were not observed. The exclusion of cascaded SBS components also prevented four-wave mixing as there were insufficient frequencies with the necessary frequency shifts. The short fibre length (124m) and the normal GVD characteristics of the fibre at a wavelength of 1.064μm also impeded the FWM process. Confirmation of first order Stokes emission can be found in the steady-state characteristics presented in section 4.3.1. Higher order Stokes and anti-Stokes components introduce dramatic "kinking" in both the transmitted pump and the Stokes

emission [15]. The kinking is caused by the contribution of the new higher-order Stokes component to the transmitted pump or the original Stokes intensity, depending upon the direction of propagation of the new frequency. Kinking was not observed in the steady state behaviour of SBS, Figure 4.4, and it was therefore concluded that the Stokes emission was first-order over the whole pump operating regime.

4.3.4 Analysis of Dynamics

To provide a quantitative characterisation of the chaos found in region III, correlation dimension measurements were performed using the Grassberger-Procaccia algorithm [16]. A typical data set of 16,000 points was taken from the time series in Figure 4.9 (a). A convergent correlation dimension of D_2 = 2.1 was found for an embedding dimension greater than 6, Figure 4.11(a).

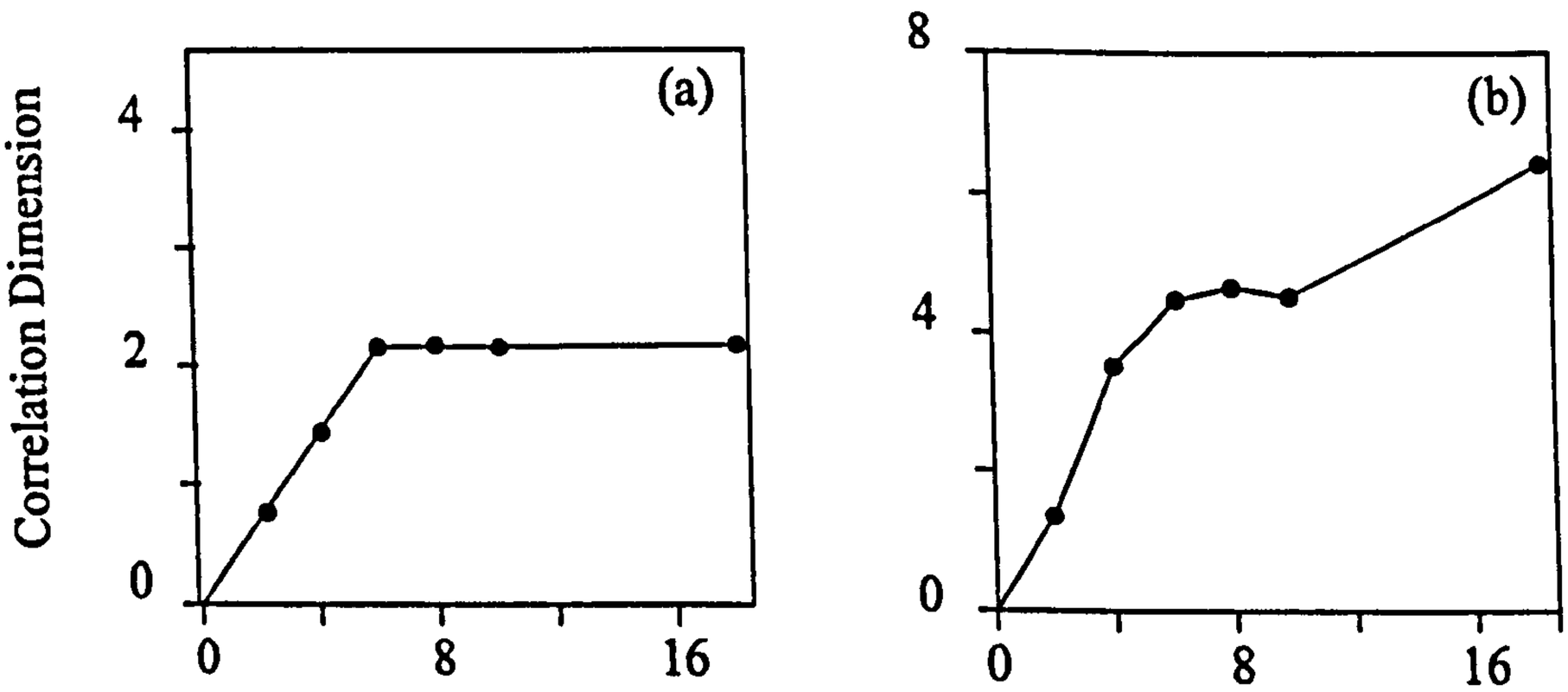

Figure 4.11 Dimension analysis of data taken from the (a) chaotic window and (b) close to threshold.

This result proves the existence of low-dimensional chaos in region III. By contrast, dimensional analysis of the erratic-aperiodic signal in the vicinity of threshold (region I) revealed a lack of definable correlation dimension, Figure 4.11(b). The absence of a convergent dimension indicates stochastic behaviour of the Stokes emission in the region close to threshold.

4.3.5 Comparison with Theoretical Predictions

Theoretical investigations of SBS generated in the presence of external feedback were obtained by other members of the same research group, in parallel with the experimental work described in this thesis. The theoretical data was found by solving the four coupled equations presented in section 4.1.1. The value for the external reflectivity was based upon the experimental measurement with $R_1 = R_2 = 3.3\%$. The gain g was chosen as the control parameter because it was proportional and equivalent to the pump intensity, equation (10) chapter 3.

The time averaged intensities of the Stokes signal and transmitted pump are illustrated in Figure 4.12. The transmitted pump increased linearly with the external pump until it reached SBS threshold. At threshold, a distinctive "shoulder" appeared before the onset of strong SBS emission. From the theoretical simulation, the shoulder effect was found to be dependant upon the value of the modulation parameter u. This implied that an increase in the phase modulation term reduced the rate of pump saturation around threshold. The SBS signal exhibited a linear dependence upon the incident pump power, with windows of distinctive dynamics emerging in regions I-V.

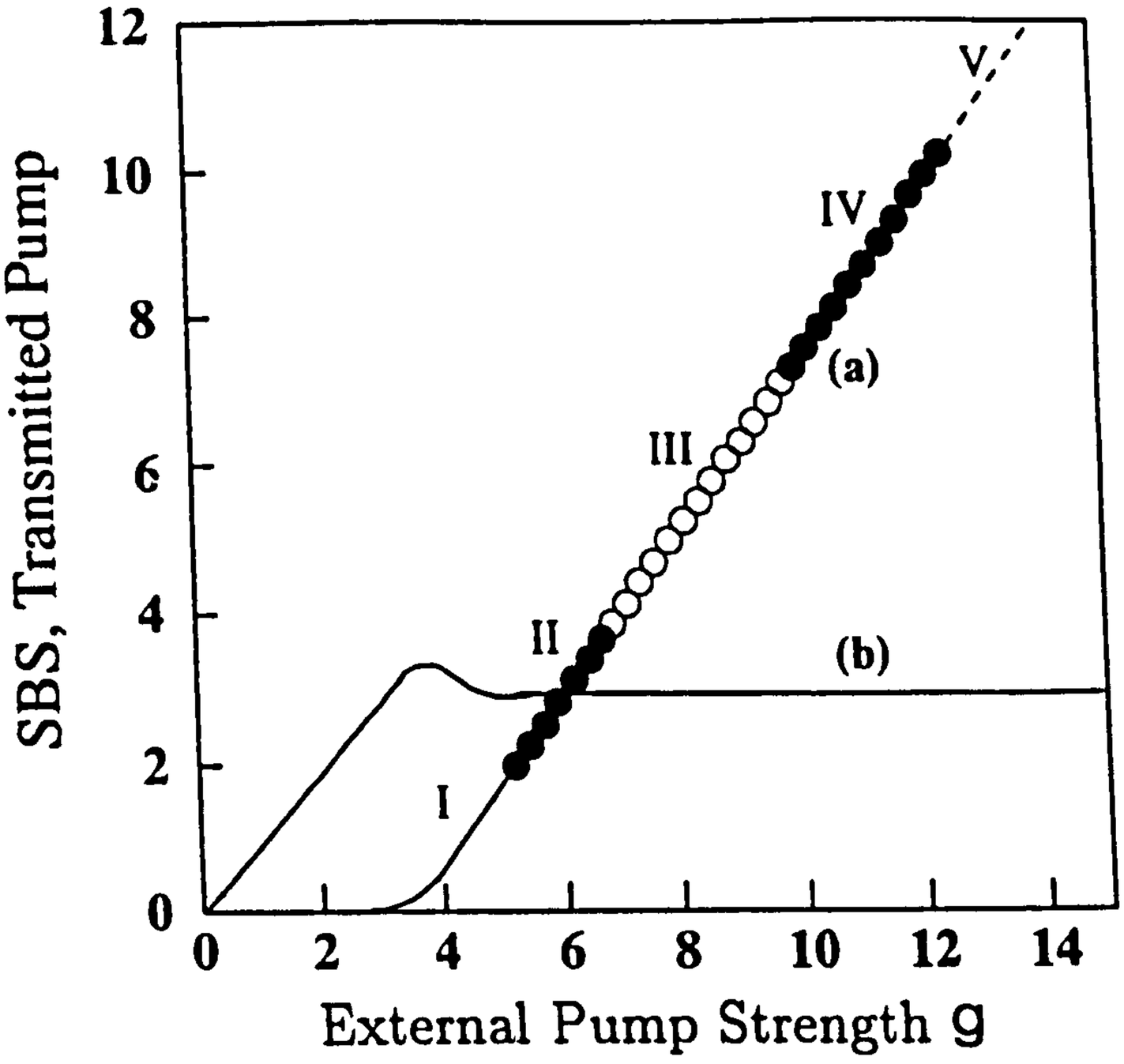

Figure 4.12 Theoretical steady-state characteristics of (a) Stokes signal and (b) transmitted pump as a function of pump strength g. The regions I-V indicate parameter windows for different forms of dynamical behaviour.

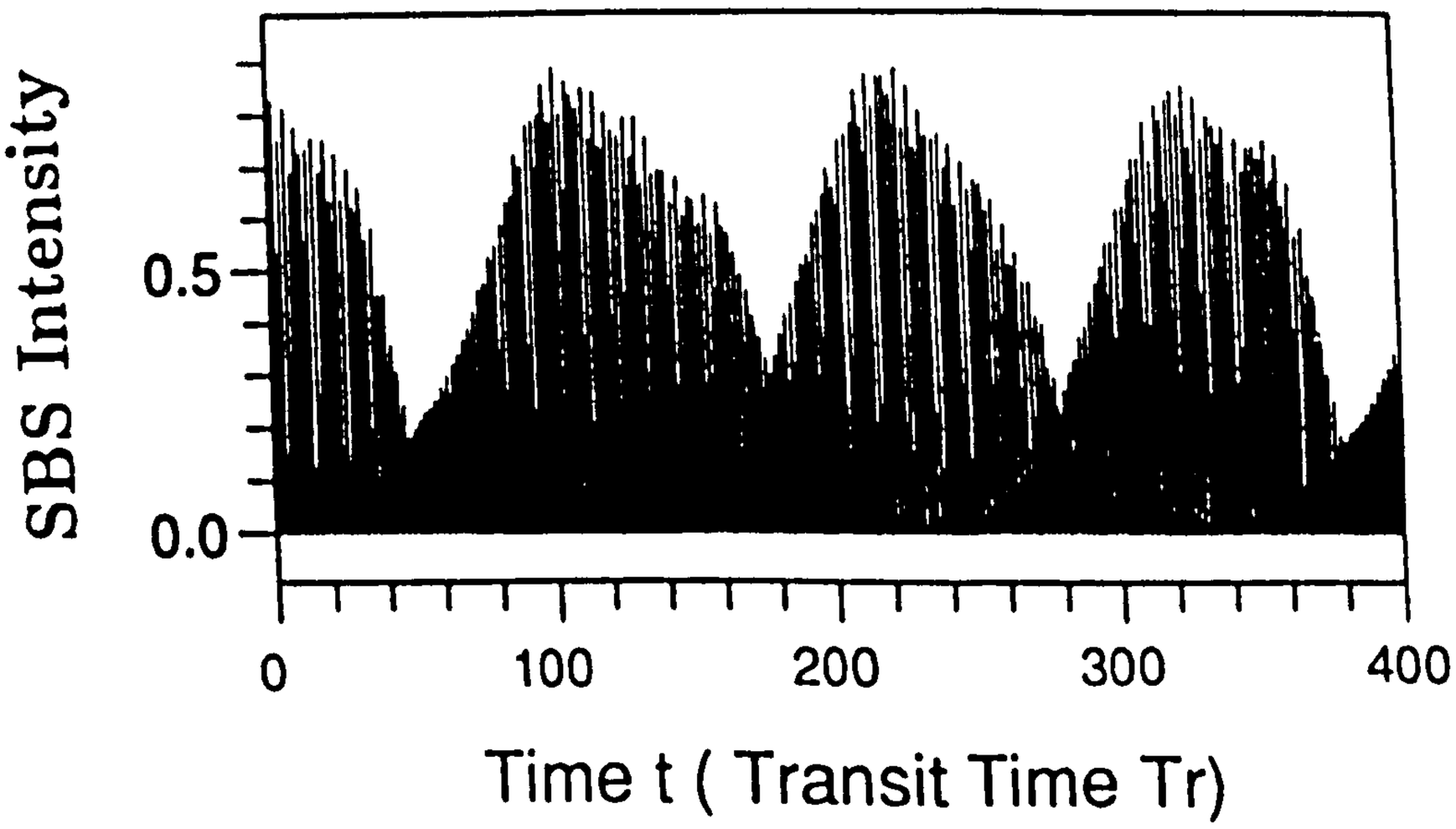

Figure 4.13 Time series of the Stokes emission just after SBS threshold (region I).

The first window of dynamical behaviour (region I), is composed of erratic bursts lasting for a duration of hundreds of T_R , containing within the slowly modulated envelope fast relaxation oscillations of period $2T_R$, Figure 4.13. This is in agreement with the experimental results obtained in the same region just above threshold.Other examples of the typical complex temporal dynamics found in regions II-IV are shown in Figure 4.14. Robust limit cycle behaviour was found to persist throughout region II, with the time series containing regular sustained relaxation oscillations whose period was proportional to the round trip of the medium. However, the onset of sustained relaxation oscillations occurred before the SBS intensity became equal in strength to the transmitted pump intensity, Figure 4.12. In region III a second slower frequency emerged which gave rise to quasiperiodic motion, indicated by the torus in the phase portrait. Adjustment of the control parameter g in the same region induces a loss of stability in the quasiperiodicity which results in chaos, Figure 4.14(f). The dynamical evolution from region II to III, particularly the transition from limit-cycle to torus and finally chaos, is strongly suggestive of a Ruelle-Takens-Newhouse [17] route to chaos. Upon further increase in the pump intensity, the chaos collapses to a small window of quasiperiodic motion, region IV. The quasiperiodic motion only existed over a small parameter window, and the most dominant dynamical features in the region were stable sustained relaxation oscillations of period T_R. Finally, in region V quasi-d.c. emission was found after being preceded by a gradual reduction in the amplitude of limit cycle. The quasi-d.c. emission contained randomly distributed temporal bursts over the whole of region V, Figure 4.15.

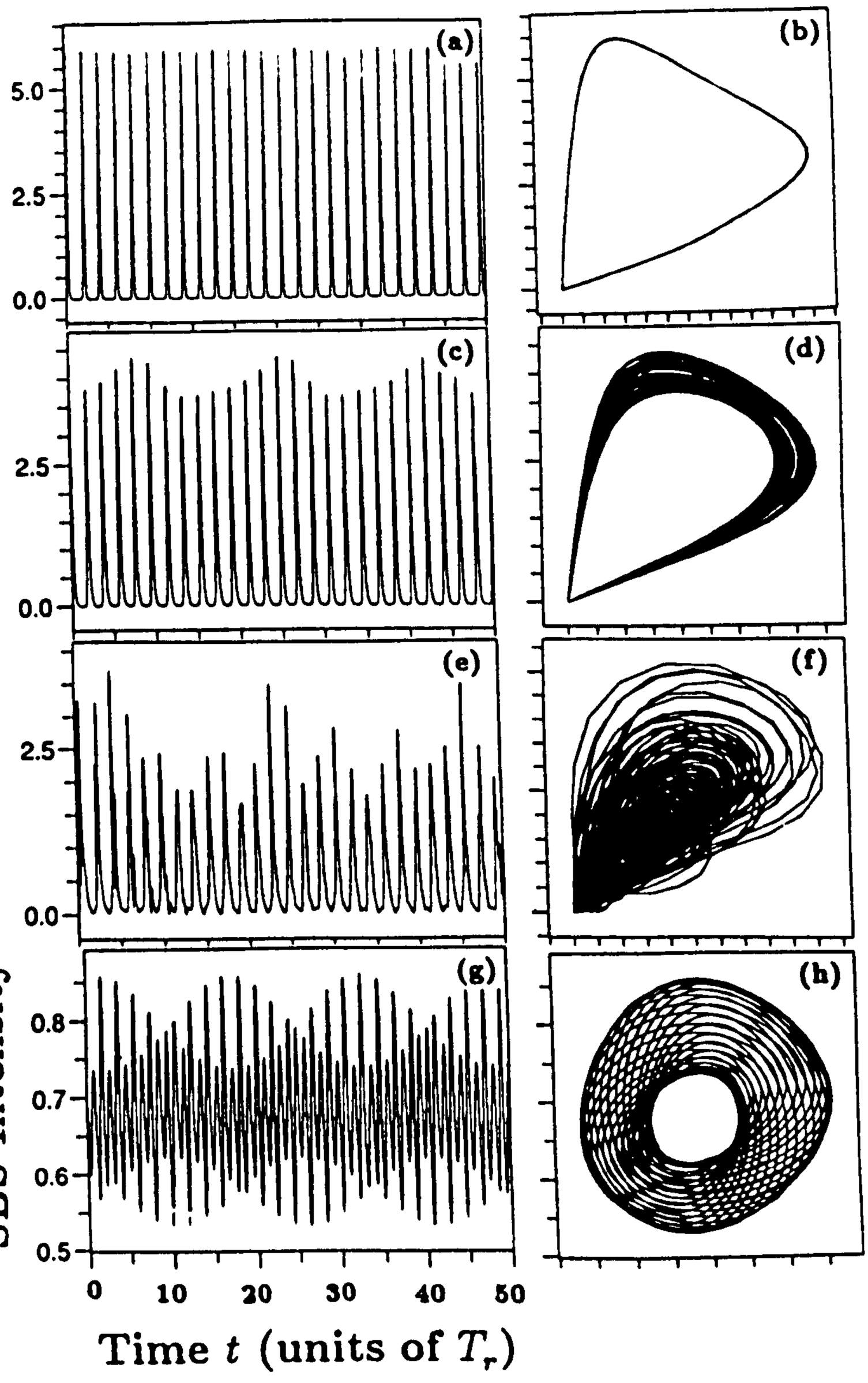

Figure 4.14 Time series (left-hand column) and corresponding phase portraits (right-hand column) of the Stokes signals in regions II-IV of Figure 4.12. (a) and (b) periodic motion in region II. (c) and (d) quasiperiodic motion evolving into chaos (e) and (f), region III. Finally quasiperiodic motion (g) and (h) in region IV after the collapse of chaos.

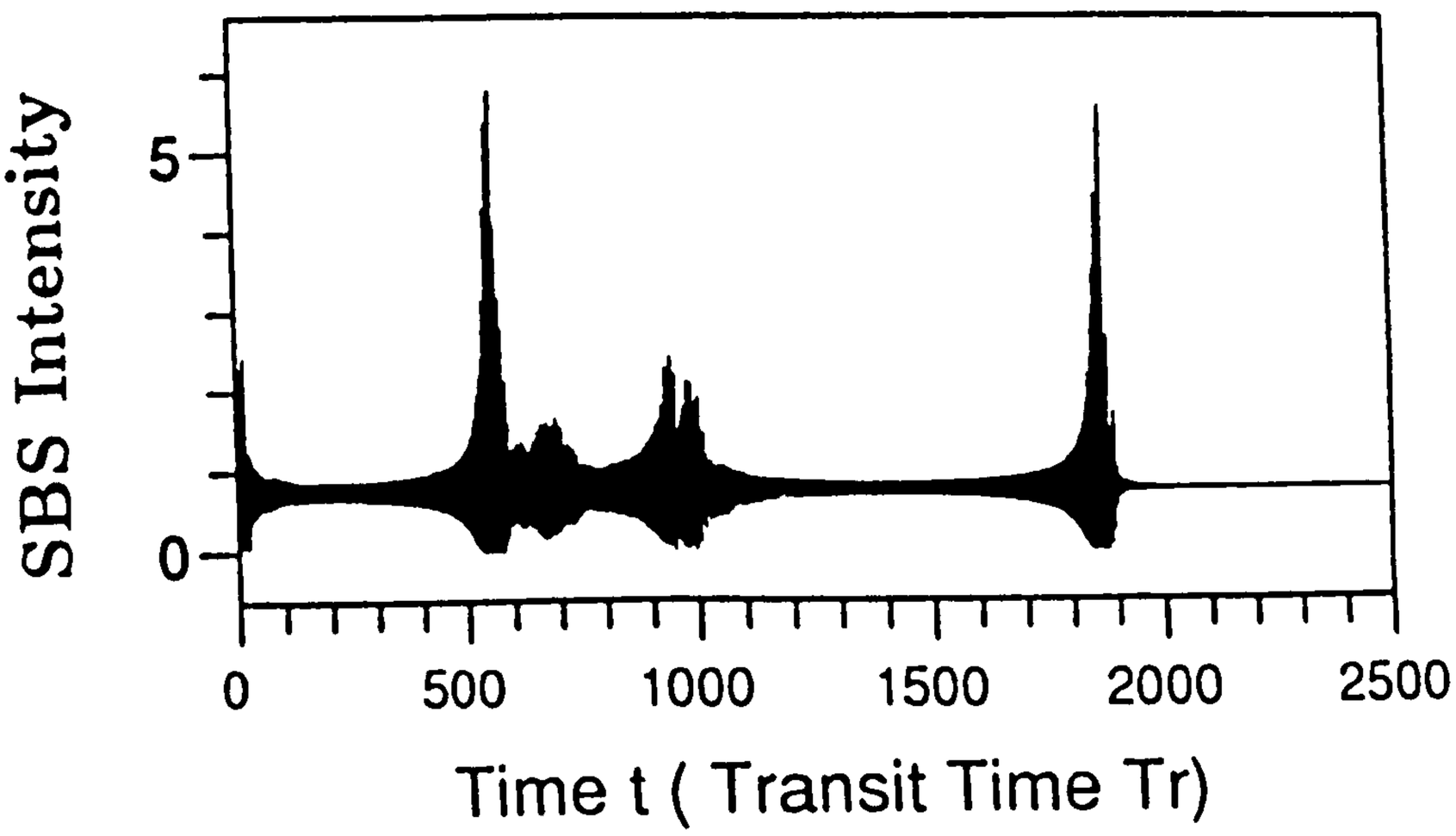

Figure 4.15 Stokes signal intensity showing train of random transient bursts with the appearance of stable cw emission, region V.

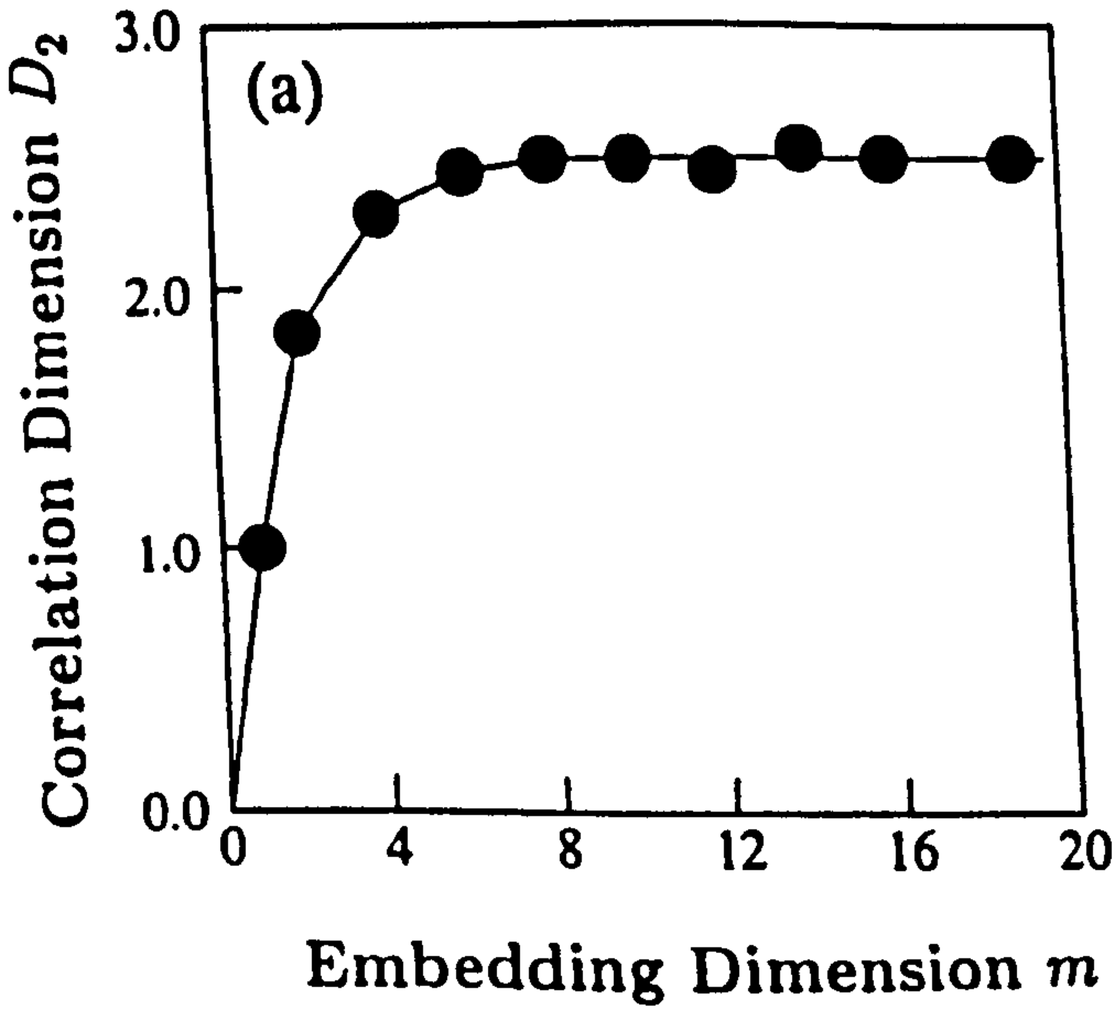

Figure 4.16 Correlation dimension D_2 versus embedding dimension for theoretically generated data sets in region III.

The suppression of the dynamics in region V implies the Brillouin gain has become saturated, especially at the relatively high pump levels. Also, another interesting feature of the quasi-d.c. window was the periodic modulation of the Stokes field even when the intensity output was constant. This indicates the persistence of phase modulation in the stimulated process. As before, correlation dimension analysis was used to quantify the topological properties of the strange attractor generated from the chaotic time series. Typical theoretical data sets contained between 20,000~40,000 points with ~100 points representing the resolution of each transient peak. A convergent correlation dimension of $D_2 \sim 2.4$ was measured for an increasing embedding dimension greater than 6, Figure 4.16. The quantitative characterisation of the aperiodic SBS signal confirmed the existence of low dimensional chaos.

Overall, there exists a good agreement between experimental results and theoretical findings. Both quantitative and qualitative analysis of the results show clearly defined similarities. This suggests that the physical model developed involving interplay between the gain, feedback and nonlinear refraction is in agreement with the descriptions of the dynamical features of SBS generated in an optical fibre with the inclusion of external feedback. The amount of feedback in particular was found to be critical for the generation of both deterministic dynamics and chaos. The gain proved to be an excellent control parameter for both the experiment and the theoretical model, revealing the possibility of a quasiperiodic route to chaos. The inclusion of noise, (to represent the initiation of the stimulated process from spontaneous scattering), played no significant role in the evolution of the dynamics. Experimentally and theoretically the SBS emission produced in close proximity to threshold, displayed stochastic characteristics. However, for strong SBS emission (P_0 = 270 mW) in the presence of external feedback the

stochastic behaviour was undetectable and the dynamical evolution of the system became deterministic [18]. The incorporation of nonlinear refraction effects, most notably self-phase and cross-phase modulation, are fundamental in describing the observed complicated, deterministic dynamical evolution of the SBS process. Another factor which played a critical role in determining if the SBS process became chaotic was the polarisation properties of the optical fibre. Previous reports have demonstrated only periodic and quasiperiodic behaviour of SBS generated in polarisation preserving fibre with feedback [19]. The experimental and theoretical findings presented in this chapter clearly indicate the existence of chaotic SBS in non-polarisation preserving optical fibre. A recent theoretical analysis into the dynamics of the stimulated Brillouin process [20], has identified how the non-polarisation property of the fibre is essential in providing an extra degree of freedom for the existence of chaos.

There do exist several differences between experiment and theory. The theoretical analysis predicted chaos collapsing into quasiperiodicity before stabilising into regular periodic oscillations. The window for the emergence of this new dynamical feature is quite small [8] and the possibility of the experimental set-up having insensitive control of the pump power cannot be neglected. Theory also reveals a minor discrepancy in the stable-emission window, region V. Numerical simulations reveal the random temporal bursts decreasing in appearance until pure stable cw Stokes emission is observed. However, in the experiment pure continuous emission was always interrupted by small irregular bursts which occurred on relatively long time scales when compared with the round trip time of the cavity. These bursts in the quasi-d.c. region have been successfully removed by previous authors [19] using an active stabilisation feedback loop to remove the effects of environmental noise. Therefore, the random bursts in the d.c. region were

attributed to environmental effects. Another consideration concerning both low dimensional chaos and higher harmonics is the wavelength dependence of the fibre loss. In previous experiments visible lasers were employed as the pump [5-7,19,21] at these pump wavelengths the predominant loss mechanism is Rayleigh scattering in the fibre, with typical values being in the region of 18-20 dB/km from 0.5-0.65μm [22]. Also in the blue-green region of the visible spectrum germania doped (GeO_2), silica cored fibres can exhibit unusual nonlinear transmission characteristics. The main mechanisms associated with the nonlinear transmission are two-photon absorption processes and the formation of colour centres, both linked to the germania dopant [23 ,24]. Operating in the infra-red region of the fibre considerably reduces the scattering losses and eliminates the possibility of colour centre formation. For the wavelength used in our experiment, λ=1.064μm, the attenuation in the fibre was reduced to 1.45dB/km. This significant reduction in the loss has implications for the dynamical process. Primarily, with more optical power being available, the nonlinear interaction will be enhanced compared to a high loss fibre. In particular the efficiency of the nonlinear process will be increased. Recalling the figure of merit relationship from, chapter 1, which shows the increase in efficiency of a nonlinear process in an optical fibre compared to a bulk medium,

$$\frac{(IL_{eff})_{fibre}}{(IL_{eff})_{bulk}} = \frac{\lambda}{\pi\omega_0^2\alpha}$$

and using the above relationship to calculate the improvement factor, a direct comparison can be made between a visible and an infra-red laser. For a visible laser, typically Argon ion, the fibre loss is 20dB/km for a wavelength of 514.5nm. Combined with a spot radius of 1.5μm, the improvement factor for a typical visible laser is ~2×10^7. At a pump wavelength of 1.064μm the fibre loss is 1.45dB/km, and with a spot size of 2.5μm the

improvement factor is ~2×10^8. Clearly, the infra-red wavelength produced by a Nd:YAG laser improves the efficiency of a nonlinear process by an order of magnitude. Also lowering the amount of light scattering reduces the amount of heating in the fibre, and hence there will be less change in the optical path length. This could explain why no higher harmonics were observed in the experiment using the longer pump wavelength, and also the importance of low loss for chaotic scattering.

4.4 Variable Reflectivity

Having established both the role and the significance of feedback upon the temporal response of SBS for a system with variable pump power, the effect of varying external reflectivity while maintaining a constant pump is investigated. The same experimental set-up as before was used to pump and monitor the SBS process, however a modification was required to accommodate the addition of variable external feedback

4.4.1 Experimental Set-up

The same single-mode optical fibre as used in previous studies was employed as the Brillouin medium. To provide a fibre cavity with variable reflectivity the following modifications were made to the experimental set-up, Figure 4.17. The entrance to the fibre incident to the pump beam was accurately cleaved close to the Fresnel limit to provide a fixed reflectivity of R =3.3%. The exit of the fibre was polished by the procedure described in section 3.3.1, to remove the small amount of natural reflectivity. The polished exit of the fibre was then mounted upon an xyz opto-mechanical support,

and the emerging light from the fibre exit was then coupled back into the fibre by using a 100% reflector. Movement of the polished fibre exit through the focus of the launch microscope objective, altered the amount of light coupled back into the fibre. This technique provided an accurate and stable method for controlling the effective reflectivity R_2 of the fibre exit.

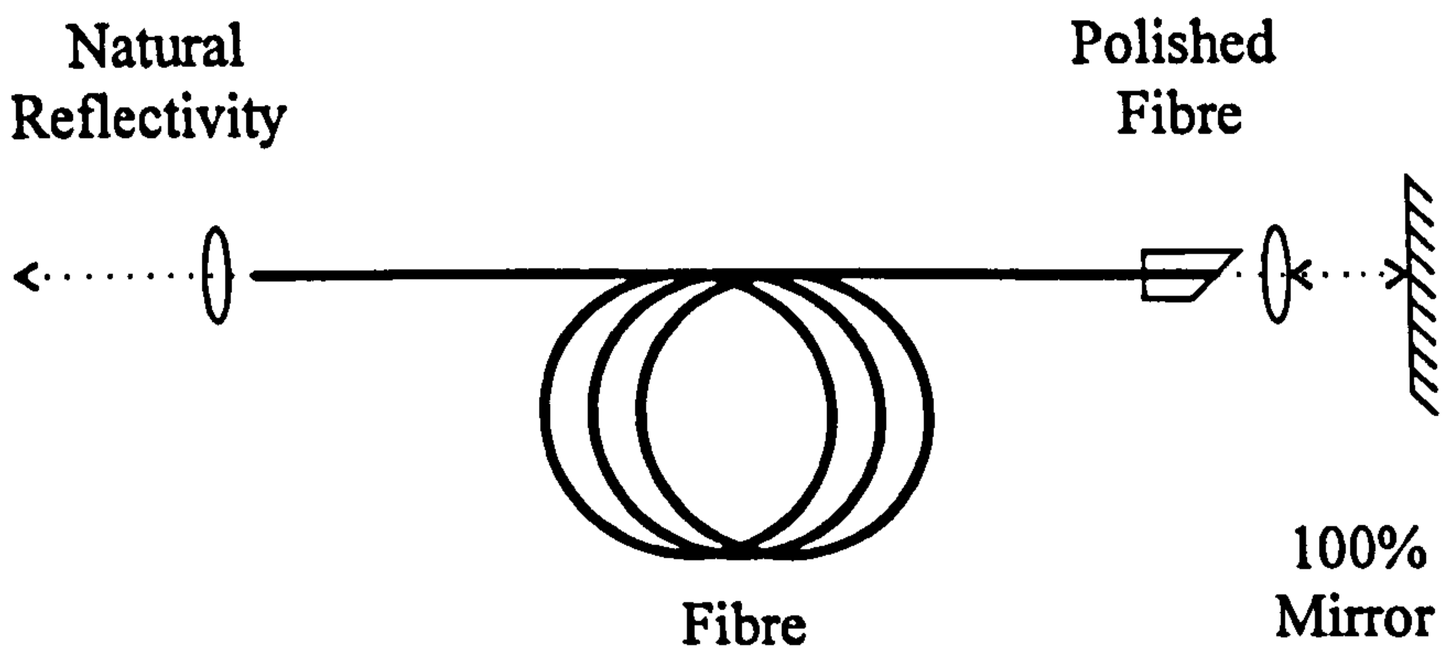

Figure 4.17 Variation of external reflectivity utilising a high reflector and the fibre launch condition.

Measurement of the external reflectivity involved monitoring the interference fringes present in the back reflected light. The height of the fringes was proportional to the amount of reflectivity experienced by the light at the fibre exit. Therefore, by comparing the relative signal height for both the blocked and unblocked reflector at a fixed pump power, the effective external reflectivity could be estimated. Careful adjustment of the fibre launch position allowed the external reflectivity (R_2) be varied from 10^{-4} to 20%, corresponding to a cavity reflectivity ($R = R_1R_2$) between 3.3×10^{-8} to 6.6×10^{-3}.

4.4.2 Dynamical Behaviour of SBS with Variable Reflectivity

The results obtained for SBS produced with variable values of external reflectivity for a constant pump power are shown in Figure 4.18 and Figure 4.19. The entrance to the fibre had a fixed natural reflectivity (R_1 = 3.3%) and the external reflectivity (R_2) was varied from 10^{-4} to 20% for a fixed pump power of 450mW. This pump power corresponded to the centre of the chaotic region for a fibre with natural reflectivity. For the lowest feedback level the Stokes emission is highly aperiodic and displays a broad band spectrum indicative of noise, Figure 4.18(a). The temporal profile of the signal is indistinguishable from previous recordings obtained for SBS generated in a fibre without external feedback. The level of feedback is insufficient to suppress the noise associated with the spontaneous scattering which initiates the stimulated Brillouin process. An increase in the external reflectivity reveals the emergence of a weak periodic structure whose signature is clearly indicated in the power spectrum, Figure 4.18(c). The period of this weak signal is proportional to the round trip time of the cavity $2T_R$. At this low feedback level cavity effects are beginning to influence the temporal structure of the Stokes signal. However, higher frequency components still exist providing evidence that deterministic evolution is starting to dominate for weak feedback. The transition to robust sustained relaxation oscillations occurs for a relatively small increase in reflectivity (3.3×10^{-5}), Figure 4.18(e) and (g). The period of these oscillations corresponds directly to the round trip cavity time of the fibre. The temporal shape and period of oscillation for the level of feedback agree with previous reports by Bar-Joseph et al [2].

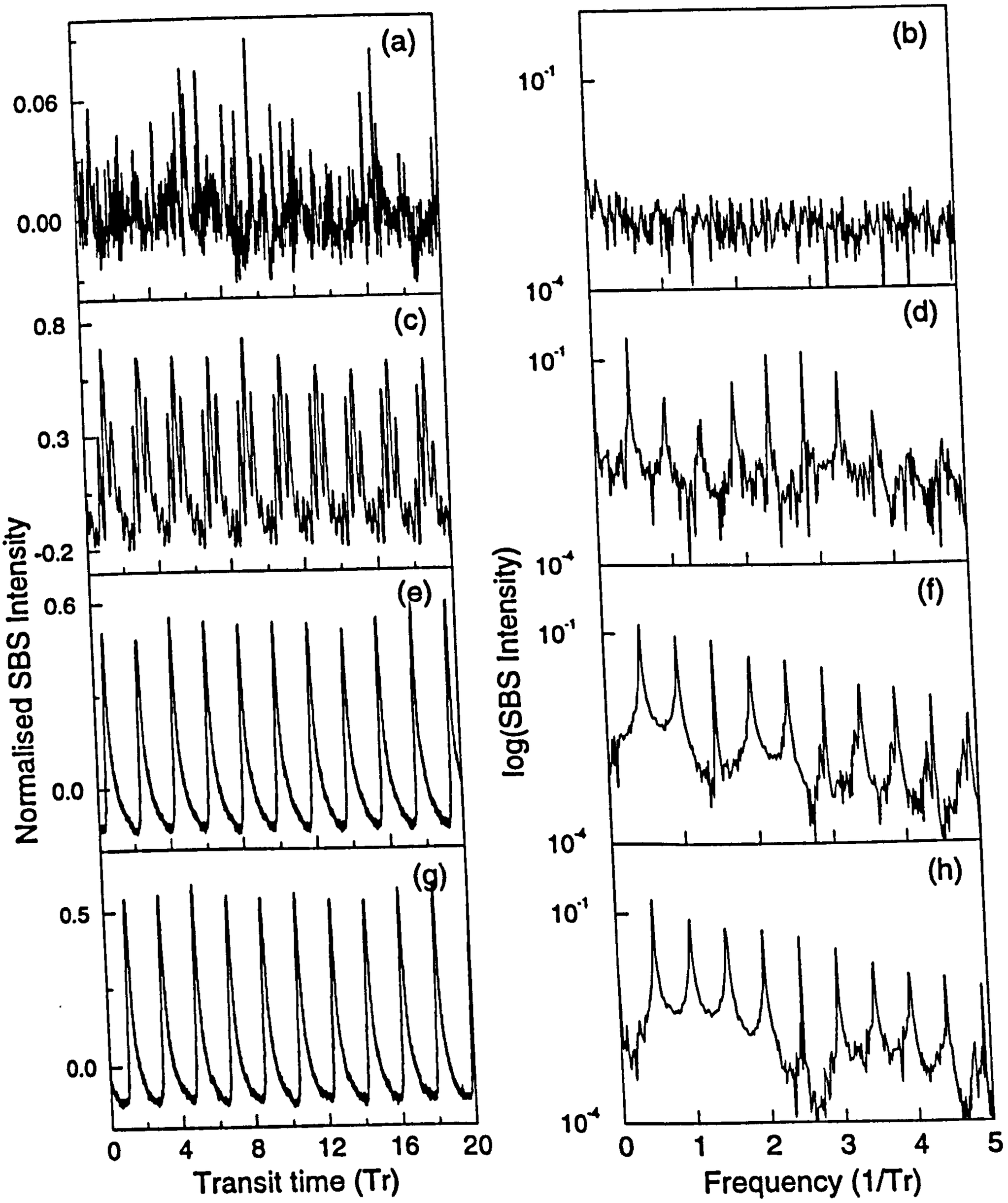

Figure 4.18 Time series (left hand column) and corresponding fast Fourier transform (right hand column) illustrating the dependence of dynamical features upon different levels of feedback. The cavity reflectivity ($R = R_1R_2$) was (a-b) 3.3×10^{-8}, (c-d) 3.3×10^{-6}, (e-f) 3.3×10^{-5} and (g-h) 3.3×10^{-4}.

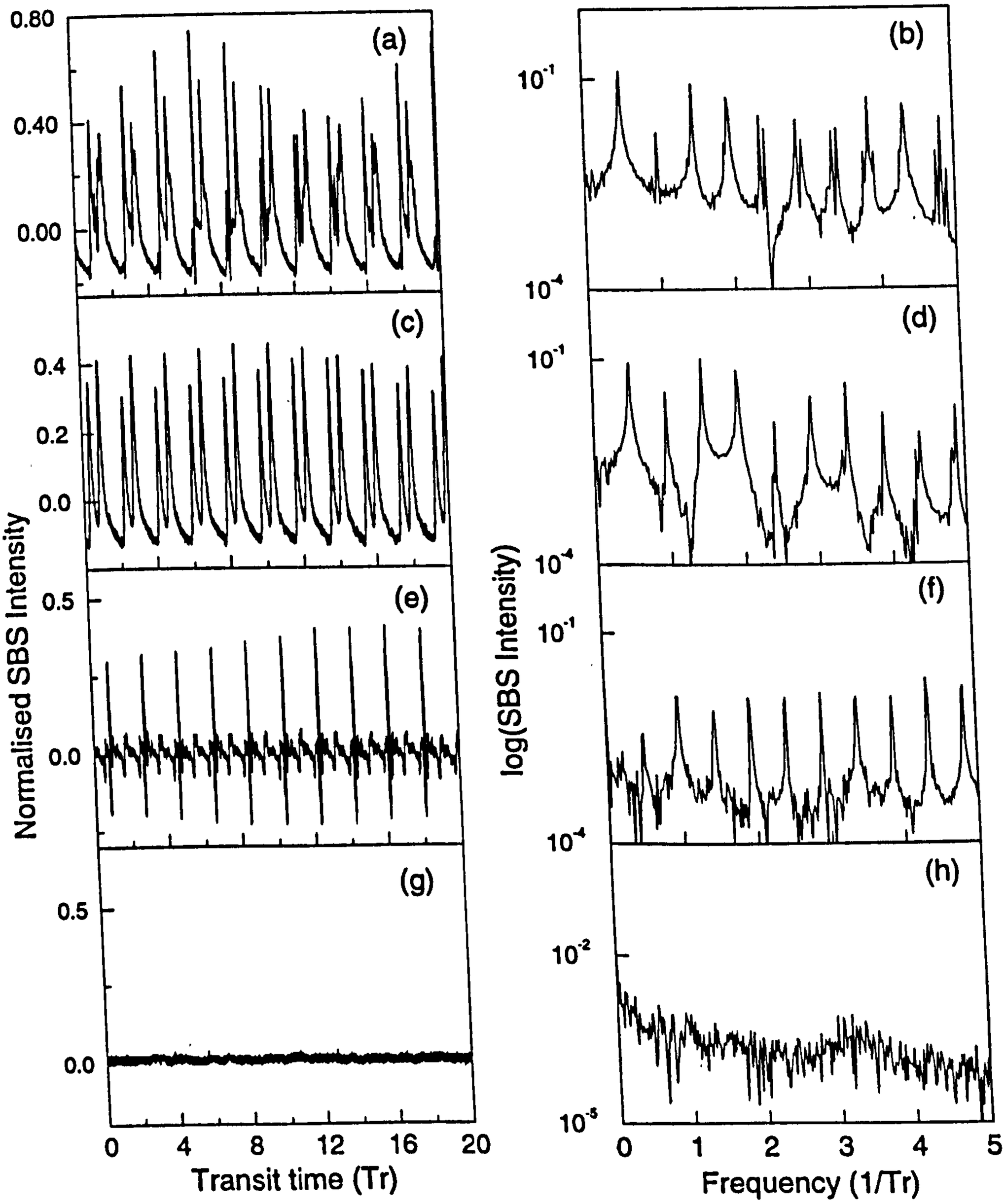

Figure 4.19 Time series (left hand column) and corresponding fast Fourier transform (right hand column) illustrating the dependence of dynamical features upon different levels of feedback. The cavity reflectivity ($R = R_1R_2$) was (a-b) 8.25×10^{-4}, (c-d) 2.0×10^{-3}, (e-f) 3.3×10^{-3} and (g-h) 6.6×10^{-3}.

Stable oscillation of the Stokes emission exists for a range of cavity reflectivity, from 3.3×10^{-5} to 3.3×10^{-4}. Quasiperiodic motion was observed with a further increase in the external feedback, with a slower frequency component just detectable in the power spectrum, Figure 4.19(b). The quasiperiodicity gave rise to a time series with a higher harmonic approaching T_R, for an increase in the control parameter. Towards a relatively high reflectivity ($R_2 = 20\%$), the Stokes signal displayed stable continuous emission after being preceded by random bursts in the higher harmonics, Figure 4.19(e). The power spectra in Figure 4.19(f) shows a strong peak at the higher frequency corresponding to T_R.

Increasing the external feedback of the fibre increases the conversion efficiency of the stimulated Brillouin scattering process. An indication of the increase in conversion efficiency is provided by comparing the average SBS intensity generated for two different values of cavity reflectivity. For the lowest external reflectance (3.3×10^{-8}), where the SBS was aperiodic, the average power produced by the system was 40mW. For the highest reflectance (6.6×10^{-3}), equivalent to cw Stokes emission, the average SBS power had increased dramatically to a value of 400mW. This represents an increase in conversion efficiency from 8% to 88% for a constant pump power of 450mW. Using the external feedback as the control parameter demonstrated similar forms of dynamical behaviour as observed when the external pump was the principal variable in the system. The transition from stochastic to deterministic evolution has a critical dependence upon the amount of external feedback. The progression in the complexity of the dynamics from sustained relaxation oscillations to quasiperiodic motion, through to stable emission relied upon the density of photons inside the fibre, and the nonlinear refractive index.

Chaotic motion was not observed in the Stokes signal for the fixed power level of 450mW. Increasing the fixed power level to a slightly higher value, 500mW, reduced the dynamical region considerably with quasi-d.c. behaviour dominating for an external reflectivity of 2.6×10^{-3}. The external feedback proved to be an insensitive control variable in contrast to the external pump.

4.4.3 Comparison with Theoretical Predictions

The theoretical findings presented in Figure 4.20 show various forms of dynamical features obtained by varying the cavity reflectivity for a fixed external pump power. From previous theoretical analysis [8] deterministic features were predicted for an SBS amplifier [9], which was seeded by a signal strong enough in intensity to dominate the contributions of spontaneous Brillouin scattering. The selection of the seed strength depended directly upon the cavity reflectivity of the system. For the fibre used in both the analytical model and the experiment a critical cavity reflectivity of $R_c = 7.6\times10^{-8}$ was calculated. Below this critical value the spontaneous noise will dominate the Stokes emission. Above the critical feedback level, the cavity will suppress the noise contribution allowing the evolution of deterministic dynamics. For the lowest value of cavity reflectivity (3.3×10^{-8}) which was below the critical level ($R_c = 7.6\times10^{-8}$), the SBS signal was found to be aperiodic and noise dominated for a fixed pump level of 500mW, Figure 4.20(a). Increasing the amount of feedback to a level above the critical value allows the Stokes emission to become periodic with sustained relaxation oscillations of period $2T_R$

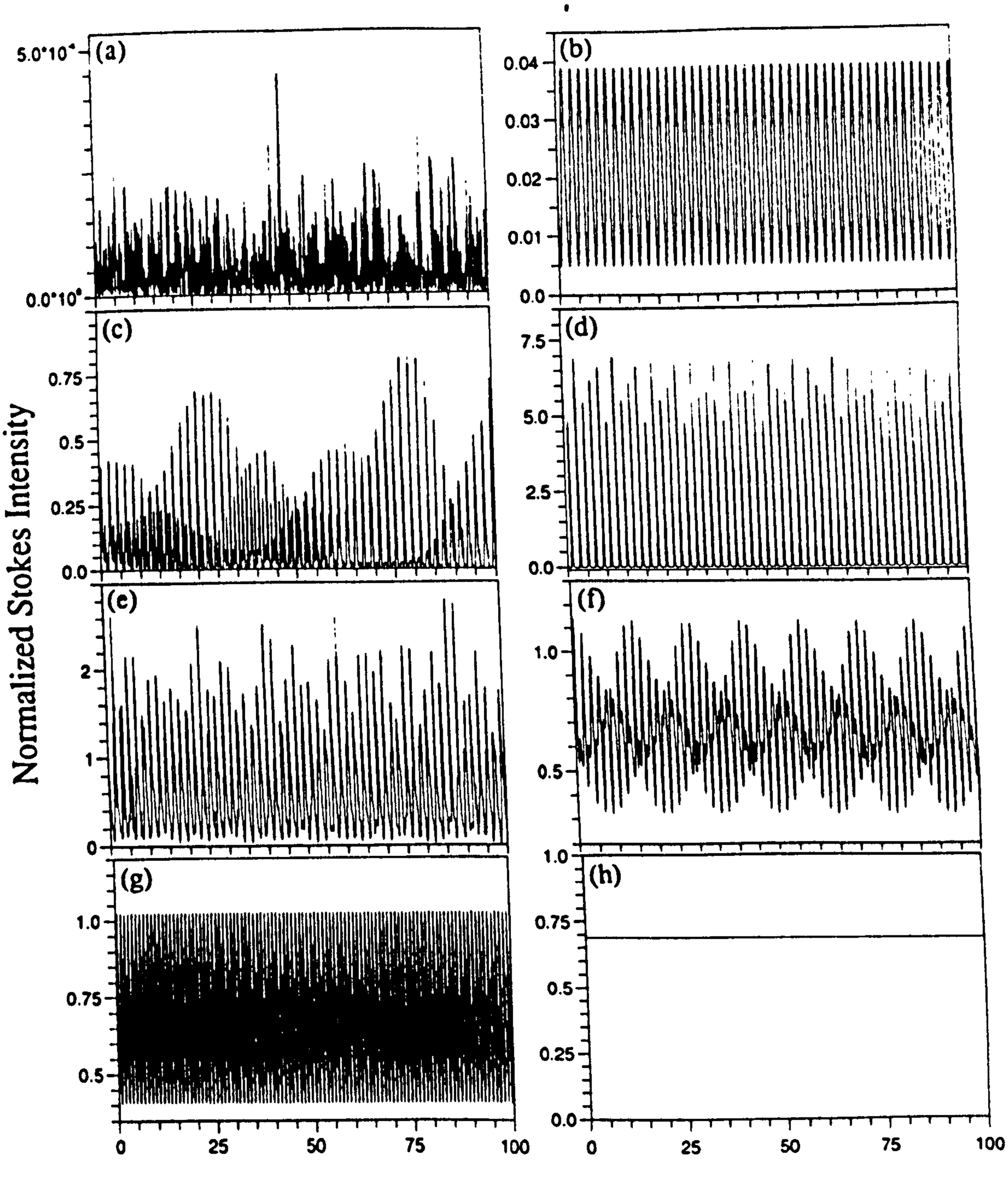

Figure 4.20 Theoretical results illustrating dependence of dynamical features upon the reflectivity R for a gain g = 8.0 (500mW). (a) 1.0×10^{-8}, (b) 2.5×10^{-7}, (c) 1.0×10^{-6}, (d) 2.3×10^{-4}, (e) 9.0×10^{-4}, (f) 3.0×10^{-3}, (g) 4.0×10^{-3}, and (h) 6.4×10^{-3}.

dominating the signal, Figure 4.20(b). The experimental result shows the emergence of the periodic signal, however there is still aperiodicity present in the Stokes emission. This difference could be due to environmental contributions from the laboratory which do not exist in the analytical model. Two regions of quasiperiodic behaviour were observed separated by a window of chaotic emission. The experimental findings contained two separate forms of quasiperiodicity Figure 4.19(a) and (c), however chaos was not observed. Finally at the higher feedback levels, the SBS emission becomes stable after passing through a region of stable oscillations with lower period, T_R. A comparison between the experimental findings and the theoretical predictions indicates similar trends in dynamical evolution. Both systems demonstrate aperiodic emission at low feedback levels and the establishment of periodic, quasiperiodic and stable quasi-d.c. emission for increasing increments in the control parameter. The omission of chaos from the experimental results is related to the level of external pump power. For the promotion of rich dynamics including chaos, low feedback and operation at high pump levels is required to enhance the nonlinear refraction of the medium. Similar feedback levels were implemented in both systems, but the theoretical model incorporated a slightly higher pump level leading to an increase in the nonlinear refraction and hence the observation of chaos.

4.5 Conclusions

The nonlinear dynamics of stimulated Brillouin scattering generated in a single-mode optical fibre with external feedback have been investigated experimentally. The

addition of external feedback dramatically changes the dynamics and steady-state features of the SBS process. Even the presence of a relatively small amount of feedback, e.g. the natural reflectivity introduced by Fresnel reflections at the cleaved fibre ends, can lead to deterministic periodic behaviour. The experimental results showed good agreement with theoretical findings obtained from a model which included the effects of both noise and the nonlinear refractive index of the fibre. Several different experimental configurations were implemented in order to explore the significance of external feedback upon the dynamical behaviour of SBS.

For a fibre with weak feedback, The appearance of deterministic behaviour was attributed to the effects of filtering by the weak fibre cavity. If the reflected Stokes signal was greater than the contributions of the noise (spontaneous Brillouin scattering), then the reflected Stokes signal dominated the amplification process giving rise to deterministic behaviour. Increasing the external feedback by using the natural reflectivity of the cleaved fibre ends, revealed several interesting new features in the dynamics which had not been observed before and were all control parameter (pump power) dependent. Distinguishable forms of behaviour such as sustained relaxation oscillations, quasiperiodicity and quasi-d.c. emission were observed and agreed qualitatively with previous findings by other authors. However, in the quasiperiodic region of operation chaotic Stokes emission was observed for the first time. Upon leaving the chaotic region the dynamics became periodic i.e. sustained relaxation oscillations, with a lower period T_R. Analysis of the chaotic behaviour in region III revealed strange attractor which had a dimension of ~2.1. Both experimental results and theoretical findings showed good qualitative and quantitative agreement. The final experimental configuration demonstrated the effect of using a variable reflectivity for a fixed pump power. At low

reflectivity's the dynamics were aperiodic and stochastic, similar to the weak cavity case with low pump power. Increasing the reflectivity revealed periodic, quasiperiodic and finally quasi-d.c. behaviour at the highest pump power. These features also agreed with theoretical findings and confirmed the importance of both SPM and XPM terms for promoting rich dynamical behaviour.

4.6 References

[1] E.P.Ippen and R.H.Stolen, "Stimulated Brillouin Scattering in Optical Fibres", Appl. Phys. Lett. Vol.**21**(11), pp.539-540, (1972).

[2] I.Bar-Joseph, A.A.Frieseman, E.Lichtman and R.G.Waarts, "Steady and Relaxation oscillations of stimulated Brilluoin scattering in single-mode optical fibres", J. Opt. Soc. Am. B/Vol.**2**(10), pp.1606-1611, (1985).

[3] R.W.Boyd, *Nonlinear Optics,* (Academic press, INC., Boston, 1992).

[4] A.B.Grudinin, E.M.Dianov, D.V.Korobkin, A.M.Prokhorov, V.N.Serkin and D.V.Khaidarov, JETP Lett. Vol.**46**, pp.221-, (1987).

[5] W.Lu, A.Johnstone and R.G.Harrison, "Deterministic dynamics of stimulated scattering phenomena with external feedback", Phys. Rev. A Vol.**46**(7), pp.4114-4122, (1992).

[6] W.Lu and R.G.Harrison, "Nonlinear dynamical and chaotic features in stimulated scattering phenomena", Europhys. Lett. Vol.**16**(7), pp.655-660, (1991).

[7] A.Johnstone, W.Lu, J.S.Uppal and R.G.Harrison, "Sustained and bursting oscillations in stimulated Brilluoin scattering with external feedback in optical fibre", Optics. Comm. Vol.**81**(3,4), pp.222-224, (1991).

[8] Dejin Yu, "Deterministic Dynamics and Noise of Stimulated Light Scattering in Optical Fibres", Phd Thesis, Heriot-Watt University, 1994 (unpublished).

[9] D.Yu and R.G.Harrison, Technical Digest in EQEC'94, (Amsterdam, The Netherlands, 1994).

[10] M.Born and E.Wolf, *Principles of Optics*, 5th edition, Pergamon Press (1975).

[11] Private communication with York Fibres Ltd., for a SM1000 optical fibre.

[12] E.Picholle, C.Montes, C.Leycuras, O.Legrand and J.Botineau, "Observation of Dissipative Superluminous Solitons in a Brillouin Fibre Laser", Phys. Rev. Lett. Vol.66(11), pp.1454-57, (1991).

[13] K.O.Hill, D.C.Johnson, and B.S.Kawasaki, "cw generation of multiple Stokes and anti-Stokes Brillouin-Shifted frequencies", Appl. Phys. Lett. Vol.29(3), pp.185-87, (1976).

[14] K.O.Hill, D.C.Johnson, B.S.Kawasaki and R.I.MacDonald, "cw three-wave mixing in single-mode fibres", Jou. Appl. Phys. Vol.49(10), pp.5098-106, (1978).

[15] P.Labudde, P.Anlinker and H.P.Weber, "Transmission of narrow band high power laser radiation through optical fibres", Optic. Commun. Vol.32(3), pp.385-90, (1980).

[16] P.Grassberger and I.Procaccia, Phys. Rev. Lett. Vol.50, pp.346-, (1983).

[17] D.Ruelle and F.Takens, Commun. Math. Phys. Vol.20, p167 (1971) and S.Newhouse, D.Ruelle and F.Takens, Commun. Math. Phys. 64, p35 (1978).

[18] R.G.Harrison, P.M.Ripley and W.Lu, "Observation and characterisation of deterministic chaos in stimulated Brillouin scattering with weak feedback", Phys. Rev.A Vol.49(1), pp.R24-27, (1994).

[19] M.Dammig, G.Zinner, F. Mitschke and H.Welling, "Stimulated Brillouin scattering in fibres with and without external feedback", Phys. Rev.A Vol.48(4), pp.3301-09, (1993).

[20] D.Yu, W.Lu and R.G.Harrison, "Physical origin of dynamical stimulated Brillouin scattering in optical fibres with feedback", Phys. Rev.A Vol.**51**(1), pp.669-74, (1995).

[21] A.L.Gaeta and R.W.Boyd, J. Nonlinear Opt.Phys., Vol.1, pp.581, (1992).

[22] S.R.Nagel, J.B.MacChesney and K.L.Walker, *Optical Fibre Communications*, (Academic Press, 1985).

[23] L.J.Poyntz-Wright, M.E.Fermann and P.st.J.Russell, "Nonlinear transmission and colour centre dynamics in germano-silicate fibres at 420-540 nm",Opt.Lett., Vol.13(11), pp.1023-25, (1988).

[24] V.Mizrahi, S.LaRochelle and G.I.Stegeman, "Physic of photosensetive-grating formation in optical fibres", Phys.Rev.A., Vol.43(1), pp.433-38, (1991).

5. Dynamical Behaviour of a Driven SBS Oscillator

5.1 Introduction

The driven nonlinear oscillator is of fundamental importance in numerous nonlinear dynamical systems ranging from physics, electronics, chemistry, biology, pathology and many other diverse disciplines. The simple experimental implementation and theoretical description of a driven nonlinear oscillator combine to provide a valuable tool for the investigation of both bifurcation theory, and the universality laws of nonlinear dynamics [1] and chaos, e.g. scaling laws associated with the routes to chaos [2]. In chapter 4 the emission of an SBS oscillator consisting of a first-order Stokes wave generated in an optical fibre with natural feedback, was found to exhibit deterministic behaviour which depended upon the incident pump intensity (control parameter). To provide a driven nonlinear oscillator an acousto-optic modulator (AOM) is incorporated into the experimental pumping arrangement, (with the appropriate modifications), to modulate the pump intensity. In the following chapter the dynamical behaviour of a periodically driven SBS oscillator is investigated experimentally with and without external feedback. A brief comparison is made with theoretical findings with particular emphasis placed upon the route to chaos and the characterisation of the attractor.

5.2 The Driven SBS Oscillator

The model used to represent the driven SBS oscillator is based upon the theoretical description outlined in chapter 4, section 4.1. The stimulated Brillouin scattering process in an externally bounded system involves a four wave interaction in a spatially extended medium i.e. optical fibre. The four waves, illustrated in figure 4.1, are the incident pump wave E_P, the counter-propagating Stokes wave E_S, an acoustic wave A and the co-propagating reflected Stokes wave E'_S. The equations for the SBS process are given below in normalised form, and include terms to account for the spontaneous noise initiation and the effects of nonlinear refraction, i.e. SPM and XPM from four-wave mixing [3].

$$\frac{\partial E_P}{\partial \eta} + \frac{\partial E_P}{\partial \xi} + \frac{1}{2}\beta E_P = -gE_S A + iu\left[|E_P|^2 + 2|E_S|^2\right]E_P$$

$$\frac{\partial E_S}{\partial \eta} - \frac{\partial E_S}{\partial \xi} + \frac{1}{2}\beta E_S = gE_P A^* + iu\left[|E_S|^2 + 2|E_P|^2\right]E_S$$

$$\frac{1}{\beta_A}\frac{\partial A}{\partial \eta} + A = E_P E_S^* + f(\eta,\xi)$$

$$\frac{\partial E'_S}{\partial \eta} + \frac{\partial E'_S}{\partial \xi} + \frac{1}{2}\beta E'_S = 2iu\left[|E_P|^2 + |E_S|^2\right]E'_S$$

The normalised time and space co-ordinates are $\eta = t / T_R$ and $\xi = z / L$, where T_R is the transit time of the light waves in the fibre of length L, ($T_R = nL / c$). The normalised power loss of the light waves in the fibre is given by $\beta = \alpha L$ and the relaxation rate of the acoustic waves in the medium is represented by the expression $\beta_A = \pi \Delta\nu_B T_R$, where α and $\Delta\nu_B$ are the loss coefficient of the fibre and the spontaneous Brillouin linewidth

respectively. A Langevin noise term $f(\eta,\xi)$ is included in the acoustic wave equation to account for spontaneous Brillouin scattering [4], which is attributed to the random thermal fluctuations in the density of the medium. For the case of weak external feedback ($R_1R_2 << 1$) the boundary conditions are simplified to

$$E'_S, E_S(\eta,\xi=0) = \sqrt{R}_1 E_S(\eta,\xi=0)$$

$$E_S(\eta,\xi=1) = \sqrt{R}_2 E'_S, E_S(\eta,\xi=1)$$

where the reflectivities of the fibre entrance and exit are R_1 and R_2. For the driven SBS oscillator the incident pump wave E_P is modified by the following relationship.

$$E_P(z=0) = \sqrt{I_P}$$

The modulated intensity of the incident pump I_P is given by the expression below and

$$I_P = I_0\left(1 - a_m \sin^2(\omega t/2)\right)$$

incorporates both the amplitude (a_m), and frequency of modulation (ω) with the incident pump upon the AOM represented by I_0. The inclusion of the AOM to modulate the pump intensity provides two additional degrees of freedom for the original SBS oscillator. Comparison of this system with another non-autonomous system, such as the driven van der Pol oscillator [5] which has been studied extensively, reveals a significant difference. The driven van der Pol oscillator is described by a set of ordinary differential equations which contain a driving term. The driven SBS oscillator presented here, is a spatially extended system described by a set of partial differential equations and is driven through the boundary condition. In the next section the AOM is characterised prior to experimental studies and the modification of the pumping arrangement to allow the incorporation of the AOM device is also discussed.

5.2.1 Experimental Arrangement

In an acousto-optic modulator (AOM) the principle physical mechanism responsible for the operation of the device is the scattering of light waves from acoustic waves. The propagation of an acoustic wave through a medium induces mechanical strains, which via the photoelastic effect produces a change in the refractive index of the medium. The general relationship between the change in the refractive index upon the application of a mechanical strain will not be discussed here. However, a simple case will be presented which will permit an understanding of the acoustic-optic effect and in particular its role in the modulation of a light beam. An illustration outlining the mechanism of acousto-optic modulation is shown in Figure 5.1.

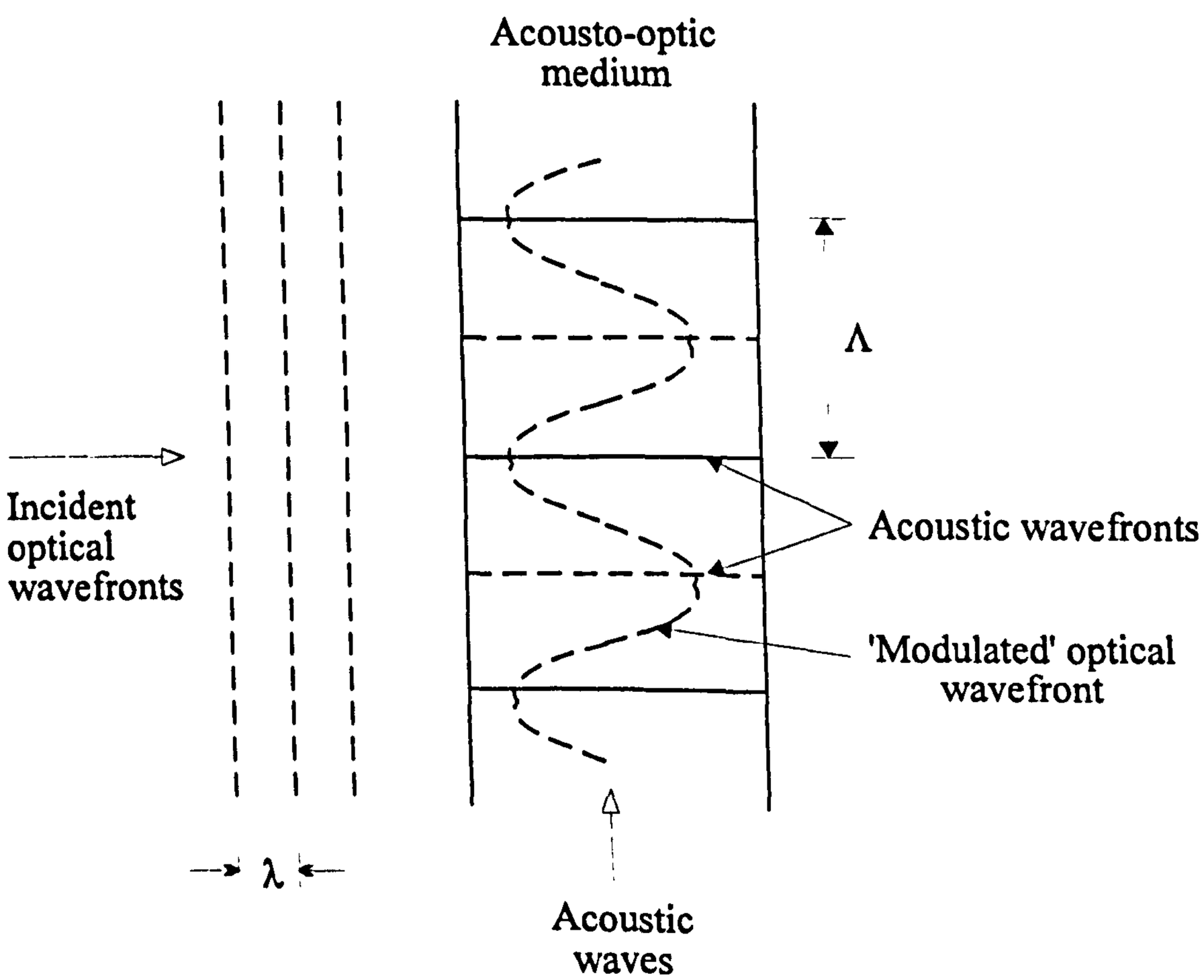

Figure 5.1 Schematic illustration outlining the principle mechanism of acousto-optic modulation

In the schematic diagram above a monochromatic light wave, of wavelength λ, is incident upon a medium in which an acoustic wave has produced, via the photoelastic effect, a sinusoidal variation in the refractive index. The wavelength of the variation in the refractive index depends upon the wavelength of the acoustic wave, Λ. The peaks and troughs of the acoustic wave generate corresponding pressure maximas (solid horizontal lines) and minimas (dashed horizontal lines) in the refractive index of the medium. As the light propagates through the medium it encounters the higher refractive index associated with the pressure maxima, and will travel at a lower velocity than the light travelling through the region which contains the pressure minima. The optical wavefront therefore acquires a sinusoidal modulation as it traverses the medium. The velocity of the acoustic wave in the medium (in the region of 10^4 ms^{-1}) is significantly less than the velocity of the optical wave ($10^8 ms^{-1}$), and therefore the variation in the refractive index appears stationary to the incident optical wavefront. As the components of the optical wavefronts propagate in a direction normal to the acoustic wavefronts in the medium, extensive re-distribution of the light flux will occur with higher concentrations occurring at the regions of higher refractive index. The overall effect of the acoustic wave is to create a diffraction grating within the medium. Therefore, the incident light will be spatially modulated by the temporal variation in the acoustic wave i.e. diffraction grating.

There exists two types of acousto-optic modulation devices. The device type depends upon the extent of diffraction within the device. A Raman-Nath modulator presents a "thin" diffraction grating to the incident beam, and the light does not undergo any further redistribution as it leaves the modulator producing a temporal variation in the irradiance of the beam. The second type of device, a Bragg modulator (which is of

interest here), consists of a "thick" diffraction grating which extensively re-diffracts the beam before it leaves the acoustic field creating distinct diffraction orders with modulated intensity. Figure 5.2, illustrates the geometry for Bragg acousto-optic modulation. For a plane wavefront incident normal to the grating plane at an angle of incidence θ_i, Figure 5.2(a), only light will emerge from those particular directions where constructive interference occurs. Two conditions must be satisfied for constructive interference to take place.

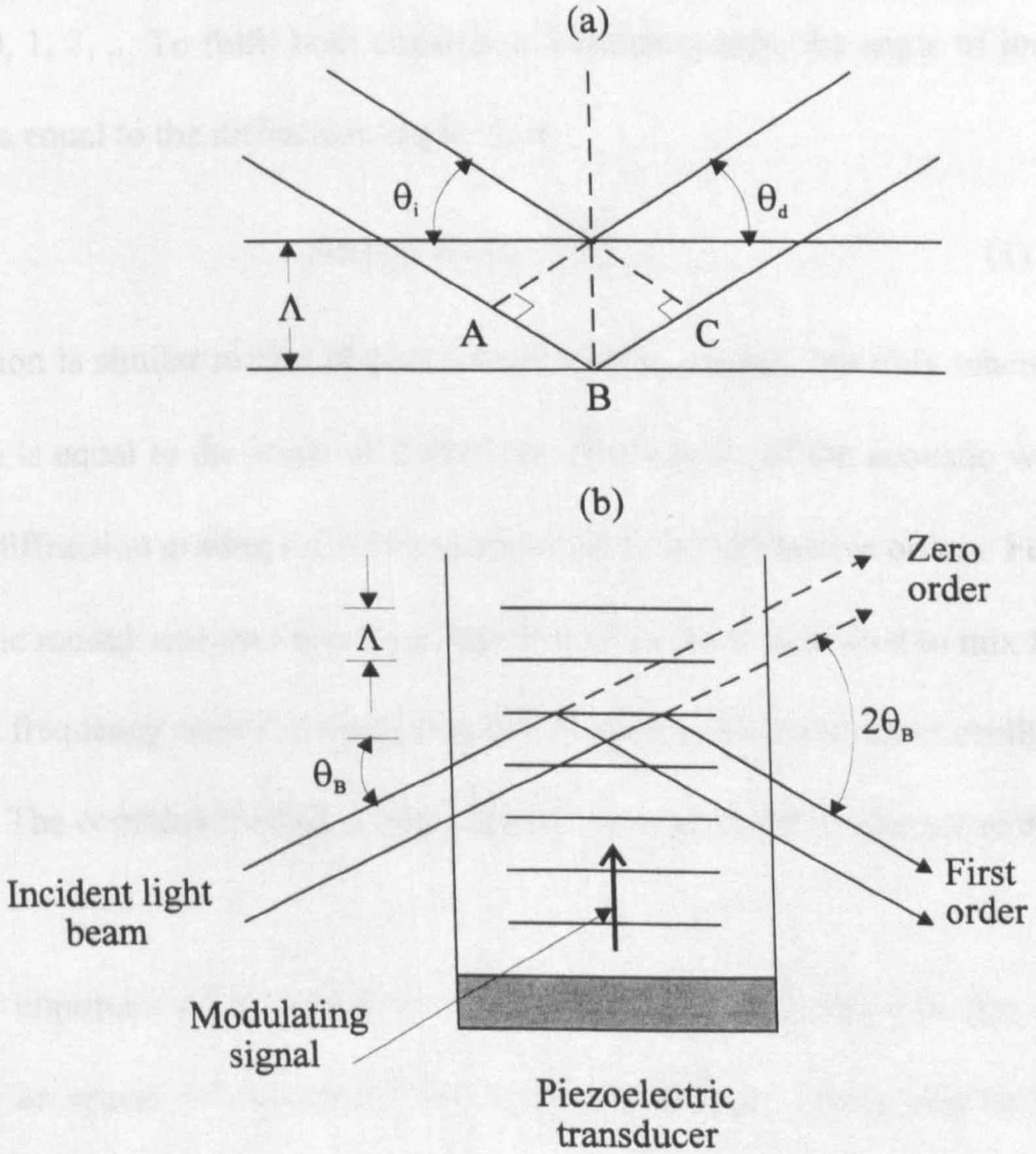

Figure 5.2 Diagram illustrating the geometry for Bragg acousto-optic modulation: (a) for constructive interference the path difference AB + BC must equal an integral number of wavelengths, and (b) the amount of light "reflected" into the first order is proportional to the amplitude of the modulating signal.

The conditions are, (i) light scattered from a grating plane must arrive in phase at the new wavefront, and (ii) light scattered from successive grating planes must also arrive in phase at the new wavefront. The first condition is easily satisfied if the angle of diffraction is equal to the angle of incidence, i.e. $\theta_d = \theta_i$. The significance of the second condition is to imply that the path difference between successive wave fronts is equal to an integral number of wavelengths, and requires the following relationship

$$\sin\theta_i + \sin\theta_d = \frac{m\lambda}{\Lambda}$$

where m = 0, 1, 2, ... To fulfil both conditions simultaneously, the angle of incidence is allowed to be equal to the diffraction angle, thus

$$\sin\theta_i = \sin\theta_d = \frac{m\lambda}{2\Lambda}. \qquad (1)$$

The diffraction is similar to that obtained from a plane grating, but only when the angle of incidence is equal to the angle of diffraction. Modulation of the acoustic wave which creates the diffraction grating induces a modulation in the diffractive orders. For efficient acousto-optic modulation an impedance matched drive module is used to mix the desired modulation frequency with the acoustic wave frequency, (a fixed local oscillator in the drive unit). The combined signal is then applied to a transducer in contact with the AOM crystal.

An important characteristic of an acousto-optic modulator is the modulation bandwidth or speed of operation. The bandwidth of the device depends upon the minimum time required for an acoustic wave to propagate across the optical beam, i.e. the time taken for the beam to be switched from zero diffraction to the first order. The minimum transit time is simply $t_{min} = 2w / v_A$, where 2w is the diameter of the beam and

v_A is the velocity of the acoustic wave. In order to utilise the AOM device in a driven SBS oscillator experiment, it is imperative that the operational bandwidth of the device can adequately cover the frequency region of interest. From chapter 4 (section 4.3.2), the full bandwidth of the SBS oscillator i.e. optical fibre with natural feedback, was found to be dependent upon the type of dynamical behaviour. The bandwidth of the chaotic power spectrum was found to be approximately 5MHz ($3T_R$). To determine the bandwidth of the AOM (Isle Optics Ltd. model LM080) to be used in the experiment, the period of the grating or acoustic wavelength must be found first in order to calculate the acoustic velocity.

The diffraction angle θ_d was calculated by measuring the displacement between the first and zero order over a fixed distance d. For a fixed distance of 285mm from the AOM exit to a screen, the displacement between the first and zero order was measured to be 3.7mm. For these values the diffraction angle was $\theta_d = 0.74°$. The period of the grating was calculated from equation (1) and found to be 42μm, (recalling that the wavelength of the light was 1.064μm and m = 1 for the first order). A value for the velocity of the acoustic wave could then be estimated from the relationship $v_A = f\Lambda$, where f is the frequency of the acoustic wave. From the manufacturer's specifications [6] the acoustic frequency or "carrier" frequency was found to be 80MHz, producing an acoustic velocity of $3360ms^{-1}$. The theoretically predicted bandwidth of the AOM for a laser beam of diameter 2.5mm was found to be ($1/t_{min} = v_A/2w$) 1.34MHz. For comparison the bandwidth of the AOM device was determined experimentally using a low power beam (10mW), and the results are displayed in Figure 5.3. In the experiment

the diffraction efficiency of the AOM is monitored as a function of the modulation frequency. The diffraction efficiency was determined from the following relationship,

$$\eta(\%) = \frac{I_1(ac)}{I_0(dc)}$$

where $I_1(ac)$ represents the optical power diffracted into the first order when the modulating ac signal is applied, and $I_0(dc)$ is the power transmitted through the device (zero order) when there is no applied signal to the AOM crystal. The AOM was found to operate with a constant diffraction efficiency of 35% for a beam of diameter 2.5mm over a frequency range of 5 - 450kHz. However, the diffraction efficiency of the device started to fall dramatically at a frequency of 500kHz, Figure 5.3 with a 3dB point (half power) occurring at approximately 1.5MHz. The measured bandwidth of 500kHz is significantly less than the predicted value of 1.34MHz. Clearly, the AOM device is under performing indicating that the relatively large beam diameter is unsuitable. The bandwidth of the AOM is inversely proportional to the beam diameter. Therefore, to reduce the beam diameter a 15cm convex lens was used to bring the beam to a focus in the AOM device. The bandwidth of the AOM was then measured again and the results are displayed in Figure 5.3. Inspection of the graph in Figure 5.3 reveals a considerable improvement in the operational performance of the AOM device. Primarily, the modulation bandwidth of the device has increased to a frequency of 5.5MHz with the 3dB point occurring at 8.3MHz. Secondly, the diffraction efficiency of the device has increased from 35% to 40% indicating that more of the optical power is concentrated within the active region of the AOM. With the inclusion of a lens to reduce the beam diameter the AOM device was found to be suitable for implementation into the driven SBS oscillator experiment. The

increase in the bandwidth to 5.5MHz is larger than the minimum requirement of 1.68MHz.

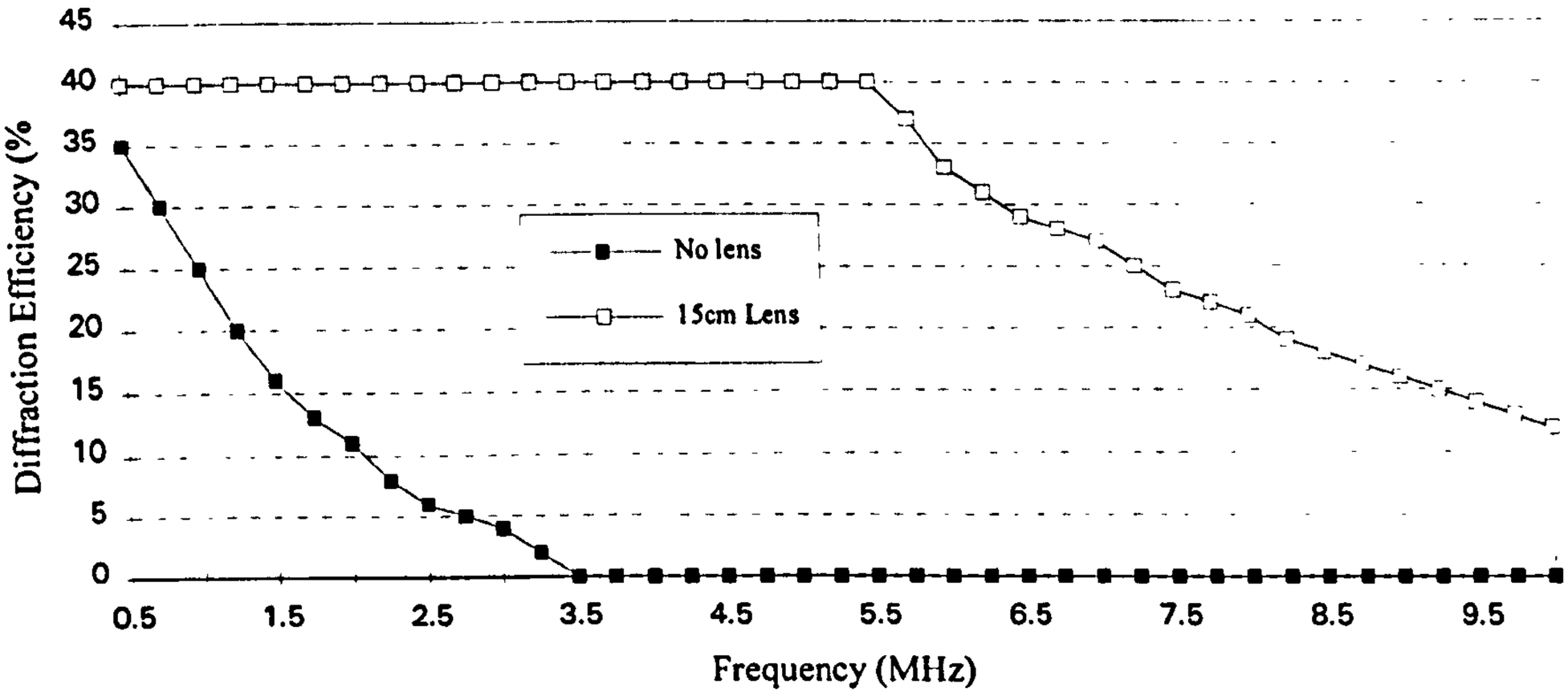

Figure 5.3 Experimental measurement of the bandwidth of the AOM device for a beam of diameter 2.5mm (no lens) and a focused beam of diameter 0.4mm (15cm lens).

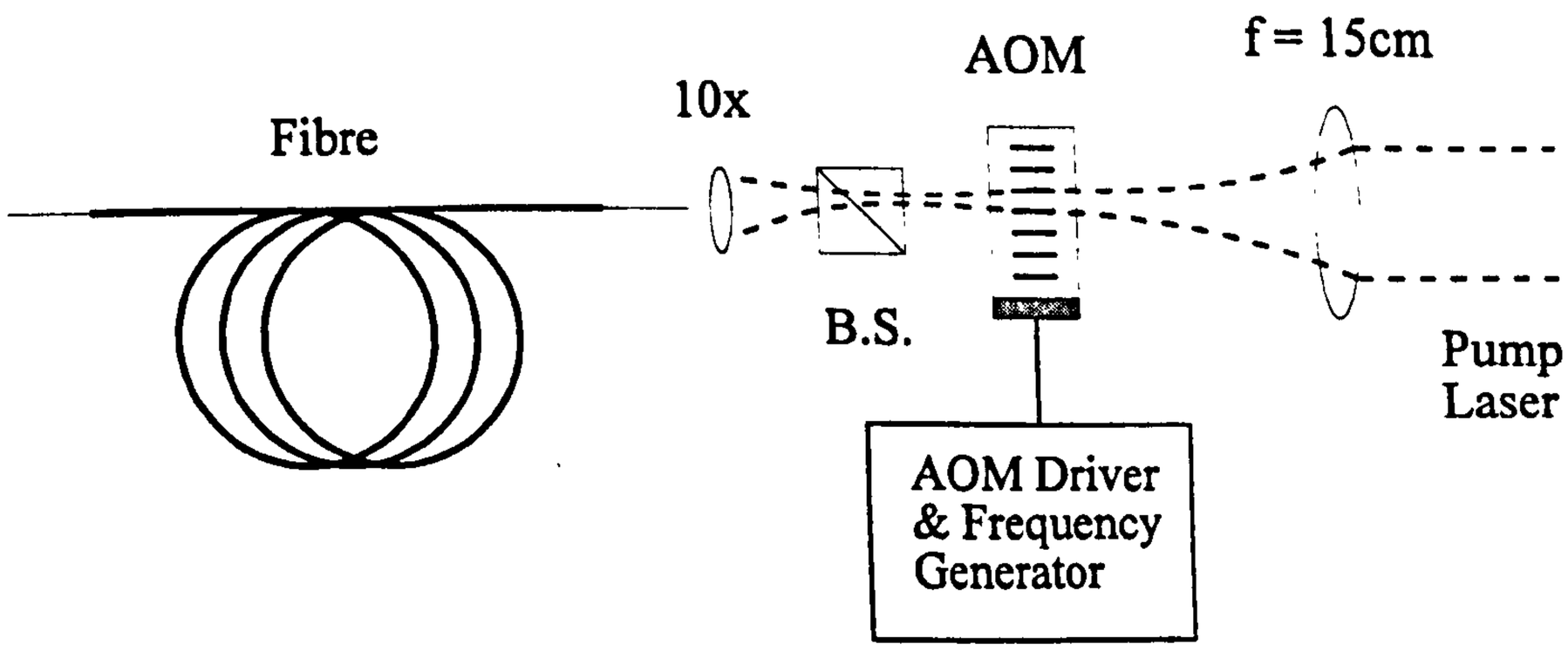

Figure 5.4 Modified experimental pumping arrangement showing the inclusion of the AOM device and the focusing element crucial for obtaining the high operational bandwidth.

The pumping arrangement described in detail in chapter 3 (section 3.2), which was used for the experimental investigation of the dynamical behaviour of SBS generated in an optical fibre, had to be modified to permit the inclusion of the AOM device and the focusing element. The new pumping configuration is illustrated in Figure 5.4. After the laser beam emerges from the beam splitter (BS), Figure 5.5, a convex lens (focal length 15cm) is used to gather the light and bring it to a focus inside the AOM device. The light that propagates directly through the AOM crystal is then launched into a single-mode, non-polarisation preserving fibre via a 10× microscope objective. A lens with a focal length of 15cm was selected because it brought the beam to a relatively "gentle" focus. Calculation of the Rayleigh length ($L_R \sim \pi w^2/\lambda$) for the 15cm lens was found to be 100mm, therefore the beam width was approximately constant over the crystal length (10mm).

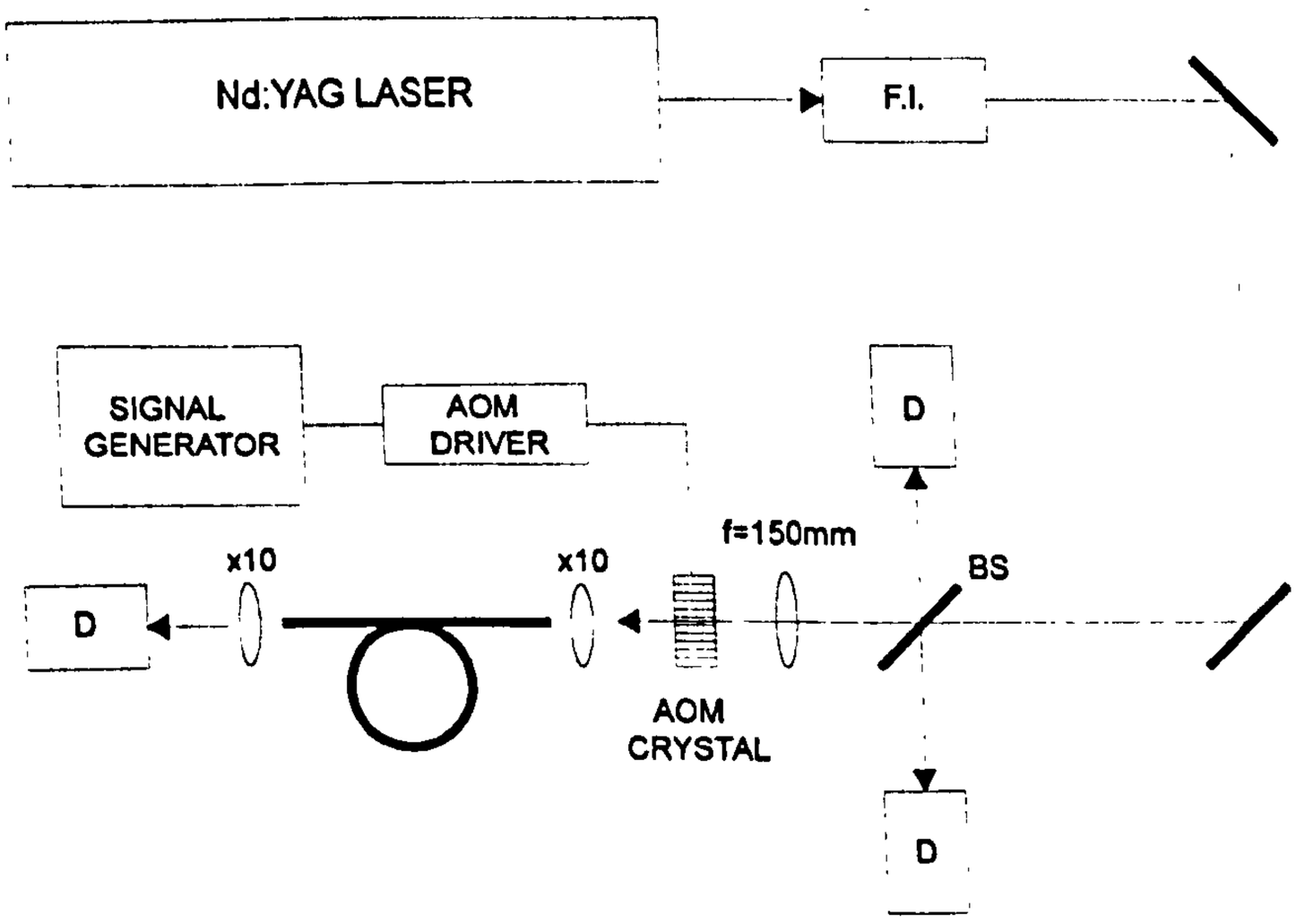

Figure 5.5 Experimental set-up used to investigate the dynamical behaviour of the driven SBS oscillator.

Application of the modulation signal produces a zero and first order beam. The light diffracted into the first order is completely out of alignment with the microscope objective and fibre launching conditions. Only the zero order beam is coupled into the fibre. Therefore, in this configuration the AOM device is acting as an "acousto-optic beam deflector", with power being deflected from the zero order into the first order beam thus providing a modulated pump to drive the SBS oscillator.The temporal behaviour of the Stokes emission from the driven SBS oscillator was monitored using the same detection system described in chapter 3 (section 3.3 and 3.3.2), which comprised of a fast silicon photodiode coupled to a cascaded pair of amplifiers (Comlinear CLC100). A frequency generator (Hewlett Packard HP8647A, range 250kHz-1GHz) was used to provide the driving frequency to the AOM driver (Isle optics Ltd. model MD080). The output from the AOM driver was connected via a BNC cable to the AOM device which was attached to an opto-mechanical mount. The opto-mechanical mount had translational movement in the xyz direction and both pitch and yaw. The translational movement was required to ensure that the aperture of the AOM device was located at the focus of the laser beam. The pitch and yaw movement was essential to ensure that the AOM grating was normal to the incident beam in order to provide optimum diffraction efficiency.

5.3 Dynamical Behaviour of a Driven SBS Oscillator

In the following section several aspects of the dynamical behaviour of a driven SBS oscillator will be presented. The time averaged output characteristics of the driven SBS oscillator are observed for varying depths of modulation. The temporal behaviour of

the oscillator is then examined with and without the presence of external feedback. Finally, the dynamics observed for the case of external feedback are analysed and compared with theoretical findings obtained from the model described in section 5.2.

5.3.1 Time averaged (Steady State) Behaviour of a driven SBS oscillator

The temporal behaviour of the Stokes emission from the driven SBS oscillator displayed fluctuations in the intensity which persisted before the onset of threshold through to the higher pump powers (800mW). The intensity variations below threshold are attributed to a combination of the spontaneous scattering process and the Fabry-Perot effects of the fibre cavity. Above threshold the stimulated scattering process contains rich forms of deterministic dynamical behaviour. To find the steady state behaviour of the driven SBS oscillator the same procedure implemented in chapters 3 and 4 was used. The relatively fast dynamical behaviour of both the Stokes and transmitted pump intensities (μs) was averaged using a pyroelectric power meter with a slow response time (ms). The time averaged intensities of both the Stokes and transmitted pump signals are shown in Figure 5.6. The solid black lines represent the averaged temporal output without modulation. The dashed lines indicate both the Stokes and transmitted pump intensities generated for various modulation depths with the frequency kept constant ($1/2T_R$ = 870kHz). The modulation depth was varied initially from 5% to 40% in 5% incremental steps to allow the performance of the AOM crystal to be assessed in the presence of the high optical powers required for pumping. The upper operating limit of the AOM device was found to be 25%. Operation above this limit would lead to damage of the AOM crystal through a combination of local heating by the focused laser beam and global

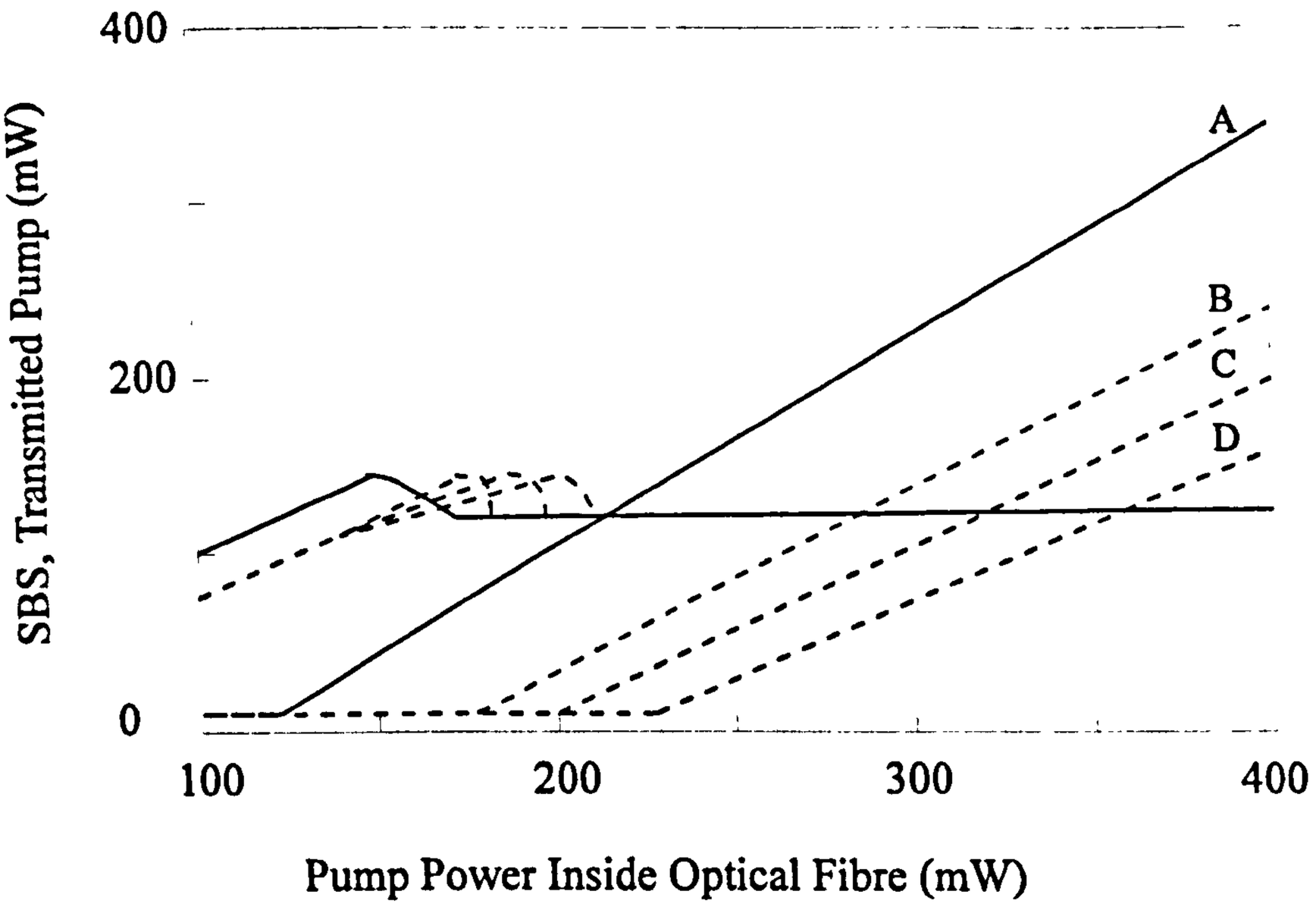

Figure 5.6 The output response of the driven SBS oscillator, (optical fibre with external feedback), showing both the transmitted pump and Stokes emission; without modulation (A) and with modulation, (B) 15%, (C) 20%, and (D) 25%.

heating generated by an increase in the R.F. power from the drive unit. Close inspection of the graph reveals new features which appear as a direct consequence of modulation. The curves become displaced upon increasing modulation depth which is attributed to the reduction of the time averaged pump power. The intensity of the Stokes emission is linear for an increase in pump intensity. The decrease in the gradient of the Stokes emission curves for increasing modulation depth is caused by the reduced energy conversion efficiency of the SBS process. This is also responsible for the more pronounced "shoulder effect" on the corresponding plots of the transmitted pump signal, compared to that for a pump without modulation, chapter 4,(section 4.3.2).

5.3.2 Dynamical Behaviour of SBS in an open flow system with modulated pump

For comparison with the driven SBS oscillator the dynamical behaviour of SBS generated in an open flow system, i.e. a fibre without external feedback, with a modulated pump was investigated. A single-mode, non-polarisation preserving fibre implemented in previous experiments, (chapters 3 and 4) was used as the Brillouin medium. The ends of the fibre were polished using the same technique outlined in chapter 3 (section 3.3.1) to remove the natural Fresnel reflectivity inherent to the cleaved ends. With no modulation signal applied to the AOM, the light was coupled into the optical fibre via a microscope objective. The input power was increased (400mW) until the onset of strong stimulated scattering (Figure 3.4, chapter 3). The frequency of the drive signal was set at a frequency which corresponded to the round trip time of the fibre, i.e. twice the transit time ($2T_R$). The amplitude of the drive was then applied in order to initiate acousto-optic modulation of the pump beam intensity. The modulation depth was increased from 15% to 25% in 5% intervals while the frequency was kept constant. At each modulation interval the intensity of the Stokes emission was monitored. To compensate for the reduction of average pump intensity through modulation, the peak power was increased until the measured Stokes emission was equal in intensity to that generated without modulation (80mW). By following this procedure the same average pump power was used in the SBS process. The dynamical behaviour of the Stokes emission generated in an open flow system with modulated pump is shown in Figure 5.7. The time series and FFT of the SBS without modulation, Figure 5.7(a) display random spiking on time scales faster than the round trip time. These characteristics are identical to the results obtained in chapter 3 (section 3.5.1). The application of modulation reveals

two new features in both the times series and the frequency spectrum, Figures 5.7(c) to (h). The intensity of the Stokes emission consists of fast irregular peaks superimposed upon a weak slow modulation with a period of $2T_R$, Figure 5.7(c). As the depth of modulation is increased the slow modulation becomes more predominant with a clearly visible periodicity, Figure 5.7(g). The frequency spectrum of the Stokes emission remains broadband throughout the variation of the modulation depth. The only significant change in the frequency spectrum is the appearance of a peak ($1/2T_R$) corresponding to the drive frequency, which increases in amplitude with modulation. Varying the frequency of the drive while keeping the depth of modulation constant presented no significant transformation in the dynamical behaviour of the system. The period of modulation in the Stokes intensity depended directly upon the drive frequency. The Fourier spectrum always remained broadband with a peak representing the applied signal. The same temporal response was observed for different pump power levels. This provided strong evidence that modulation of the pump intensity created modulation in the Stokes emission. However, the relatively fast (5-100ns) stochastic signal associated with SBS generated without feedback [7], was always present throughout the experiment. Apart from the dynamical behaviour attributable to the operation of the AOM device, no new dynamical features were observed.

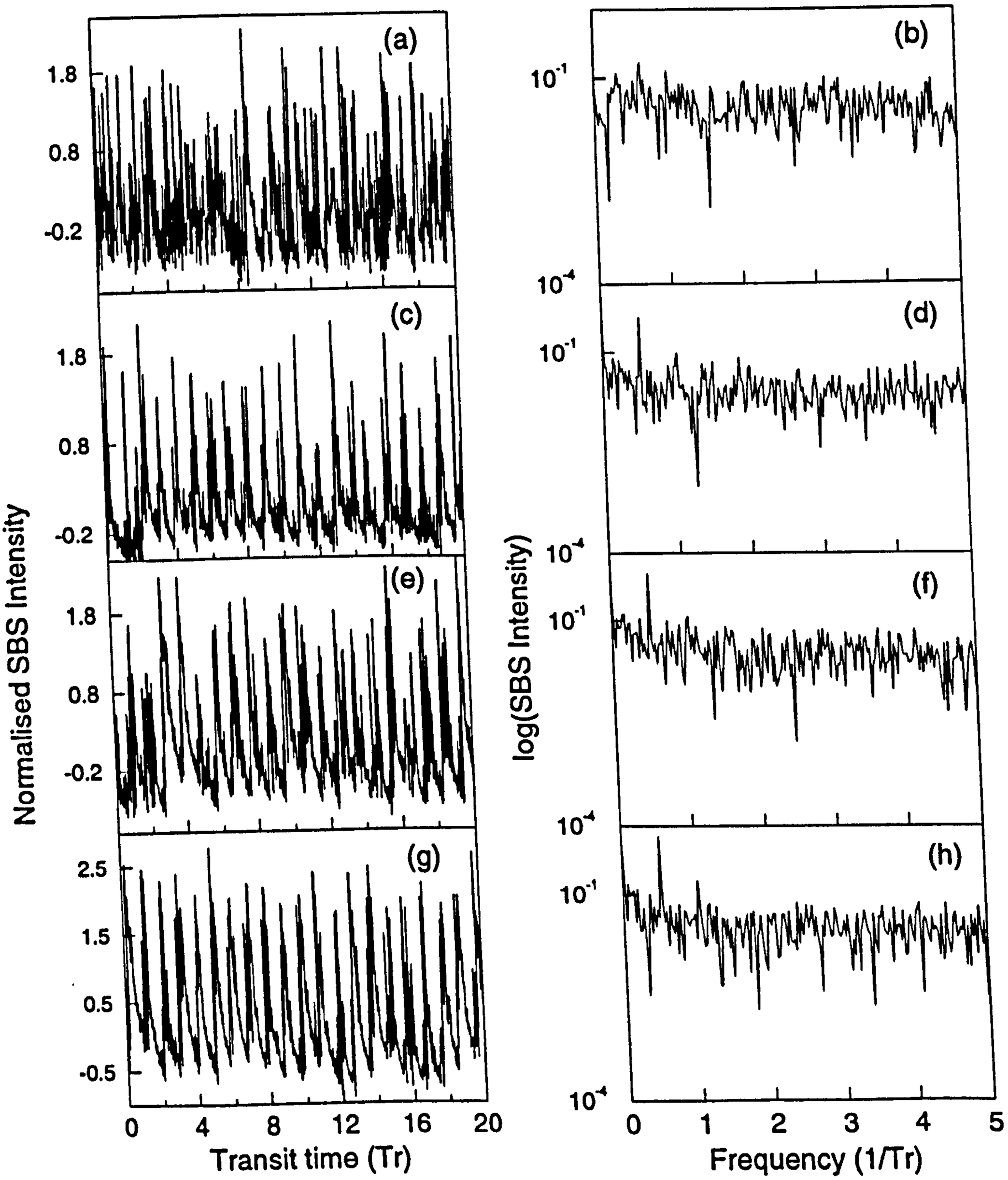

Figure 5.7 Experimental time series (left column) and power spectra (right column) illustrating the dynamical behaviour of SBS in an open flow system with a modulated pump. (a-b) no modulation, (c-d) 15%, (e-f) 20% and (g-h) 25% modulation.

5.3.3 Dynamical behaviour of the driven SBS Oscillator

The inclusion of external feedback in the form of natural Fresnel reflectivity suppresses the noise associated with spontaneous Brillouin scattering which initiates the stimulated Brillouin scattering process. The filtering of the spontaneous noise by the fibre cavity allows for the production of deterministic features [8]. At relatively low pump levels (250 - 350mW) the most notable form of deterministic behaviour are the sustained relaxation oscillations whose period depends upon the length of the fibre. The length of the fibre (124m) used in the experiment produces oscillations with a period of 1.21μs ($2T_R$), frequency 870kHz ($1/2T_R$). This allows the AOM to be operated in a regime with sufficient available bandwidth for modulation of the pump intensity over a range of appropriate frequencies for the system i.e. harmonics and sub-harmonics [9] of the fundamental frequency. Modulating the SBS oscillator in the periodic region ensures that any new dynamical behaviour will arise directly from the modulation of the pump intensity. Also, operating the AOM device with relative low power levels will prevent optical damage occurring inside the AOM crystal. The ends of the fibre were cleaved to provide a reflectivity of 3.3% at each end. By fixing the modulation depth and varying the drive frequency the global behaviour of the SBS oscillator was investigated. The drive frequency was varied from 435kHz ($1/4T_R$) to 1.74MHz ($1/T_R$) which corresponded to the sub-harmonic and harmonic of the free spectral range (FSR) of the fibre cavity ($1/2T_R$). The modulation depths of interest were 15, 20 and 25%. A similar experimental technique discussed in the previous section was used to optimise the average pump power. By monitoring the intensity of the Stokes emission when the pump intensity was modulated, the peak power could be increased to retain the same average power. This

was confirmed by fixing the drive frequency to $2T_R$ and inspecting the Stokes emission to ensure that sustained relaxation oscillations were present in the oscillator output. A table displaying the different types of dynamical behaviour observed in the Stokes emission from a driven SBS oscillator, for a fixed modulation depth with swept drive frequency, is illustrated in Figure 5.8.

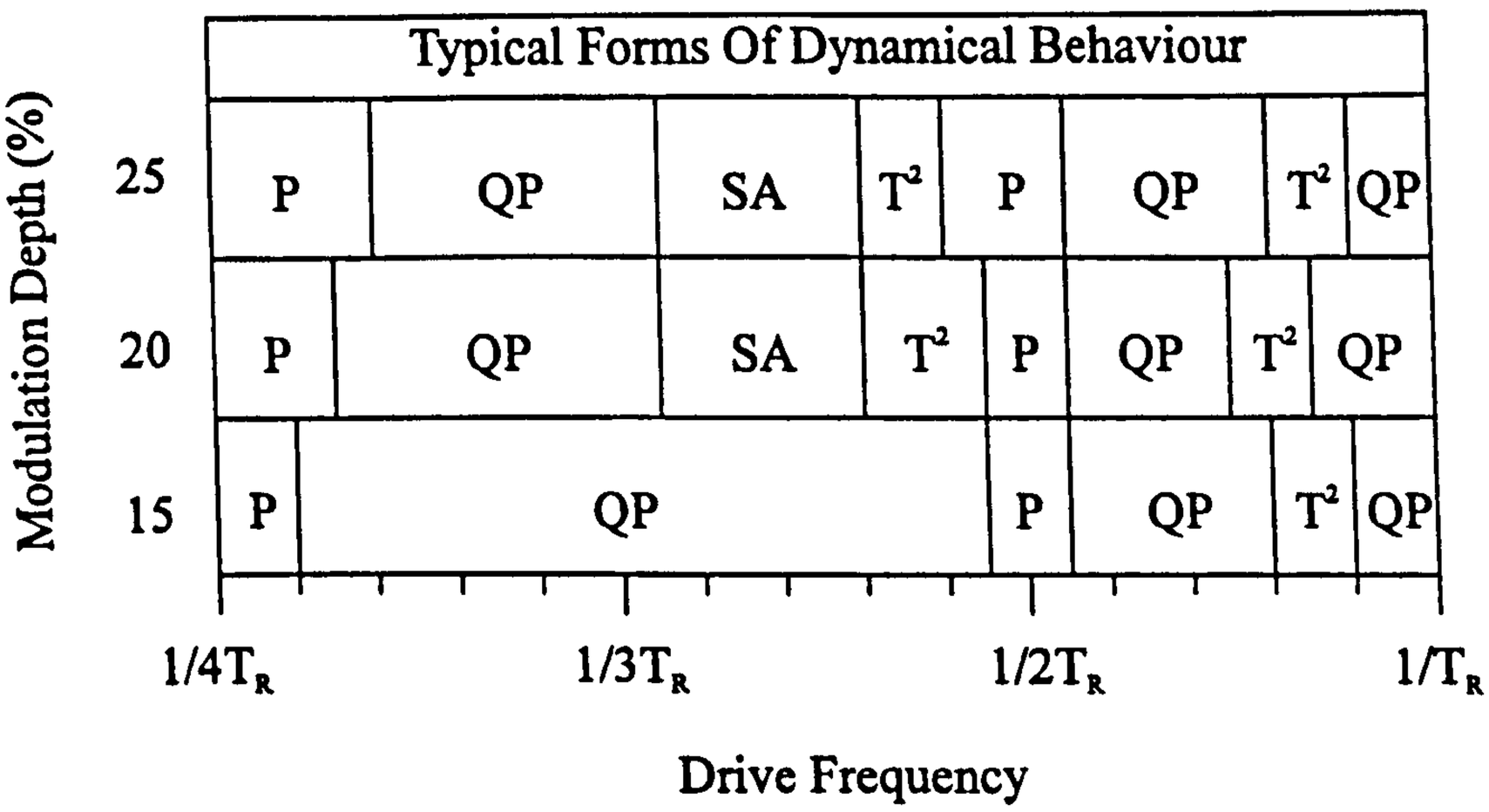

Figure 5.8 Table illustrating the different forms of classifiable dynamical behaviour observed in the Stokes emission for a fixed modulation depth with swept drive frequency. Key to labels: P = periodic, QP = quasiperiodic (beating), T^2 = torus and SA = strange attractor.

Typical examples of the different forms of dynamical behaviour are shown in Figure 5.9 and Figure 5.10. In Figure 5.9(a) periodic sustained relaxation oscillations were observed when the drive frequency of the AOM was located in the vicinity of the fundamental frequency of the oscillator, $1/2T_R$, or the harmonics ($1/4T_R$ and $1/T_R$). The limit cycle reconstructed in phase space confirms the periodic motion of the oscillator output. Inspection of the power spectra reveals peaks occurring at both the fundamental

frequency $1/2T_R$ and the drive frequency $1/4T_R$. When the AOM was operated in other frequency regions, $1/4T_R$ - $1/T_R$, quasiperiodic Stokes emission was found to be common behaviour within which the temporal waveforms were quite diverse. Examples illustrating the two main types of quasiperiodic motion are shown in Figures 5.9(d) and 5.10(a). The first example displays periodic Stokes emission contained within a slowly varying envelope. This form was predominant over a broad range of drive frequencies and occurred at each modulation depth. The low frequency component responsible for the enveloping effect was attributed to the beating of the drive frequency with the fundamental (FSR) frequency or its harmonics, Figure 5.9(f). The phase portrait reveals a broadening in the limit cycle structure which arises due to the slow modulating envelope at the beat frequency. The second form of quasiperiodic behaviour existed in frequency regions close to the first harmonic at all modulation depths, and close to the fundamental harmonic for depths of modulation exceeding 15%. This type of motion had a complicated temporal profile, Figure 5.10(a), with the spiralling, toroidal motion becoming apparent in the phase portrait and FFT, Figures 5.10(b) and (c). Chaotic emission was experimentally found to exist in a small domain for both 20, and 25% depths of modulation. The time series appeared random in amplitude and the reconstructed phase portrait revealed the existence of a "strange attractor", Figures 5.10(d) and (e).

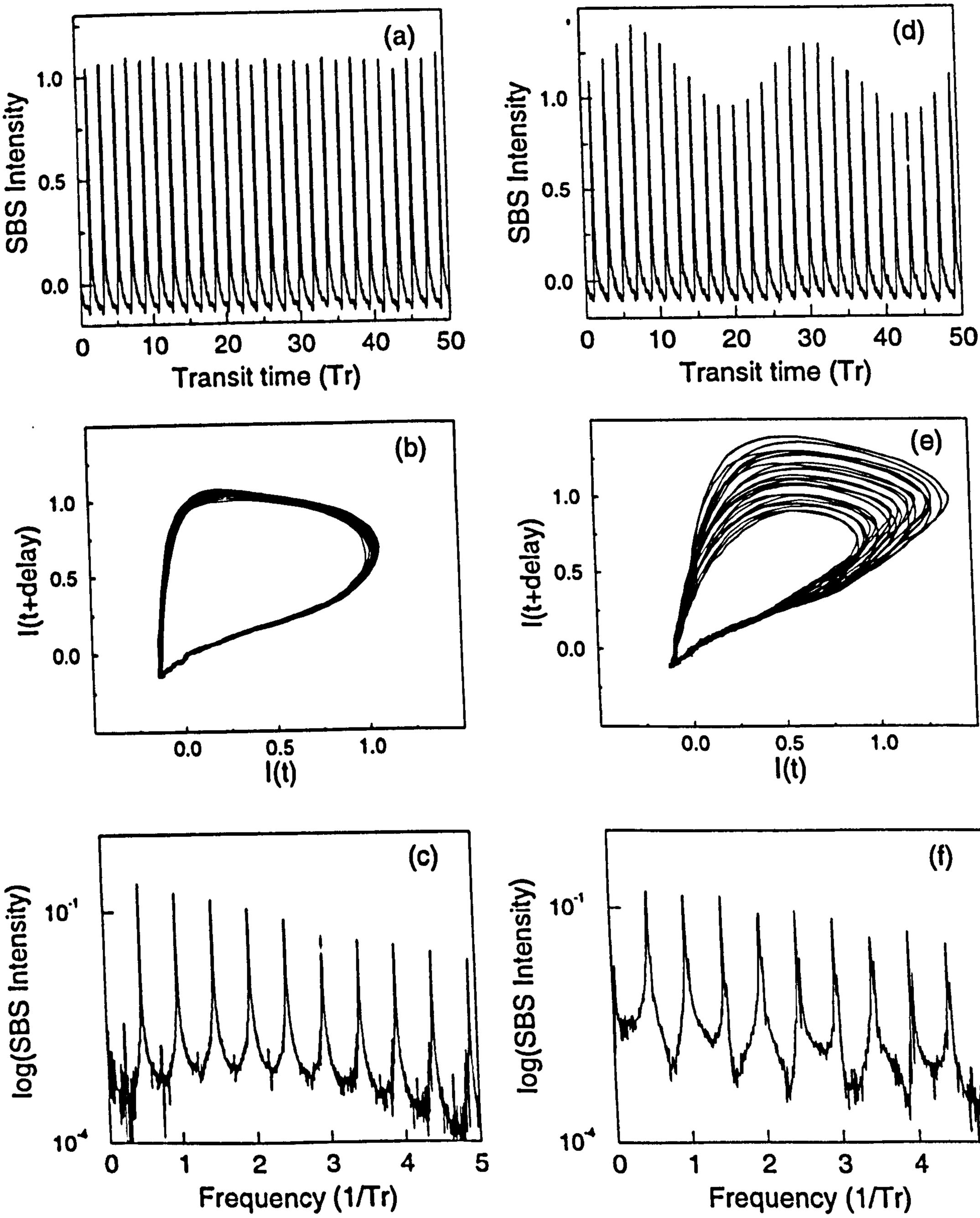

Figure 5.9 Time series (top row), phase portrait (middle row) and Fast Fourier Transform (bottom row) analysis of both periodic (a-c) and quasiperiodic (e-f) emission from a driven SBS oscillator.

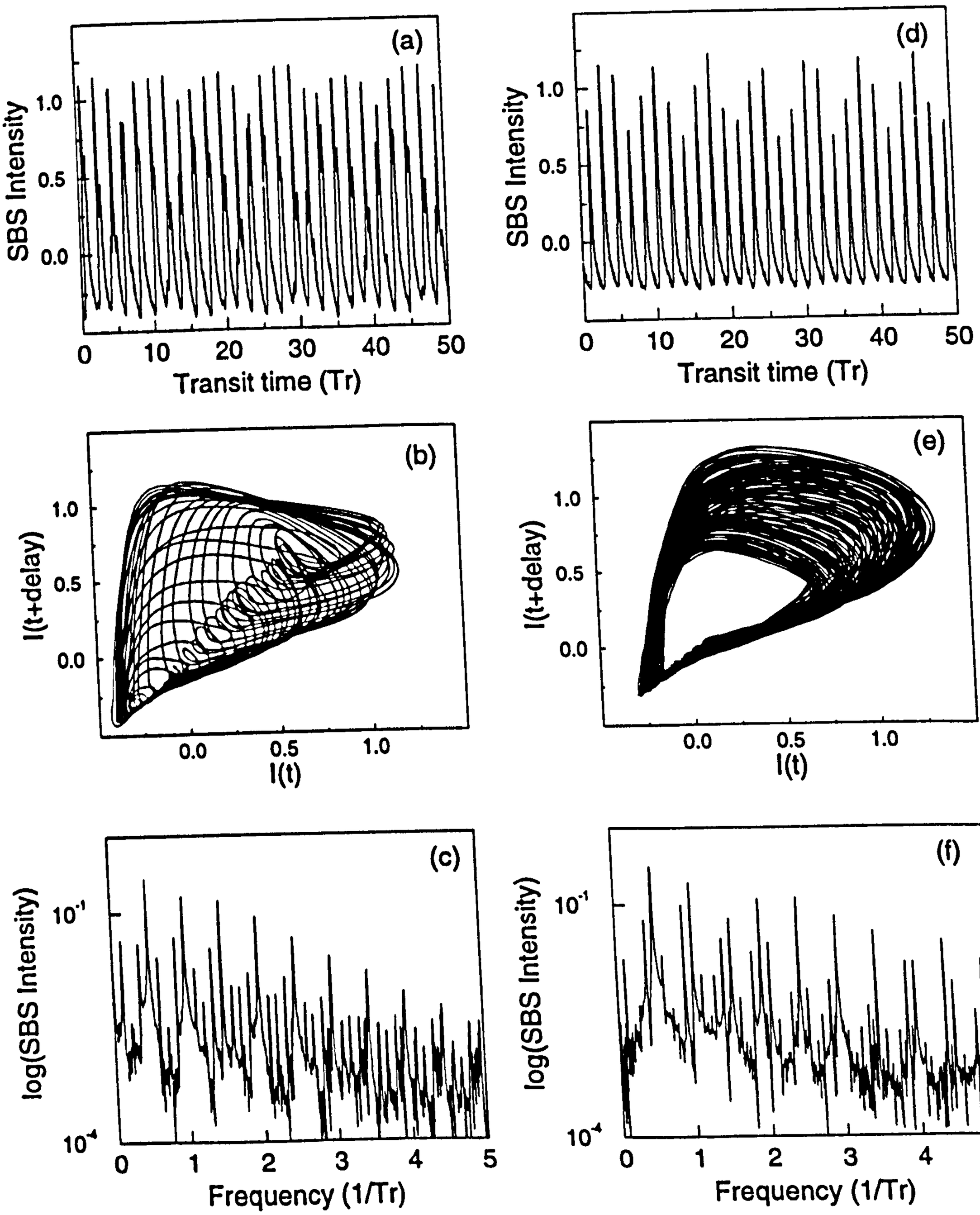

Figure 5.10 Time series (top row), phase portrait (middle row) and Fast Fourier Transform (bottom row) analysis of both toroidal (a-c) and chaotic (e-f) emission from a driven SBS oscillator.

The fast Fourier transform of the chaotic emission showed both complex structure and an almost continuous spectrum, Figure 5.10(f).

5.4 Analysis of Results

In the following section the route to chaos will be examined by utilising the drive frequency and modulation depth as the control parameters. The experimental results will then be compared with theoretical findings found by other members of the same research group. Also correlation dimensional analysis will be applied to both sets of results to provide a quantitative measure of the chaotic state.

5.4.1 Route to Chaos

Initial attempts at trying to identify the route to chaos by fixing the modulation depth of the AOM and varying the drive frequency proved inconclusive. Therefore, the drive frequency was fixed at a setting of 610kHz ($1/2.9T_R$) which corresponded to a domain boundary between quasiperiodic and chaotic behaviour, and the depth of modulation was increased in 1% increments from 0 to 25%. The average pump power was preserved by increasing the peak pump power to compensate for the modulation. The dependence of the dynamical behaviour of the Stokes emission for an increase in the selected control parameter, i.e. modulation depth, is displayed in Figures 5.11 and 5.12. For a modulation of 5% the time series of the Stokes emission is both periodic and stable which is also shown in the phase portrait and FFT, Figure 5.11(a) to (c) respectively. An increase in the modulation to 10% transforms the emission to a quasiperiodic signal.

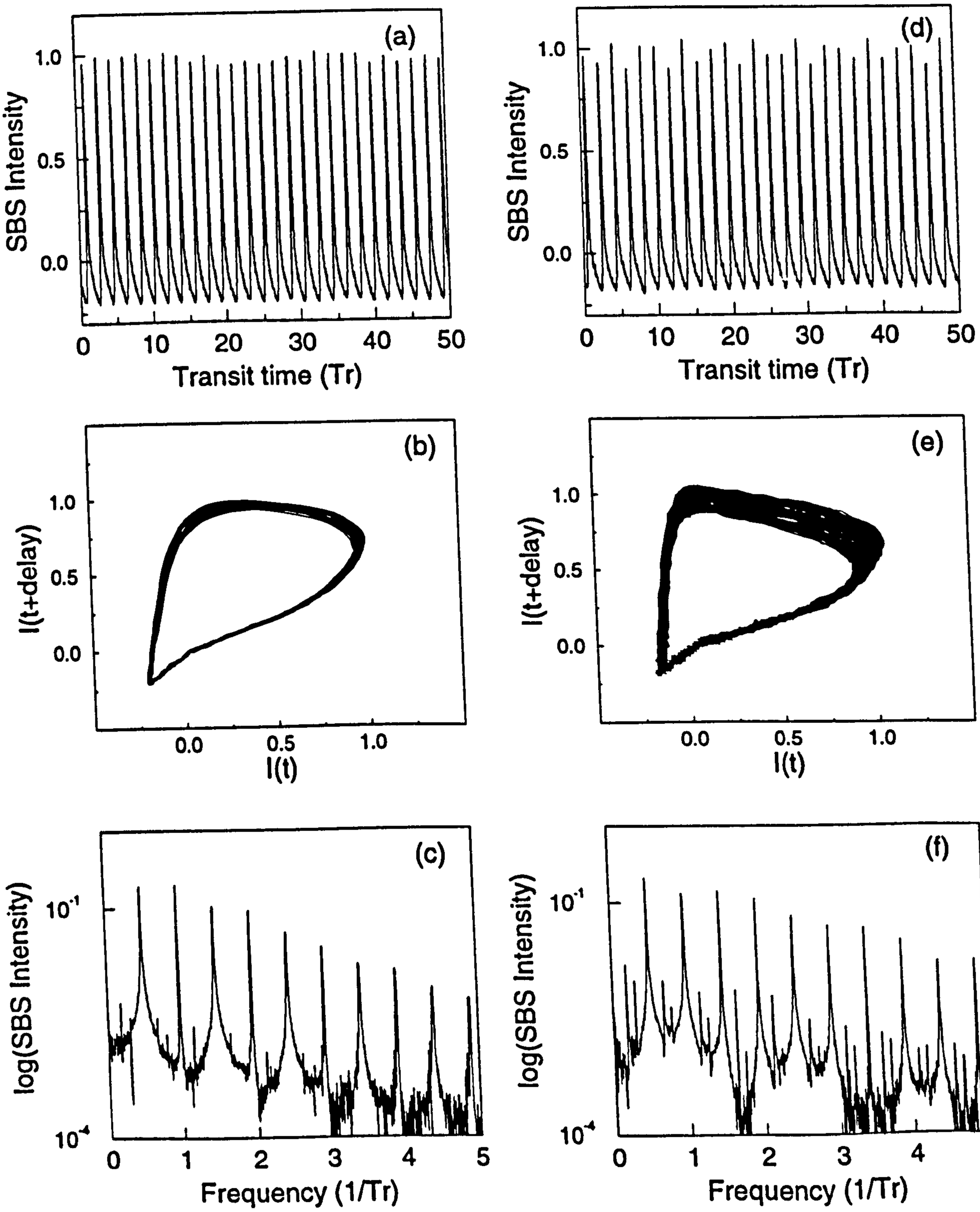

Figure 5.11 Time series (top row), phase portrait (middle row) and Fast Fourier Transform (bottom row) of dynamical behaviour encountered on the route to chaos for a driven SBS oscillator with increasing modulation depth. (a-c) Periodic emission at 5%, and (e-f) emerging quasiperiodic motion at 10%.

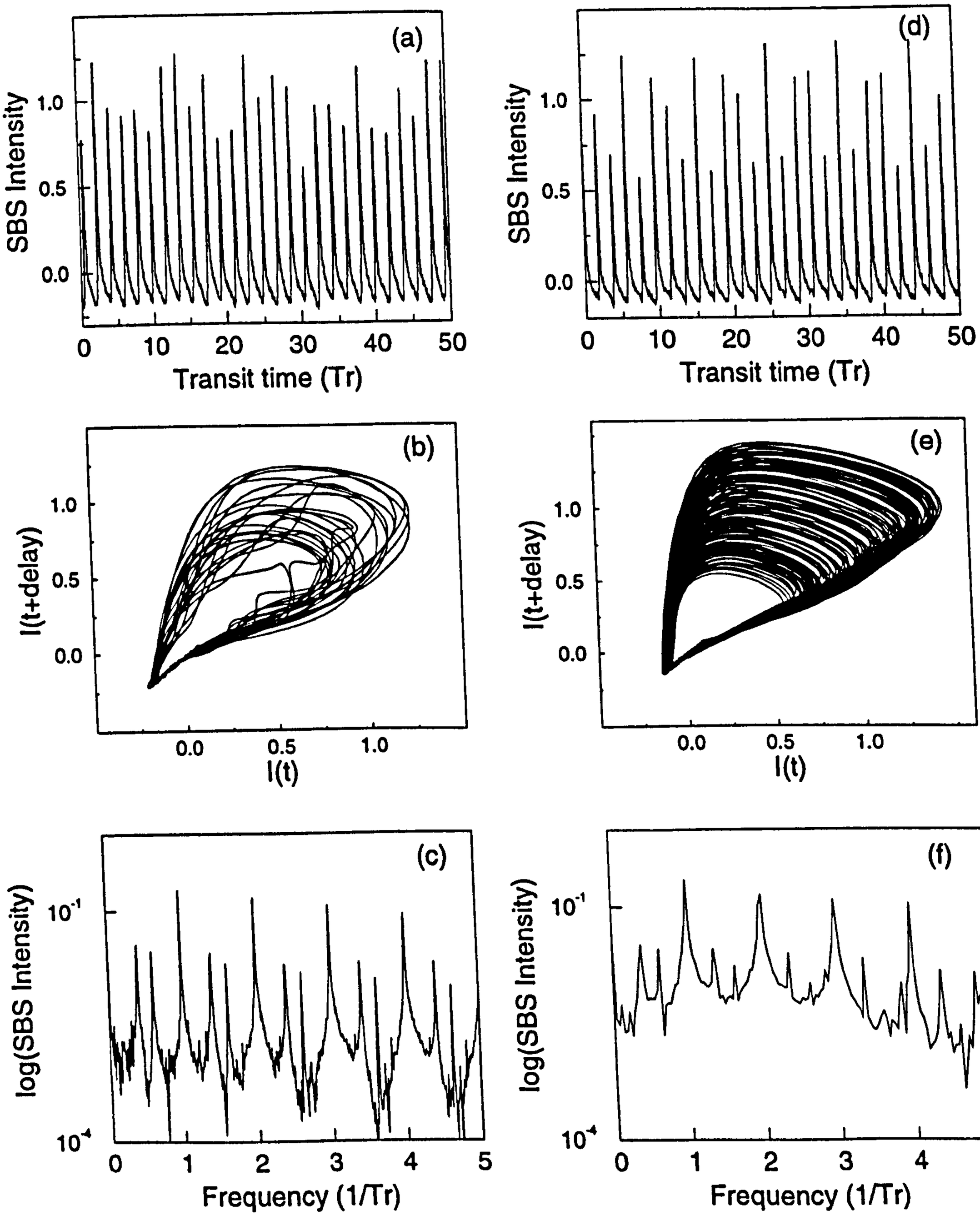

Figure 5.12 Time series (top row), phase portrait (middle row) and Fast Fourier Transform (bottom row) of dynamical behaviour encountered on the route to chaos for a driven SBS oscillator with increasing modulation depth. (a-c) Quasiperiodic motion at 20%, and finally (e-f) chaotic emission at 25%.

The quasiperiodic motion became more predominant at 20% with spiralling, wrapping toroidal motion being clearly observable in the phase portrait, Figure 5.12(c). The emergence of a third new frequency can be found in the power spectra which also reveals the dominant harmonic of the FSR frequency, $(1/T_R)$. Finally, for a modulation depth of 25%, the quasiperiodic motion loses stability and the evolution of the Stokes emission becomes chaotic. This was confirmed by the aperiodic amplitude of the waveform, Figure 5.12(d), and the presence of a reconstructed "strange attractor" in phase space, Figure 5.12(e). The power spectrum exhibits an apparent lifting when compared to the previous spectra. Even though a continuous power spectrum can be attributed to noise, the existence of a "strange attractor" through the adjustment of a control parameter provides firm evidence of chaotic behaviour. The first report of a quasiperiodic route to chaos predicted the creation of a three frequency torus [10] followed by chaos for an adjustment of a control parameter. However, Ruelle, Takens and Newhouse [11] have demonstrated that a parameter dependent two frequency torus can be destroyed in phase space and become chaotic in the presence of perturbations e.g. noise. The generation of a torus followed by the emergence of chaos for a change in the experimental control parameter, provides a clear indication of a Ruelle-Takens-Newhouse, quasiperiodic route to chaos.

5.4.2 Comparison with Theoretical Findings and Characterisation of the Attractor

The theoretical results presented in this section were obtained from the model discussed in section 5.2. Figure 5.13 illustrates two examples of theoretical dynamical behaviour showing both complex quasiperiodic motion and the slow enveloping effect

attributed to the beating of the drive frequency with the fundamental (FSR) frequency or its harmonics. The quasiperiodic emission was generated for a drive frequency of 600kHz with a modulation of 25%, Figure 5.13(a). The theoretical Stokes emission with the slowly varying envelope, Figure 5.13(b), used a drive frequency of 1.78MHz for the same modulation. The experimental dynamics presented in section 5.3.3 show a strong agreement with the theoretical findings, matching the forms of dynamical behaviour for the appropriate frequency regions.

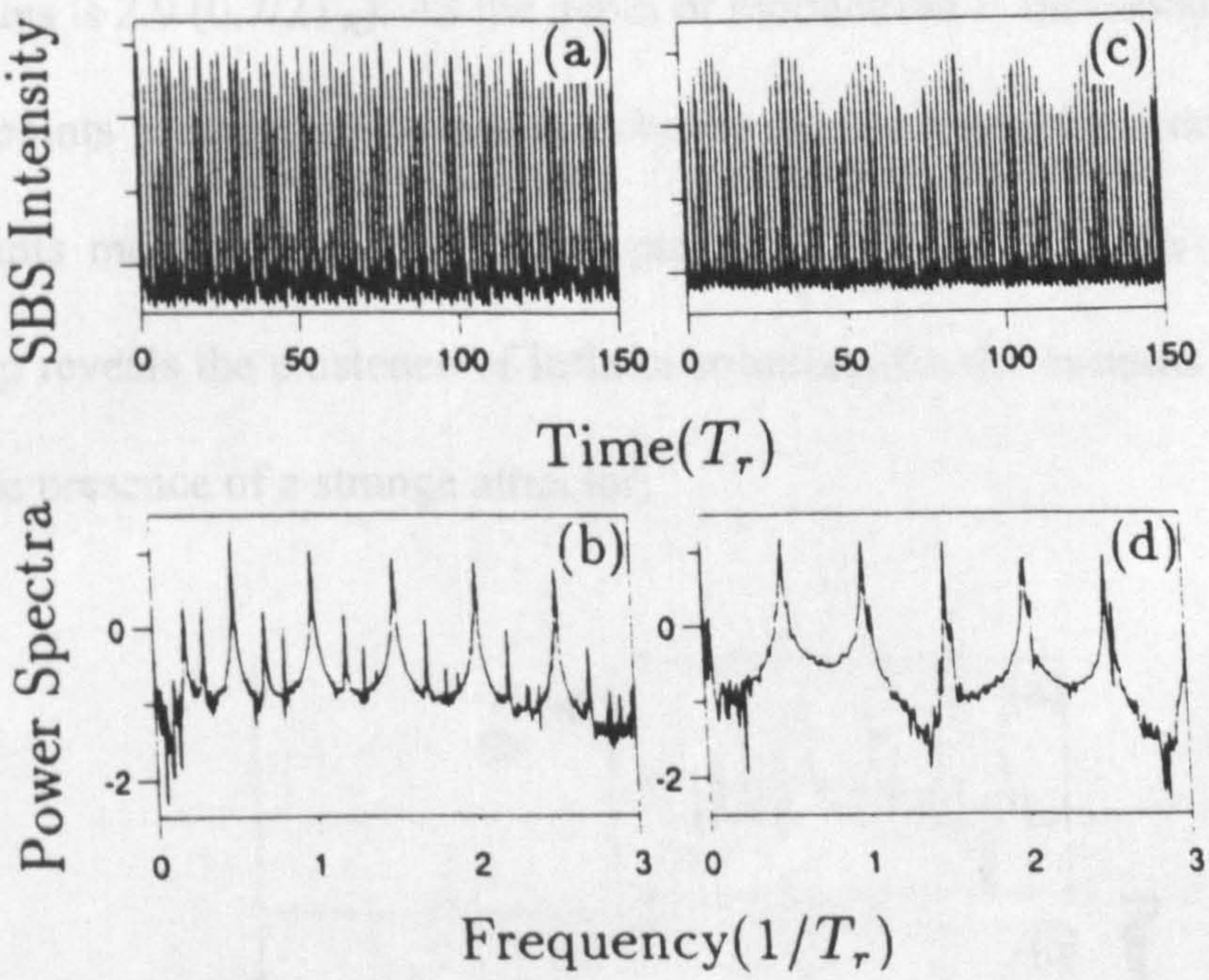

Figure 5.13 Theoretical Stokes emission and corresponding power spectra for different drive frequencies, (a) and (b) at 600kHz, and (c) and (d) at 1.78MHz, the modulation depth being held constant at 25%.

The theoretical route to chaos is shown in Figure 5.14, for an increasing depth of modulation. The drive frequency used in the model was fixed at value of $0.7/2T_R$, (609kHz). For a clearer analysis of the route to chaos a Poincaré Map is used to examine the trajectories of the dynamics in phase space. A Poincaré Map consists of a two

dimensional plane which slices through the high dimensional phase space. This provides a relatively simple method for observing dynamical trajectories as they traverse the attractor of interest. In Figure 5.14(c), the Poincaré map reveals an ellipse composed of discrete points. The analogy of this process is to imagine taking a slice through a hollow ring. The discrete points represent individual trajectories as they travel around the attractor passing through the Poincaré section. The elliptical shape indicates the presence of a two frequency torus which is associated with quasiperiodic motion. The ratio of the two frequencies is 2.9 ($0.7/2T_R$). As the depth of modulation is increased, Figure 5.14(b), the discrete points in phase space occur more frequently until at a modulation depth of 32% the points merge into a continuous perimeter. The continuous perimeter in the Poincaré map reveals the existence of infinite solutions for the systems trajectories, thus indicating the presence of a strange attractor.

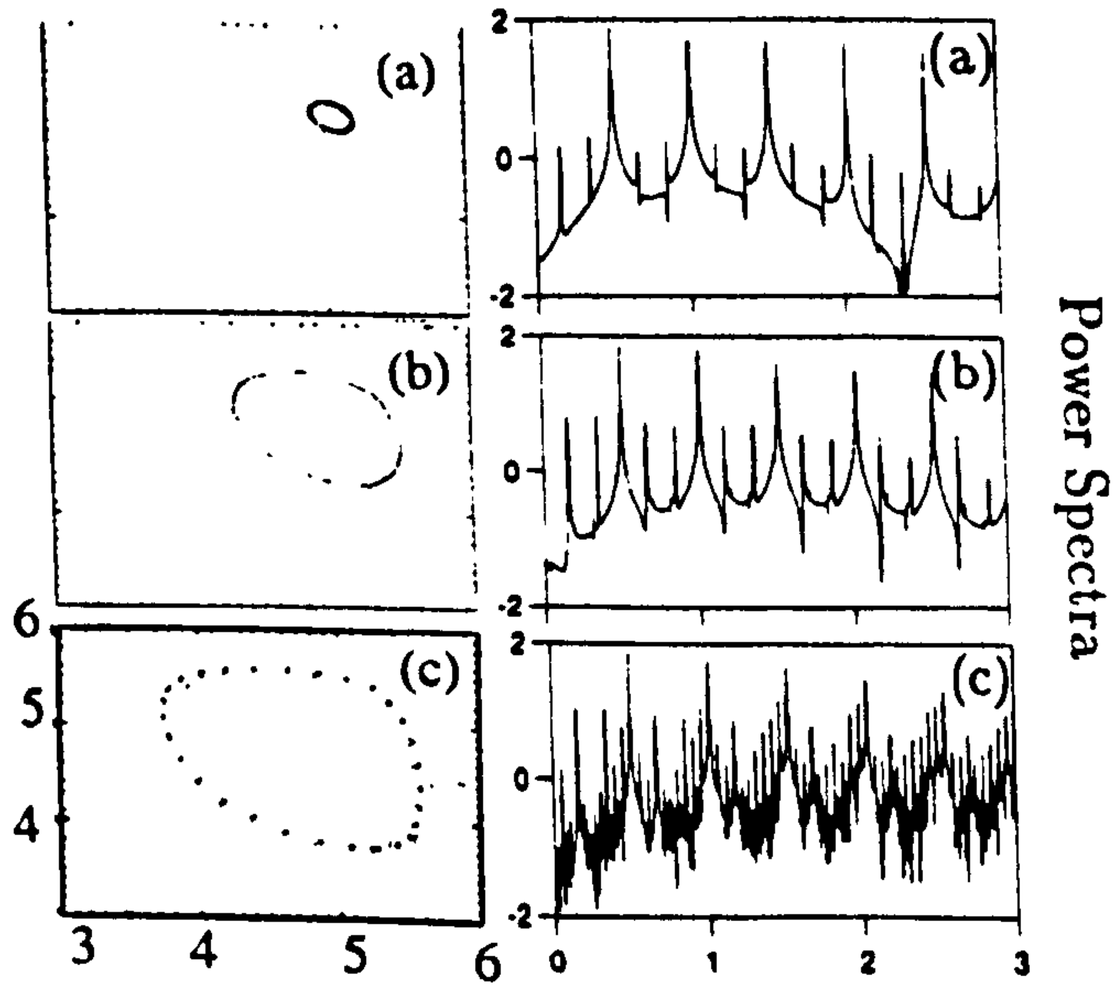

Figure 5.14 Quasiperiodic route to chaos upon increasing the depth of modulation 5, 20, 32%, from bottom to top, the modulation frequency being held at $0.7/2T_R$.

Further evidence of a theoretical route to chaos is provided by the power spectra, Figure 5.14(a)-(c). A predominant peak located at the fundamental frequency ($1/2T_R$) can be seen quite clearly in the power spectrum for a modulation of 5%. As the modulation depth increases, the power spectrum becomes more complicated with the appearance of higher harmonics. The chaotic state is signified by a slight lifting and the formation of an almost continuous spectrum, Figure 5.14(a). The Grassberger-Procaccia algorithm was used to determine the correlation dimension for both experimental and theoretical data sets, Figure 5.15.

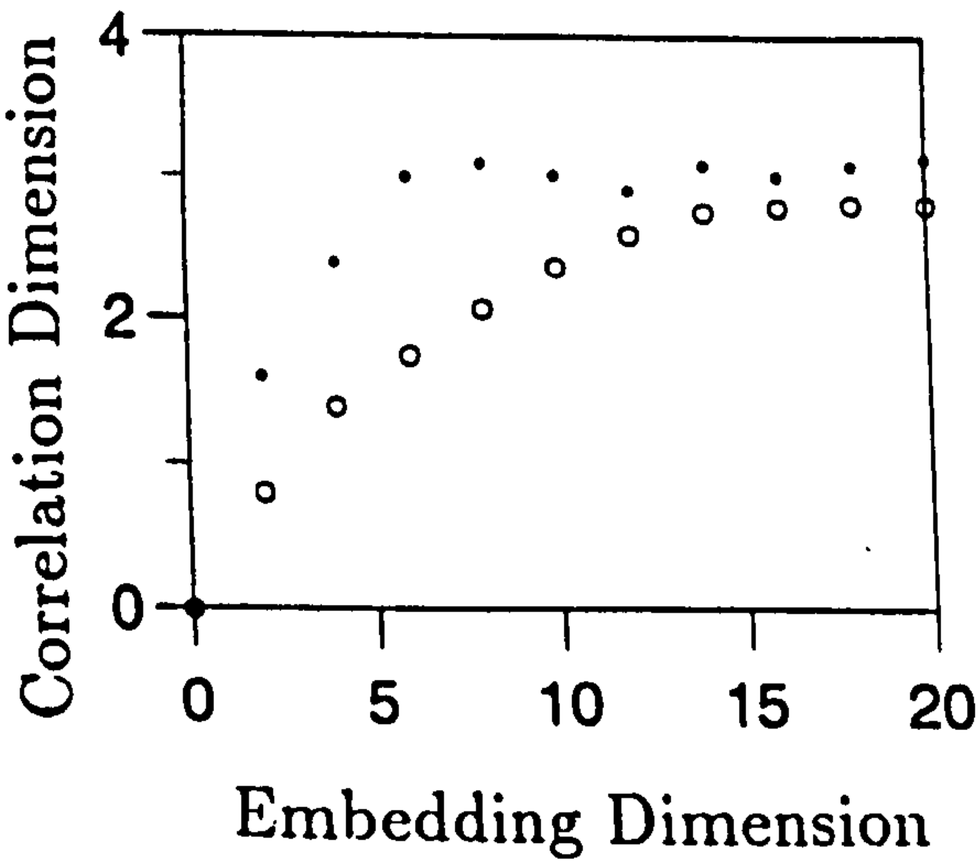

Figure 5.15 Correlation Dimension Vs embedding dimension for weak chaotic Stokes emission. The closed and open circles correspond to experimental and theoretical measurements respectively.

The value of the converged correlation dimension, D_2 =3.15 for the experimental set, gives reasonable agreement with the theoretical measurement D_2 = 2.9. A slow convergence against the embedding dimension and a slightly larger fractal dimension are a direct result of instrument induced noise.

5.5 Conclusions

In this chapter the dynamical behaviour of a spatially extended, non-autonomous SBS oscillator, driven locally by a periodically modulated pump through the boundary condition has been investigated experimentally. For SBS generated in an optical fibre without external feedback, the modulated pump creates a corresponding modulation in the Stokes intensity. However, the underlying stochastic dynamics of the open flow SBS system prevailed over the range of control parameters explored in the experiments. The addition of external feedback gave rise to deterministic features in the Stokes emission which displayed a range of dynamical features when driven with a modulated pump. The time averaged (steady state) characteristics of the driven SBS oscillator showed a displacement in both the transmitted pump "shoulder" and the SBS curves. The displacement revealed a decrease in the SBS conversion efficiency which was attributed to the reduction of the time averaged pump power. The dynamical behaviour of the driven SBS oscillator depended upon the choice of control parameter settings. For drive frequencies located at the fundamental frequency or sub-harmonics, periodic oscillations were observed. However, slight detuning of the drive frequency gave rise to quasiperiodic motion caused by frequency beating. Toroidal motion and chaos was also found through sweeping of the drive frequency at a fixed modulation depth. At a fixed frequency of 610kHz, chaos was found via the quasiperiodic route for increasing modulation depth. The experimental results showed both strong qualitative and quantitative agreements with theoretical findings. In particular the quasiperiodic route to

chaos through an increase in modulation depth. Quantitative analysis of both sets of results using correlation dimension techniques provided an experimental fractal dimension of ~3.15. This shows reasonable agréement with the theoretical value of ~2.9, accounting for experimental noise.

5.6 References

[1] J.M.T.Thompson and H.B.Stewart, *Nonlinear Dynamics and chaos*, (John Wiley & Sons, 1987).

[2] U.Parlitz and W.Lauterborn, "Period-doubling cascades and devil's staircases of the driven van der Pol oscillator", Phys.Rev.A, Vol.**36**(3), pp.1428-33, (1987).

[3] W.Lu and R.G.Harrison, "Nonlinear dynamical and chaotic features in stimulated scattering phenomena", Europhs.Lett., Vol.**16**(7), pp.655-60, (1991), and W.Lu, A.Johnstone, and R.G.Harrison, "Deterministic dynamics of stimulated scattering phenomena with external feedback", Phys.Rev.A, Vol.**46**(&), pp.4114-22, (1992).

[4] R.W.Boyd, K.Rzazewski and P.Narum, "Noise initiation of stimulated Brillouin scattering", Phys.Rev.A, Vol.**42**(9), pp.5514-21, (1990).

[5] B.van der Pol, "Forced oscillations in a circuit with nonlinear resistance", Phil.Mag., Vol.7(3), pp.65-80, (1927).

[6] Private communication with Isle Optics Ltd.

[7] R.G.Harrison, J.S.Uppal, A.Johnstone and J.V.Maloney, "Evidence of chaotic stimulated Brillouin scattering in optical fibres", Phys.Rev.Lett., Vol.**65**(2), pp.167-70, (1990).

[8] R.G.Harrison, P.M.Ripley and W.Lu, "Observation and characterisation of deterministic chaos in stimulated Brillouin scattering with weak feedback", Phys.Rev.A, Vol.**49**(1), pp.R24-27, (1994).

[9] J.H.Baxter, M.Bocko and D.H.Douglas, "Behaviour of a nonlinear resonator driven at subharmonic frequencies", Phys.Rev.A, Vol.41(2), pp.619-25, (1990).

[10] D.Ruelle and F.Takens, "On the Nature of Turbulence", Commun. Math. Phys., Vol.20, pp.167-92, (1971).

[11] S.Newhouse, D.Ruelle and F.Takens, "Occurrence of strange Axiom A attractors near quasiperiodic flows on T_m (m = 3 or more)", Commun.Math.Phys.,Vol.64, pp.35, (1978).